Institut für Astronomische und Physikalische Geodäsie

Integrated Sensor Analysis of the GRACE Mission

Björn Frommknecht

Vollständiger Abdruck der von der Fakultät für Bauingenieur- und Vermessungswesen der Technischen Universität München zur Erlangung des akademischen Grades eines

Doktor-Ingenieurs (Dr.-Ing.)

genehmigten Dissertation.

Vorsitzender:	Univ.-Prof. Dr.-Ing. M. Schilcher
Prüfer der Dissertation:	
	1. Univ.-Prof. Dr.-Ing., Dr.h.c. R. Rummel
	2. Univ.-Prof. Dr.-Ing. J. Müller, Leibniz Universität Hannover

Die Dissertation wurde am 31.10.2007 bei der Technischen Universität München eingereicht und durch die Fakultät für Bauingenieur- und Vermessungswesen am 06.12.2007 angenommen.

Abstract

The geodetic twin satellite mission GRACE delivers gravity field models of the Earth of unprecedented accuracy. However, the originally defined mission baseline is not (yet) reached. Among others, deficiencies in the gravity field sensor system or the related signal processing could be responsible for the degraded performance.

In this work the GRACE gravity field sensor system is subject to an integrated sensor analysis.

First, models of the satellites' environment are derived, including models for the direct gravitational accelerations caused by the Earth, the Sun and the Moon and indirect effects like Earth and ocean tides. Among the non-gravitational forces air drag, solar radiation pressure and Earth albedo are investigated. The purpose of this part of the work is to model what the gravity sensor system should 'feel'.

The second part contains mathematical models of the individual elements of the gravity field sensor system, the star sensor, the accelerometer,the K-band ranging system and the GPS receiver, to derive an understanding of how the sensors detect their environment.

The third part consists of the analysis of the raw instrument data. The real measurement signals are analyzed and the measurement performance in terms of a noise level is derived. They are compared to the model output and the derived noise level to the one specified by the instruments' manufacturers.

Finally the processing of the raw instrument data to the level that is used for the gravity field determination is investigated. A main processing step for all sensors is the application of an anti-aliasing low-pass filter. Alternative filters are tested and evaluated against the filter used for the official data processing.

Zusammenfassung

Die Satellitenmission GRACE liefert Schwerefeldmodelle bisher nicht verfügbarer Qualität. Aber die vor dem Start anvisierte Genauigkeit ist (noch) nicht erreicht worden. Neben anderen möglichen Ursachen könnten Fehler im Schwerefeldmesssystem und in der dazugehörigen Signalverarbeitung für die reduzierte Genauigkeit verantwortlich sein.

In dieser Arbeit wird das GRACE Schwerefeldmesssystem einer integrierten Sensoranalyse unterzogen.

Zunächst werden Modelle der Satellitenumgebung vorgestellt. Unter den direkten gravitativen Kräften werden die Erdanziehung sowie die Anziehung von Sonne und Mond modelliert, unter den indirekten gravitativen Kräften werden Erd- und Ozeangezeiten vorgestellt. Unter den nicht-gravitativen Kräften werden der Luftwiderstand, der Strahlungsdruck der Sonne und Erdalbedo untersucht. Diese Modelle geben Auskunft darüber, was das Schwerefeldmesssystem detektieren soll.

Im zweiten Teil werden mathematische Modelle der einzelnen Sensoren des Schwerefeldmesssystems erarbeitet. Im einzelnen werden der Beschleunigungsmesser, der Sternsensoren, das K-band Abstandsmesssystem und der GPS-Empfänger modelliert, um eine Vorstellung darüber zu erlangen, wie die Satelliten ihre Umgebung wahrnehmen.

Im nächsten Teil werden die rohen Messdaten der Instrumente untersucht. Die Messsignale werden analysiert und die Qualität der Sensoren, wie auch die der Messung, wird über das Fehlerniveau bestimmt. Die gemessenen Signale werden mit den Erwartungen aus den Modellen verglichen, insbesondere wird das aus den Messungen abgeleitete Rauschniveau mit den durch die Intrumentenhersteller gegebenen Spezifikationen verglichen.

Schließlich wird die Prozessierung von Rohdaten zu Daten, die für die Schwerefeldbestimmung verwendet werden, untersucht. Ein Hauptschritt der Umwandlung ist die Anwendung eines Tiefpassfilters um die Datenrate ohne das Auftreten von Aliasingeffekten reduzieren zu können. Verschiedene alternative Filter werden diskutiert und miteinander verglichen.

Contents

Part I.

Introduction

1. Overview of the GRACE mission

GRACE (Gravity Recovery And Climate Experiment) is a joint project of the National Aeronautics and Space Administration (NASA) and the German Space Center (DLR). The mission has been proposed in 1996 jointly by the University of Texas at Austin, Center for Space Research (UTCSR), the GeoForschungsZentrum Potsdam (GFZ), the Jet Propulsion Laboratories (JPL), Space Systems/Loral (SSL), the Deutsches Zentrum für Luft- und Raumfahrt e.V. (DLR), and Astrium GmbH. The GRACE mission is successor to the CHAMP mission and was selected as the second mission in NASA's Earth Science System Pathfinder project (ESSP). The Principal Investigator is Prof. Byron Tapley (UTCSR), the Co-Principal Investigator of the mission is Prof. Ch. Reigber of the GeoForschungsZentrum Potsdam. The goal of the mission is to derive highly accurate models of the Earth gravity field for a period of at least five years. As an additional goal, GPS measurements are used to recover profiles of the ionosphere and the troposphere by limb sounding.

Unlike the single satellite mission CHAMP, the GRACE mission consists of two identical satellites, GRACE A and GRACE B, resp. Tom and Jerry. The satellite constellation is depicted in figure 1.1.

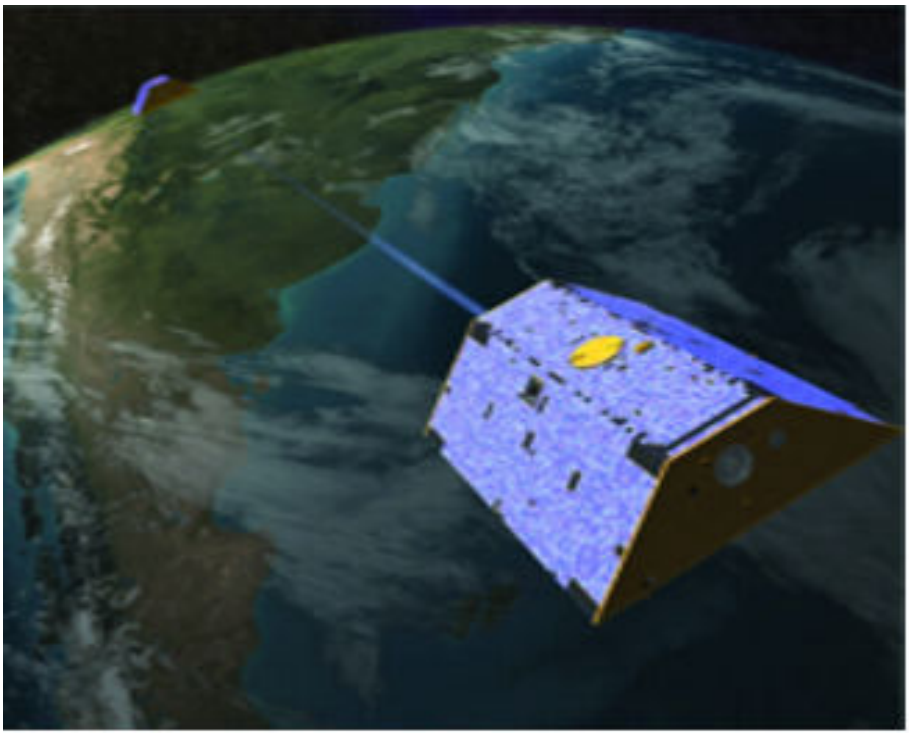

Figure 1.1: Overview of the GRACE satellites configuration. Considering the satellite in the front, the GPS antenna and the star sensor baffles are visible. The K-band microwave link is indicated as a blue ray. On the back side of the satellite, the ion thruster used for orbit maintenance is visible.

Each satellite is equipped with a GPS Turbo Rogue Space Receiver that allows precise orbit determination. In order to be able to take into account the effect of non-gravitational forces, both satellites are equipped with ultra-sensitive Super STAR capacitive accelerometers. An absolute novelty is the use of a K-band microwave link between the satellites to measure the inter-satellite distance with micrometer

accuracy.

To guarantee sufficient power supply and to enable operation of the K-band system, the attitude of the satellites is observed by star sensors and controlled by cold gas attitude thrusters and magnetic torque rods.

The GRACE satellites were successfully launched on March 17, 2002 from Plesetsk Cosmodrome in Russia. The inclination of the satellites orbits is about 89° , the semi-major axis was about 6870 km, the eccentricity was almost zero: 0.001. Since then the orbit decayed to an altitude of about 460 km. The nominal distance between the two satellites is 220 ±50 km.

2. Definition of integrated sensor analysis

The subject to the integrated sensor analysis is a complex system consisting of several individual sensors. The purpose of the integrated sensor analysis is to understand

- the functionality of each individual sensor,
- the interaction between the individual sensors and their operation as a sensor system.

The former is achieved by deriving mathematical models of the measurement process of each sensor. A common way is to model the signal that is to be sensed and then to model the error behavior of the sensor. The error behavior of the sensor is usually given by the manufacturer. The combination of the simulated signal and simulated error is a good approximation of the real measurement behavior.

The latter is reached by combining the individual models to form the 'integrated' model: The signal flow in the sensor systems is derived, thus the dependencies can be modeled. Also the processing steps necessary to transform between the individual data levels are investigated.

3. Goals and topics of the work

This work consists of three parts:

- The description of the forces acting on the GRACE satellites,
- the description of the GRACE system simulator and
- the description of the real data processing and analysis.

The first part describes models for volume forces and surface forces that act on the GRACE satellites including models for gravitational forces like the gravity of the Earth or the effects caused by third bodies like the Sun or the Moon. Among the surface forces atmospheric drag models, models for solar radiation pressure and for Earth albedo are analyzed. Special emphasis is put on the analysis of the atmospheric drag models, as at the orbit height of GRACE air drag is the dominant surface force.

The second part describes how the GRACE gravity field sensor system 'feels' its environment. Measurement models for the sensors that constitute the gravity field sensor system, namely the star sensor, the accelerometer, the K-band ranging system and the GPS receiver are derived as mathematical models.

The third part is devoted to the analysis of the real satellite data. Performance estimates for the individual instruments are derived and compared to the theoretical performance estimated in the second part. Also the transformation from raw satellite data to the data level that is used for the gravity field determination is investigated.

Part II.

Force models

4. Gravitational forces

4.1. Introduction

The gravitational forces are by far the strongest forces that act on the satellites and mainly determine their orbits and relative motion. In the following sections the different kinds of gravitational forces will be briefly introduced. In terms of magnitude one expects that the gravitational forces of the Earth are strongest, followed by the forces caused by Moon, Sun and the solid Earth and ocean tides.

4.2. Earth gravity field

The gravitational accelerations are the first derivative of the gravitational potential of the Earth. The potential and its first order derivatives can be expressed in the following way:

$$V_i = \frac{GM}{r} \sum_{l=0}^{l_{max}} \lambda_i \left(\frac{R}{r}\right)^l \sum_{m=0}^{l} p\,(\alpha \cos(m\lambda) + \beta \sin(m\lambda)), \tag{4.1}$$

with

differentiation w.r.t	λ_i	p	α	β
none	1	$\bar{P}_{lm}$	$\bar{C}_{lm}$	$\bar{S}_{lm}$
r	$-\frac{(l+1)}{r}$	$\bar{P}_{lm}$	$\bar{C}_{lm}$	$\bar{S}_{lm}$
θ	1	$\bar{P'}_{lm}$	$\bar{C}_{lm}$	$\bar{S}_{lm}$
λ	1	$m\bar{P}_{lm}$	$\bar{S}_{lm}$	$-\bar{C}_{lm}$

The normalized associated Legendre functions and their derivatives are computed by recursive formulas. For convenience, the following substitutions were made: $P_{lm} = \bar{P}_{lm}(\cos\theta)$, $P'_{lm} = \frac{\partial \bar{P}_{lm}(\cos\theta)}{\partial\theta}$.

$$\begin{aligned}
P_{lm} &= \eta \cos\theta P_{l-1,m} - \sigma P_{l-2,m}, && (4.2)\\
P_{l,l-1} &= \tau \cos\theta P_{l-1,l-1}, && (4.3)\\
P_{ll} &= \nu \sin\theta P_{l-1,l-1}, && (4.4)\\
P'_{lm} &= \eta(\cos\theta P'_{l-1,m} - \sin\theta P_{l-1,m}) - \sigma P'_{l-2,m}, && (4.5)\\
P'_{l,l-1} &= \tau(\cos\theta P'_{l-1,l-1} - \sin\theta P_{l-1,l-1}), && (4.6)\\
P'_{ll} &= \nu(\sin\theta P'_{l-1,l-1} + \cos\theta P_{l-1,l-1}), && (4.7)
\end{aligned}$$

with the normalization factors:

$$\eta = \sqrt{\frac{(2l+1)(2l-1)}{(l+m)(l-m)}}, \sigma = \sqrt{\frac{(l+m)(l-m)}{(2l+1)(2l-1)}}, \tau = \sqrt{2l+1}, \nu = \sqrt{\frac{2l+1}{2l}}. \tag{4.8}$$

The initial values are: $P_{0,0} = 1$, $P_{1,0} = \sqrt{3}\cos\theta$, $P_{1,1} = \sqrt{3}\sin\theta$, $P'_{0,0} = 0$, $P'_{1,0} = -\sqrt{3}\sin\theta$, $P'_{1,1} = \sqrt{3}\cos\theta$.

To obtain the accelerations in cartesian coordinates, the first order derivatives in spherical coordinates have to be transformed using the chain rule:

$$\ddot{x}_e = \frac{\partial V}{\partial x} = \frac{\partial V}{\partial r}\frac{\partial r}{\partial x} + \frac{\partial V}{\partial \theta}\frac{\partial \theta}{\partial x} + \frac{\partial V}{\partial \lambda}\frac{\partial \lambda}{\partial x}, \tag{4.9}$$

$$\ddot{y}_e = \frac{\partial V}{\partial y} = \frac{\partial V}{\partial r}\frac{\partial r}{\partial y} + \frac{\partial V}{\partial \theta}\frac{\partial \theta}{\partial y} + \frac{\partial V}{\partial \lambda}\frac{\partial \lambda}{\partial y}, \tag{4.10}$$

$$\ddot{z}_e = \frac{\partial V}{\partial z} = \frac{\partial V}{\partial r}\frac{\partial r}{\partial z} + \frac{\partial V}{\partial \theta}\frac{\partial \theta}{\partial z}, \tag{4.11}$$

where the partial derivations are simply derived from geometry:

$$\partial r/\partial x = \sin\theta \cdot \cos\lambda, \tag{4.12}$$

$$\partial r/\partial y = \sin\theta \cdot \sin\lambda, \tag{4.13}$$

$$\partial r/\partial z = \cos\theta, \tag{4.14}$$

$$\partial \theta/\partial x = \cos\theta \cdot \cos\lambda/r, \tag{4.15}$$

$$\partial \theta/\partial y = \cos\theta \cdot \sin\lambda/r, \tag{4.16}$$

$$\partial \theta/\partial z = -\sin\theta/r, \tag{4.17}$$

$$\partial \lambda/\partial x = -\sin\lambda/(r \cdot \sin\theta), \tag{4.18}$$

$$\partial \lambda/\partial y = \cos\lambda/(r \cdot \sin\theta). \tag{4.19}$$

For simulation purposes or for orbit integration it is necessary to transform these accelerations from the earth-fixed system to the inertial system.

Figure 4.1 shows the resulting accelerations in the Inertial Reference Frame (IRF). The magnitude is about 8.4 m/s^2 or about 84% of the acceleration on the Earth's surface. We notice a modulation with the orbit frequency, as the distance from the satellite to the Earth and its velocity vary during a revolution. The first term of the spherical harmonic expansion of the gravity field, i.e. l=0, accounts for 99% of the gravitational acceleration, a expansion up to degree 2, i.e. including the effect of the Earth's oblateness, represents about 99.99% of the characteristics of the gravitational acceleration of the Earth. Thus an expansion up to degree 2 seems to be sufficient for most purposes except gravity field determination studies of course.

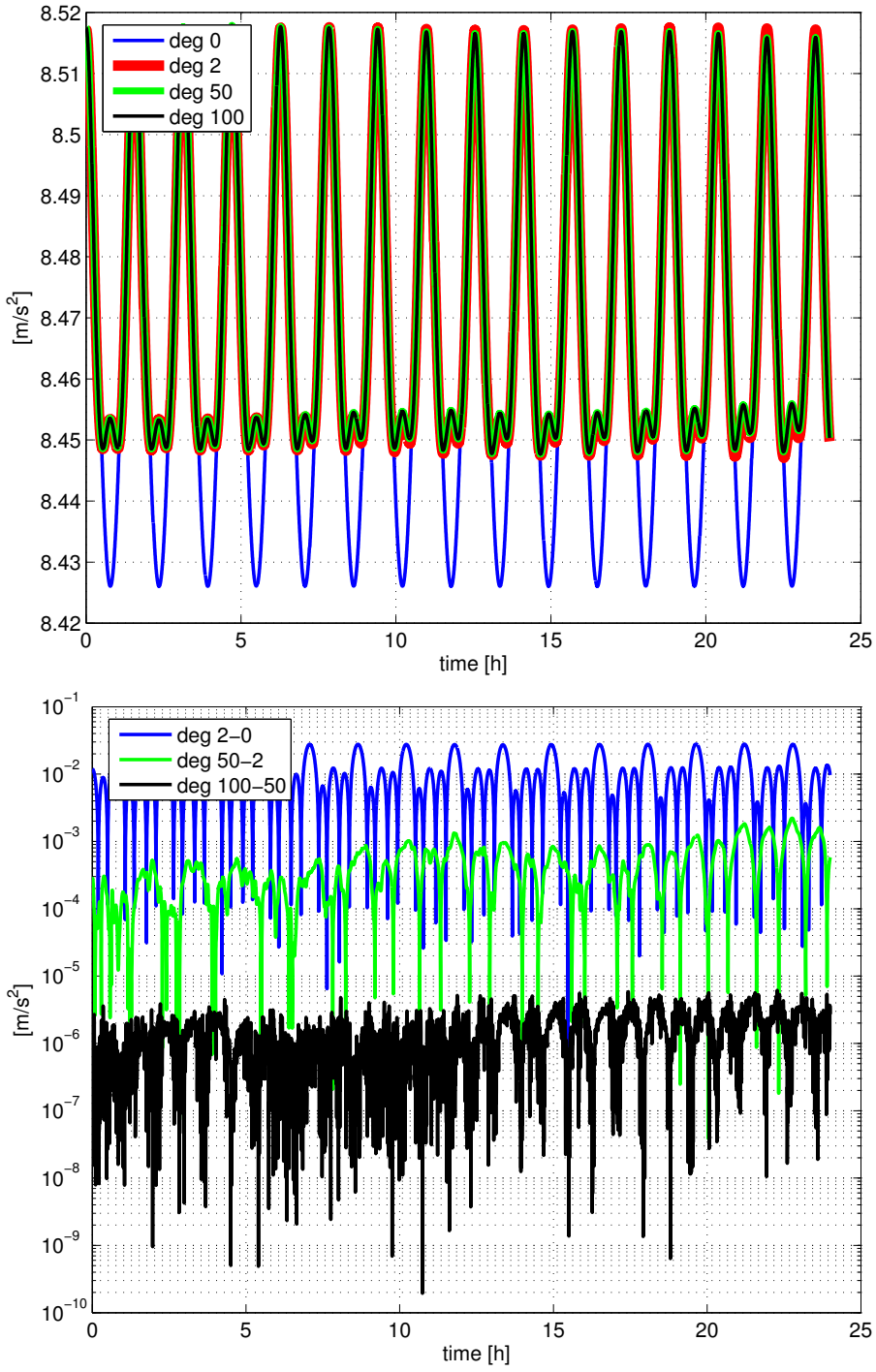

Figure 4.1: The top panel shows the gravitational accelerations induced by the Earth. The different lines show the accelerations resulting from an evaluation of the spherical harmonic series up to a certain degree. The bottom panel shows the change in acceleration from one evaluation level to the other. It seems that it is sufficient to evaluate the Legendre series up to degree 2 for simulations, as the change for higher degrees is very small.

4.3. Gravitational forces of third bodies

Gravitational forces caused by third bodies the gravitational forces caused by all other celestial bodies than the Earth. In terms of magnitude the tidal forces of Sun and Moon are dominating.

4.3.1. Direct tides

The gravitational acceleration of a third body can be described as the acceleration of a point mass M, cf. Montenbruck and Gill (2000):

$$\ddot{\bar{r}}_{sat,i} = GM \cdot \frac{\bar{r}_{body} - \bar{r}_{sat}}{|\bar{r}_{body} - \bar{r}_{sat}|^3}, \tag{4.20}$$

with

$\bar{r}_{body}$	the geocentric position vector of the body,
$\bar{r}_{sat}$	the geocentric position vector of the satellite,
GM	the gravitational constant times the mass of the attracting body.

In an earth-fixed coordinate system the acceleration of the satellite is derived as the difference between the acceleration of the satellite caused by the body and the acceleration of the Earth caused by the body:

$$\begin{aligned} \ddot{\bar{r}}_{sat,e} &= \ddot{\bar{r}}_{sat,i} - \ddot{\bar{r}}_{Earth,i} \\ &= GM \left(\frac{\bar{r}_{body} - \bar{r}_{sat}}{|\bar{r}_{body} - \bar{r}_{sat}|^3} - \frac{\bar{r}_{body}}{|\bar{r}_{body}|^3} \right). \end{aligned} \tag{4.21}$$

Figure 4.2 shows the tidal acceleration of the 'satellite relative to the Earth'-two body system due to

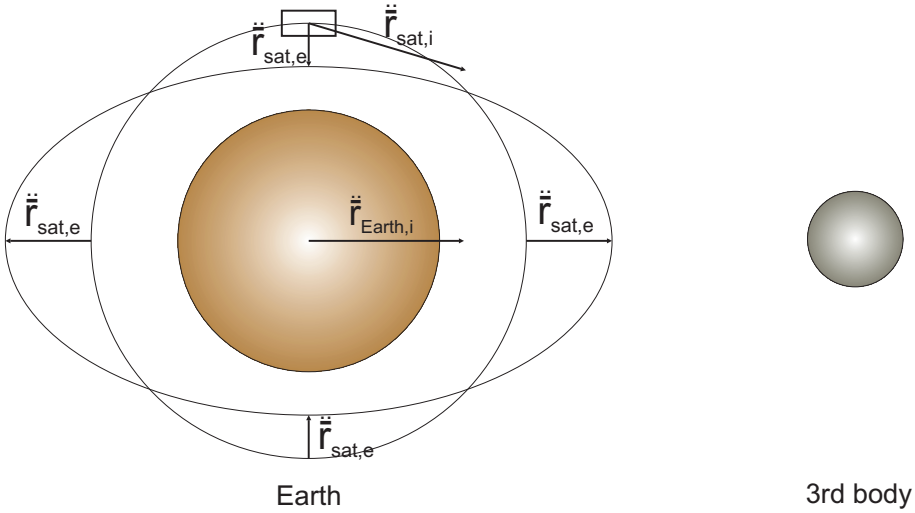

Figure 4.2: Tidal ellipse of relative acceleration with respect to the center of an accelerated coordinate system. In this example the resulting acceleration on a satellite caused by a third body like the Sun or the Moon in the earth-fixed coordinate system is shown.

a third body. It has the form of a tidal ellipse. We realize that the satellite is accelerated away from the Earth if it is in front of or behind the Earth and that the resulting acceleration is directed towards the Earth if the satellite is above or below the Earth.

This equation can not only be applied to a satellite orbiting the Earth, it also describes the relative acceleration of mass elements of a body with respect to its center of mass. Equation (4.21) therefore also describes the solid Earth tidal deformation due to Sun and Moon.

4.3.2. Indirect tides of third bodies

As mentioned above, the tidal forces of the other planets of our solar system deform the Earth. The deformation depends on the local properties of the Earth's crust. The so called 'Love numbers' reflect the elasticity of the Earth's crust. The deformation leads to a change of the mass distribution of the Earth in an earth-fixed coordinate system and therefore has to be taken into account when modeling the forces acting on a satellite. As this effect is not caused directly by the gravitating body, it is called indirect. In principle not only the Earth is deformed by this effect, but also all the other planets. For satellites orbiting the Earth this effect is neglected, as the other planets are assumed to be point masses.

The change in the mass distribution of the Earth causes a change of the geopotential. It is expanded in a series of spherical harmonic coefficients and described in more detail e.g. in McCarthy (2006). We will give here only a brief outline:

$$\Delta\bar{C}_{nm} - i\Delta\bar{S}_{nm} = \frac{k_{nm}}{2n+1}\sum_{j=2}^{3}\frac{GM_j}{GM_E}\left(\frac{R_E}{R_j}\right)\bar{P}_{nm}(\sin\Phi_j)e^{-im\lambda_j}, \tag{4.22}$$

where

k_{nm}	is the nominal Love number for degree n and order m,
R_E	is the equatorial radius of the Earth,
GM_j	is the gravitational parameter for the Moon ($j = 2$) and the Sun (j=3),
GM_E	is the gravitational parameter for the Earth,
R_j	is the distance from geocenter to Moon or Sun,
Φ_j	is the body fixed geocentric latitude of the Moon or the Sun,
λ_j	is the body fixed geocentric longitude of the Moon or the Sun,
and $\bar{P}_{nm}$	are the normalized associated Legendre functions.

The redistribution of the masses depends also on the frequency band affected by the different tidal effects, therefore a 'frequency dependent correction' to the equation above has to be derived:

$$\Delta\bar{C}_{nm} - i\Delta\bar{S}_{nm} = \sum_{f(n,m)} A(f(n,m))\cdot e^{i\theta_{f(n,m)}}, \tag{4.23}$$

where

$f(n,m)$	is the frequency of the excitation,
$A(f(n,m))$	is the amplitude of the excitation,
$\theta_{f(n,m)}$	accounts for the Earth rotation and the type of the tide.

The needed amplitudes and frequencies are tabulated in McCarthy (2006).

4.3.3. Ocean tides

The oceans react to the tidal forces as well. There are two effects:

1. the change in the mass distribution of the Earth due to the movement of the water,
2. the change in the mass distribution of the Earth due to the changed load on the Earth's crust caused by the changing water load.

The effect on the geopotential is again formulated as a change in the spherical harmonic coefficients:

$$\Delta\bar{C}_{nm} - i\Delta\bar{S}_{nm} = F_{nm}\sum_{s(n,m)}\sum_{+}^{-}(C^{\pm}_{snm} \mp S^{\pm}_{snm})e^{\pm i\theta_{snm}}), \tag{4.24}$$

where

F_{nm}	accounts for the changed load on the crust,
$C^{\pm}_{snm}, S^{pm}_{snm}$	are the ocean tide coefficients for the tide type s,
$\theta_{s_{nm}}$	is the argument of the tide type s.

The summation over + and - denotes the respective addition of the retrograde and prograde waves.

The interested reader may consult McCarthy (2006) for a more detailed description.

4.3.4. Solid Earth pole tides

The pole tides are generated by the centrifugal effect of the polar motion. They affect only the geopotential coefficients C_{21} and S_{21}:

$$\Delta\bar{C}_{21} = C_1 \cdot (m_1 - C_2 \cdot m_2), \tag{4.25}$$
$$\Delta\bar{S}_{21} = C_1 \cdot (m_1 + C_2 \cdot m_2), \tag{4.26}$$

where

C_1	$= 1.333 \cdot 10^{-9}$,
C_2	$= 0.0115$,
m_1, m_2	are the wobble variables directly related the polar motion variables (x_p, y_p).

A detailed description is to be found in McCarthy (2006).

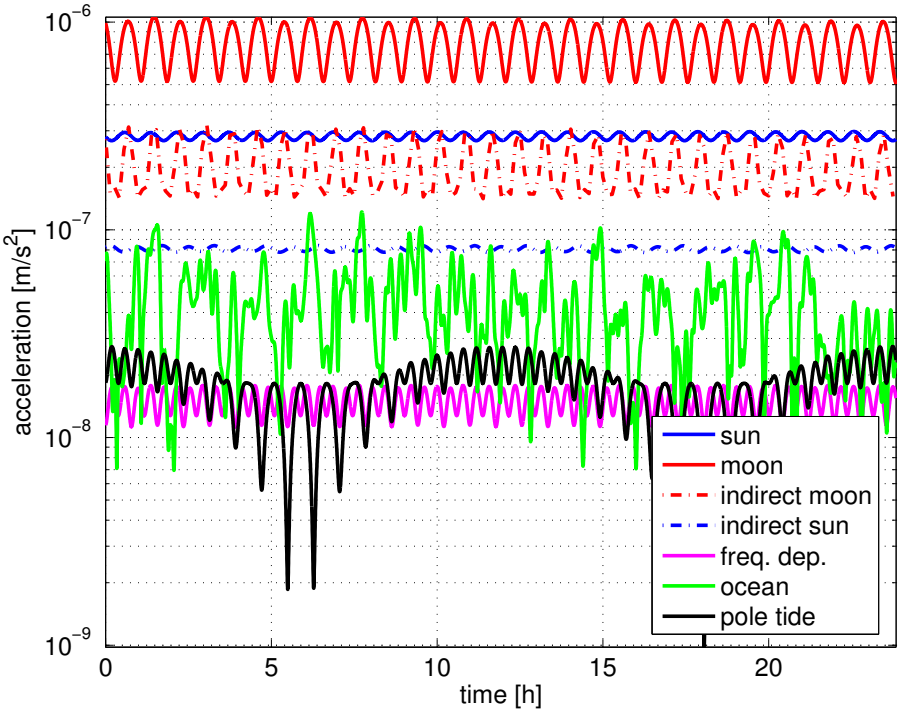

Figure 4.3: Tidal accelerations due to Sun and Moon over one day for a GRACE satellite.

Figure 4.3 shows the tidal accelerations on a GRACE satellite caused by Sun and Moon in an earth-fixed inertial reference frame over one day. We notice a strong signal on twice per revolution for all constituents. The direct tidal acceleration caused by the Moon is strongest at a level of $7 \cdot 10^{-7}$ m/s^2 followed by the direct tidal acceleration caused by the Sun at a level of about $3 \cdot 10^{-7}$ m/s^2, i.e. the

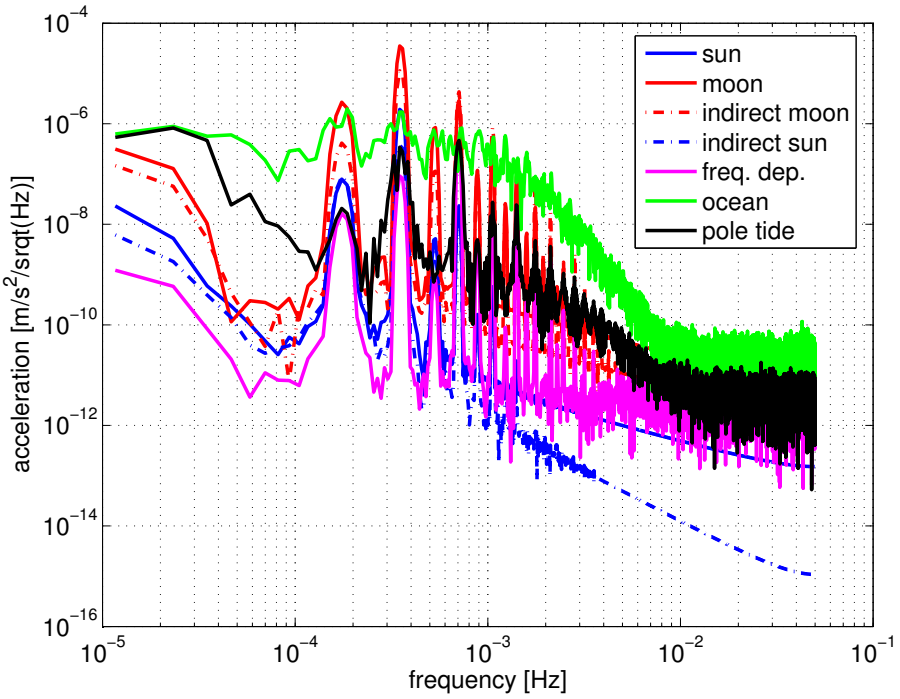

Figure 4.4: Power spectral density of the tidal accelerations caused to Sun and Moon for a GRACE satellite.

tidal force of the Moon is about three times stronger than the tidal force caused by the Sun. The ratio between the forces of Sun and Moon depends on the orientation of the orbit with respect to the positions of Sun and Moon. Here the orbit normal points towards the Sun, i.e. the distance between the satellite and the Sun is almost constant, therefore the force is also almost constant. The orbit plane is aligned with the direction to the Moon, therefore the exerted force by the Moon varies strongly.

The magnitude of the indirect tidal accelerations caused by the Moon are at level of about $2 \cdot 10^{-7}$ m/s^2, those caused by the Sun are at level of about $8 \cdot 10^{-8}$ m/s^2 . The accelerations caused by the ocean tides vary between $1 \cdot 10^{-8}$ m/s^2 and $1 \cdot 10^{-7}$ m/s^2. The magnitude of the frequency dependent corrections is about $1.5 \cdot 10^{-8}$ m/s^2, the pole tide varies between $3 \cdot 10^{-9}$ m/s^2 and $2 \cdot 10^{-8}$ m/s^2 and shows also a semidiurnal period. All effects can be detected by the GRACE sensor system, as its sensitivity is about $3 \cdot 10^{-10}$ m/s^2.

In order to compare the variations of the different effects, we consider figure 4.4, where the tidal accelerations are displayed in the frequency domain as a power spectral density. We notice that the dominant frequencies are harmonics of the orbit frequency. The dominant amplitudes are found on twice per revolution. Concerning the magnitude of the different effects, the direct tides of the Moon are strongest, followed by the ocean tides, the indirect tides of the Moon, the direct tides of the Sun, the indirect tides of the Sun, the pole tides and the frequency dependent corrections. The ocean tides show a less strong correlation with harmonics of the orbit frequency, they seem to be rather independent from the satellite's position.

5. Non-gravitational forces

5.1. Introduction

The non-gravitational forces acting on the satellites are significantly smaller than the major gravitational ones. Depending on the orbit height, either the solar radiation pressure (as for high orbiting GPS satellites) or the atmospheric drag and earth albedo (as for low orbiting satellites) have significant influence on the forces acting on the satellites. As the GRACE satellites are low orbiting satellites, we expect dominant influence of the atmospheric drag, followed by the earth albedo and the solar radiation pressure.

We did not investigate the effects of anisotropic thermal emission, the recoil from the radiowave beams used for the data downlink, electrostatic effects and others that are considered negligible.

The main emphasis was put on the analysis of different air drag models, as the air drag is the dominant non-gravitational force. A general idea was to assess if the accelerometer measurements can be replaced by model outputs.

In the following sections we will first present a macro model of the GRACE satellites, that is a prerequisite for all force models, and then present the individual models.

5.2. Macro-model of the GRACE satellites

Figure 5.1 shows an engineering drawing of the view from the front and figure 5.2 shows the view from the side of a GRACE satellite.

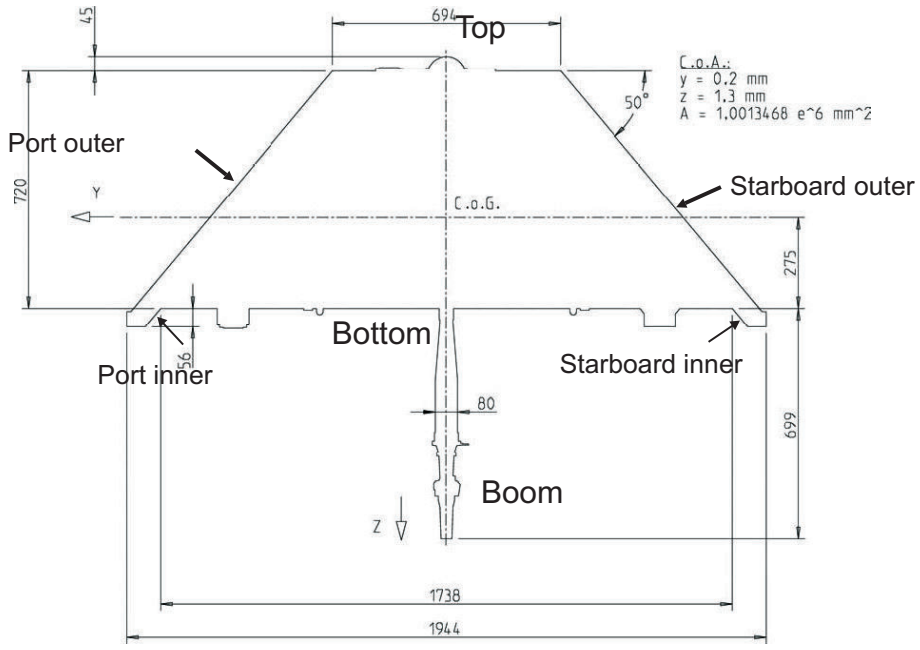

Figure 5.1: Engineering drawing of the front of a GRACE satellite. Image from Bettadpur (2007).

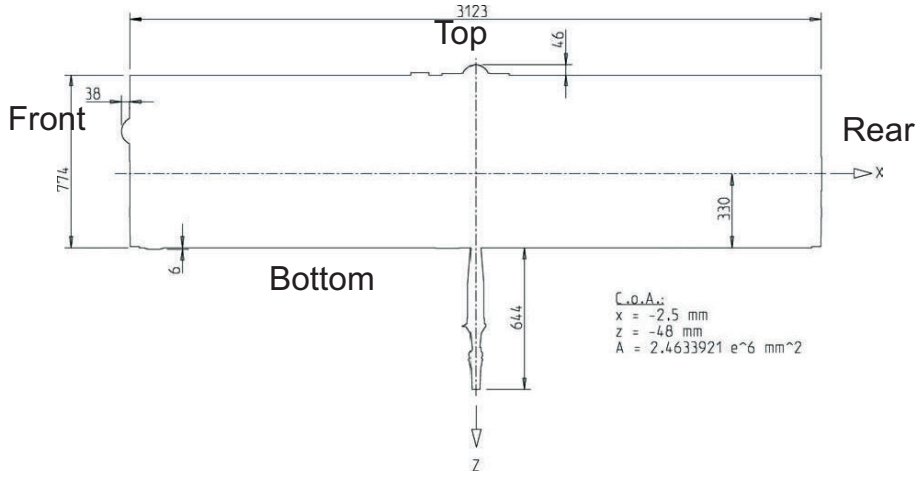

Figure 5.2: Engineering drawing of the side of a GRACE satellite. Image from Bettadpur (2007).

Table 5.2 shows the properties of the individual surface elements of the used macro-model of the GRACE satellites. The surface element location, area, normal vector in the SRF, the coefficients describing the interaction with visible light and infra-red radiation and the type of material is given.

Table 5.1: Parameters of the surface model of the GRACE satellites from Bettadpur (2007).

#	location	$A[\mathrm{m}^2]$	$\widehat{\mathrm{n}}$	C_s	C_d	C_s^{ir}	C_d^{ir}	material
1	Front	0.96	$\begin{pmatrix} +1.00 \\ +0.00 \\ +0.00 \end{pmatrix}$	0.40	0.26	0.23	0.15	SiOx/Kapton
2	Rear	0.96	$\begin{pmatrix} -1.00 \\ +0.00 \\ +0.00 \end{pmatrix}$	0.40	0.26	0.23	0.15	SiOx/Kapton
3	Starboard (outer)	3.16	$\begin{pmatrix} +0.00 \\ +0.77 \\ -0.64 \end{pmatrix}$	0.05	0.30	0.03	0.16	Si Glass Solar Array
4	Starboard (inner)	0.23	$\begin{pmatrix} +0.00 \\ -0.77 \\ +0.64 \end{pmatrix}$	0.40	0.26	0.23	0.15	SiOx/Kapton
5	Port (outer)	3.16	$\begin{pmatrix} +0.00 \\ -0.77 \\ -0.64 \end{pmatrix}$	0.05	0.30	0.03	0.16	Si Glass Solar Array
6	Port (inner)	0.23	$\begin{pmatrix} +0.00 \\ +0.77 \\ +0.64 \end{pmatrix}$	0.40	0.26	0.23	0.15	SiOx/Kapton
7	Nadir	6.07	$\begin{pmatrix} +0.00 \\ +0.00 \\ +1.00 \end{pmatrix}$	0.68	0.20	0.19	0.06	Teflon
8	Zenith	2.17	$\begin{pmatrix} +0.00 \\ +0.00 \\ -1.00 \end{pmatrix}$	0.05	0.30	0.03	0.16	Si Glass Solar Array
9	Boom	0.05	only for forces in x and y direction	0.40	0.26	0.23	0.15	SiOx/Kapton

5.3. Air drag

5.3.1. Introduction

Air drag is the force acting on the surface of a body caused by interaction with the surrounding gas mixture consisting of one or more atomic or molecular species.

Both GRACE satellites are Low Earth Orbiters (LEOs) at an altitude of less than 500 km above the Earth's surface. In this case air drag is the major non-gravitational force acting on the satellites, cf. Klinkrad and Fritsche (1998).

As both GRACE satellites are identical, the analysis is confined to one satellite, it is assumed that the results are applicable to the other one as well. The potential effect of the leading satellite shielding the following one is not investigated.

As a general formula we give according to e.g. Sagirov (1970):

$$\overline{\mathrm{F}}_{drag} = \frac{1}{2}\,\rho\,V^2\,A\,\overline{\mathrm{C}}, \tag{5.1}$$

where

$\overline{\mathrm{F}}_{drag}$	is the air drag force vector,
A	is the area of the surface,
$\overline{\mathrm{C}}$	is the ballistic coefficient vector,
ρ	is the density of the ambient air,
V	is the magnitude of the velocity of the satellite relative to the atmosphere.

The ballistic coefficient vector $\overline{\mathrm{C}}$ reflects the properties of the interaction of the incoming molecules with the surface. It is the sum of two vectorial components defined either in the {pressure,shear} system with the unit vectors $\{\widehat{\mathrm{n}},\widehat{\mathrm{t}}\}$ or in the system {drag,lift} defined by the unit vectors $\{\widehat{\mathrm{u}}_\mathrm{D},\widehat{\mathrm{u}}_\mathrm{L}\}$:

$$\overline{\mathrm{C}} = -(C_D \cdot \widehat{\mathrm{u}}_\mathrm{D} + C_L \cdot \widehat{\mathrm{u}}_\mathrm{L}) \tag{5.2}$$

and

$$\overline{\mathrm{C}} = -(C_n \cdot \widehat{\mathrm{n}} + C_t \cdot \widehat{\mathrm{t}}). \tag{5.3}$$

The unit vectors for the decomposition of the forces are given as:

$$\widehat{\mathrm{u}}_\mathrm{D} = \frac{\overline{\mathrm{V}}}{V} = \widehat{\mathrm{V}}, \tag{5.4}$$

$$\widehat{\mathrm{u}}_\mathrm{L} = \frac{\widehat{\mathrm{n}} - \widehat{\mathrm{u}}_\mathrm{D} \cdot \cos\phi}{\sin\phi}, \tag{5.5}$$

$$\widehat{\mathrm{t}} = \widehat{\mathrm{n}} \times \frac{(\widehat{\mathrm{V}} \times \widehat{\mathrm{n}})}{\sin\phi}, \tag{5.6}$$

where

$\widehat{\mathrm{V}}$	is the unit vector of the relative velocity,
$\widehat{\mathrm{n}}$	is the surface normal unit vector,
$\widehat{\mathrm{t}}$	is the surface tangent unit vector,
ϕ	is the angle between the vector of relative velocity and the surface normal.

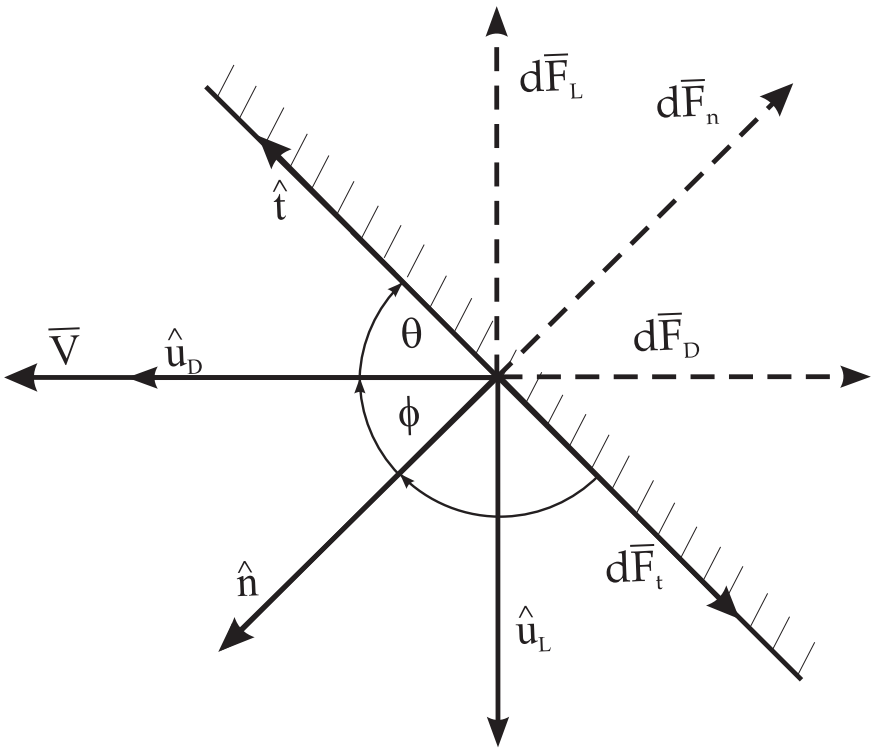

Figure 5.3: Depiction of the decomposition of the air drag force into a component $d\overline{F}_p$ in opposite direction of the surface normal, $\hat{n}$ and a component $d\overline{F}_t$ in the opposite direction of the tangent, $\hat{t}$. The angle between the surface normal and the relative velocity is ϕ, the angle between the relative velocity and the surface tangent is θ. It is also common to split up the force into a component $d\overline{F}_D$ in opposite direction of the relative velocity $\overline{V}$ and a component $d\overline{F}_L$ perpendicular to $\overline{V}$. The corresponding unit vectors $\hat{u}_D$ and $\hat{u}_L$ have the opposite direction as the components of the acting force.

The different ballistic coefficients can be transformed from one system to the other by the following formulas:

$$\begin{aligned}\begin{pmatrix} C_D \\ C_L \end{pmatrix} &= \begin{pmatrix} \cos(-\phi) & \sin(-\phi) \\ -\sin(-\phi) & \cos(-\phi) \end{pmatrix} \cdot \begin{pmatrix} 1 & 0 \\ 0 & -1 \end{pmatrix} \cdot \begin{pmatrix} C_n \\ C_t \end{pmatrix} \\ &= \begin{pmatrix} C_n \cdot \cos\phi + C_t \cdot \sin\phi \\ C_n \cdot \sin\phi - C_t \cdot \cos\phi \end{pmatrix}, \end{aligned} \tag{5.7}$$

$$\begin{aligned}\begin{pmatrix} C_n \\ C_t \end{pmatrix} &= \begin{pmatrix} 1 & 0 \\ 0 & -1 \end{pmatrix} \cdot \begin{pmatrix} \cos(\phi) & \sin(\phi) \\ -\sin(\phi) & \cos(\phi) \end{pmatrix} \cdot \begin{pmatrix} C_D \\ C_L \end{pmatrix} \\ &= \begin{pmatrix} C_D \cdot \cos\phi + C_L \cdot \sin\phi \\ C_D \cdot \sin\phi - C_L \cdot \cos\phi \end{pmatrix}. \end{aligned} \tag{5.8}$$

Also by definition we get:

$$\overline{C} = \frac{\overline{F}_{drag}}{\frac{1}{2}\,\rho\,V^2\,A}. \tag{5.9}$$

The ballistic coefficients are thus just a scaling for the dynamic pressure $\frac{1}{2}\rho V^2$, that is well known from Bernoulli's equation.

As a first conclusion we see that the magnitude of the air drag depends on:

1. the density of the ambient air,
2. the velocity of the satellite with respect to the atmosphere,
3. the area of the surface,

4. and the ballistic coefficient vector.

In the following sections we give a detailed derivation of the involved quantities, except the area of the surface, which does not need explanation.

5.3.2. Air density models

Air density models deliver the number densities of different atmospheric species as well as the ambient air temperature. As an example for an air density model, MSIS 86 is briefly introduced.

MSIS86

The Mass Spectrometer Incoherent Scatter Model 1986 (MSIS86) is an improved version of MSIS83 and is described in Hedin (1987). Special emphasis is put on the representation of the morphology of the polar regions under both quiet and disturbed magnetic conditions. MSIS86 computes the density of H, He, O, N_2, O_2, Ar and N from the following quantities:

- time,
- altitude,
- longitude and latitude,
- solar flux (F107A and F107),
- geomagnetic activity (three hour AP-values.)

The data used for this model is derived from various satellites and also includes data from rocket probes and ground stations.

Table 5.2: Relative density of the different atmospheric species delivered by MSIS86 at 500 km height.

Atmospheric species	relative density [%]
H	$< 5\%$
He	$< 25\%$
O	$> 75\%$
N_2	$< 25\%$
O_2	$< 5\%$
Ar	$< 5\%$
N	$< 5\%$

The total air density at the height of GRACE is at a level of 0.2 to $1.4{\cdot}10^{-12}$ kgm^{-3}, which is very low compared to the density at sea level of about 1 kgm^{-3}. There is a seasonal as well as a daily period, as shown in figure 5.4 for the daily period and figure 5.5 for the seasonal period. It is interesting that the bulge of maximum density arrives at about 14h local time, i.e. about two hours after noon. The temperature at satellite height varies between 700 and 1300°K, cf. figure 5.6. The relative densities of the different constituents are given in table 5.2. We notice that by far the most important contributor is atomic oxygen, followed by helium and nitrogen. The contribution of each of the other atmospheric constituents to the total mass density is below 5 % for all local times and seasons.

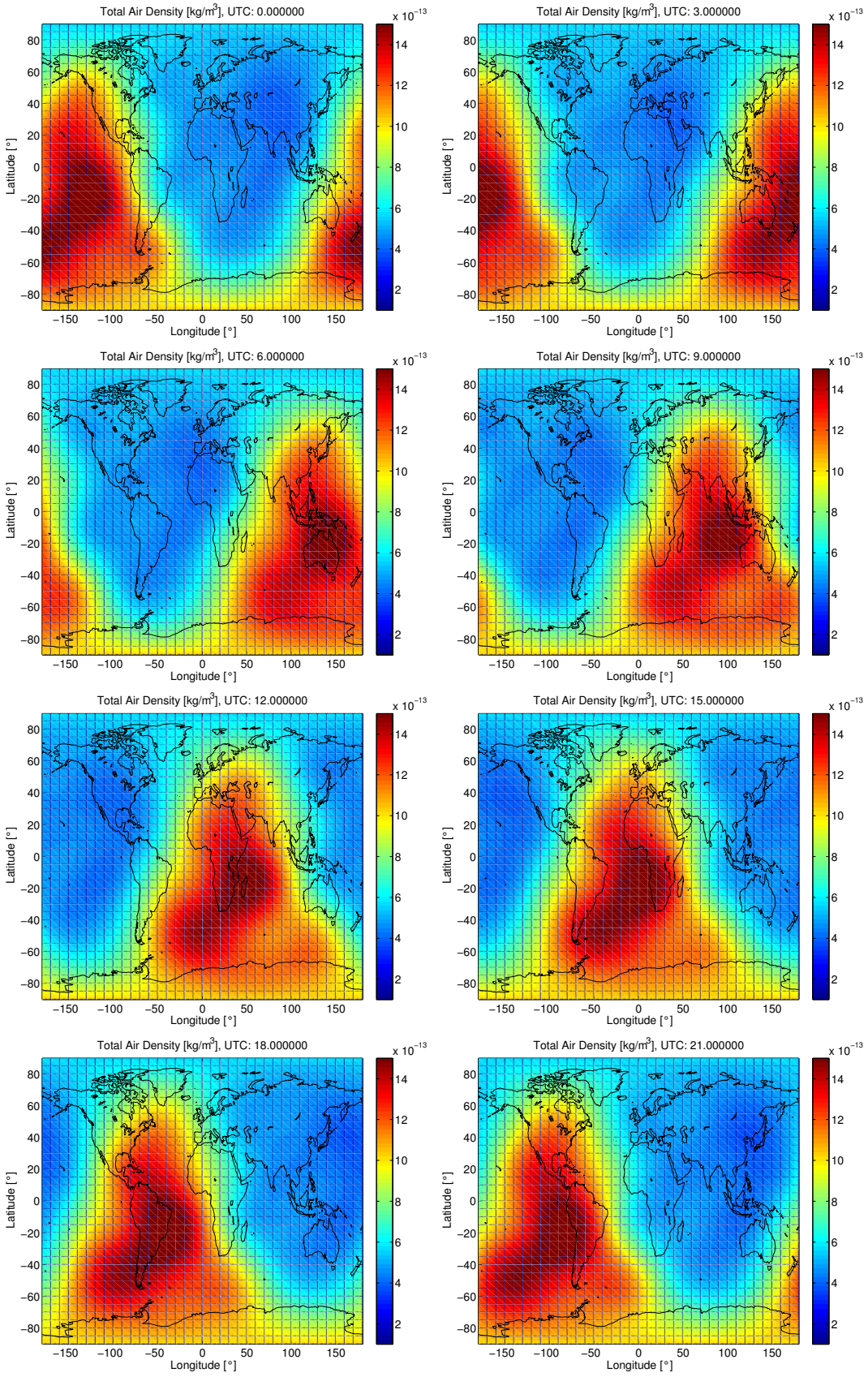

Figure 5.4: Total air mass density over one day at 500 km height at three hour intervals for 1st of January.

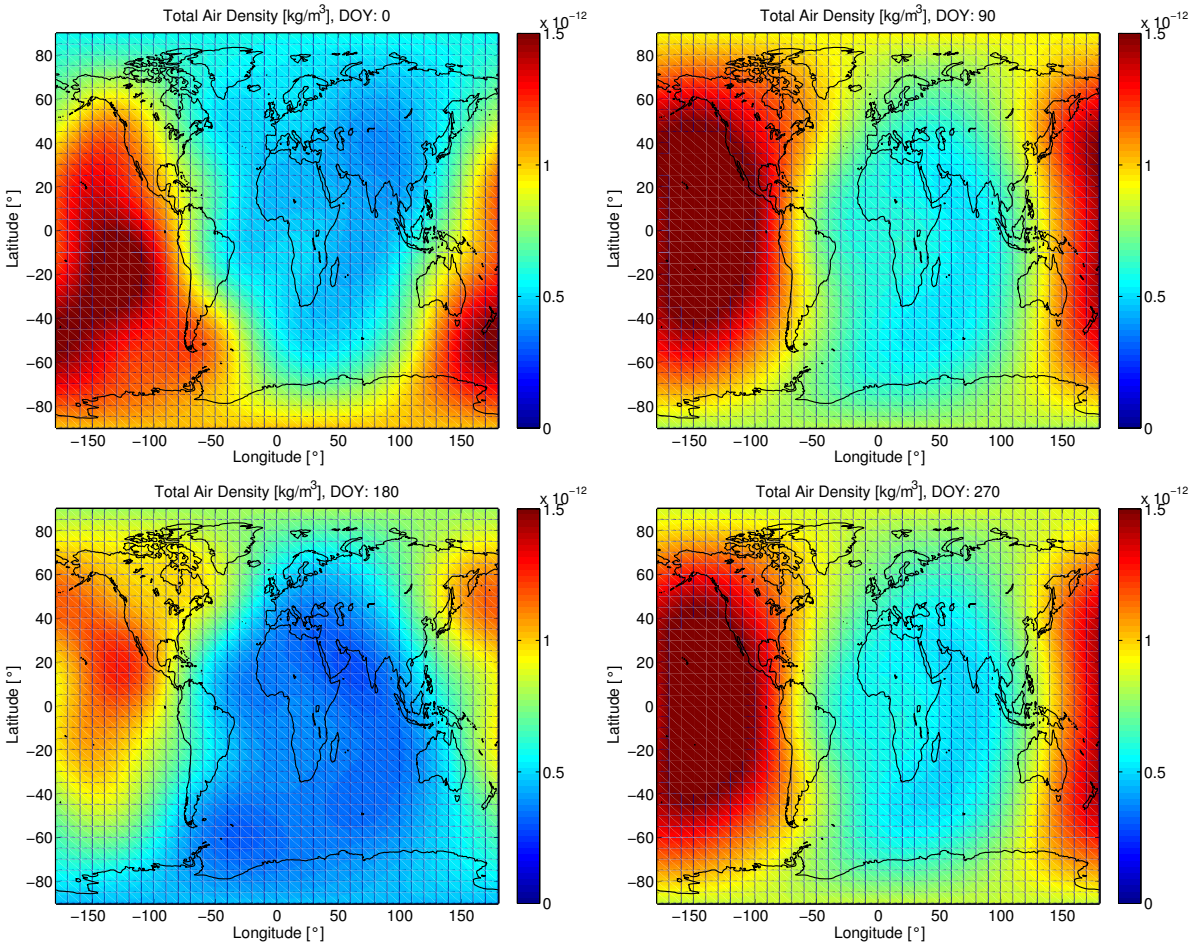

Figure 5.5: Total air mass density over one year at 500 km height at 90 day intervals for 0 h local solar time.

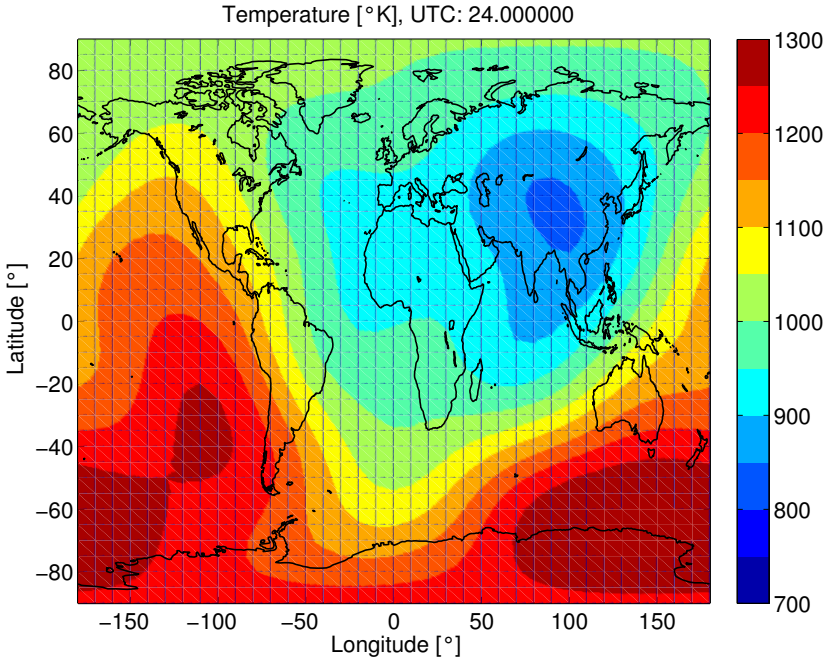

Figure 5.6: Ambient air temperature at 500 km height for 1st of January.

5.3.3. Velocity of the satellite relative to the atmosphere

The velocity of the satellite with respect to the atmosphere is defined by (cf. Gerstl (1998)):

$$\overline{\mathrm{V}} = \overline{\mathrm{V}}_{sat} - \overline{\mathrm{V}}_{atmos} = \overline{\mathrm{V}}_{sat} - (\overline{\omega} \times \overline{\mathrm{x}}_{sat} + \overline{\mathrm{V}}_{wind}), \tag{5.10}$$

where

$\overline{\mathrm{V}}_{sat}$	is the velocity of the satellite
$\overline{\mathrm{V}}_{atmos}$	is the velocity of the atmosphere
$\overline{\omega}$	is the vector of the angular velocity of the earth
$\overline{\mathrm{x}}_{sat}$	is the position of the satellite
$\overline{\mathrm{V}}_{wind}$	is the wind vector.

The expression for the velocity of the atmosphere can be split up into two parts. The first arises from the assumption that the atmosphere rotates with the Earth. The rotation velocity reaches its maximum at the equator and decreases towards the polar regions. The second part takes into account that, in addition to this rotation, there are also winds in the thermosphere. A common wind model is the Horizontal Wind Model 1993 (HWM93) described in Hedin et al. (1988), Hedin et al. (1991) and Hedin et al. (1996). HWM93 is an empirical model. Data used for this model stem from Dynamics Explorer 2 and Atmosphere Explorer E as well as from terrestrial data from incoherent scatter radar and Fabry-Perot optical interferometers.

HWM93 describes the wind vector field by a spherical harmonic expansion of two vector fields: an irrotational field and an solenoidal field. Hence four coefficients are needed for each harmonic degree and order. Using these coefficients, amplitude and phase of the meridional and zonal winds can be computed. Formulas are given in the appendix of Hedin et al. (1988).
HWM93 computes the meridional (N-S) and the zonal (E-W) wind-speed from the same quantities as the air density is derived from.

Vertical wind speed, which is generally less than 1 cm/s, see ESA (2000), can be neglected. The horizontal winds show a strong daily variation but almost no seasonal variation. At the height of GRACE, the horizontal wind speed can reach up to 300 m/s, cf. fig 5.7. The main effects take place at polar regions.

5.3.4. Force models for the derivation of the drag coefficient

Introduction

Before a force model is derived, some assumptions about the kind of flow regime the satellite encounters have to be made. A characteristic quantity for separating the different kinds of flow regimes is the Knudsen number:

$$K = \frac{\lambda}{L}, \tag{5.11}$$

where λ is the mean free molecular path and L is the characteristic length of the considered body. The mean free molecular path is a measure of the path a molecule can travel after reflection without colliding with other molecules. If $K \gg 1$, the theory of free molecular flow is applicable. The GRACE orbit height fulfills the conditions for the free molecular flow, cf. Koppenwallner (1988). In the free molecular flow regime the molecular character of the air is pronounced. Additionally we make the following assumptions:

- There are no multiple reflections,
- the velocity of the satellite relative to the atmosphere molecules is $\overline{\mathrm{V}}$.

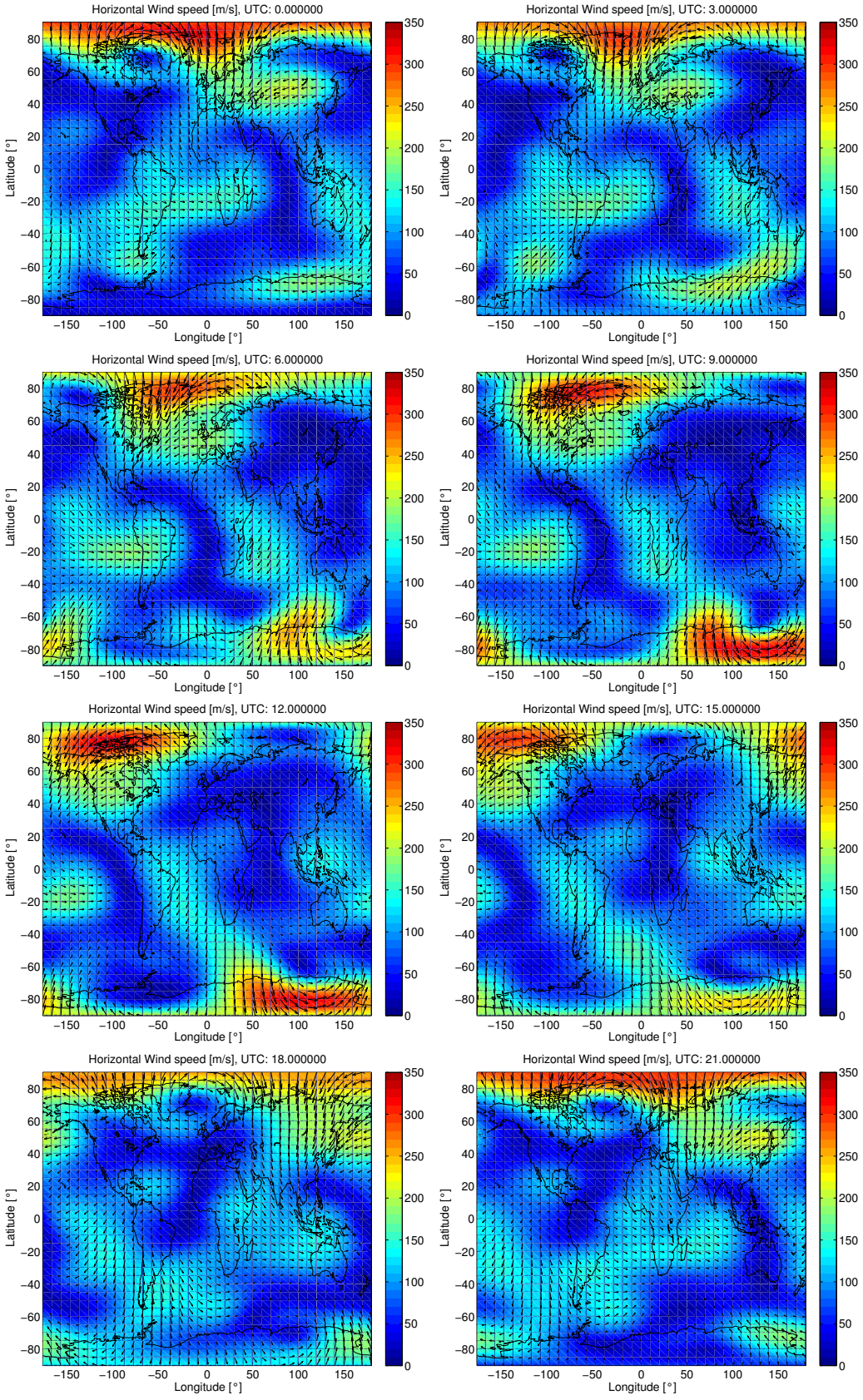

Figure 5.7: Meridional and zonal wind speed computed from HWM93 over one day at 500 km height

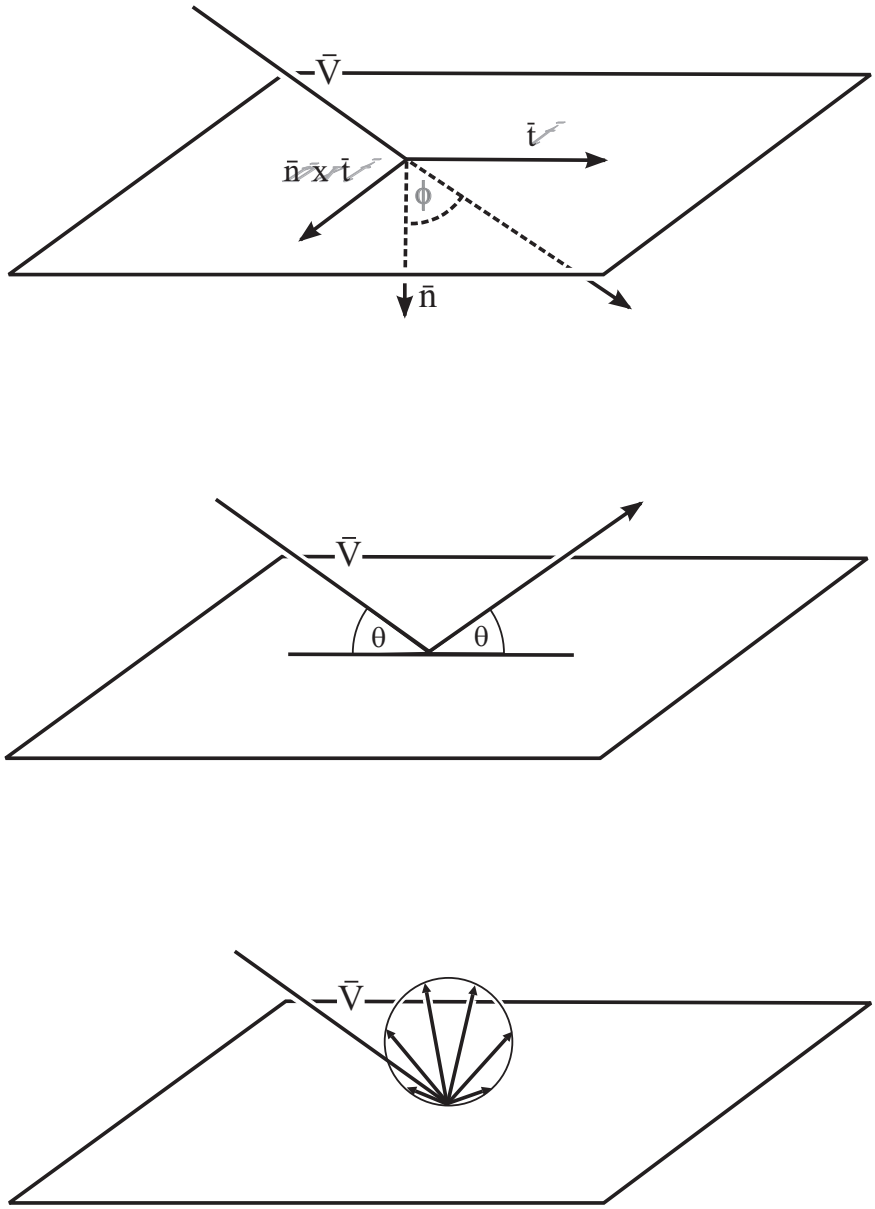

Figure 5.8: Interaction of a molecule with a surface element. In the first row the decomposition of the force is depicted, in the second row the case of specular reflection is displayed, in the third row the case of diffuse reflection is shown.

Interaction of a molecule with a surface element

Figure 5.8 shows the basic situation of all described force models: the impact of a molecule on a surface element of the satellite. The molecule's velocity is $\overline{\mathrm{V}}$, the relative velocity of the satellite with regard to the atmosphere. There are two types of reflection which describe the extreme possibilities of the action after the impact. We have diffuse reflection if the atmospheric molecule accommodates on the surface of the satellite and its kinetic energy is transformed into heat until the residual kinetic energy equals the energy it would have at the temperature of the surface element. The atmospheric molecule is then re-emitted in an arbitrary direction with a velocity corresponding to the temperature of the surface element. In case of diffuse reflection, the force exerted on the surface element has a component in the opposite direction of the surface normal (pressure) and in direction of the surface tangent (shear). If no energy is transformed into heat, we have specular reflection, i.e. the tangential component of the velocity of the molecule remains unchanged, the normal component changes its sign as the impacting molecule is instantly reflected at the surface element molecules. In case of specular reflection the exerted force acts only in the opposite direction of the surface element normal.

Basic force model

For the most simplified and also most common force model it is assumed that the incoming particles are reflected mainly diffusely. The force is split up into the direction of the relative velocity and perpendicular to it (drag and lift), but it is assumed that the lift is zero. Furthermore it is assumed that the ballistic coefficient has a fixed value and that for all molecules the relative velocity is $\overline{\mathrm{V}}$:

$$\overline{\mathrm{F}}_{Sat} = \frac{1}{2}\rho V^2 A\overline{\mathrm{C}}, \tag{5.12}$$

$$\overline{\mathrm{C}} = -2.2 \cdot \cos\phi \cdot \widehat{\mathrm{V}}. \tag{5.13}$$

This very simple force model may not be sufficient to model all occurring effects, thus more complex models are derived in the following subsections.

Standard two parameter force model

In this subsection we derive a standard force model for both extreme possibilities of interaction of the incoming molecule with the surface element:

- The molecule is reflected specularly or
- the molecule is reflected diffusely.

The derivation is based on Newton's second law:

$$\Delta\overline{\mathrm{F}} = \frac{\Delta\overline{\mathrm{p}}}{\Delta t} \tag{5.14}$$

and Newton's third law

$$\overline{\mathrm{F}} = -\overline{\mathrm{F}}'. \tag{5.15}$$

The first case is depicted in figure 5.9. For practical reasons the collision is split up into two parts:

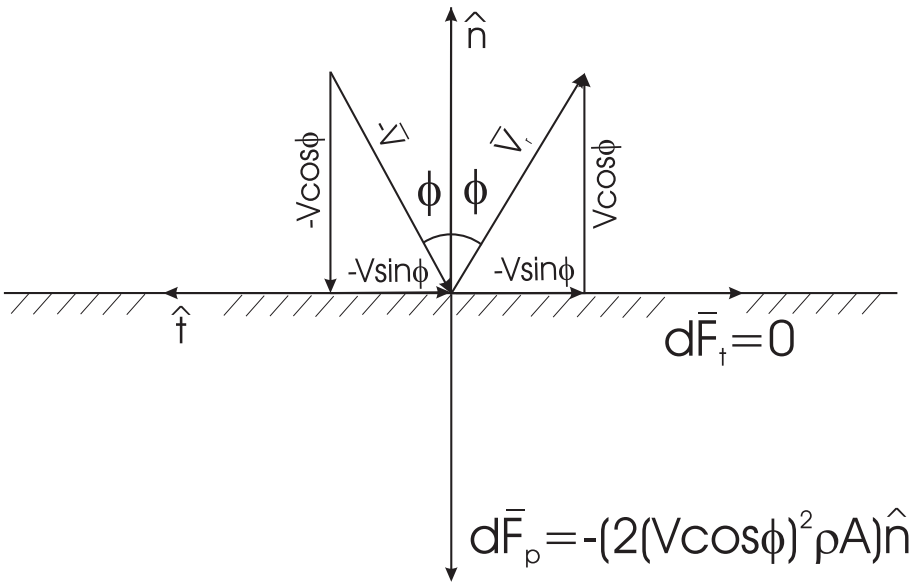

Figure 5.9: Specular reflection

impact and reflection, i.e. we will derive the change of impulse from after the impact to before the impact and from after the reflection to before the reflection:

$$\Delta\overline{\mathrm{p}}_{\mathrm{i}} = \overline{\mathrm{p}}_{\mathrm{ai}} - \overline{\mathrm{p}}_{\mathrm{bi}}, \tag{5.16}$$
$$\Delta\overline{\mathrm{p}}_{\mathrm{r}} = \overline{\mathrm{p}}_{\mathrm{ar}} - \overline{\mathrm{p}}_{\mathrm{br}}, \tag{5.17}$$
$$\Delta\overline{\mathrm{p}} = \Delta\overline{\mathrm{p}}_{\mathrm{i}} + \Delta\overline{\mathrm{p}}_{\mathrm{r}}. \tag{5.18}$$

We get:

$$\overline{\mathrm{p}}_{\mathrm{bi}} = \begin{pmatrix} -V\cdot\cos\phi \\ -V\cdot\sin\phi \end{pmatrix} m, \tag{5.19}$$
$$\overline{\mathrm{p}}_{\mathrm{ai}} = \begin{pmatrix} 0 \\ 0 \end{pmatrix} m, \tag{5.20}$$
$$\Longrightarrow \Delta\overline{\mathrm{p}}_{\mathrm{i}} = \begin{pmatrix} +V\cdot\cos\phi \\ +V\cdot\sin\phi \end{pmatrix} m \tag{5.21}$$

and

$$\overline{\mathrm{p}}_{\mathrm{br}} = \begin{pmatrix} 0 \\ 0 \end{pmatrix} m, \tag{5.22}$$
$$\overline{\mathrm{p}}_{\mathrm{ar}} = \begin{pmatrix} +V\cdot\cos\phi \\ -V\cdot\sin\phi \end{pmatrix} m, \tag{5.23}$$
$$\Longrightarrow \Delta\overline{\mathrm{p}}_{\mathrm{r}} = \begin{pmatrix} +V\cdot\cos\phi \\ -V\cdot\sin\phi \end{pmatrix} m, \tag{5.24}$$

which leads to

$$\Delta\overline{\mathrm{p}} = \begin{pmatrix} +V\cdot\cos\phi \\ +V\cdot\sin\phi \end{pmatrix} m + \begin{pmatrix} +V\cdot\cos\phi \\ -V\cdot\sin\phi \end{pmatrix} m, \tag{5.25}$$
$$= \begin{pmatrix} +2V\cdot\cos\phi \\ 0 \end{pmatrix} m, \tag{5.26}$$

with

V	magnitude of the relative velocity vector,
ϕ	angle between the relative velocity and the surface normal, $\equiv$ angle of incidence,
m	mass of the incoming molecule.

Equation (5.26) gives us the impulse change of one particle. To derive the total force, we first have to know how many particles hit the satellite per unit time and per unit area. This number is given by:

$$N_{inc} = N_{vol}\cdot V\cos\phi, \tag{5.27}$$

with

N_{inc}	the number of incoming molecules $[\frac{1}{\mathrm{s}\cdot\mathrm{m}^2}]$,
N_{vol}	the number of molecules per cubic meter $[\frac{1}{\mathrm{m}^3}]$,

N_{vol} is given by the air density model.

As

$$\Delta\overline{\mathrm{F}} = \frac{\Delta\overline{\mathrm{p}}}{\Delta t}, \tag{5.28}$$

we get for the total force exerted on the molecules:

$$\Delta\overline{\mathrm{F}} = + \begin{pmatrix} 2V \cdot \cos\phi \\ 0 \end{pmatrix} m \cdot N_{inc} \cdot A \tag{5.29}$$

$$= + \begin{pmatrix} 2V \cdot \cos\phi \\ 0 \end{pmatrix} m \cdot N_{vol} \cdot V \cos\phi \cdot A \tag{5.30}$$

$$= + \begin{pmatrix} 2 \\ 0 \end{pmatrix} (V \cdot \cos\phi)^2 \cdot \rho \cdot A, \tag{5.31}$$

with ρ the mass density of the incoming molecule species. The satellite exerts this force on the molecules. According to Newton's third law, the force on the satellite is the same as on the molecules but with opposite sign:

$$\Delta\overline{\mathrm{F}}_{sat} = - \begin{pmatrix} 2 \\ 0 \end{pmatrix} (V \cdot \cos\phi)^2 \cdot \rho \cdot A. \tag{5.32}$$

For the vector $\overline{\mathrm{C}}$ we get, if we use definition (5.3):

$$\overline{\mathrm{C}} = -4 \cdot (\cos\phi)^2 \cdot \hat{\mathrm{n}} + 0 \cdot \hat{\mathrm{t}}. \tag{5.33}$$

So for specular reflection the ballistic coefficients have a maximal value of 4, which is much higher than the standard value of 2.2. It is to be noted that for this model no force in direction of the tangent is exerted, but only in direction of the surface normal.

The second case of diffuse reflection is depicted in figure 5.10. We get:

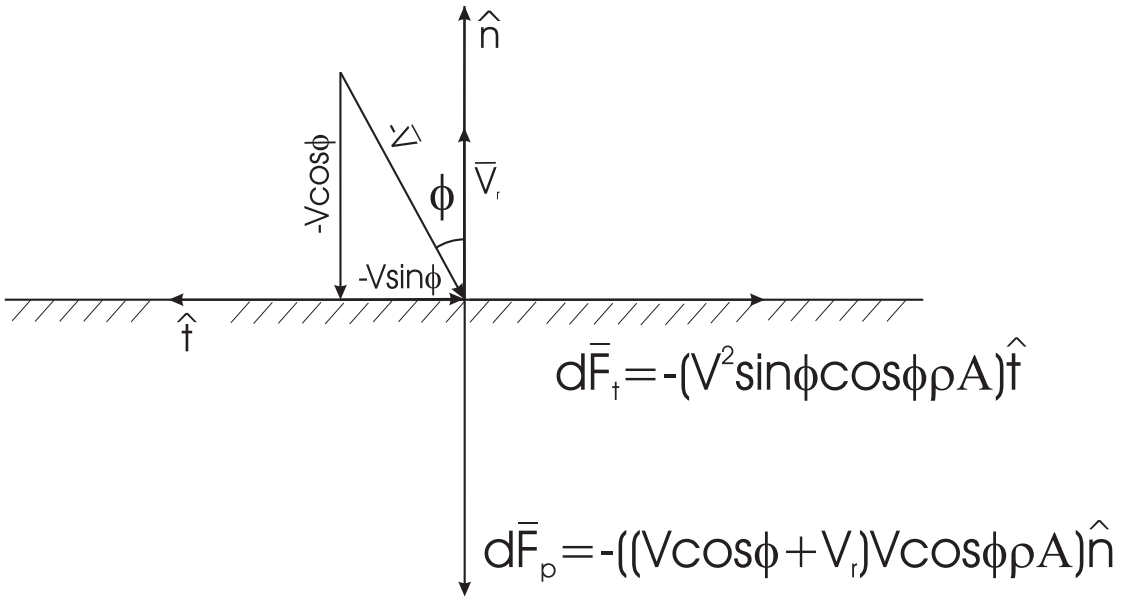

Figure 5.10: Diffuse reflection

$$\overline{\mathrm{p}}_{\mathrm{bi}} = \begin{pmatrix} -V \cdot \cos\phi \\ -V \cdot \sin\phi \end{pmatrix} m, \tag{5.34}$$

$$\overline{\mathrm{p}}_{\mathrm{ai}} = \begin{pmatrix} 0 \\ 0 \end{pmatrix} m, \tag{5.35}$$

$$\Longrightarrow \Delta\overline{\mathrm{p}}_{\mathrm{i}} = \begin{pmatrix} V \cdot \cos\phi \\ V \cdot \sin\phi \end{pmatrix} m \tag{5.36}$$

and

$$\overline{\mathrm{p}}_{\mathrm{br}} = \begin{pmatrix} 0 \\ 0 \end{pmatrix} m, \tag{5.37}$$

$$\overline{\mathrm{p}}_{\mathrm{ar}} = \begin{pmatrix} V_r \\ 0 \end{pmatrix} m, \tag{5.38}$$

$$\Longrightarrow \Delta\overline{\mathrm{p}}_{\mathrm{r}} = \begin{pmatrix} V_r \\ 0 \end{pmatrix} m, \tag{5.39}$$

which leads to

$$\Delta\overline{\mathrm{p}} = \begin{pmatrix} V \cdot \cos\phi \\ V \cdot \sin\phi \end{pmatrix} m + \begin{pmatrix} V_r \\ 0 \end{pmatrix} m \tag{5.40}$$

$$= \begin{pmatrix} V \cdot \cos\phi + V_r \\ V \cdot \sin\phi \end{pmatrix} m. \tag{5.41}$$

For the force on the molecules we get:

$$\Delta\overline{\mathrm{F}} = \begin{pmatrix} V \cdot \cos\phi + V_r \\ V \cdot \sin\phi \end{pmatrix} V \cos\phi \cdot \rho \cdot A \tag{5.42}$$

and for the force on the satellite:

$$\Delta\overline{\mathrm{F}}_{sat} = -\begin{pmatrix} (\cos\phi)^2 + \frac{V_r}{V} \cdot \cos\phi \\ \sin\phi \cdot \cos\phi \end{pmatrix} V^2 \cdot \rho \cdot A. \tag{5.43}$$

This leads to a $\overline{\mathrm{C}}$:

$$\overline{\mathrm{C}} = -2 \cdot \left[\left((\cos\phi)^2 + \frac{V_r}{V} \cdot \cos\phi \right) \cdot \hat{\mathrm{n}} + (\sin\phi \cdot \cos\phi) \cdot \hat{\mathrm{t}} \right]. \tag{5.44}$$

We note that the ballistic coefficients in case of diffuse reflection are smaller than in case of specular reflection. In direction of the surface normal, the maximal value is four, however the ratio $\frac{V_r}{V}$ is smaller than one if one assumes realistic values for the temperature of the reflected stream. In direction of the tangent, the maximal value is one for $\phi = 45°$ because of the $\cos\phi \cdot \sin\phi$ term. In contrast to the case of specular reflection the force has also a component in the direction of the surface tangent.
These two extreme possibilities of reflection do not reflect reality. In reality, the reflection is partly specular and partly diffuse. Let us now assume that a part $(1 - \sigma)$ is reflected specularly and that a part σ is reflected diffusely. σ is the accommodation coefficient and describes which part of the incoming particles takes part in an energy exchange with the struck surface. We then get:

$$\Delta\overline{\mathrm{F}}_{sat} = -\left[(1-\sigma) \begin{pmatrix} 2(\cos\phi)^2 \\ 0 \end{pmatrix} \right. \tag{5.45}$$

$$\left. + \sigma \begin{pmatrix} (\cos\phi)^2 + \frac{V_r}{V} \cdot \cos\phi \\ \sin\phi \cdot \cos\phi \end{pmatrix} \right] V^2 \cdot \rho \cdot A, \tag{5.46}$$

$$= -\left[(2-\sigma) \begin{pmatrix} (\cos\phi)^2 \\ 0 \end{pmatrix} + \sigma \begin{pmatrix} \frac{V_r}{V} \cdot \cos\phi \\ \sin\phi \cdot \cos\phi \end{pmatrix} \right] V^2 \cdot \rho \cdot A \tag{5.47}$$

and

$$\overline{\mathrm{C}} = -2 \cdot \left[\left((2-\sigma)(\cos\phi)^2 + \sigma \frac{V_r}{V} \cdot \cos\phi \right) \cdot \hat{\mathrm{n}} + \sigma \, (\sin\phi \cdot \cos\phi) \cdot \hat{\mathrm{t}} \right]. \tag{5.48}$$

If we assume that there is a separate accommodation coefficient for the normal and the tangential energy exchange, we get:

$$\overline{\mathrm{C}} = -2 \cdot \left[\left((2-\sigma_n)(\cos\phi)^2 + \sigma_n \frac{V_r}{V} \cdot \cos\phi \right) \cdot \hat{\mathrm{n}} + \sigma_t \, (\sin\phi \cdot \cos\phi) \cdot \hat{\mathrm{t}} \right]. \tag{5.49}$$

This is identical to the formulation given in Mazanek et al. (2000). The given formulation does still not take into account that the incoming molecules have, in addition to the macroscopic velocity $\overline{\mathrm{V}}$, a microscopic velocity $\overline{\mathrm{u}}$. This velocity is different for each molecule, but the distribution is according to a Maxwell-Boltzmann distribution:

$$f(\overline{\mathrm{u}}) = \frac{\rho}{m\pi^{\frac{3}{2}}\tilde{v}^3} \exp\left(-\frac{m\overline{\mathrm{u}}^2}{2kT}\right), \tag{5.50}$$

with

- m molecule mass,
- $\tilde{v}$ most probable velocity in the distribution,
- k Boltzmann constant,
- T ambient air temperature.

The velocity of the molecules relative to the surface element is then

$$\overline{\mathrm{w}} = \overline{\mathrm{V}} + \overline{\mathrm{u}} \tag{5.51}$$

and

$$\overline{\mathrm{u}} = \overline{\mathrm{w}} - \overline{\mathrm{V}}. \tag{5.52}$$

So the distribution function becomes:

$$\begin{aligned} f(\overline{\mathrm{w}}, \overline{\mathrm{V}}) &= \frac{\rho}{m\pi^{\frac{3}{2}}\tilde{v}^3} \exp\left(-\frac{m(\overline{\mathrm{w}} - \overline{\mathrm{V}})^2}{2kT}\right) && (5.53)\\ &= \frac{\rho}{m\pi^{\frac{3}{2}}\tilde{v}^3} \exp\left(\frac{-\overline{\mathrm{w}}^2 - \overline{\mathrm{V}}^2 + 2\cdot\overline{\mathrm{w}}\cdot\overline{\mathrm{V}}}{\tilde{v}^2}\right) && (5.54)\\ &= \frac{\rho}{m\pi^{\frac{3}{2}}\tilde{v}^3} \exp\left(-\frac{w^2}{\tilde{v}^2}\right) && (5.55)\\ &\cdot \quad \exp\left(-S^2\right)\cdot\exp\left(2\frac{S}{\tilde{v}}\cdot(w_x\cos\phi + w_y\sin\phi)\right), && (5.56) \end{aligned}$$

with S the molecular speed ratio: $S = \frac{V}{\tilde{v}}$, $\tilde{v} = \sqrt{\frac{2kT}{m}}$ and $\overline{\mathrm{V}} = \begin{pmatrix} V\cdot\cos\phi \\ V\cdot\sin\phi \\ 0 \end{pmatrix}$.

The number of incoming particles is now given by:

$$N_{inc} = \int_{-\infty}^{+\infty} dw_z \int_{-\infty}^{+\infty} dw_y \int_{0}^{+\infty} w_x \cdot f dw_x. \tag{5.57}$$

It is clear that only molecules that have a positive velocity component w_x can hit the surface and only those have to be accounted for. The force due to the incoming molecules in direction of the surface normal is then given by:

$$\begin{aligned} d\overline{\mathrm{F}}_{i,n} &= -\int_{-\infty}^{+\infty} dw_z \int_{-\infty}^{+\infty} dw_y \int_{0}^{+\infty} w_x \cdot w_x \cdot f dw_x \cdot A \cdot m \cdot \hat{\mathrm{n}} && (5.58)\\ &= -\rho V^2 A \left[\frac{1}{2\sqrt{\pi}S^2}\Pi(S\cos\phi)\right]\cdot\hat{\mathrm{n}}, && (5.59) \end{aligned}$$

where

$$\Pi(S\cos\phi) = S\cos\phi\ \exp(-S\cos\phi^2) + \sqrt{\pi}\ \left(0.5 + S\cos\phi^2\right)\left[1 + \mathrm{erf}(S\cos\phi)\right] \tag{5.60}$$

is the pressure function. Note that as ρ is the total mass density the pressure function is a measure for that fraction of the total number of molecules in a unit volume that hit the surface and have a velocity

component in direction of the surface normal. For the force in the direction of the tangent we get:

$$d\overline{\mathrm{F}}_{i,t} = -\int_{-\infty}^{+\infty} dw_z \int_{-\infty}^{+\infty} dw_y \int_{0}^{+\infty} w_y \cdot w_x \cdot f dw_x \cdot A \cdot m \cdot \widehat{\mathrm{t}} \tag{5.61}$$

$$= -\rho V^2 A \left[\frac{S\sin\phi}{2\sqrt{\pi}S^2}\chi(S\cos\phi)\right] \cdot \widehat{\mathrm{t}}, \tag{5.62}$$

$$\chi(S\cos\phi) = \exp(-S\cos\phi^2) + \sqrt{\pi}\, S\cos\phi\, \left[1 + \mathrm{erf}(S\cos\phi)\right] \tag{5.63}$$

is the particle flow function. Similarly to the pressure function, the particle flow function is a measure for the fraction of the molecules that hit the surface and have a velocity component in direction of the surface tangent. For the reflected molecules in case of specular reflection we get:

$$d\overline{\mathrm{F}}_{r,spec,n} = -\int_{-\infty}^{+\infty} dw_z \int_{-\infty}^{+\infty} dw_y \int_{0}^{+\infty} w_x \cdot w_x \cdot f dw_x \cdot A \cdot m \cdot \widehat{\mathrm{n}} \tag{5.64}$$

$$= -\rho V^2 A \left[\frac{1}{2\sqrt{\pi}S^2}\Pi(S\cos\phi)\right] \cdot \widehat{\mathrm{n}} \tag{5.65}$$

and for the force in direction of the tangent:

$$d\overline{\mathrm{F}}_{r,spec,t} = +\int_{-\infty}^{+\infty} dw_z \int_{-\infty}^{+\infty} dw_y \int_{0}^{+\infty} w_y \cdot w_x \cdot f dw_x \cdot A \cdot m \cdot \widehat{\mathrm{t}} \tag{5.66}$$

$$= +\rho V^2 A \left[\frac{S\sin\phi}{2\sqrt{\pi}S^2}\chi(S\cos\phi)\right] \cdot \widehat{\mathrm{t}}. \tag{5.67}$$

In the case of diffuse reflection we get:

$$d\overline{\mathrm{F}}_{r,diff,n} = -\int_{-\infty}^{+\infty} dw_z \int_{-\infty}^{+\infty} dw_y \int_{0}^{+\infty} w_x \cdot f dw_x \cdot \frac{V_r}{V} \cdot A \cdot m \cdot \widehat{\mathrm{n}} \tag{5.68}$$

$$= -\rho V^2 A \left[\frac{S}{2\sqrt{\pi}S^2} \cdot \frac{V_r}{V}\chi(S\cos\phi)\right] \cdot \widehat{\mathrm{n}} \tag{5.69}$$

and for the force in direction of the tangent:

$$d\overline{\mathrm{F}}_{r,diff,t} = 0. \tag{5.70}$$

In the case of diffuse reflection it is assumed that all reflected molecules have the same velocity V_r, the distribution function f is only required to get the number of the incoming molecules, which is the same as the number of reflected molecules. V_r is identical to the most probable velocity in the Maxwellian velocity distribution. The tangential force for diffusely reflected molecules is zero because in the sum the individual tangential effects of the reflected molecules cancel themselves. If we again assume that a fraction of the particles is reflected diffusely and the complement is reflected specularly, we get:

$$\Delta\overline{\mathrm{F}}_{sat} = -\left\{\left[\left(\frac{(2-\sigma)}{2\sqrt{\pi}S^2}\Pi(S\cos\phi)\right) + \frac{\sigma S}{2\sqrt{\pi}S^2} \cdot \frac{V_r}{V} \cdot \chi(S\cos\phi)\right]\widehat{\mathrm{n}}\right. \tag{5.71}$$

$$\left. + \left[\frac{\sigma S\sin\phi}{2\sqrt{\pi}S^2} \cdot \chi(S\cos\phi)\right]\widehat{\mathrm{t}}\right\} V^2 \cdot \rho \cdot A. \tag{5.72}$$

Again assuming normal and tangential accommodation coefficients and knowing that

$$\frac{V_r}{V} = \frac{\sqrt{\pi}}{2S}\sqrt{\frac{T_w}{T}}, \tag{5.73}$$

we get:

$$\Delta\overline{\mathrm{F}}_{sat} = -\left\{\left[\left(\frac{(2-\sigma_n)}{2\sqrt{\pi}S^2}\Pi(S\cos\phi)\right) + \frac{\sigma_n}{2S^2} \cdot \frac{1}{2}\sqrt{\frac{T_w}{T}} \cdot \chi(S\cos\phi)\right]\widehat{\mathrm{n}}\right.$$

$$\left. + \left[\frac{\sigma_t S\sin\phi}{2\sqrt{\pi}S^2} \cdot \chi(S\cos\phi)\right]\widehat{\mathrm{t}}\right\} V^2 \cdot \rho \cdot A. \tag{5.74}$$

So far the equations assumed only one atmospheric species and one surface element. From now on the notation will take into account that there are several atmospheric constituents and surface elements. For the atmospheric constituent i and the surface element k the total force is given by:

$$\begin{aligned}\Delta\overline{\mathrm{F}}_{sat}^{(i,k)} &= -\left\{\left[\left(\frac{(2-\sigma_n^{(i,k)})}{2\sqrt{\pi}S_{(i)}^2}\Pi(S^{(i)}\cos\phi^{(k)})\right)+\frac{\sigma_n^{(i,k)}}{2S_{(i)}^2}\cdot\frac{1}{2}\sqrt{\frac{T_w^{(k)}}{T}}\cdot\chi(S^{(i)}\cos\phi^{(k)})\right]\widehat{\mathrm{n}}^{(k)}\right.\\ &+ \left.\left[\frac{\sigma_t^{(k)}S^{(i)}\sin\phi^{(k)}}{2\sqrt{\pi}S_{(i)}^2}\cdot\chi(S^{(i)}\cos\phi^{(k)})\right]\widehat{\mathrm{t}}^{(k)}\right\}V^2\cdot\rho^{(i)}\cdot A^{(k)}. \qquad (5.75)\end{aligned}$$

For the vector of ballistic coefficients we find:

$$\overline{\mathrm{C}}^{(i,k)} = -\left(C_n^{(i,k)}\cdot\widehat{\mathrm{n}}^{(k)}+C_t^{(i,k)}\cdot\widehat{\mathrm{t}}^{(k)}\right), \qquad (5.76)$$

$$C_n^{(i,k)} = 2\left[\left(\frac{(2-\sigma_n^{(i,k)})}{2\sqrt{\pi}S_{(i)}^2}\Pi(S^{(i)}\cos\phi^{(k)})\right)+\frac{\sigma_n^{(i,k)}}{2S_{(i)}^2}\cdot\frac{1}{2}\sqrt{\frac{T_w^{(k)}}{T}}\cdot\chi(S^{(i)}\cos\phi^{(k)})\right], \qquad (5.77)$$

$$C_t^{(i,k)} = 2\left[\frac{\sigma_t^{(i,k)}S^{(i)}\sin\phi^{(k)}}{2\sqrt{\pi}S_{(i)}^2}\cdot\chi(S^{(i)}\cos\phi^{(k)})\right], \qquad (5.78)$$

which is identical to the formulation given in Schaaf and Chambre (1961).

Alternative two parameter force model

Another alternative is to decompose the force into the directions of the relative velocity and the surface normal. We start from equation (5.74).

Let

$$\widehat{\mathrm{t}}^{(k)}\sin\phi^{(k)} = \widehat{\mathrm{V}}-\widehat{\mathrm{n}}^{(k)}\cos\phi^{(k)}, \qquad (5.79)$$

$$S_n^{(i,k)} = S^{(i)}\cos\phi^{(k)}, \qquad (5.80)$$

then

$$\begin{aligned}\Delta\overline{\mathrm{F}}_{sat}^{(i,k)} &= -\frac{A^{(k)}\,\rho^{(i)}V^2}{2}\left\{\left[\frac{2-\sigma_n^{(i,k)}}{\sqrt{\pi}S_{(i)}^2}\,\Pi(S_n^{(i,k)})+\frac{\sigma_n^{(i,k)}}{2S_{(i)}^2}\,\sqrt{\frac{T_w^{(k)}}{T}}\,\chi(S_n^{(i,k)})\right.\right.\\ &- \left.\frac{\sigma_t^{(i,k)}\cos\phi^{(k)}}{S^{(i)}\sqrt{\pi}}\,\chi(S_n^{(i,k)})\right]\widehat{\mathrm{n}}^{(k)}\\ &+ \left.\left[\frac{\sigma_t{}^{(k)}}{S^{(i)}\sqrt{\pi}}\,\chi(S_n^{(i,k)})\right]\widehat{\mathrm{V}}\right\}. \qquad (5.81)\end{aligned}$$

Let

$$\Gamma_1(S_n^{(i,k)}) = \frac{1}{2\sqrt{\pi}}\Big[\chi(S_n^{(i,k)})\Big], \qquad (5.82)$$

$$\Gamma_2(S_n^{(i,k)}) = \frac{1}{2\sqrt{\pi}}\Big[\Pi(S_n^{(i,k)})\Big], \qquad (5.83)$$

then

$$\begin{aligned}\Delta\overline{\mathrm{F}}_{sat}^{(i,k)} &= -A^{(k)}\,\rho^{(i)}V^2\left\{\left[\frac{2-\sigma_n^{(i,k)}}{S_{(i)}^2}\,\Gamma_2(S_n^{(i,k)})+\frac{\sigma_n^{(i,k)}}{2S_{(i)}^2}\,\sqrt{\frac{T_w^{(k)}}{T}}\,\sqrt{\pi}\,\Gamma_1(S_n^{(i,k)})\right.\right. \qquad (5.84)\\ &- \left.\left.\frac{\sigma_t^{(i,k)}\cos\phi^{(k)}}{S^{(i)}}\,\Gamma_1(S_n^{(i,k)})\right]\widehat{\mathrm{n}}^{(k)}+\left[\frac{\sigma_t^{(k)}}{S^{(i)}}\,\Gamma_1(S_n^{(i,k)})\right]\widehat{\mathrm{V}}\right\}.\end{aligned}$$

Let

$$\frac{V_r^{(i,k)}}{V} = \frac{\sqrt{\pi}}{2}\sqrt{\frac{T_w^{(k)}}{T}}\,\frac{1}{S^{(i)}}, \tag{5.85}$$

$$\Rightarrow \sqrt{\frac{T_w^{(k)}}{T}} = \frac{V_r^{(i,k)}}{V}\,\frac{2}{\sqrt{\pi}}\,S^{(i)}, \tag{5.86}$$

then

$$\begin{aligned}\Delta\overline{\mathrm{F}}_{sat}^{(i,k)} = & -A^{(k)}\,\rho^{(i)}V^2\left\{\left[\frac{2-\sigma_n^{(i,k)}}{S_{(i)}^2}\,\Gamma_2(S_n^{(i,k)}) + \frac{\sigma_n^{(i,k)}}{S^{(i)}}\,\frac{V_r^{(i,k)}}{V}\,\Gamma_1(S_n^{(i,k)})\right.\right.\\ & \left.\left. - \frac{\sigma_t^{(i,k)}\cos\phi^{(k)}}{S^{(i)}}\,\Gamma_1(S_n^{(i,k)})\right]\widehat{\mathrm{n}}^{(k)} + \left[\frac{\sigma_t^{(i,k)}}{S^{(i)}}\,\Gamma_1(S_n^{(i,k)})\right]\,\widehat{\mathrm{V}}\right\}.\end{aligned} \tag{5.87}$$

Equation (5.87) is identical to the formulation of the force due to air drag in Thalhammer (1989). In contrast to the previous formulation the force is not split up into perpendicular components:

$$\Delta\overline{\mathrm{F}}_{sat}^{(i,k)} = \frac{1}{2}\,\rho^{(i)}V^2\,A^{(k)}\,\overline{\mathrm{C}}^{(i,k)}, \tag{5.88}$$

where

$$\overline{\mathrm{C}}^{(i,k)} = -\left(C_n^{(i,k)}\,\widehat{\mathrm{n}}^{(k)} + C_D^{(i,k)}\,\widehat{\mathrm{V}}\right), \tag{5.89}$$

$$C_n^{(i,k)} = 2\left[\frac{2-\sigma_n^{(i,k)}}{S_{(i)}^2}\,\Gamma_2(S_n^{(i,k)}) + \frac{\sigma_n^{(i,k)}}{S^{(i)}}\,\frac{V_r^{(i,k)}}{V}\,\Gamma_1(S_n^{(i,k)}) - \frac{\sigma_t^{(i,k)}\cos\phi^{(k)}}{S^{(i)}}\,\Gamma_1(S_n^{(i,k)})\right], \tag{5.90}$$

$$C_D^{(i,k)} = 2\left[\frac{\sigma_t^{(i,k)}}{S^{(i)}}\,\Gamma_1(S_n^{(i,k)})\right]. \tag{5.91}$$

Force model using only one accommodation coefficient

A more simplified form of the force model can be derived if it is assumed that the normal and tangential accommodation coefficients are equal. We start again from equation (5.74).

Then, with

$$\sigma_n^{(i,k)} = \sigma_t^{(i,k)} = \sigma^{(i,k)}, \tag{5.92}$$

we find

$$\begin{aligned}\Delta\overline{\mathrm{F}}_{sat}^{(i,k)} = & -A^{(k)}\frac{\rho^{(i)}V^2}{2S_{(i)}^2}\left\{\left[\frac{(2-\sigma^{(i,k)})}{\sqrt{\pi}}\Pi(S_n^{(i,k)}) + \frac{\sigma^{(i,k)}}{2}\sqrt{\frac{T_w^{(k)}}{T}}\chi(S_n^{(i,k)})\right]\widehat{\mathrm{n}}^{(k)}\right.\\ & \left. + \left[\frac{\sigma^{(i,k)}}{\sqrt{\pi}}S_t^{(i,k)}\,\chi(S_n^{(i,k)})\right]\widehat{\mathrm{t}}^{(k)}\right\}.\end{aligned} \tag{5.93}$$

Now the acting force is decomposed into a part due to diffuse reflection and a part due to specular reflection. We derive:

$$\Delta\overline{\mathrm{F}}_{sat}^{(i,k)} = \frac{1}{2}\,\rho^{(i)} V^2\, A^{(k)} \overline{\mathrm{C}}^{(i,k)}, \tag{5.94}$$

$$\overline{\mathrm{C}}^{(i,k)} = -\left[\sigma^{(i,k)}\,\overline{\mathrm{C}}_d^{(i,k)} + (1-\sigma^{(i,k)})\,\overline{\mathrm{C}}_s^{(i,k)}\right], \tag{5.95}$$

$$\begin{aligned}\overline{\mathrm{C}}_d^{(i,k)} &= \frac{1}{S_{(i)}^2}\left\{\left[\frac{1}{\sqrt{\pi}}\Pi(S_n^{(i,k)}) + \frac{1}{2}\sqrt{\frac{T_w^{(k)}}{T}}\chi(S_n^{(i,k)})\right]\widehat{\mathrm{n}}^{(k)}\right. \\ &+ \left.\left[\frac{1}{\sqrt{\pi}} S_t^{(i,k)}\,\chi(S_n^{(i,k)})\right]\widehat{\mathrm{t}}^{(k)}\right\},\end{aligned} \tag{5.96}$$

$$\overline{\mathrm{C}}_s^{(i,k)} = \frac{1}{S_{(i)}^2}\left\{\left[\frac{2}{\sqrt{\pi}}\Pi(S_n^{(i,k)})\right]\widehat{\mathrm{n}}^{(k)}\right\}, \tag{5.97}$$

which is identical to Klinkrad and Fritsche (1998).

Force model using the thermal accommodation coefficient

The following force model is based on a slightly different concept. To describe the interaction of the incoming molecules and the surface element, only the thermal accommodation coefficient α is used:

$$\alpha = \frac{E_i - E_r}{E_i - E_w} = \frac{T_i - T_r}{T_i - T_w}. \tag{5.98}$$

It is defined as the ratio between the amount of energy that has actually been exchanged between the surface element and the incoming molecule and the amount of energy that could have been exchanged if perfect accommodation occurred (T_w is the wall temperature). For perfect accommodation, $\alpha = 1$, all incoming molecules are reflected diffusely; for the case of vanishing energy exchange, $\alpha = 0$, all molecules are reflected specularly.

According to Gerstl (1998) the thermal accommodation coefficient α can be described in dependence of the mass of the incoming molecule species and the mass of the surface element molecules:

$$\alpha_{(i,k)} = \frac{4 m_i m_k}{(m_i + m_k)^2}, \tag{5.99}$$

with

- m_k mass of the molecules of surface element k,
- m_i mass of the atmospheric constituent i impacting on surface element k.

A molecule that hits the surface element k under an angle $\theta_I^{(k)}$, that is defined as the angle between the relative velocity and the surface tangent, is reflected diffusely inside a cone with a cone angle of $\nu_r^{(i,k)}$. The angle between the axis of the cone and the surface element is $\theta_R^{(i,k)}$ (see figure 5.11). It is

$$\cos\theta_R^{(i,k)} = \left(\cos\theta_I^{(k)}\right)^{1/(1-\alpha_{(i,k)})^2}, \tag{5.100}$$

$$\nu_R^{(i,k)} \approx \cos(0.535185 \arcsin\alpha_{ik}). \tag{5.101}$$

We get for the drag coefficient $C_D^{(i,k)}$:

$$C_D^{(i,k)} = 2\left(1 - \sqrt{1-\alpha_{(i,k)}}\,\nu_R^{(i,k)}\cos(\theta_I^{(k)} + \theta_R^{(i,k)})\right). \tag{5.102}$$

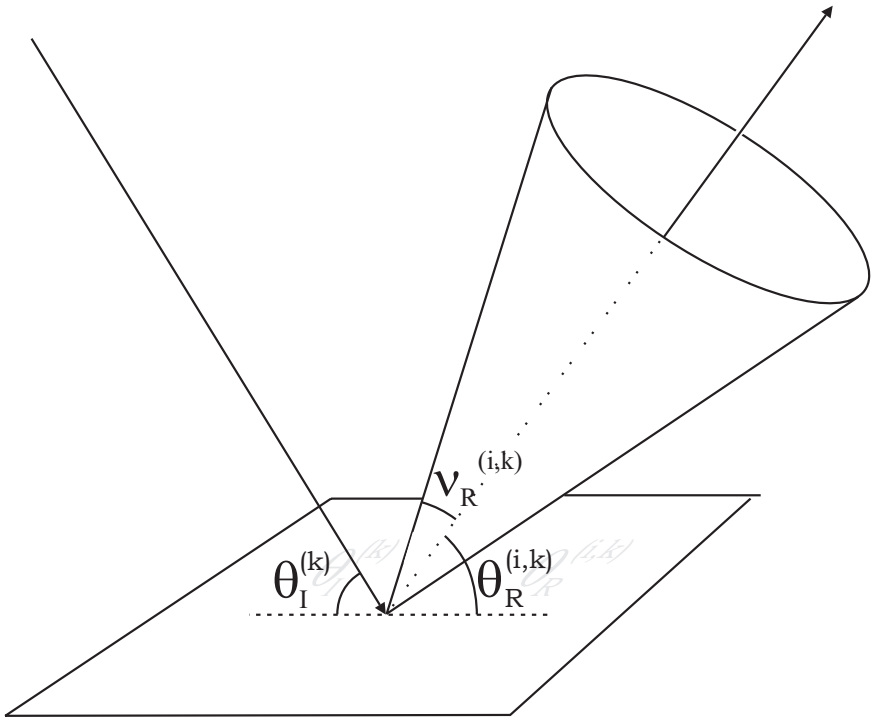

Figure 5.11: One parameter accommodation model. Diffuse reflection is assumed. The incoming molecule is reflected within a cone of certain aperture. Depicted are the angle $\theta_I^{(i,k)}$, the cone angle $\nu_r^{(i,k)}$ and the angle between the cone and the surface element $\theta_R^{(i,k)}$.

For the lift coefficient $C_L^{(i,k)}$ we get:

$$C_L^{(i,k)} = 2\left(\sqrt{1-\alpha_{(i,k)}}\;\nu_R^{(i,k)}\sin(\theta_I^{(k)}+\theta_R^{(i,k)})\right). \tag{5.103}$$

Finally, we derive for the total force due to drag and lift $\Delta\overline{\mathrm{F}}_{sat}^{(i,k)}$:

$$\Delta\overline{\mathrm{F}}_{sat}^{(i,k)} = \frac{1}{2}\,\rho^{(i)}\,V^2 A^{(k)}\cdot\overline{\mathrm{C}}^{(i,k)}, \tag{5.104}$$

with

$$\overline{\mathrm{C}}^{(i,k)} = -\left(C_D^{(i,k)}\cdot\hat{\mathrm{u}}_\mathrm{D} + C_L^{(i,k)}\cdot\hat{\mathrm{u}}_\mathrm{L}\right). \tag{5.105}$$

Empirical model

The model formulation from Mazanek et al. (2000) has been derived before, we just repeat it for completeness:

$$\Delta\overline{\mathrm{F}}_{sat}^{(i,k)} = \frac{1}{2}\,\rho^{(i)}V^2A^{(k)}\overline{\mathrm{C}}^{(i,k)}, \tag{5.106}$$

$$\overline{\mathrm{C}}^{(i,k)} = -\left(\,C_n^{(i,k)}\,\hat{\mathrm{n}}^{(k)} + C_t^{(i,k)}\,\hat{\mathrm{t}}^{(k)}\right), \tag{5.107}$$

$$C_n^{(i,k)} = 2\left[(2-\sigma_n^{(i,k)})\,\cos^2\phi^{(k)} + \sigma_n^{(i,k)}\,\frac{V_r^{(i,k)}}{V}\cos\phi^{(k)}\right], \tag{5.108}$$

$$C_t^{(i,k)} = 2\left[\sigma_t^{(i,k)}\cos\phi^{(k)}\sin\phi^{(k)}\right], \tag{5.109}$$

where

$$\sigma_n^{(i,k)} = a_n - b_n \exp(-c_n E^{(i)} \cos^2 \phi^{(k)}), \tag{5.110}$$
$$\sigma_t^{(i,k)} = a_t - b_t \exp(-c_t E^{(i)} \sin^{\frac{3}{4}} \phi^{(k)}), \tag{5.111}$$

with

a_n, b_n, c_n	normal accommodation curve fit parameters - nominally 1.0, 0.9, 0.28,
a_t, b_t, c_t	tangential accommodation curve fit parameters - nominally 1.67, 1.67, 0.147,
$E^{(i)}$	collision activation energy in [eV].

The collision activation energy is given by

$$E^{(i)} = \frac{1}{2} m^{(i)} V^2, \tag{5.112}$$

where $m^{(i)}$ is the mass of the incoming particle species in [kg]. Equation (5.112) gives the energy in [J], to get it in [eV] as required, the result has to be scaled by $1.6 \cdot 10^{-19}$. The speciality of this model is that in contrast to, e.g., the standard two parameter force model the numerical values for the normal and tangential accommodation coefficients can be estimated and have not to be guessed.

Model comparison and discussion

We have derived now a series of drag models with different levels of sophistication and based on different assumptions. Let us now compare them. The basic force model shall be denoted as simple model. The model using the thermal accommodation coefficient from Gerstl (1998) shall be denoted model G, the model from Schaaf and Chambre (1961) shall be denoted model S&C, the model from Thalhammer (1989) shall be denoted model T, the model from Klinkrad and Fritsche (1998) shall be denoted model K and finally the model from Mazanek et al. (2000) shall be denoted model M.

Table 5.3: Different force models for air drag derivation.

model	input quantities	unknown inputs	force split up	velocity distribution	equations
simple	$\overline{\mathrm{V}}$, A, ρ	none	drag and lift	no	(5.13)
G	m_i, $\overline{\mathrm{V}}$, m_k, $\hat{\mathrm{n}}$, A, ρ	none	drag and lift	no	(5.102):(5.105)
S & C	m_i, $\overline{\mathrm{V}}$, $\hat{\mathrm{n}}$, A, ρ, σ_n, σ_t, T_w	σ_n, σ_t, T_w	pressure and shear	yes	(5.71):(5.78)
T	m_i, $\overline{\mathrm{V}}$, $\hat{\mathrm{n}}$, A, ρ, σ_n, σ_t, T_w	σ_n, σ_t, T_w	drag and pressure	yes	(5.87)
K	m_i, $\overline{\mathrm{V}}$, $\hat{\mathrm{n}}$, A, ρ, σ, T_w	σ, T_w	pressure and shear	yes	(5.94):(5.97)
M	$\overline{\mathrm{V}}$, $\hat{\mathrm{n}}$, A, ρ, E, T_w	T_w	pressure and shear	no	(5.106):(5.109)

The derived models can be divided into three groups:

1. Models that require no unknown inputs like the simple model and model G,
2. analytical models like S & C, T and K that represent the standard two, respectively one parameter accommodation models; they can be transformed into each other analytically and require the surface reflection coefficients and the surface temperature as an input,
3. experimental models like model M that derives the surface reflection coefficients from experimental data. It requires the surface temperature as input.

The comparison will be done in terms of the vector of ballistic coefficients. We will use the decomposition of forces in the direction of the relative velocity and perpendicular to it, meaning drag and lift. The simple force model introduced in the first place will also be included in the comparison. However as it assumes fixed values for C_D and C_L, only differences to the other models will be shown. For the results presented here, $T = 1100°$ K and $\rho = 10^{-12}$ kg/m^3 was used.

Derivation of the surface temperature T_w

The derivation of the surface temperature is complicated as the GRACE satellites are not rotating but kept in a nominal attitude, i.e. it is very likely that there will be temperature gradients. In this study this effect is neglected. For the results in this subsection $T_w = 450°$K will be used.

Derivation of the normal and tangential accommodation coefficients

For the models S & C, T and K the numerical values of the accommodation coefficients need to be defined. In order to make the results comparable to the other models, the definition of the thermal accommodation coefficient from model G is used. The normal and tangential accommodation coefficient are set equal to the derived thermal accommodation coefficient for each atmospheric species.

Model G

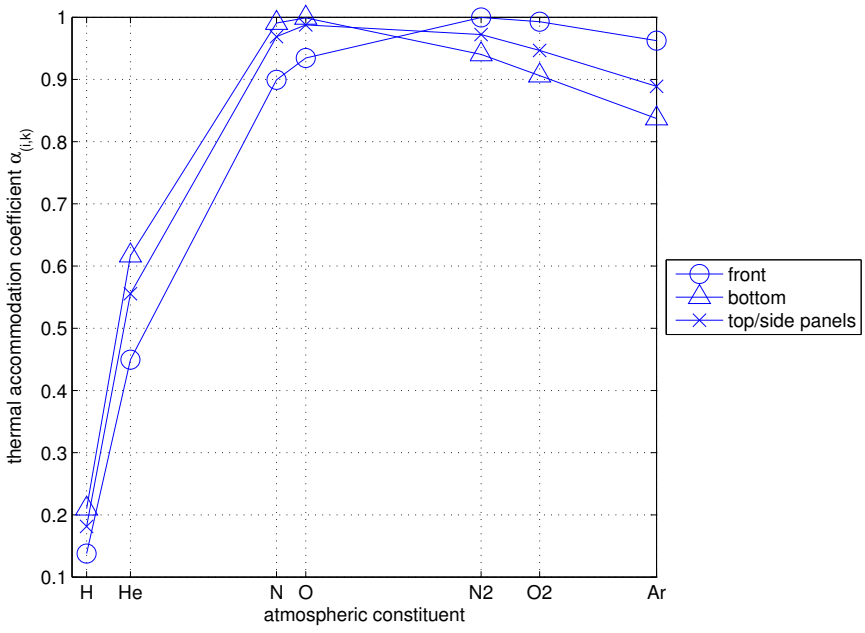

Figure 5.12: Thermal accommodation coefficient α_{ik} depending on the surface type and the incoming molecule type.

Apart from the 'standard' inputs, which are relative velocity, outward surface normal and density, model G requires the atomic masses of the atmospheric molecules and the surface element material. These two quantities $m^{(i)}$ and $m^{(k)}$ are then used to derive the thermal accommodation coefficient α_{ik}. Typically 7 types of atmospheric constituents are considered: H, He, O, N_2, O_2, Ar and N. Atomic oxygen accounts for more than 75 % of the constituents, followed by helium and nitrogen, that each contribute more than 20 %, see table (5.2). Helium is a rather light species, its atomic mass is 4u, atomic oxygen and nitrogen are rather heavy species with a mass of 16u and 28u per molecule. The GRACE surface elements consist of three different kinds of materials: aluminium (front and rear), silicon dioxide (side

panels and top) and teflon (bottom). Figure 5.12 shows the thermal accommodation coefficient for the three different kinds of surfaces and for all atmospheric constituents in the order of their relative atomic mass. One notices that except for H, He and Ar the accommodation coefficient has a value above 0.9 for all surfaces, i.e. the incoming molecules are mainly reflected diffusely. For H the value of the accommodation coefficient is around 0.2, i.e. the incoming molecules are mainly reflected specularly. For He the value of the accommodation coefficient is around 0.5-0.6, i.e. the incoming molecules are reflected specularly and diffusely in equal parts. The next quantities that are derived are the angle between the axis of the reflection cone and the surface element $\theta_R^{(i,k)}$ (shown on the left panel of figure 5.13) and the cone angle $\nu_r^{(i,k)}$ (shown on the right panel of figure 5.13). Concerning $\theta_R^{(i,k)}$ it can be stated that for an angle of incidence of 90° the value is zero regardless of the considered atmospheric constituent. For angles of incidence between 0° and 90°, $\theta_R^{(i,k)}$ varies depending the atmospheric constituents: Except for H and He, $\theta_R^{(i,k)}$ is mostly 90°, i.e. we have diffuse reflection. For these two atmospheric constituents $\theta_R^{(i,k)}$ is proportional to the angle of incidence $\phi^{(k)}$, as for them specular reflection is applicable. The cone angle $\nu_r^{(i,k)}$ varies between 42° and 57°, taking on its largest value for H (specular reflection) and its lowest value for O (diffuse reflection).

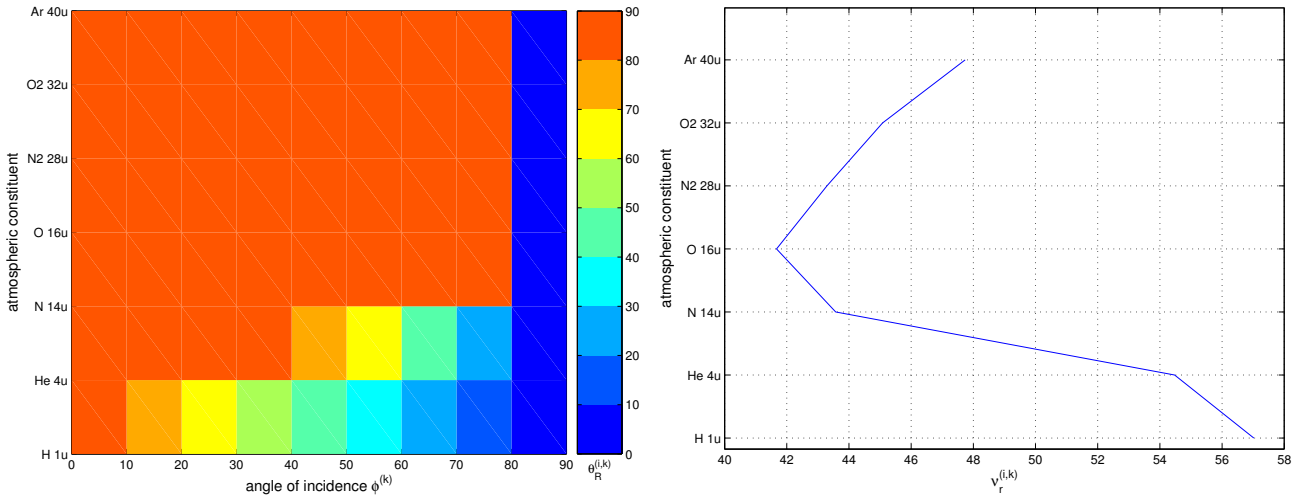

Figure 5.13: Left panel: Angle between the surface element and the reflection cone $\theta_R^{(i,k)}$ depending on the atmospheric constituents and the angle of incidence $\phi^{(k)}$. Right panel: Cone angle $\nu_r^{(i,k)}$ depending on the atmospheric constituents

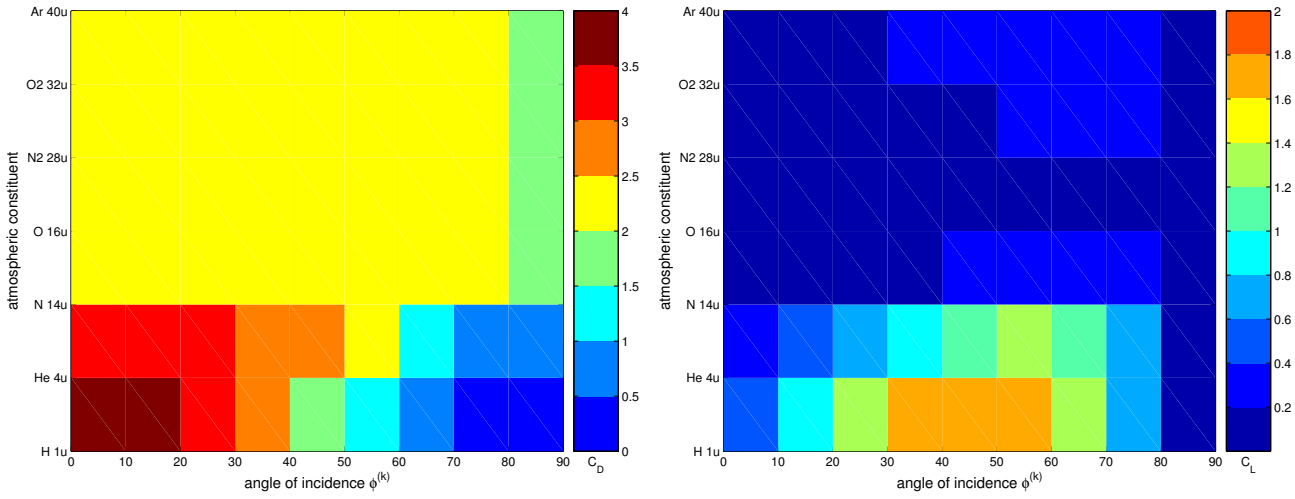

Figure 5.14: Left panel: C_D from model G, depending on the atmospheric constituent and the angle of incidence $\phi^{(k)}$. Right panel: C_L from model G, depending on the atmospheric constituent and the angle of incidence $\phi^{(k)}$.

Based on these values C_D and C_L are derived, cf. figure 5.14. We note that the C_D values for H and He (specular reflection) are again proportional to the angle of incidence, the maximum value being 4.0 for H and an angle of incidence of 90°. We also note that for the other five atmospheric constituents (diffuse reflection) the C_D value ranges from 2.0 to 2.5, which agrees with the standard value of 2.2 given e.g. in Sagirov (1970), except for angles of incidence above 80°. The values of C_L for all angles of incidence are below 0.4 for all atmospheric constituents (diffuse reflection) except H and He (specular reflection). For H, C_L takes on values of up to 1.8 for angles of incidence between 30° and 60°. The values of H and He depend on the angle of incidence.

Models S & C, T and K

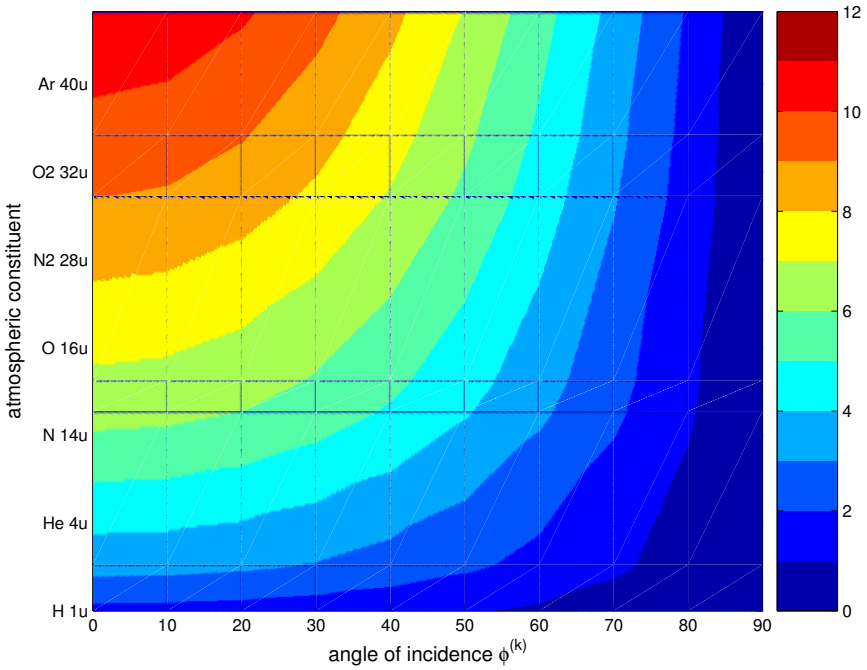

Figure 5.15: S_n from model S & C, depending on the angle of incidence $\phi^{(k)}$ and the atmospheric constituents

As the three models are identical in principle, we only show the results of the model from Schaaf and Chambre (1961). The first quantity to be derived for these models is the molecular speed ratio S_n scaled by $\cos\phi$. It is defined as the ratio between the magnitude of the relative velocity and the most probable velocity of the incoming molecules, cf. figure 5.15. We note that S_n is proportional to the square root of the atomic mass of the atmospheric constituents and to the cosine of the angle of incidence ϕ. It takes on values from 0 to 12, i.e. the satellite is up to 12 times faster than the molecules themselves. S_n is input for the next quantities to be derived: the pressure function and the particle flow function, depicted in figure 5.16. The pressure function values range from 0 to 450 and show the same behavior as the $S_n^{(i,k)}$ values: proportionality to the square root of the atomic mass of the atmospheric constituents and to the cosine of the angle of incidence. The particle flow function values magnitude is only one tenth of the magnitude of the values of the pressure function, they range from 0 to 40 and show again the same behavior as $S_n^{(i,k)}$.

From the pressure function and the particle function the values of $C_D^{(i,k)}$ and $C_L^{(i,k)}$ can be derived. They are shown in figure 5.17. We note that the $C_D^{(i,k)}$ vary again from 0 to 4.0, taking on maximal values for low angles of incidence and for the constituents H and He (specular reflection). For the remaining atmospheric constituents (diffuse reflection) the values are lower than 2.5 and decrease with increasing angle of incidence in contrast to the behavior of model G. The $C_L^{(i,k)}$ values are significantly

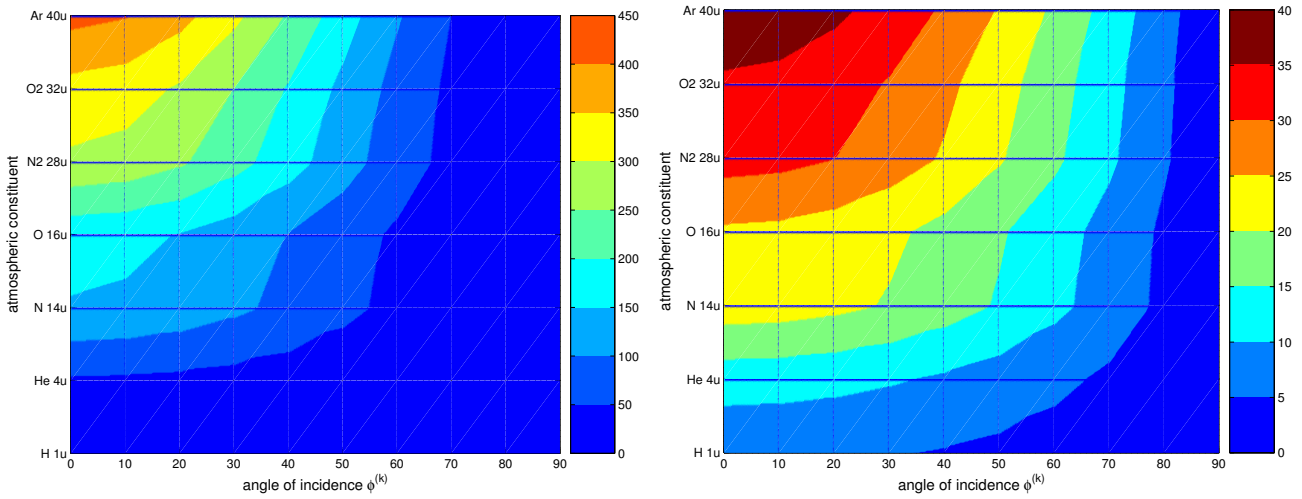

Figure 5.16: Left panel: Pressure function $\Pi(S_n^{(i,k)})$ as a function of the angle of incidence $\phi^{(k)}$ and the atmospheric constituents. Right panel: Particle flow function $\chi(S_n^{(i,k)})$ as a function of the angle of incidence $\phi^{(k)}$ and the atmospheric constituents

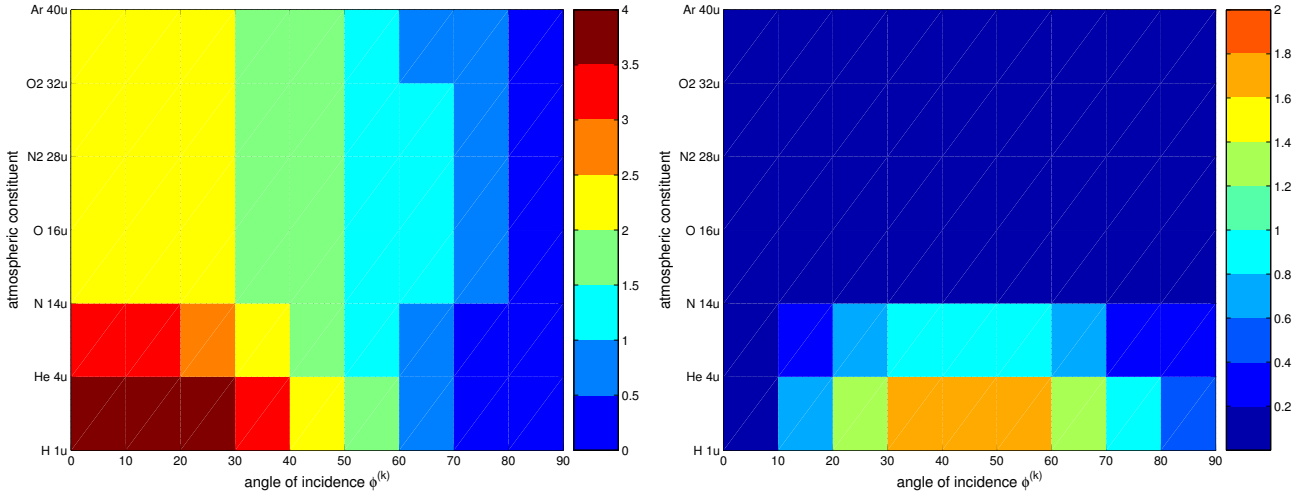

Figure 5.17: Left panel: $C_D^{(i,k)}$ of model S & C, as a function of the angle of incidence $\phi^{(k)}$ and of the atmospheric constituents. Left panel: $C_L^{(i,k)}$ of model S & C, as a function of the angle of incidence $\phi^{(k)}$ and of the atmospheric constituents

smaller with a maximal value of 1.8 at 45° angle of incidence and decreasing towards 0° and 90°. It is interesting that for the atmospheric constituents that are diffusely reflected (all but H and He), the values are rather low (below 0.2) and seemingly independent from the angle of incidence. Therefore it can be stated that the lift forces are about 10 % in magnitude of the drag forces. Here model S & C and model G behave very similar.

Model M

For model M, the normal and tangential accommodation coefficients originally taken from Knechtel and Pitts (1973) are determined empirically. The tangential accommodation coefficients have been corrected to yield a $C_D^{(i,k)}$ value of 2.2 for a spherical satellite.

The left panel of figure 5.18 shows the normal accommodation coefficients. As expected their maximum value is one. In contrast to the previous models, they show a direct correlation to the angle of incidence

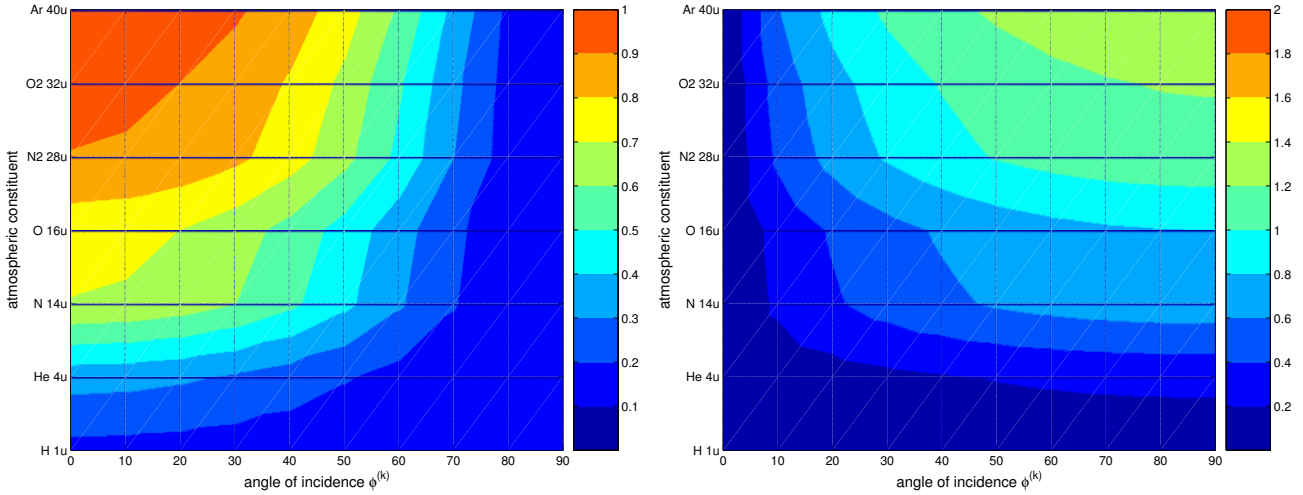

Figure 5.18: Left panel: $\sigma_n^{(i,k)}$ for model M, as a function of the angle of incidence $\phi^{(k)}$ and the atmospheric constituents. Right panel: $\sigma_t^{(i,k)}$ for model M, as a function of the angle of incidence $\phi^{(k)}$ and the atmospheric constituents

and to the mass of the atmospheric constituent. Only a rather small part of the particles is reflected mainly diffusely. The right panel of figure 5.18 shows the tangential accommodation coefficients. Their

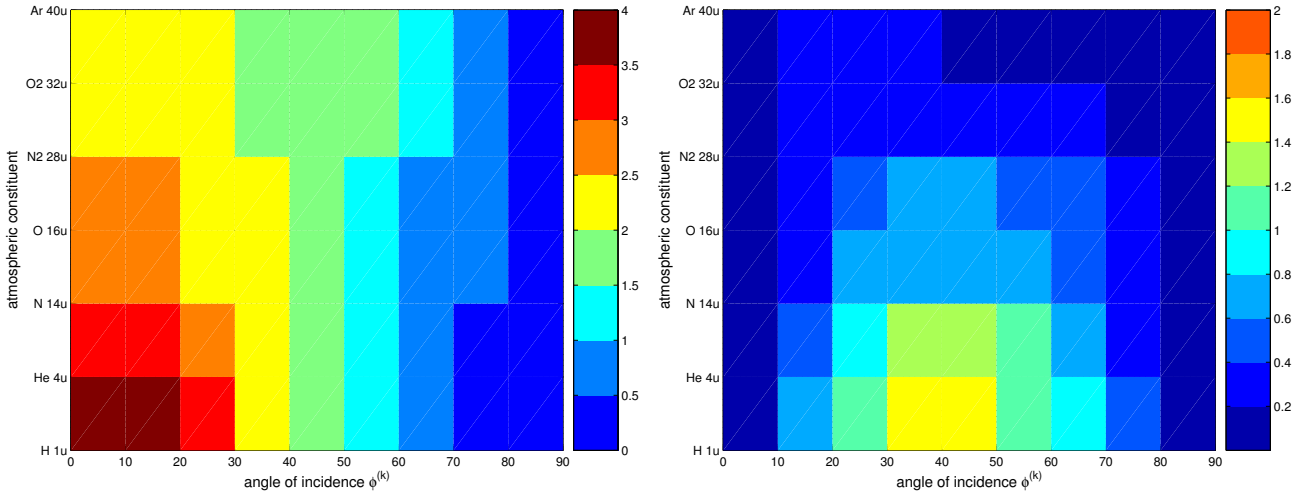

Figure 5.19: Left panel: $C_D^{(i,k)}$ from model M, depending on the angle of incidence $\phi^{(k)}$ and the atmospheric constituents. Right panel: $C_L^{(i,k)}$ from model M, depending on the angle of incidence $\phi^{(k)}$ and the atmospheric constituents

maximum value is not one, as expected, but about 1.4. The reason lies in the correction that was applied to the coefficients. For the main contributor to the atmospheric drag, O, the values are smaller than one and consequently physically meaningful. For the constituents heavier than O, the accommodation coefficient is larger than one and thus no longer physically meaningful.

The left panel of figure 5.19 shows the derived values for $C_D^{(i,k)}$. The maximal values are up to 4.0 again, they are reached for H and He, similar to the other models. For the diffusely reflected species the $C_D^{(i,k)}$ value is smaller than 2.5. It decreases with increasing angle of incidence unlike model G. The right panel of figure 5.19 shows the derived values for $C_L^{(i,k)}$. The maximal values are up to 1.6, which is smaller than for model G and for model S & C. There is no clear separation between the specularly reflected H and He and the other atmospheric constituents, at least not as pronounced as for the other models.

Model differences

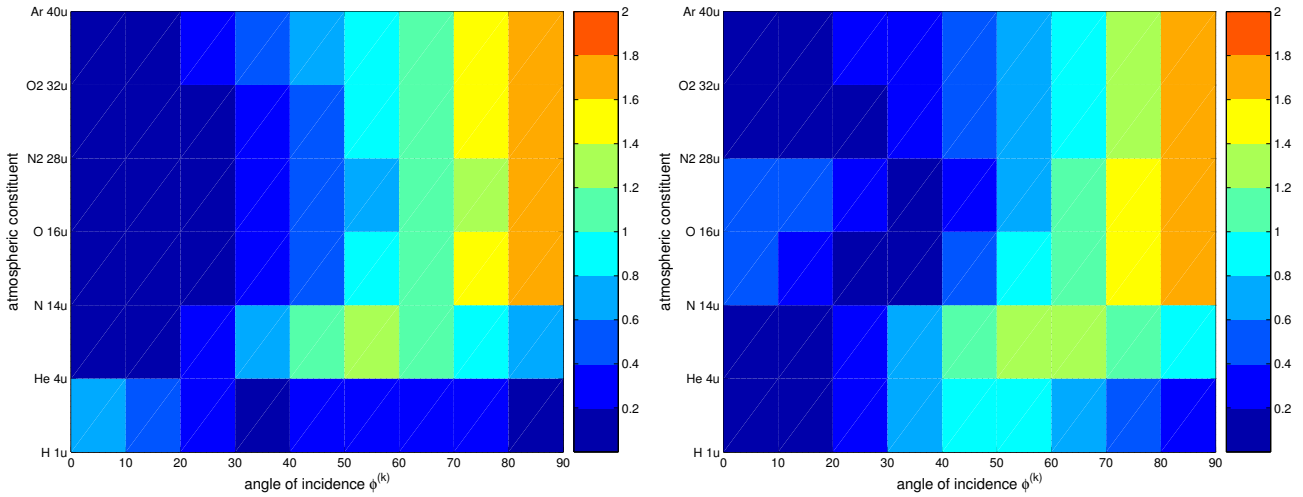

Figure 5.20: Left panel: Comparison of $C_D^{(i,k)}$ from model G with $C_D^{(i,k)}$ from model S & C. Right panel: Comparison of $C_D^{(i,k)}$ from model G with $C_D^{(i,k)}$ from model M.

In order to compare the output of the different models the differences between the $C_D^{(i,k)}$ and $C_L^{(i,k)}$ values as a function of the angle of incidence $\phi^{(k)}$ and of the atmospheric constituents are formed. The ballistic coefficients are just a scaling of the dynamic pressure $\frac{1}{2}\rho V^2$. For GRACE, $V = 7.3\ \frac{\mathrm{km}}{\mathrm{s}}$ and $\rho = 1 \cdot 10^{-12}\ \frac{\mathrm{kg}}{\mathrm{m}^3}$ is assumed, therefore the dynamic pressure is about $2.5 \cdot 10^{-5}\ \frac{\mathrm{N}}{\mathrm{m}^2}$, or, in terms of acceleration, if we assume a mass of 450 kg, it is about $6 \cdot 10^{-8}\ \frac{\mathrm{m}}{\mathrm{s}^2}\frac{1}{\mathrm{m}^2}$.

The left panel of figure 5.20 shows the difference in the $C_D^{(i,k)}$ value between model G and model S & C. We notice that for angles of incidence up to 50°, the differences are below 0.4, but start to rise to a level of up to 1.8 for large angles. Only for H the differences remain low, regardless of the angle of incidence. In terms of acceleration the differences rise up to about $8.4 \cdot 10^{-8}\ \frac{\mathrm{m}}{\mathrm{s}^2}\frac{1}{\mathrm{m}^2}$. The right panel of

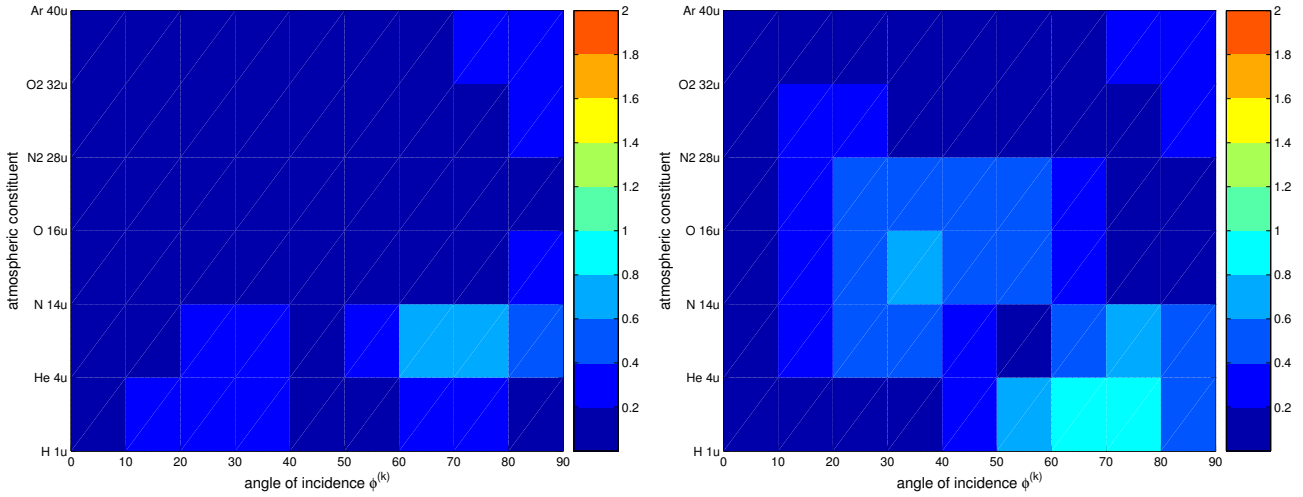

Figure 5.21: Left panel: Comparison of $C_L^{(i,k)}$ from model G with $C_L^{(i,k)}$ from model S & C. Right panel: Comparison of $C_L^{(i,k)}$ from model G with $C_L^{(i,k)}$ from model M.

figure 5.20 shows the difference in the $C_D^{(i,k)}$ value between model G and model M. The differences are very similar to the differences between model G and model S & C.

The left panel of figure 5.21 shows the difference in the $C_L^{(i,k)}$ value between model G and model S

& C. The differences are throughout below 0.2 except for some higher differences for He at angles of incidence between 60° and 80° that amount to a maximum value of 0.8. So in terms of acceleration the differences are in essence below $2.4 \cdot 10^{-9} \frac{\mathrm{m}}{\mathrm{s}^2} \frac{1}{\mathrm{m}^2}$; only for He they rise up to $4.8 \cdot 10^{-8} \frac{\mathrm{m}}{\mathrm{s}^2} \frac{1}{\mathrm{m}^2}$. The right

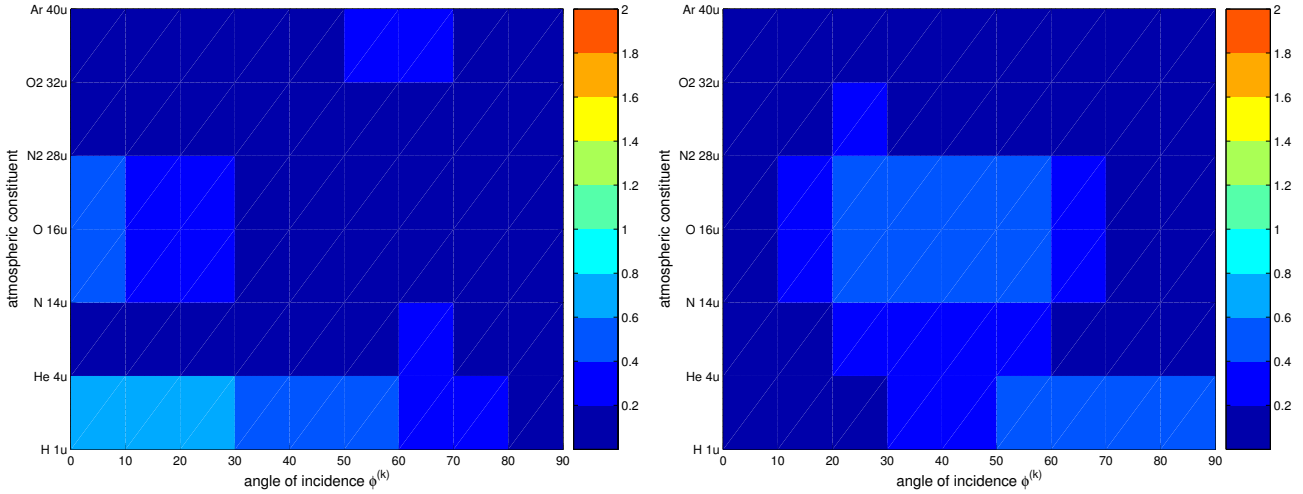

Figure 5.22: Left panel: Comparison of $C_D^{(i,k)}$ from model S & C with $C_D^{(i,k)}$ from model M. Right panel: Comparison of $C_L^{(i,k)}$ from model S & C with $C_L^{(i,k)}$ from model M

panel of the figure shows the difference between models G and M for the value of $C_L^{(i,k)}$. It reaches its maximum of 1 for H at angles of incidence between 60° and 80° .

The left panel of figure 5.22 shows the difference in the $C_D^{(i,k)}$ value between model M and model S & C. The differences are throughout below 0.2, except for H. At low angles of incidence the differences rise up to 0.8. Also for high angles of incidence for N and O, the differences are up to 0.6. The differences in terms of accelerations amount up to a level of $4.8 \cdot 10^{-8} \frac{\mathrm{m}}{\mathrm{s}^2} \frac{1}{\mathrm{m}^2}$. The right panel of figure 5.22 shows the difference in the $C_L^{(i,k)}$ value between model M and model S & C. Maximum differences of up to 0.6 occur for an angle of incidence between 20° and 70° for N and O and for H for an angle of incidence between 50° and 90° . The acceleration differences per unit area are at a level of $4.8 - 6 \cdot 10^{-8} \frac{\mathrm{m}}{\mathrm{s}^2} \frac{1}{\mathrm{m}^2}$.

Conclusions:

- Concerning the $C_D^{(i,k)}$ values, there are significant differences between model G and model S & C and between model G and model M, mainly for larger angles of incidence. The differences between model S & C and model M are much smaller despite the fact that different accommodation coefficients are used.
- Concerning the $C_L^{(i,k)}$ values, there are again significant differences between model G and model S & C and model G and model M, mainly for H and He. The differences between model S & C and model M are smaller but none the less significant, as they reach a level of $4.8 \cdot 10^{-8} \frac{\mathrm{m}}{\mathrm{s}^2} \frac{1}{\mathrm{m}^2}$ for O and N.

In order to evaluate how close each model is to reality, their output together with the output of the other models for non-conservative forces is compared to the real GRACE accelerometer measurements in section (5.6). In the following we will also compare the model output in terms of the total force acting on the satellite.

Derivation of the total force on the satellite

The force models presented so far deliver the force per unit area and per particle species. In order to get the total force on the whole satellite, one has to sum up the effects of the individual molecular species

Table 5.4: Statistic parameters of the different air drag models.

model	σ m/s^2	mean m/s^2	min m/s^2	max m/s^2
simple	x: $+5 \cdot 10^{-08}$	x: $-1 \cdot 10^{-07}$	x: $-2 \cdot 10^{-07}$	x: $-3 \cdot 10^{-08}$
	y: $+3 \cdot 10^{-10}$	y: $-2 \cdot 10^{-10}$	y: $-1 \cdot 10^{-09}$	y: $+7 \cdot 10^{-10}$
	z: $+6 \cdot 10^{-10}$	z: $+1 \cdot 10^{-09}$	z: $+3 \cdot 10^{-10}$	z: $+3 \cdot 10^{-09}$
M	x: $+6 \cdot 10^{-08}$	x: $-2 \cdot 10^{-07}$	x: $-3 \cdot 10^{-07}$	x: $-5 \cdot 10^{-08}$
	y: $+2 \cdot 10^{-09}$	y: $-3 \cdot 10^{-10}$	y: $-7 \cdot 10^{-09}$	y: $+5 \cdot 10^{-09}$
	z: $+7 \cdot 10^{-10}$	z: $+9 \cdot 10^{-10}$	z: $-2 \cdot 10^{-09}$	z: $+6 \cdot 10^{-09}$
S & C	x: $+7 \cdot 10^{-08}$	x: $-2 \cdot 10^{-07}$	x: $-4 \cdot 10^{-07}$	x: $-5 \cdot 10^{-08}$
	y: $+6 \cdot 10^{-09}$	y: $-9 \cdot 10^{-10}$	y: $-2 \cdot 10^{-08}$	y: $+1 \cdot 10^{-08}$
	z: $+5 \cdot 10^{-09}$	z: $+6 \cdot 10^{-09}$	z: $-1 \cdot 10^{-08}$	z: $+2 \cdot 10^{-08}$
G	x: $+6 \cdot 10^{-08}$	x: $-1 \cdot 10^{-07}$	x: $-3 \cdot 10^{-07}$	x: $-4 \cdot 10^{-08}$
	y: $+7 \cdot 10^{-09}$	y: $-1 \cdot 10^{-09}$	y: $-2 \cdot 10^{-08}$	y: $+1 \cdot 10^{-08}$
	z: $+2 \cdot 10^{-09}$	z: $+2 \cdot 10^{-09}$	z: $-6 \cdot 10^{-09}$	z: $+2 \cdot 10^{-08}$

over all areas. The surface model of the GRACE satellites was presented in section 5.2 and is used now to determine the individual area. The total force is:

$$\overline{\mathrm{F}}_{total} = \frac{1}{2}\rho^{(i)}V^2 \sum_k A^{(k)} \cdot \sum_i \overline{\mathrm{C}}^{(i,k)} \cdot \frac{N_d^{(i)}}{\sum_i N_d^{(i)}}. \tag{5.113}$$

$N_d^{(i)}$ is the number density of the constituent i and ρ is now the total mass density of all incoming molecules.

Figure 5.23 and table 5.4 show a comparison of the different models. Let us first take a look at the along-track accelerations shown in the upper two panels of the figure. The top left panel shows the different model outputs in the time domain. They behave similar in terms of magnitude, offset and variability: The magnitude varies between $-4 \cdot 10^{-8}$ m/s^2 and $-3 \cdot 10^{-7}$ m/s^2. The standard deviation is about $6 \cdot 10^{-8}$ m/s^2 and the mean value is $-1 \cdot 10^{-7}$ m/s^2, cf. table 5.4. The top right panel shows the corresponding root PSD. Again the models behave similar. It is interesting that a strong signal is not only visible at once per revolution (at $2 \cdot 10^{-4}$ Hz), but also at $1 \cdot 10^{-4}$ Hz, that is caused by the air density variations. The signal at once per revolution is dominant. At high frequencies all PSDs level out at about $1 \cdot 10^{-7}$ m/s$^2/\sqrt{\text{Hz}}$.

Now we take a look at the cross-track accelerations in the time domain shown in the middle left panel. Here model G and model S & C agree well. The outputs of the simple model and model M are different from them and from each other. Comparing table 5.4, we see that the simple model delivers the smallest output. Here the mean value of $-2 \cdot 10^{-10}$ m/s^2, as well as the variability of $3 \cdot 10^{-10}$ m/s^2 is smallest, followed by model M showing a larger variability of $2 \cdot 10^{-9}$ m/s^2. The models G and S & C show a mean value of $-1 \cdot 10^{-9}$ m/s^2 and a standard deviation of $6 \cdot 10^{-9}$ m/s^2. The maximal values for them range between $-2 \cdot 10^{-8}$ m/s^2 and $1 \cdot 10^{-8}$ m/s^2. The middle right panel shows the root PSD of the model cross-track accelerations. Now all models except the simple model show a dominant signal at once per revolution, as for the simple model only forces in direction of the relative velocity are considered. The simple model shows the smallest signal, followed by model M and then models G and S & C.

The radial model accelerations time series is shown in the lower left panel. Here the simple model and model M agree well. Model G and model S & C behave differently than the simple model and model M. Among them, they are similar, but the mean value is different. Concerning the variability, the simple model and model M show a similarly small value of $6 \cdot 10^{-10}$ m/s^2, followed by model G with $2 \cdot 10^{-9}$ m/s^2. Model S & C shows the largest standard deviation of $5 \cdot 10^{-9}$ m/s^2. The mean value of $6 \cdot 10^{-9}$ m/s^2 from model S & C is largest. The simple model and model M show mean values around $1 \cdot 10^{-09}$ m/s^2.

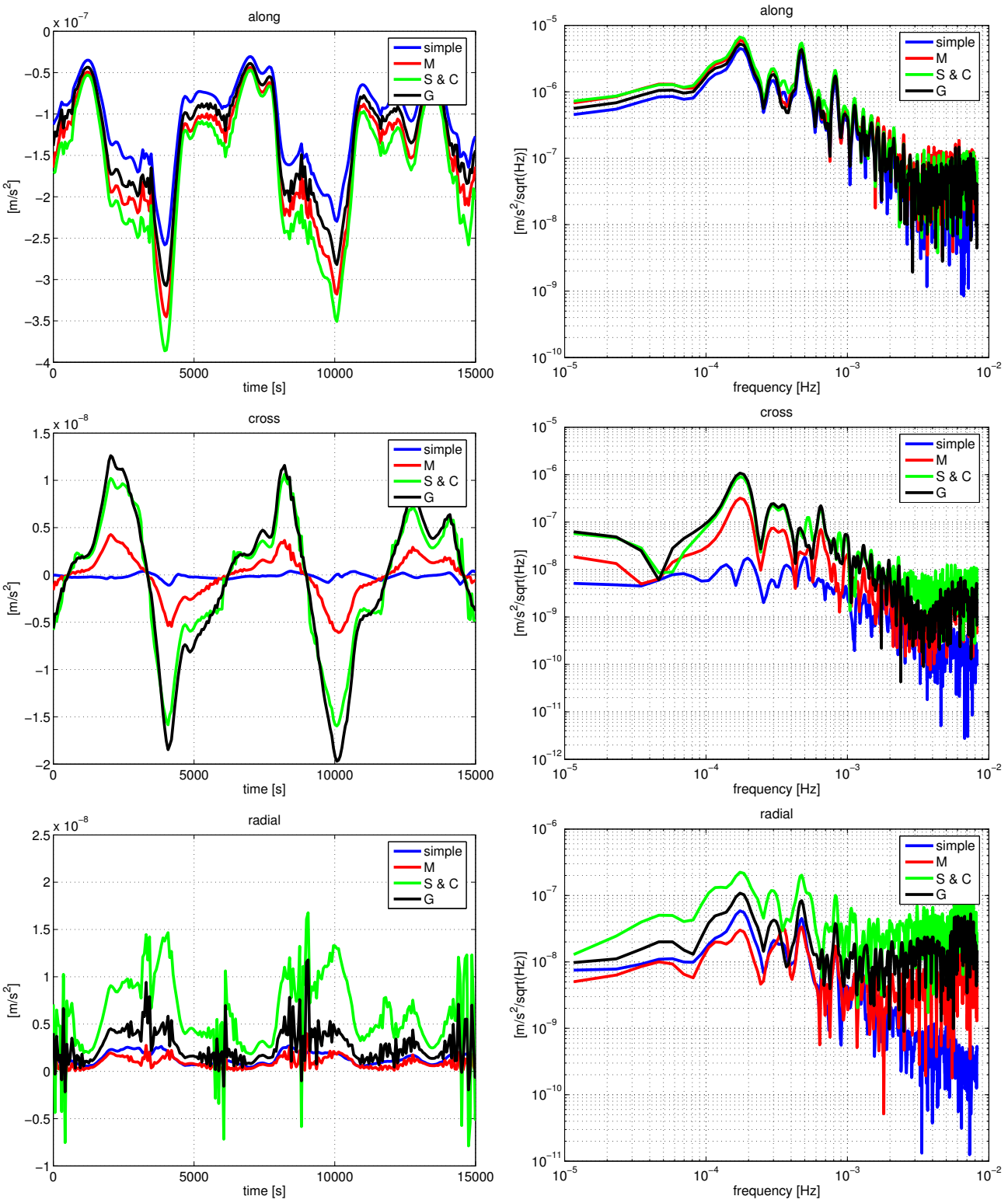

Figure 5.23: Comparison of the different air drag models. The left panels show along-track, cross-track and radial component in the time domain, the panels to the right show the corresponding root PSDs.

Conclusions

In principle the different models agree well, especially for the dominant along-track component. Here the use of more sophisticated models like model S & C or model G seems not be necessary, the difference to the most simple model is small. Concerning the cross-track and radial components, the differences

between the models are more pronounced. During the comparison with the real measurements it will be difficult to decide which one performs better, as here solar radiation pressure and earth albedo are the dominant effects.

5.4. Solar radiation pressure

5.4.1. Introduction

Solar radiation pressure is caused by the illumination of a body by the Sun. At a first glance it may sound strange that the Sun's light causes a significant pressure on such a relatively small object as a satellite, but apart from the gravitational forces and the air drag, solar radiation pressure has a significant influence. The measured accelerations are mainly due to air drag and solar radiation pressure.

We will first introduce a simple model of the shadow of the Earth, before we continue to present the model for the solar radiation pressure induced accelerations on the satellite.

5.4.2. Shadow of the Earth

We will model the shadow of the Earth in this work as simple as possible and therefore use a cylindrical shadow model, cf. Wermuth (2000) and figure 5.24. Input quantities are the position vector of the satellite in the IRF and the current position of the Sun in the IRF given as right ascension and declination. The distance to the Sun is assumed to be infinite, therefore the incoming sunlight rays are parallel. The Earth then casts a shadow of a cylindrical form and infinite extent. As a next step, the IRF satellite position is rotated by the right ascension α of the Sun about the z-axis and then by the negative declination δ of the Sun about the (new) y-axis:

$$\overline{\mathrm{r}}_{\odot}^{sat} = \underline{\mathrm{R}}_2(-\delta_{\odot})\underline{\mathrm{R}}_3(\alpha_{\odot}) \cdot \overline{\mathrm{r}}_i^{sat}. \tag{5.114}$$

The position of the satellite is now given in a coordinate system $\{\overline{\mathrm{e}}_{\odot=1}, \overline{\mathrm{e}}_{\odot=2}, \overline{\mathrm{e}}_{\odot=3}\}$ of which the positive x-axis is pointing towards the Sun. Using simple conditions, it can now be determined wether the satellite is inside or outside the shadow of the Earth: if $x_{\odot}^{sat} > 0$, the satellite is between Earth and Sun and therefore not inside the shadow. If the Earth is in front of the satellite ($x_{\odot}^{sat} < 0$), we check if the satellite position is inside the cylindrical Earth shadow, i.e. if

$$y_{\odot,sat}^2 + z_{\odot,sat}^2 \leq r_E^2. \tag{5.115}$$

In reality, the transition between sunlight and shadow is smooth, because before entering the shadow, the so-called penumbra is passed. Inside the penumbra, the satellite is illuminated by a part of the normal solar radiation, as in these regions the Sun is only partly visible.

5.4.3. Force model

The model presented here can be found in Wertz (1991). The pressure acting on a sunlit surface is the solar flux incident on the surface divided by the speed of light:

$$P = \frac{F_e}{c} \quad \left[\frac{\mathrm{kgm}^2}{\mathrm{s}^3\mathrm{m}^2} \cdot \frac{\mathrm{s}}{\mathrm{m}} = \frac{\mathrm{kg}}{\mathrm{ms}^2}\right], \tag{5.116}$$

with

F_e the solar flux, $F_e \approx 1370\mathrm{W/m}^2$,
c the velocity of light.

One part of the incoming radiation is absorbed, the other part is reflected. As for air drag, the reflection can be either specular or diffuse. We first determine the force due to absorption as:

$$\mathrm{d}\overline{\mathrm{F}}_{abs}^{(k)} = -PC_a^{(k)} \cos\phi^{(k)}\, \widehat{\mathrm{S}}\, \mathrm{d}A^{(k)} \quad (0 \leq \phi \leq 90°) \quad \left[\frac{\mathrm{kg}}{\mathrm{ms}^2} \cdot \mathrm{m}^2 = \frac{\mathrm{kgm}}{\mathrm{s}^2} = \mathrm{N}\right], \tag{5.117}$$

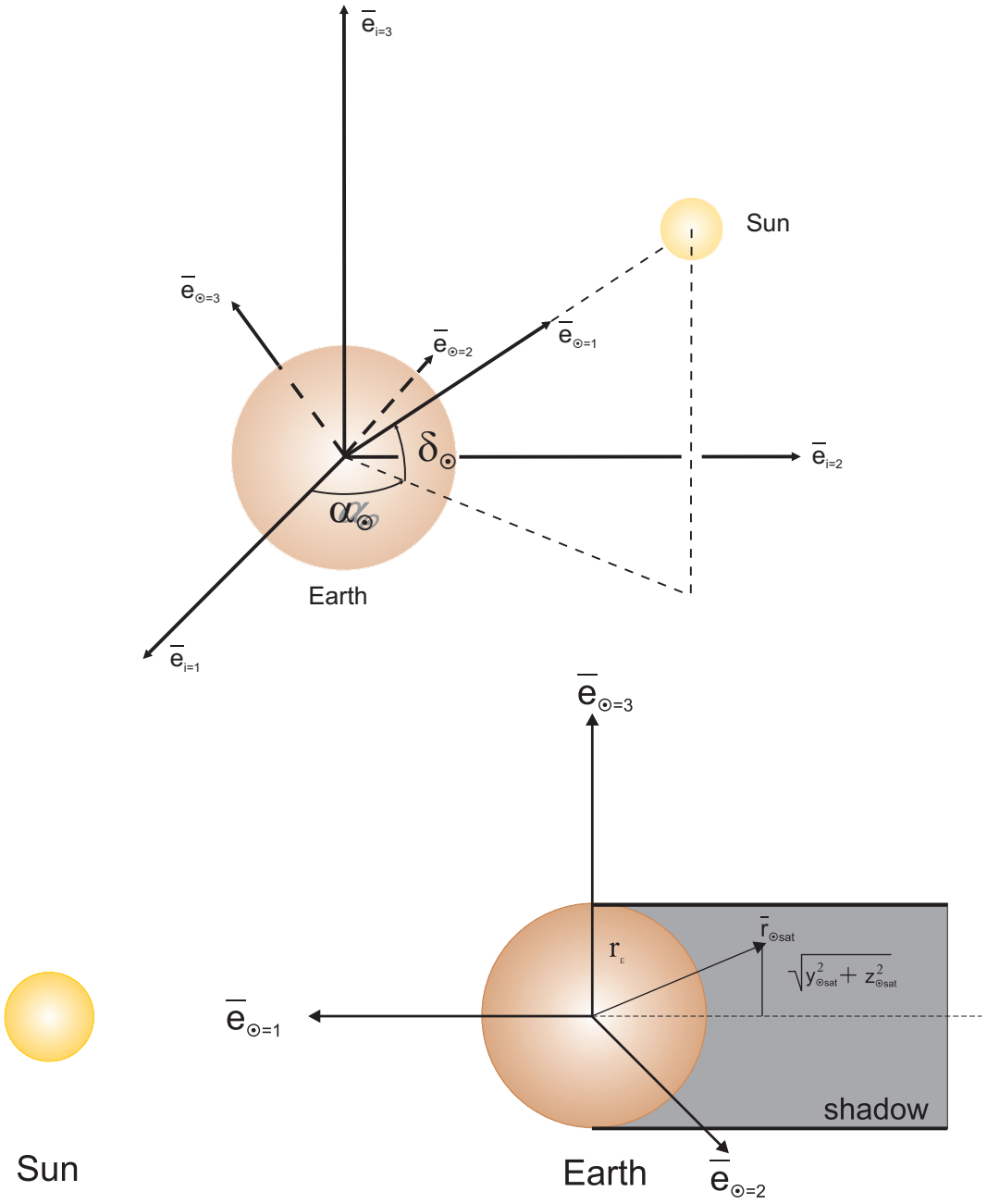

Figure 5.24: Cylindrical Earth shadow model, cf. Wermuth (2000)

where

$\widehat{\mathrm{S}} = \frac{\bar{\mathrm{r}}_{Sun} - \bar{\mathrm{r}}_{sat}}{\lvert \bar{\mathrm{r}}_{Sun} - \bar{\mathrm{r}}_{sat} \rvert}$	is the unit vector pointing from the satellite to the Sun,
$\cos\phi^{(k)} = \widehat{\mathrm{n}}^{(k)} \cdot \widehat{\mathrm{S}}$	the cosine of the angle between the surface normal and the direction to the Sun,
$C_a^{(k)}$	is the absorption coefficient,
$dA^{(k)}$	is the area of the surface element k.

If $\cos\phi^{(k)}$ is negative, the surface is not illuminated and the radiation pressure thus is zero. The force due to specular reflection can be determined as:

$$\mathrm{d}\bar{\mathrm{F}}_{spec}^{(k)} = -2PC_s^{(k)} \cos^2\phi^{(k)}\, \widehat{\mathrm{n}}^{(k)}\, \mathrm{d}A^{(k)} \quad (0 \le \phi^{(k)} \le 90°). \tag{5.118}$$

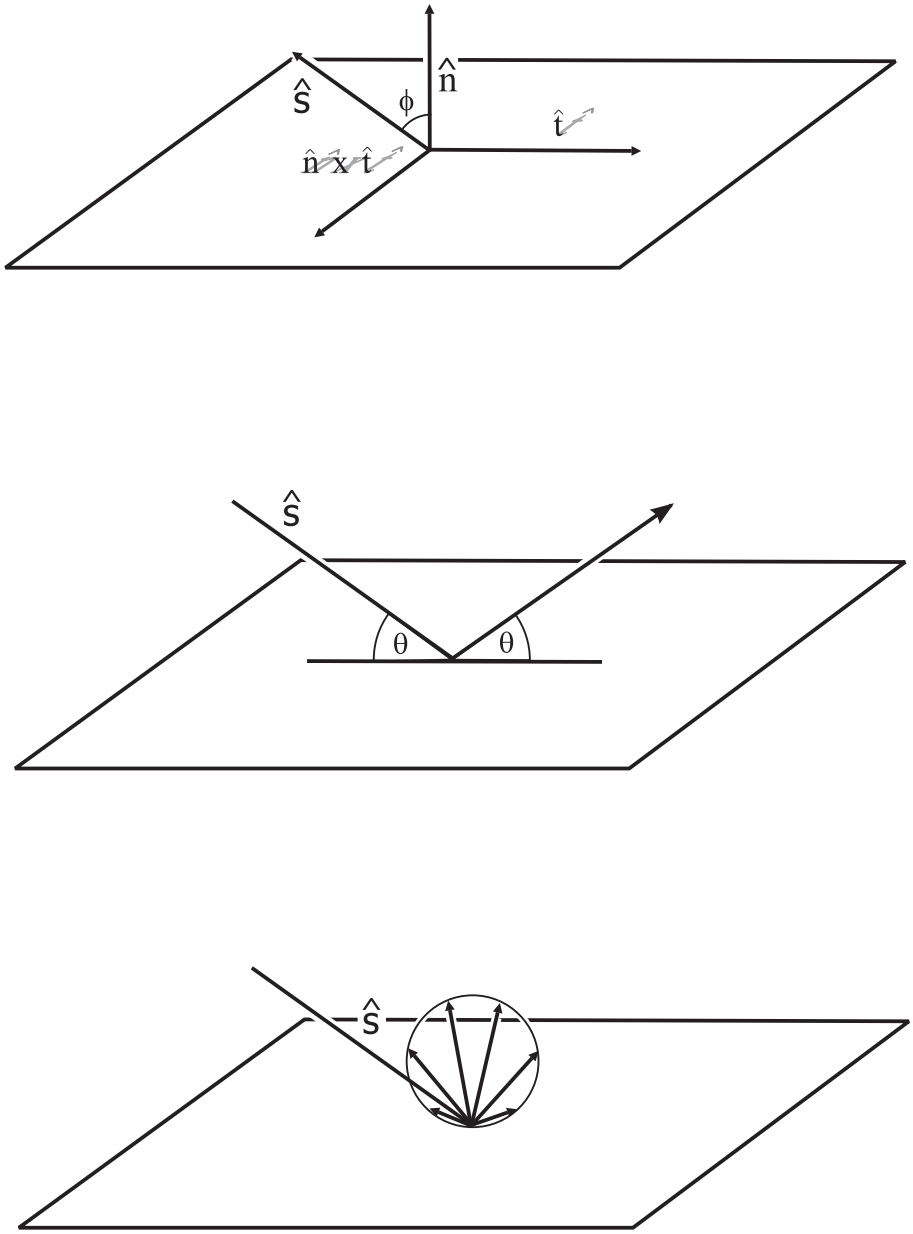

Figure 5.25: Impact geometry and reflection types for the solar radiation pressure. The second panel shows the case of specular reflection, the third panel shows the case diffuse reflection.

$C_s^{(k)}$ is the fraction of the incoming radiation that is reflected specularly. For specular reflection, the incoming radiation and the reflected radiation cause the same pressure in direction of the surface normal, but a pressure opposite in sign in direction of the tangent. Therefore only two times the pressure in direction of the surface normal remains. For the part that is reflected diffusely, there is a component acting in direction of the incident radiation due to the impact and a component acting in direction of the surface normal:

$$\mathrm{d}\overline{\mathrm{F}}_{diff}^{(k)} = PC_d^{(k)} \left(-\frac{2}{3} \cos\phi^{(k)}\, \widehat{\mathrm{n}}^{(k)} - \cos\phi^{(k)}\, \widehat{\mathrm{S}} \right) \mathrm{d}A^{(k)} \quad (0 \leq \phi^{(k)} \leq 90°). \tag{5.119}$$

$C_d^{(k)}$ is the diffusely reflected part of the incoming radiation. In reality, all three possibilities of reflection occur simultaneously:

$$\mathrm{d}\bar{\mathrm{F}}_{total}^{(k)} = -P \int \left[\left(1 - C_s^{(k)} \right) \widehat{\mathrm{S}} + 2 \left(C_s^{(k)} \cos\phi^{(k)} + \frac{1}{3}\, C_d^{(k)} \right) \widehat{\mathrm{n}}^{(k)} \right] \cos\phi^{(k)}\, \mathrm{d}A^{(k)}, \tag{5.120}$$

where $C_a^{(k)} + C_s^{(k)} + C_d^{(k)} = 1$. $C_s^{(k)}$ and $C_d^{(k)}$ are derived from the macro-model of the satellites. As the surface elements are flat, the area is $A^{(k)}$ and the total force on the surface element k is:

$$\overline{\mathrm{F}}^{(k)} = -P \left[\left(1 - C_s^{(k)}\right) \widehat{\mathrm{S}} + 2 \left(C_s^{(k)} \cos\phi^{(k)} + \frac{1}{3} C_d^{(k)} \right) \widehat{\mathrm{n}}^{(k)} \right] \cos\phi^{(k)} \, A^{(k)}. \tag{5.121}$$

The total force on the satellite due to solar radiation is then given by:

$$\overline{\mathrm{F}}_{srad} = \sum_k \overline{\mathrm{F}}^{(k)}. \tag{5.122}$$

Figure 5.26 shows the solar radiation pressure converted to an acceleration over one day in the satellite

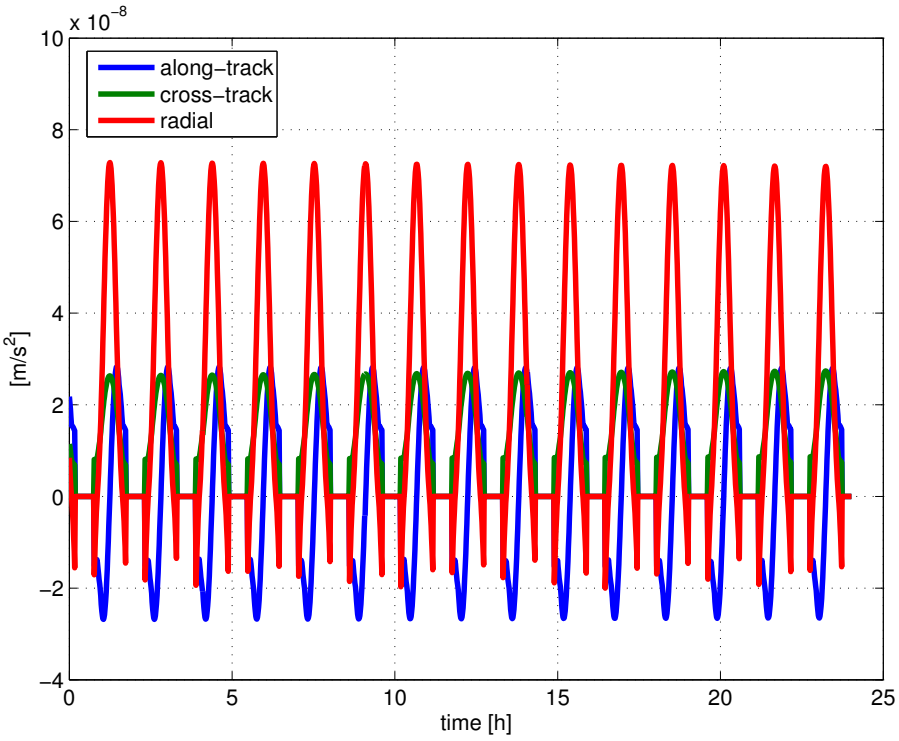

Figure 5.26: Solar radiation pressure over one day in the satellite body frame.

fixed coordinate system. For this simulation, the orbit plane is aligned with the direction to the Sun. As expected, then the radial component dominates, followed by the cross-track and along-track component. The magnitudes are up to $7 \cdot 10^{-8}\mathrm{m/s^2}$ for the radial component and around $3 \cdot 10^{-8}\mathrm{m/s^2}$ for the along-track and cross-track components. One can also identify the phases of shadow transit where the acceleration is zero.

5.5. Earth albedo

5.5.1. Introduction

In our albedo model we will consider Earth albedo as radiation re-emitted by the Earth. A comprehensive description in given in Kandel (1980). Earth albedo is caused by short-wave radiation emitted by the Sun, cf. figure 5.27. The radiation re-emitted by the Earth can be divided into short-wave radiation and long-wave or infrared radiation. The short-wave radiation results from the part of incoming solar radiation, about 25 %, that is reflected back to space at the clouds in the troposphere. The long-wave part of the re-emitted radiation results from the part of the incoming solar radiation that has been

transmitted to the Earth's surface and been absorbed there. After absorption, this radiation is then re-emitted to space as long-wave radiation in the infrared part of the electromagnetic spectrum. In our model we will only consider these two main effects, although reality is more complex. Parts of the short-wave as well as the long-wave radiation are absorbed in the different layers of the atmosphere. Other parts are transmitted to ground and then reflected back at cloud layers in the troposphere, there is also an energy flow between the short- and long-wave radiation, cf. Kandel (1980) and figure 5.27 for more details. In the following we will present models for short- and long-wave albedo.

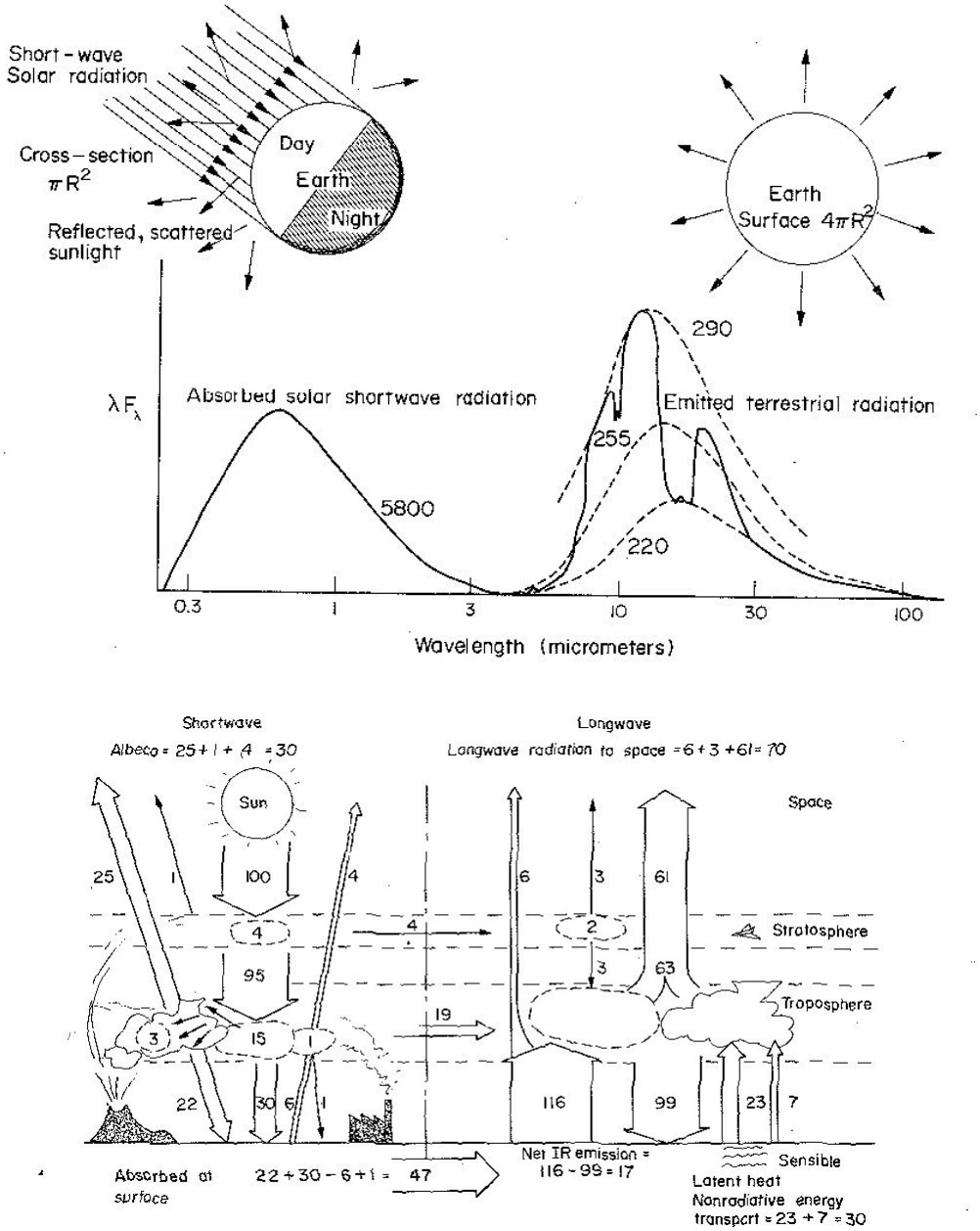

Figure 5.27: Top panel: Global radiative equilibrium. The spectrum of the incoming solar radiation and the radiation emitted by the Earth is shown. The energy of the re-emitted radiation is concentrated at longer wavelengths rather than that of the incoming radiation. Also the spectrum of the re-emitted radiation does not fully correspond to a black body spectrum. Note that the spectrum of the short-wave radiation that is reflected at the clouds of the troposphere is identical to the one of the incoming solar radiation. Lower panel: Energy budget of the Earth as a three layer model. Both figures from Kandel (1980).

5.5.2. Force model

Short-wave albedo

Concerning the short-wave albedo, we will use the model described in Bhanderi and Bak (2005). First, the amount of incoming radiation from the Sun has to be determined. It is modeled as the spectrum emitted by a body with a surface temperature of 5777 K using Planck's law. The main part of the resulting radiation's wavelength is smaller than 2 µm and covers the visible part of the spectrum up to UV radiation.

$$E_{in} = \frac{r_{Sun}^2}{1\mathrm{AU}^2} \int_0^{+\inf} E_{Sun}(\lambda, T) d\lambda = 1366.5 \text{ W/m}^2, \tag{5.123}$$

with r_{Sun} the Sun's mean radius. The incoming radiation then hits a surface element on Earth. The

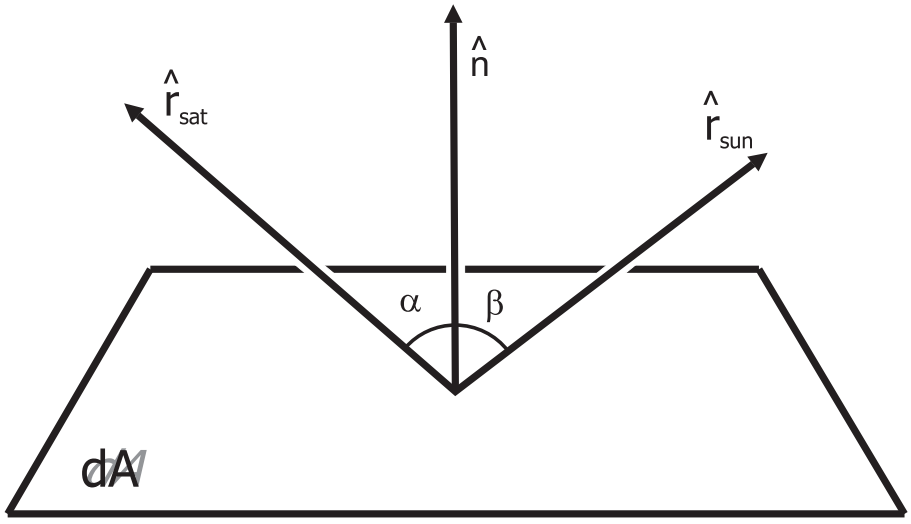

Figure 5.28: Principle albedo model. The amount of reflected radiation depends on the surface element area and the angles between the directions to the Sun and the satellite and the surface normal.

situation is depicted in figure 5.28. The radiant flux of the incoming radiation depends on the surface area dA and the angle β between the cell surface element normal $\hat{\mathrm{n}}$ and the direction to the Sun $\hat{\mathrm{r}}_{Sun}$:

$$P_c = E_{in} \cdot dA \cdot \cos\beta = E_{in} \cdot dA \cdot (\hat{\mathrm{r}}_{Sun} \cdot \hat{\mathrm{n}}). \tag{5.124}$$

The reflection is assumed to be Lambertian, i.e. we have diffuse reflection that is independent of the incident angle of the incoming reflection. The reflected radiant flux is a fraction of the incoming flux:

$$P_r = \rho \cdot P_c. \tag{5.125}$$

ρ is the mean reflectivity of the considered surface element. The irradiance of the surface element is then given by:

$$E_r = \frac{P_r}{\pi}. \tag{5.126}$$

The irradiance that reaches the satellite depends on the angle between the cell normal vector and the vector from the cell to the satellite as well as on the distance of the surface element from the satellite. The irradiance decreases proportional to the square of the distance from the irradiance source:

$$\overline{\mathrm{E}}_{sat,c}^{sw} = \frac{E_r \cdot \cos\alpha}{|\overline{\mathrm{r}}_{sat}^c|^2} \cdot \hat{\mathrm{r}}_{sat}^c, \tag{5.127}$$

where $\overline{\mathrm{r}}_{sat}^c$ is the vector from the cell c to the satellite position and $\cos\alpha$ is the angle between the cell normal vector $\hat{\mathrm{n}}$ and $\overline{\mathrm{r}}_{sat}^c$. The total irradiance on the satellite is given as the sum of all cell irradiances

that are in daylight and visible from the satellite's position:

$$\overline{\mathrm{E}}^{sw}_{sat,total} = \sum_c \overline{\mathrm{E}}^{sw}_{sat,c}. \tag{5.128}$$

The irradiance can be converted to a pressure by division by the velocity of light:

$$\overline{\mathrm{P}}^{sw}_{alb} = \frac{\overline{\mathrm{E}}^{sw}_{sat,total}}{c}. \tag{5.129}$$

For the model computations, the mean reflectivity of the surface elements of the Earth's surface is required. Reflectivity data are available from the Total Ozone Mapping Spectrometer (TOMS) project and deliver ρ.

Long-wave albedo

The second constituent of the Earth albedo is the long-wave albedo. The Earth's radiation can be modeled as that of a black body with a surface temperature of 288 °K. The spectrum of the resulting radiation is different from the one of the incoming radiation, it is mainly infrared. The radiation exitance for the Earth is about $E_{lw} = E_{in}/4 = 410$ W/m^2, cf. Kim (2000). The irradiance on the satellite from one cell of the Earth's surface is then given as:

$$\overline{\mathrm{E}}^{lw}_{sat,c} = \frac{e_{dir} \cdot E_{lw} \cdot \cos\alpha \cdot dA}{|\overline{\mathrm{r}}^c_{sat}|^2} \cdot \widehat{\mathrm{r}}^c_{sat}, \tag{5.130}$$

$$\cos\alpha = \widehat{\mathrm{n}} \cdot \widehat{\mathrm{r}}^c_{sat}. \tag{5.131}$$

dA is the cell area. e_{lw} is the emissivity of the considered cell and is given as:

$$e_{lw} = e_0 + e_1(t)P_{10}(\sin\phi_c) + e_2 P_{20}(\sin\phi_c), \tag{5.132}$$

$$e_1(t) = \bar{e} + e_{1c}\cos(\omega_e \cdot (t - t_0)) + e_{1s}\sin(\omega_e \cdot (t - t_0)). \tag{5.133}$$

The reference epoch t_0 is the epoch at the beginning of the year for which the calculation is to be carried out. $e_1(t)$ considers the annual variation of the Sun's declination. ω_e not the Earth rotation rate but the Earth revolution rate. P_{n0} are Legendre polynomials for $m = 0$. The numerical values for the used parameters are presented in table 5.5. The total irradiance on the satellite is then given as the sum of

Table 5.5: Numerical values for the parameters to be used in the long-wave albedo model, from Kim (2000).

Parameter	value
e_0	0.68
$\bar{e}$	0.00
e_{1c}	-0.07
e_{1s}	0.00
e_2	-0.18

all cell irradiances that are visible from the satellite's position:

$$\overline{\mathrm{E}}^{lw}_{sat,total} = \sum_c \overline{\mathrm{E}}^{lw}_{sat,c}. \tag{5.134}$$

The irradiance can be converted to a pressure by division by the velocity of light:

$$\overline{\mathrm{P}}^{lw}_{alb} = \frac{\overline{\mathrm{E}}^{lw}_{sat,total}}{c}. \tag{5.135}$$

Total albedo

The total albedo is given as the sum of the long- and the short-wave albedo. The resulting force on the satellite is derived in the same way as for the solar radiation pressure:

$$\overline{\mathrm{F}}_{sw}^{(k)} = -P_{alb}^{sw}\left[\left(1-C_{s,sw}^{(k)}\right)\widehat{\mathrm{P}}_{alb}^{sw}+2\left(C_{s,sw}^{(k)}\cos\phi^{(k)}+\frac{1}{3}\,C_{d,sw}^{(k)}\right)\widehat{\mathrm{n}}^{(k)}\right]\cos\phi^{(k)}\;A^{(k)}, \tag{5.136}$$

$$\overline{\mathrm{F}}_{lw}^{(k)} = -P_{alb}^{lw}\left[\left(1-C_{s,lw}^{(k)}\right)\widehat{\mathrm{P}}_{alb}^{lw}+2\left(C_{s,lw}^{(k)}\cos\phi^{(k)}+\frac{1}{3}\,C_{d,lw}^{(k)}\right)\widehat{\mathrm{n}}^{(k)}\right]\cos\phi^{(k)}\;A^{(k)}. \tag{5.137}$$

The total force on the satellite due to albedo radiation is given by the sum over all satellite surface elements k:

$$\overline{\mathrm{F}}_{alb}=\sum_{k}\left(\overline{\mathrm{F}}_{sw}^{(k)}+\overline{\mathrm{F}}_{lw}^{(k)}\right). \tag{5.138}$$

In equations (5.136) and (5.137), $\phi^{(k)}$ is the angle between the incoming radiation and the surface element normal; $A^{(k)}$ is the surface element area. The pressure vectors are usually given in the EFRF and have to be transformed to the SRF. The reflectivity coefficients $C_{s/d,sw}$ and $C_{s/d,lw}$ are given in table 5.1, where the values for the long-wave albedo are denoted with *ir* because the radiation takes place in the infrared part of the electromagnetic spectrum. The values for the short-wave albedo are the same as for the solar radiation pressure.

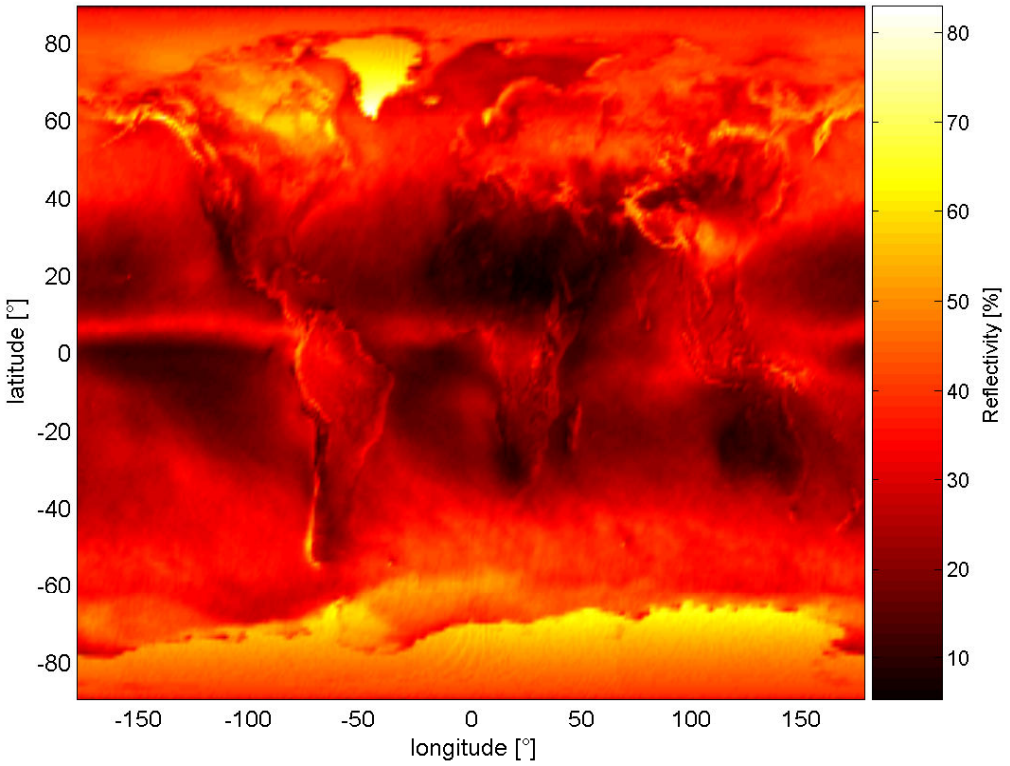

Figure 5.29: Mean reflectivity for 2005.

Let us now take a look at the short-wave albedo:

Figure 5.29 shows the mean reflectivity for the year 2005. We notice higher reflectivity over the ice covered areas of Antarctica and Greenland and lower reflectivity over the areas around the equator except for the intertropical convergence.

Figure 5.30 shows the Sun's field of view for an chosen epoch (left panel) and the corresponding satellites field of view for a realistic GRACE orbit (right panel). Figure 5.31 shows the sunlit field of view of the

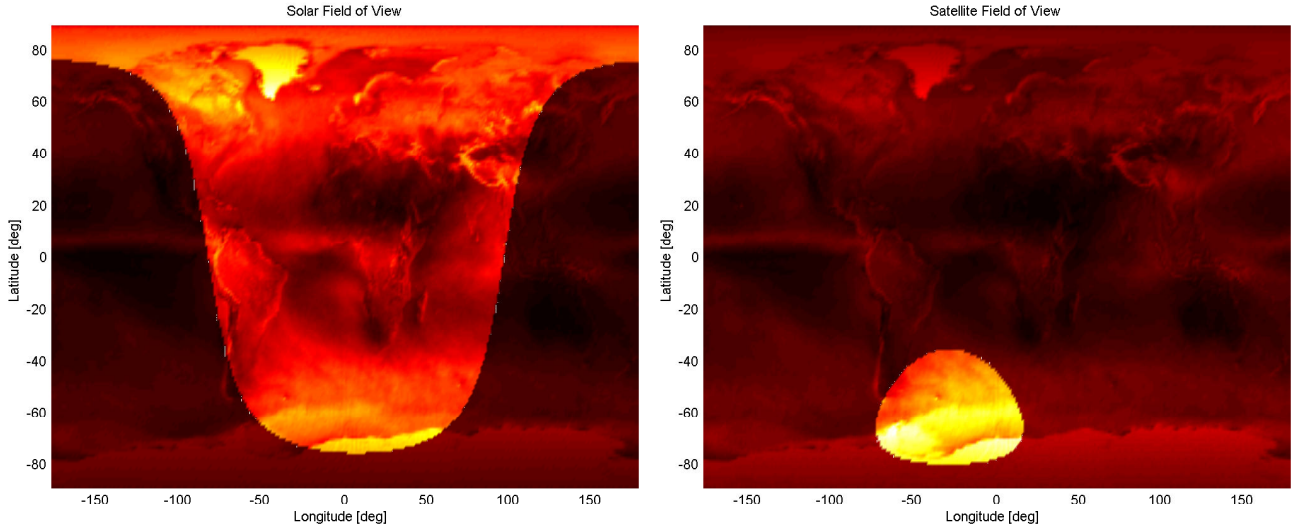

Figure 5.30: Left panel: Solar field of view. Right panel: Satellite field of view

satellite (left panel) and the resulting albedo matrix (right panel). The contribution of each cell has to be added up. The sunlit field of view is the intersection of the satellites field of view and the Sun's field of view.

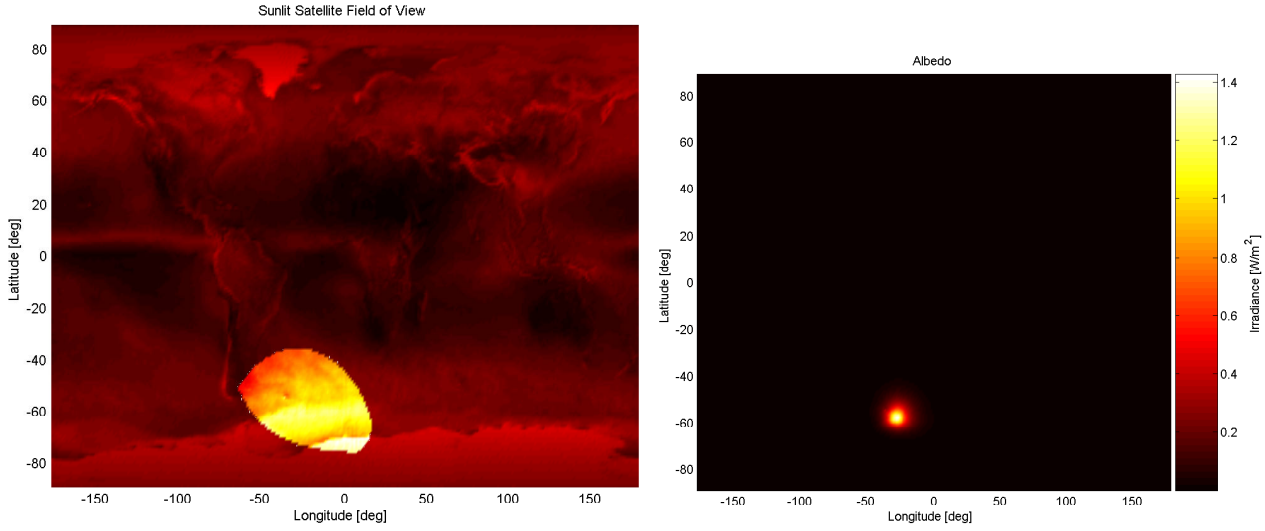

Figure 5.31: Left panel: Sunlit satellite field of view. Right panel: Short-wave albedo for a single epoch.

Figure 5.32 shows the resulting magnitude of the acceleration from the long-wave as well as the short-wave albedo. We realize that the long-wave albedo is always present and has a mean value of about $1.4 \cdot 10^{-8}$ m/s^2. The short-wave albedo is zero whenever the field of view of the satellite is in the shadow of the Earth. Generally speaking the short-wave albedo is smaller by a factor of two approximately. Both effects show a strong once per revolution signal.

Figure 5.33 shows the resulting acceleration over one day given in the satellite fixed body frame. The radial component is strongest and also biased because of the omnipresent long-wave radiation. Its magnitude is about $1.5 \cdot 10^{-8}$ m/s^2 with a variation of about $1 \cdot 10^{-8}$ m/s^2. The acceleration in along-track direction or cross-track direction is smaller by about an order of magnitude and shows no bias.

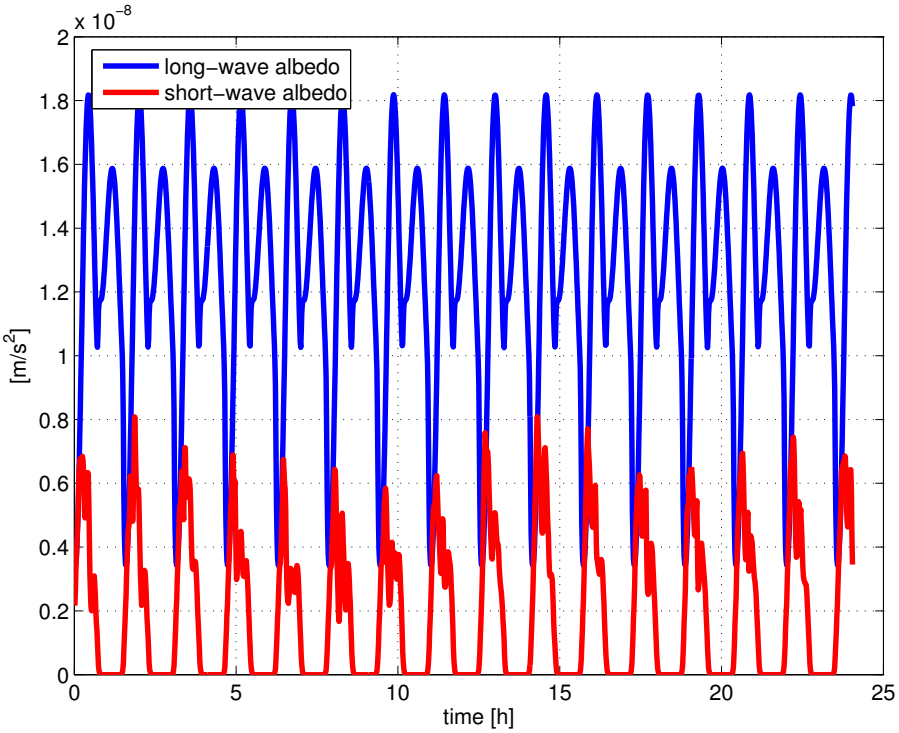

Figure 5.32: Long-wave and short-wave albedo magnitudes.

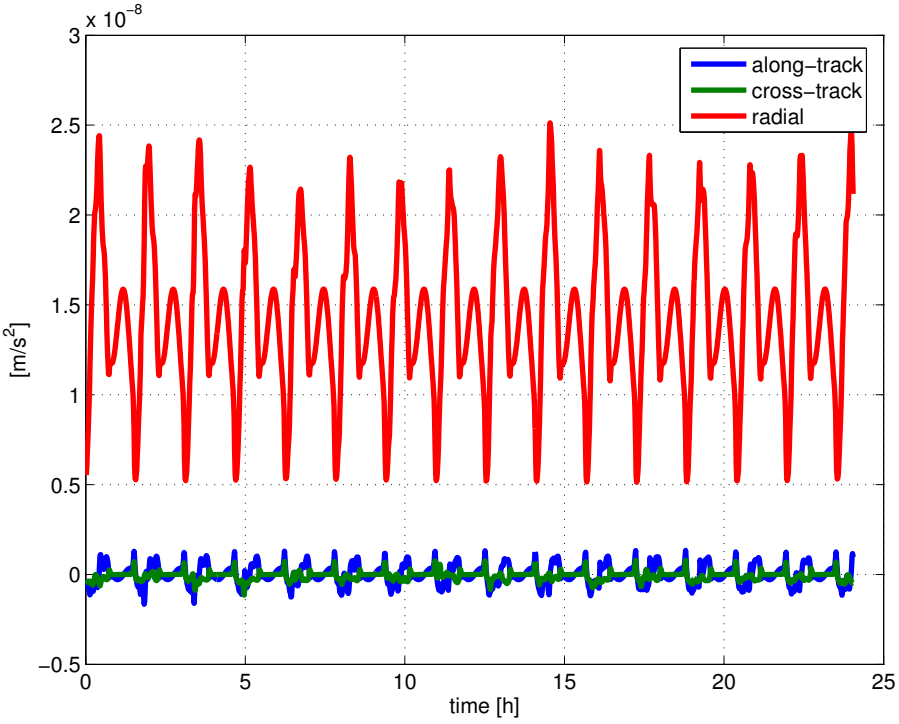

Figure 5.33: Earth albedo induced acceleration in the satellite fixed body system.

5.6. Comparison of the model results with real data

In this section, two important questions shall be answered:

Can the measured accelerations be replaced by modeled ones?

Which models have to be improved and how can this be done?

Linear acceleration

Figure 5.34 gives the comparison of the modeled surface forces with actual accelerometer measurements. As the results are similar for both satellites, the analysis is confined to the data of GRACE A. The left panels show the time series of the measured L1b linear accelerations in blue and the output of the surface force models discussed above. As we described only one model for solar radiation pressure and albedo, the use of the different air drag models produces different model outputs.

If we take a look at the top left panel showing the along-track accelerations in the SRF, we realize that the general features of the measured accelerations are reproduced and that the air drag magnitude is much higher those of solar radiation and albedo. However, there remain significant differences. All models show extra oscillations at frequencies of 2-4 cycles per revolution, not visible in the time series of the measured accelerations. The top right panel that shows the root PSD of the difference to the measured signal that confirms the observations in the time domain. The blue line represents the root PSD of the measurement. Only at the orbit frequency, the difference between the models and the measurement is smaller than the measured signal, at all other frequencies the models show effects that are not contained in the measurement. Although the models M and S & C perform slightly better in terms of magnitude of the difference to the measurements at the orbit frequency than the others, they perform slightly worse at the other frequencies.

The middle panel at the left shows the time series of the cross-track accelerations. The picture is the same as for the along-track accelerations: The order of magnitude is correct. Important features like the entry and exit of the Earth shadow seem to be modeled correctly, but significant differences remain. This is confirmed by the root PSDs (right panel) of the differences between models and measurements. Again the differences are at the level of the measurement, except at the orbit frequency. Here model M and model S & C show the smallest differences to the measurement. At the other frequencies, the performance of the different models seems to be similar.

The lower left panel shows the time series of the radial accelerations. Here the agreement between modeled accelerations and measurements seems to be better. All models perform very similar, in general the model values seem to be slightly too high. The root PSD of the differences confirms this assumption. The performance of the different models is very similar, here the difference at harmonics of the orbit frequency is smaller than the measurement itself. The difference at the other frequencies is again as large as the measured signal.

The statistic properties of the measured linear accelerations and modeled ones given in table 5.6 confirms these results.

Differential acceleration

The large differences between the modeled linear accelerations and the measured ones may decrease when the differential accelerations are analyzed. The differential acceleration magnitude should be smaller, as the two satellites are close to each other and therefore the encountered environment should be similar.

Figure 5.35 gives the comparison of the measured differential acceleration and the modeled ones, using again different air drag models.

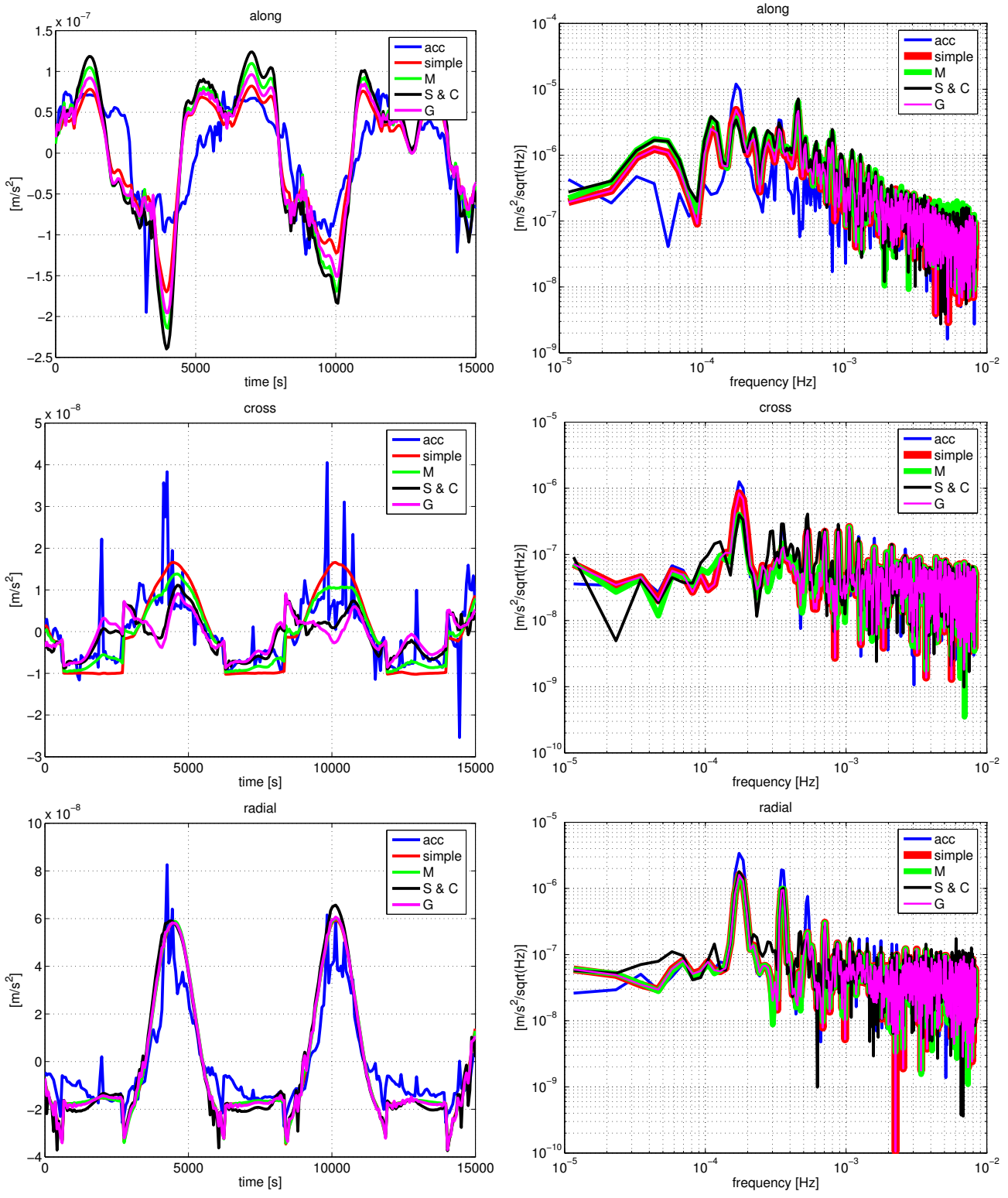

Figure 5.34: Comparison of the modeled surface forces and the actual measurement of the accelerometer. The left panels show time series of modeled accelerations for the along-track, cross-track and radial axis of the SRF and the corresponding measurements. The modeled surface forces have been derived using the different air drag models. The right panels show the root PSDs of the measured accelerations (blue) and the difference between measured accelerations and the modeled ones.

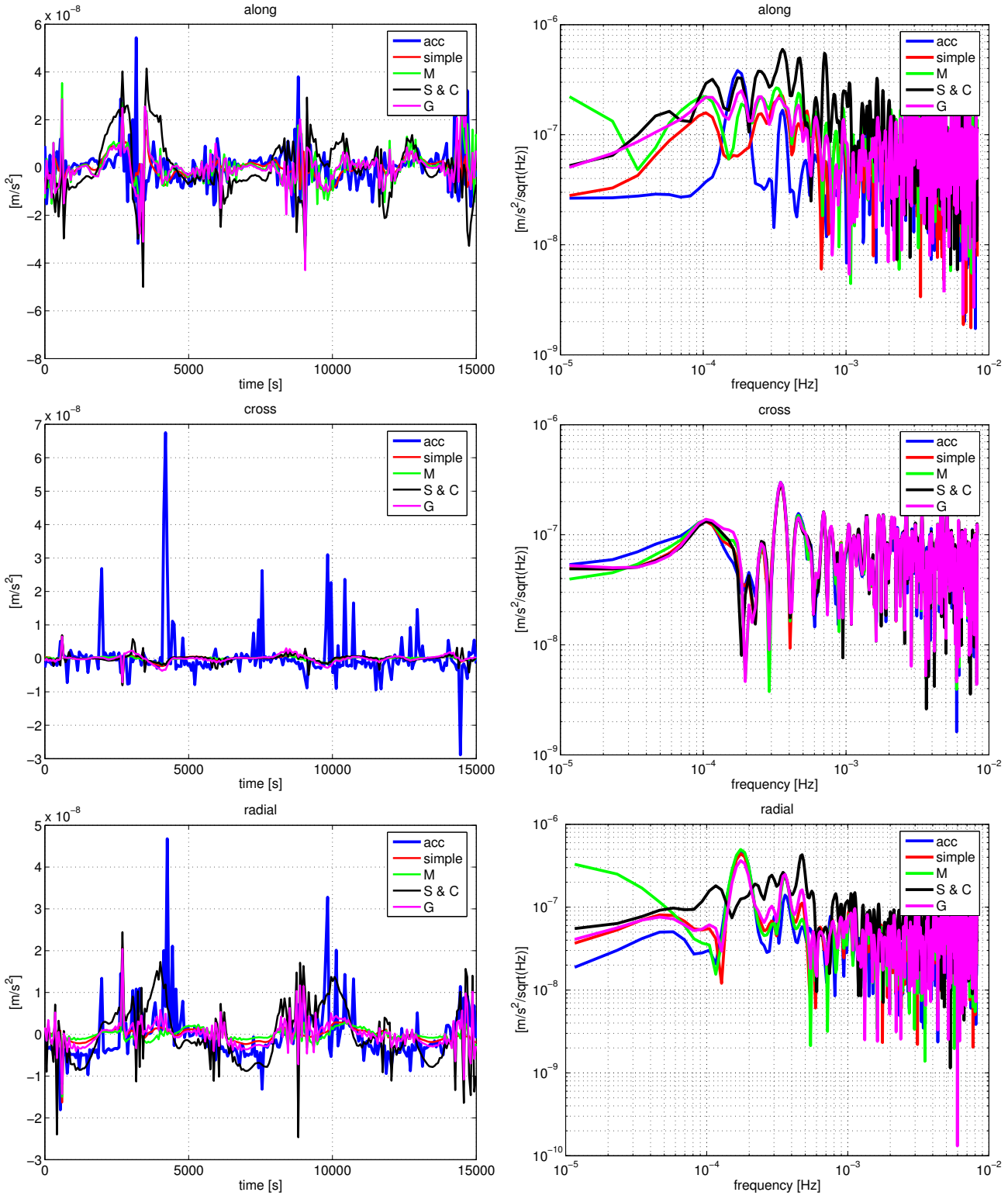

Figure 5.35: Comparison of the modeled differential acceleration and the actual measured differential acceleration. The left panels show time series of the modeled differential accelerations for the along-track, cross-track and radial axis of the SRF and the corresponding measurements. The right panels show the root PSDs of the measured differential accelerations (blue) and the difference between measured differential accelerations and the modeled ones.

Table 5.6: Statistic parameters for the measured linear acceleration on GRACE A and different models. The values are given in the SRF.

model	σ m/s^2	mean m/s^2	min m/s^2	max m/s^2
measured	x: $+6 \cdot 10^{-08}$	x: $+1 \cdot 10^{-06}$	x: $+1 \cdot 10^{-06}$	x: $+1 \cdot 10^{-06}$
	y: $+8 \cdot 10^{-09}$	y: $-3 \cdot 10^{-05}$	y: $-3 \cdot 10^{-05}$	y: $-3 \cdot 10^{-05}$
	z: $+2 \cdot 10^{-08}$	z: $+6 \cdot 10^{-07}$	z: $+5 \cdot 10^{-07}$	z: $+6 \cdot 10^{-07}$
simple	x: $+6 \cdot 10^{-08}$	x: $+1 \cdot 10^{-07}$	x: $+2 \cdot 10^{-08}$	x: $+3 \cdot 10^{-07}$
	y: $+1 \cdot 10^{-08}$	y: $-1 \cdot 10^{-08}$	y: $-3 \cdot 10^{-08}$	y: $+5 \cdot 10^{-10}$
	z: $+3 \cdot 10^{-08}$	z: $+2 \cdot 10^{-08}$	z: $-2 \cdot 10^{-08}$	z: $+8 \cdot 10^{-08}$
M	x: $+7 \cdot 10^{-08}$	x: $+2 \cdot 10^{-07}$	x: $+4 \cdot 10^{-08}$	x: $+4 \cdot 10^{-07}$
	y: $+8 \cdot 10^{-09}$	y: $-1 \cdot 10^{-08}$	y: $-3 \cdot 10^{-08}$	y: $-1 \cdot 10^{-10}$
	z: $+3 \cdot 10^{-08}$	z: $+2 \cdot 10^{-08}$	z: $-2 \cdot 10^{-08}$	z: $+8 \cdot 10^{-08}$
S & C	x: $+8 \cdot 10^{-08}$	x: $+2 \cdot 10^{-07}$	x: $+5 \cdot 10^{-08}$	x: $+4 \cdot 10^{-07}$
	y: $+5 \cdot 10^{-09}$	y: $-1 \cdot 10^{-08}$	y: $-2 \cdot 10^{-08}$	y: $-3 \cdot 10^{-10}$
	z: $+3 \cdot 10^{-08}$	z: $+1 \cdot 10^{-08}$	z: $-3 \cdot 10^{-08}$	z: $+8 \cdot 10^{-08}$
G	x: $+7 \cdot 10^{-08}$	x: $+1 \cdot 10^{-07}$	x: $+3 \cdot 10^{-08}$	x: $+3 \cdot 10^{-07}$
	y: $+5 \cdot 10^{-09}$	y: $-1 \cdot 10^{-08}$	y: $-2 \cdot 10^{-08}$	y: $-8 \cdot 10^{-10}$
	z: $+3 \cdot 10^{-08}$	z: $+2 \cdot 10^{-08}$	z: $-2 \cdot 10^{-08}$	z: $+8 \cdot 10^{-08}$

The top panel at the left shows the time series of the along-track component. The mean values are smaller by an order of magnitude, at a level of $-3 \cdot 10^{-10}$ m/s^2 to $1 \cdot 10^{-08}$ m/s^2 for all models, cf. table 5.7. The measurement's true mean value is unknown, it has therefore been detrended. The main features are represented by all models, but the simulated accelerations show additional oscillations. Concerning the variability, only the simple model agrees with the measurement, the other models show a higher standard deviation. Among themselves, the models G, S & C and M agree, but not with the simple model also in terms of mean, minimum and maximum values. The top panel at the right shows the root PSD of the measured differential acceleration and the difference to each model. All model differences show a signal slightly below once per revolution. It originates from the density model. At once per revolution the simple model performs best, the difference to the measured acceleration is lowest. The other model differences are at or above the magnitude of the measurement, also for the remaining frequencies.

The middle left panel shows the time series of the cross-track component. Here the main difference results from the fact that the models do not contain the thruster effects. The other features are reproduced well, but there are again oscillations in the models that are not real. The middle right panel shows the root PSD of the cross-track measurement and the corresponding differences between the models and the measurement. The differences are almost identical to the measurement, meaning that the dominant thruster effects have to be included in the models for a realistic model output. The models among themselves perform similar.

The lower panel at the left shows the time series of the radial component. There are significant differences between models and measurement. Again the effect of thruster events is not contained in the models, but shows up strongly in the measurement. There are also periods where the models show effects that are not contained in the measurements. The lower right panel shows the corresponding root PSD. The differences to the models are as large as the measurement itself.

The statistics of the comparison of the modeled differential acceleration and the measured one can be found in table (5.7).

Table 5.7: Statistic parameters for the measured differential acceleration and different models. The values are given in the SRF.

model	σ m/s^2	mean m/s^2	min m/s^2	max m/s^2
measured (detrended)	x: $+7 \cdot 10^{-09}$ y: $+7 \cdot 10^{-09}$ z: $+4 \cdot 10^{-08}$	x: 0 y: 0 z: 0	x: $-3 \cdot 10^{-08}$ y: $-4 \cdot 10^{-08}$ z: $-6 \cdot 10^{-08}$	x: $+5 \cdot 10^{-08}$ y: $-6 \cdot 10^{-08}$ z: $+1 \cdot 10^{-07}$
simple	x: $+5 \cdot 10^{-09}$ y: $+1 \cdot 10^{-09}$ z: $+6 \cdot 10^{-08}$	x: $-3 \cdot 10^{-10}$ y: $-3 \cdot 10^{-10}$ z: $+4 \cdot 10^{-08}$	x: $-1 \cdot 10^{-08}$ y: $-1 \cdot 10^{-08}$ z: $-3 \cdot 10^{-08}$	x: $+2 \cdot 10^{-08}$ y: $+7 \cdot 10^{-09}$ z: $+2 \cdot 10^{-07}$
M	x: $+1 \cdot 10^{-08}$ y: $+8 \cdot 10^{-10}$ z: $+6 \cdot 10^{-08}$	x: $+1 \cdot 10^{-09}$ y: $-8 \cdot 10^{-11}$ z: $+4 \cdot 10^{-08}$	x: $-5 \cdot 10^{-08}$ y: $-9 \cdot 10^{-09}$ z: $-3 \cdot 10^{-08}$	x: $+8 \cdot 10^{-08}$ y: $+7 \cdot 10^{-09}$ z: $+2 \cdot 10^{-07}$
S & C	x: $+1 \cdot 10^{-08}$ y: $+1 \cdot 10^{-09}$ z: $+6 \cdot 10^{-08}$	x: $+1 \cdot 10^{-08}$ y: $-3 \cdot 10^{-10}$ z: $+4 \cdot 10^{-08}$	x: $-4 \cdot 10^{-08}$ y: $-1 \cdot 10^{-08}$ z: $-4 \cdot 10^{-08}$	x: $+6 \cdot 10^{-08}$ y: $+1 \cdot 10^{-08}$ z: $+2 \cdot 10^{-07}$
G	x: $+8 \cdot 10^{-09}$ y: $+1 \cdot 10^{-09}$ z: $+6 \cdot 10^{-08}$	x: $+1 \cdot 10^{-09}$ y: $-4 \cdot 10^{-10}$ z: $+4 \cdot 10^{-08}$	x: $-4 \cdot 10^{-08}$ y: $-9 \cdot 10^{-09}$ z: $-3 \cdot 10^{-08}$	x: $+7 \cdot 10^{-08}$ y: $+7 \cdot 10^{-09}$ z: $+2 \cdot 10^{-07}$

Conclusions

We can conclude that the model performance for the linear accelerations is poorest on the along-track axis, followed by the cross-track axis and it is best for the radial axis. The signal on the along-track axis is mainly determined by air drag. The signal on the radial axis is mainly determined by solar radiation pressure for the considered data. The signal on the cross-track axis contains both effects and they are of the same order of magnitude. It seems that the model for the solar radiation pressure and Earth albedo are realistic and that there are problems in the air drag models.

For the differential acceleration, the signal magnitude of effects common to both satellites (air drag, solar radiation pressure and albedo) is reduced by a order of magnitude at least. The signal magnitude of effects only affecting one satellite, like thruster events, is unchanged; they now dominate the measurement signal on the cross-track and radial axis. The model performance is bad on all axes.

The first question posed at the beginning of this section, if the accelerometer measurements can be replaced by model output, can be answered as no, at least not with the models in the current state. For the differential acceleration to be modeled correctly, it is necessary to include a model of the thruster events effect on the linear acceleration.

Concerning the second question, which models can be improved, it seems that the air drag models are primarily the models to be improved.

The air drag models consist of two parts: the air density model and the model for the interaction of the molecules with the surface. As the different models perform very similar when compared to the simple model, it seems that the problem lies in the air density model. As a conclusion we find that for modeling air drag, the most simple model is sufficient as long as the air density models are not improved. The more complicated models deliver additional detail, that seems not to be exploitable at the moment, as the disagreement between model and reality is still to large. Figure 5.36 shows the geographical distribution of the differences between the model S & C as an example and the measurement. The difference magnitude seems to be increased at the poles. The differences at northern latitudes higher than 60° are larger than the differences at the South Pole. The results are similar for the other air drag models. This may indicate deficiencies in the air density model at these regions.

Possible strategies for an improvement of the density models are discussed in the outlook at the end of

the work.

Another candidate for improvement would be the wind model. It influences mainly the derivation of the relative velocity for the air drag models. The simple model does not use the wind model and performs as well as the other models, so it seems to be more promising to improve the density model first and then perhaps consider an improvement of the wind model.

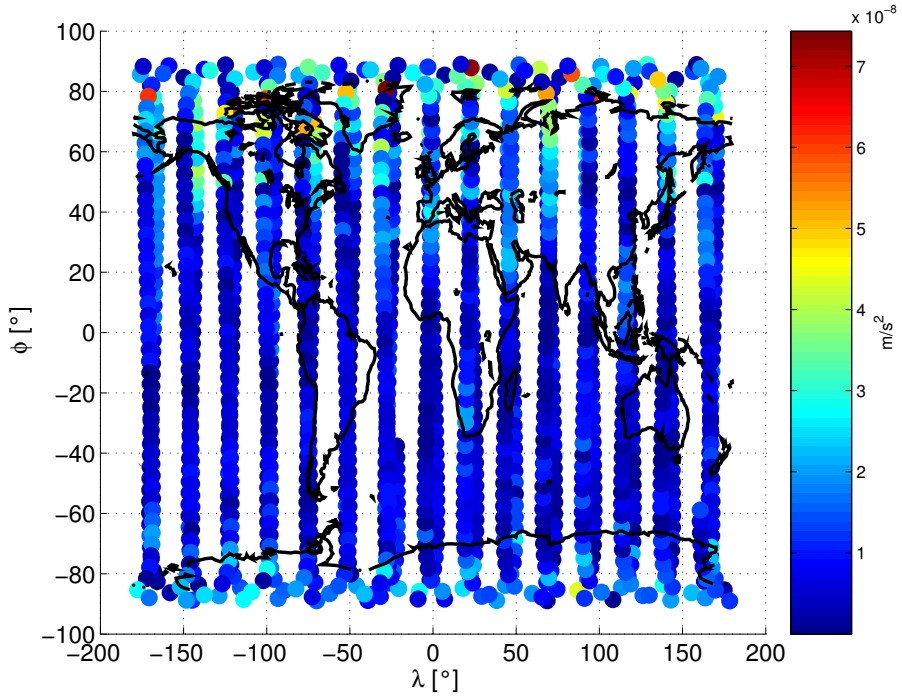

Figure 5.36: Geographical distribution of the difference between model S & C and the measured accelerations.

Part III.

Sensor models

6. Introduction

So far we have described the forces that act on the satellites. Now we think about how the on-board sensor systems detect these forces. The following sensors are modeled: the accelerometer, the star sensor, the K-band measurement system and the GPS receiver.

The first chapter gives a brief overview of the relevant sensor systems and their interaction.

In the subsequent chapters, the sensors are described each separately in terms of mathematical and logical measurement models.

7. Overview of the relevant sensor systems

In figure 7.1 the overview of the sensor system is shown. We start from the top. There are two kinds of forces that act on the satellite: the gravitational forces, denoted as G_A (green), act on the center of mass of the satellite causing linear accelerations. The gravitational forces also cause torques due to the inhomogeneous mass distribution inside the satellite. As the gravitational forces are body forces, they act as well on the proof mass of the accelerometer, i.e. an accelerometer placed at the center of mass of the satellite does not 'feel' the gravitational forces. An accelerometer, that is not located exactly at the center of mass, measures additional linear accelerations caused by gravity gradients. The surface forces, denoted as F_A (blue), act on the surface of the satellite. These forces can as well be imagined to act at the center of mass of the satellite. They also act on the center of pressure of the satellites causing rotational torques (M). The torques result in angular velocities (Ω) and angular accelerations ($\dot{\Omega}$), their magnitude depends on the inertia tensor (I_{ij}). Angular velocity and angular acceleration lead to a change in the orientation of the satellite, that is measured by the star sensors. Angular velocity and the angular acceleration cause linear accelerations of the proof mass, if the accelerometer is not perfectly placed at the center of mass. The star sensor measurements are input to the attitude control system. It applies control torques via the cold-gas thrusters and the magnetic torque rods. The linear accelerations measured by the accelerometer are downsampled as their bandwidth is limited, corresponding to a sampling rate of 10 Hz by the application of a low-pass filter and are converted from analog to digital. The position of the satellite is measured by the GPS receiver. Last but not least, the K-band system measures the differential range between the two GRACE satellites.

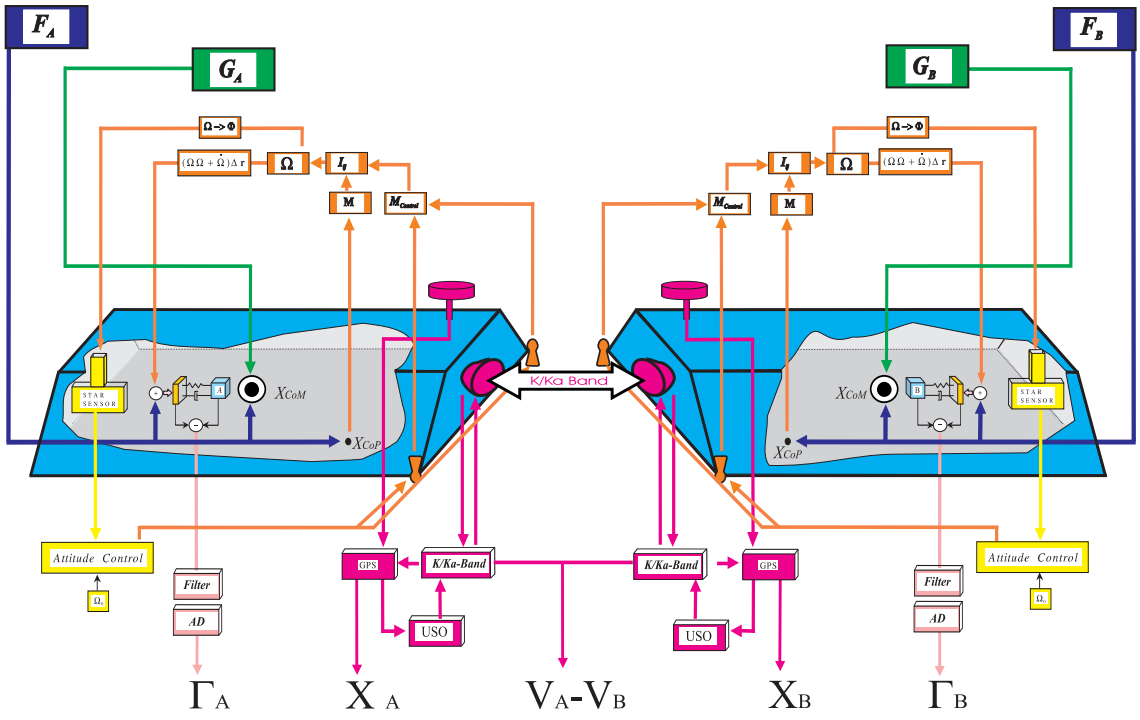

Figure 7.1: Overview of GRACE sensor system.

Figure 7.2 shows a detailed view of the satellite's interior. The abbreviations have the following meaning:

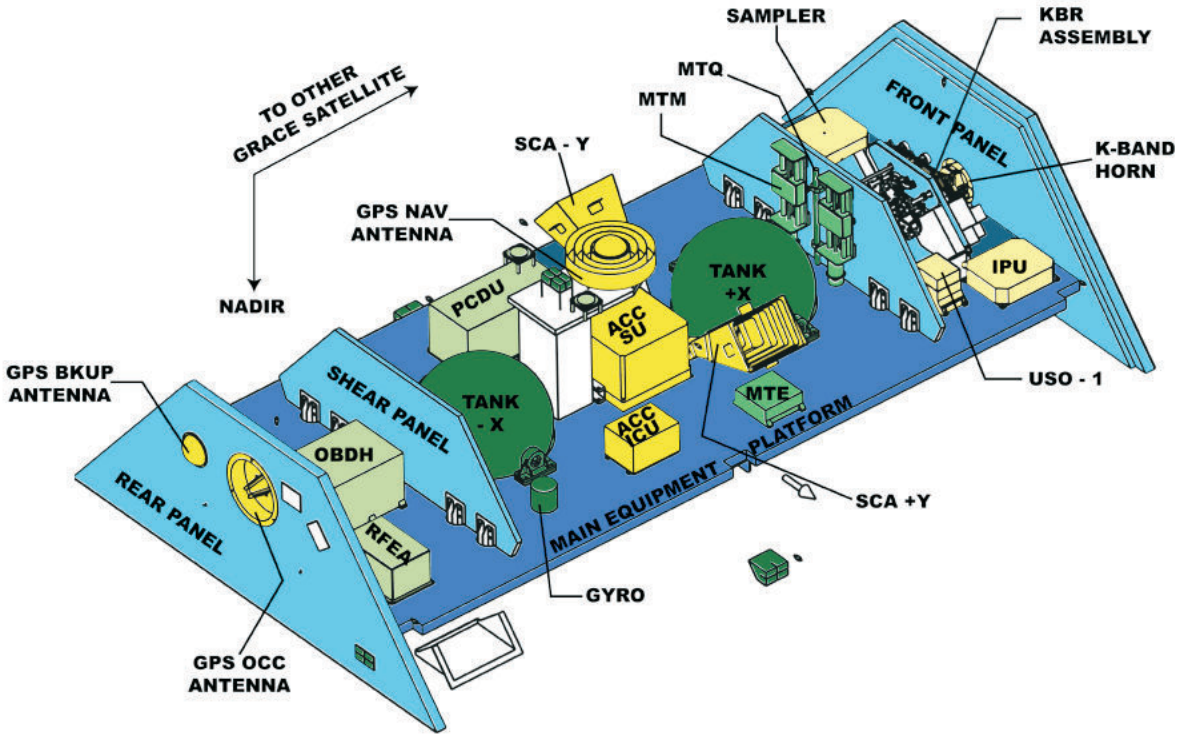

Figure 7.2: Detailed view of the different sensor systems and their location inside the satellites.

ACC ICU	SuperSTAR accelerometer interface control unit
ACC SU	SuperSTAR accelerometer sensor unit
GPS NAV antenna	GPS navigation antenna
GPS BKUP antenna	GPS backup antenna
GPS OCC antenna	GPS occultation antenna
IPU	Instrument processing unit
KBR assembly	K-band ranging system assembly
MTE	Center of mass trim assembly electronics
MTM	Center of mass trim assembly mechanism
MTQ	Magnetorquers
OBDH	On-board data handling
PCDU	Power control and distribution unit
RFEA	Radio frequency and electronics assembly
SCA +Y, SCA -Y	Star camera sensor heads
USO-1	Ultra stable oscillator

The accelerometer is located at the center of mass of the satellite. Above the accelerometer, the star sensor heads and the GPS navigation antenna is located. The mass trim mechanism and the magnetic torquers are located at the front and back shear panel. The gas tanks for the cold gas thrusters are placed symmetrically around the center of mass. At the front of the satellite, the equipment for the K-band ranging system are located: the K-band ranging system assembly, the K-band horn and the ultra stable oscillator (USO). At the back of the satellite, the on-board data handling unit, the radio frequency and electronics assembly and the GPS occultation antenna are located.

In the following chapters we will present mathematical models for the sensors that form the gravity field sensor system: the accelerometer, the star sensor, the K-band ranging system and the GPS receiver.

8. Accelerometer

8.1. Introduction

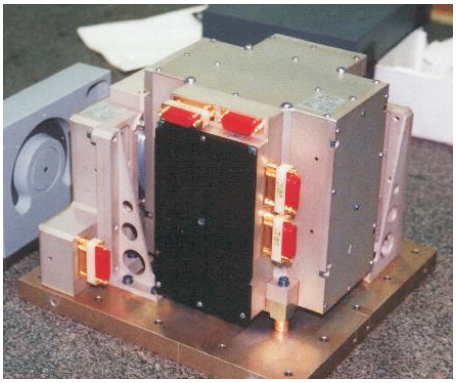

Figure 8.1: Picture of the SuperSTAR accelerometer manufactured by ONERA (image courtesy of ONERA).

The SuperSTAR accelerometer is a three-axis capacitive accelerometer. There are two high-sensitive axes and one less-sensitive axis. The proof mass is a gold-coated titan cube, its size is about 40 x 40 x 10 mm^3, its mass is 70 g. The purpose of the accelerometer is to measure the non-conservative forces acting on the satellites. If the accelerometer is not located at the center of mass of the satellite, the measured linear accelerations also contain contributions due to angular velocities, angular accelerations and gravity gradients. In principle the accelerometer consists of two parts: a position detector, that detects the position of the proof mass inside the cage and the servo mechanism, that keeps the proof mass at its nominal position.

In the following sections, the functionality for one axis will be explained, it is the same for the other two axes.

Table 8.1: Specifications of the SuperSTAR accelerometer from Hudson (2003).

Axis (SRF)	range	accuracy
x	$\pm 5 \cdot 10^{-5}$ m/s^2	$1 \cdot 10^{-10}$ m/s$^2/\sqrt{\text{Hz}}$
y	$\pm 5 \cdot 10^{-4}$ m/s^2	$1 \cdot 10^{-9}$ m/s$^2/\sqrt{\text{Hz}}$
z	$\pm 5 \cdot 10^{-5}$ m/s^2	$1 \cdot 10^{-10}$ m/s$^2/\sqrt{\text{Hz}}$
$\dot{\omega}_x$	$\pm 1 \cdot 10^{-2}$ rad/s^2	$5 \cdot 10^{-6}$ rad/s$^2/\sqrt{\text{Hz}}$
$\dot{\omega}_y$	$\pm 1 \cdot 10^{-3}$ rad/s^2	$2 \cdot 10^{-7}$ rad/s$^2/\sqrt{\text{Hz}}$
$\dot{\omega}_z$	$\pm 1 \cdot 10^{-2}$ rad/s^2	$5 \cdot 10^{-6}$ rad/s$^2/\sqrt{\text{Hz}}$

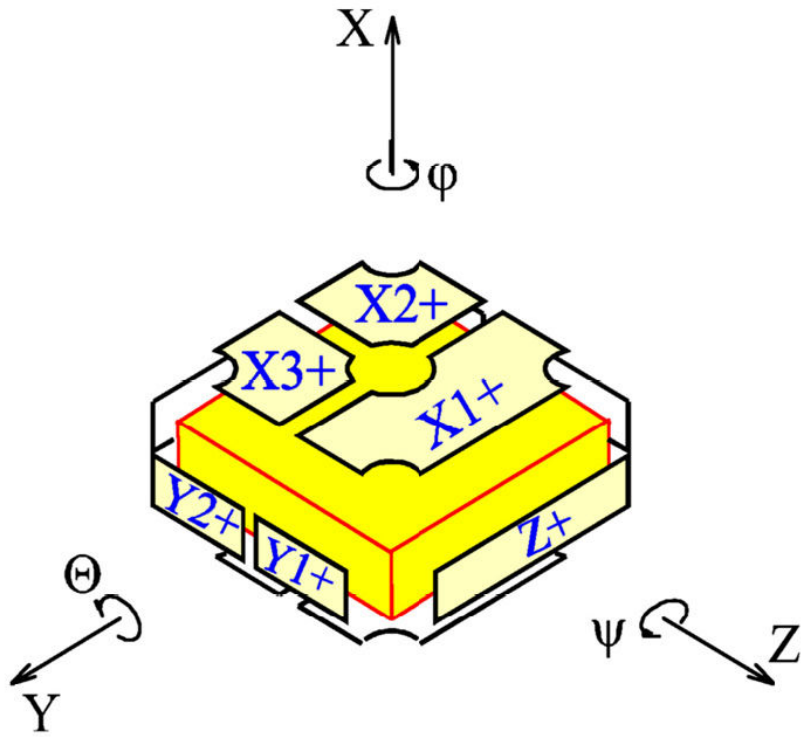

Figure 8.2: Three dimensional view of the proof mass and the electrodes. The axes refer to the accelerometer frame. Here the less-sensitive axis is the X−axis (courtesy of ONERA).

8.2. Logical model

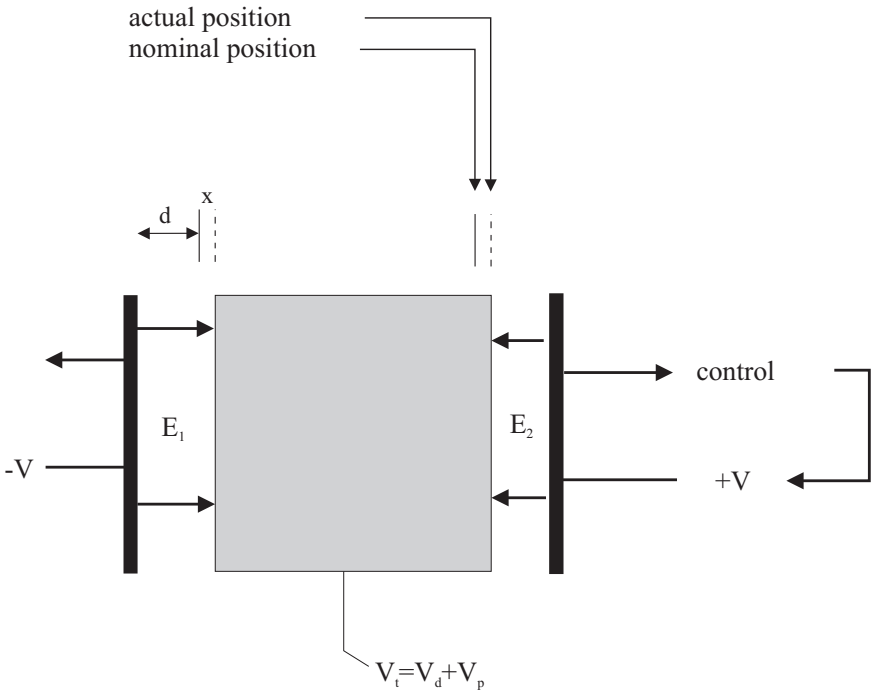

Figure 8.3: Concept of a capacitive accelerometer for one axis.

Figure 8.3 shows the schematic design for one axis. The proof mass is located between two electrodes, charged with voltage $+V$ and $-V$, respectively. The proof mass is charged with a voltage V_t consisting of the polarization voltage V_p and an alternating current, the detection voltage V_d:

$$V_t = V_p + V_d(t). \tag{8.1}$$

The frequency of the detection voltage is about 100 kHz, too high to affect the motion of the proof mass. The nominal position of the proof mass is in the middle between the electrodes, with no off-set, i.e. $x = 0$. Between the walls of the proof mass and the electrodes, two electric fields E_1 and E_2 are forming. If V and V_t are assumed to be positive and constant, the proof mass will start to move towards the electrode charged with $-V$. The gap between proof mass and electrode reduces, increasing the field and the attraction. In this configuration the accelerometer system is inherently unstable and servo control of the proof mass motion is mandatory. A capacitive detector measures the position of the proof mass by comparing the capacitances. A feedback loop including a PID (Proportional Integrative Derivative) controller determines the control voltage V and keeps the proof mass motionless at its nominal position.

8.3. Mathematical model

In this section the equation of motion of the proof mass is derived. First, we have to find a linear expression for the capacitive force acting on the proof mass. This expression can then be linked to the non-gravitational forces acting on the satellite. For the capacitive force, according to Coloumb's law, we have:

$$F_{cap,i} = \frac{1}{2}\,\epsilon_0 A E_i^2 \quad \text{for} \quad i = 1, 2, \tag{8.2}$$

where

ϵ_0 the dielectric constant,
A electrode area [m^2],
E electric field force [J].

As the attraction of field E_1 is opposite to the attraction of field E_2, the overall capacitive force is:

$$F_{cap} = \frac{1}{2}\,\epsilon_0 A(E_1^2 - E_2^2). \tag{8.3}$$

Considering $E = \frac{U}{s}$, where U is the voltage between proof mass and electrode and $s = d + x$ is the distance between proof mass and electrode, and averaging $V_d(t)$ over time we get, according to Josselin et al. (1999) and Touboul et al. (1999):

$$F_{cap} = \frac{1}{2}\,\epsilon_0 A \left(\frac{(V^2 - 2VV_p + \bar{V}_t^2)}{(d-x)^2} - \frac{(V^2 + 2VV_p + \bar{V}_t^2)}{(d+x)^2} \right), \tag{8.4}$$

with

$$\bar{V}_t^2 = V_p^2 + \bar{V}_d^2, \tag{8.5}$$

$$\bar{V}_d = \frac{\max(V_d(t))}{\sqrt{2}}. \tag{8.6}$$

This expression is nonlinear both in the displacement x of the proof mass and in the control voltage V, but becomes linear in the voltage V for $x = 0$. Expansion into a Taylor series for small x/d and neglecting higher order terms yields:

$$F_{cap}(V, x) = -\frac{2\epsilon_0 A}{d^2}\left[VV_p - \frac{x}{d}\bar{V}_t^2\right]. \tag{8.7}$$

As mentioned before, the control voltage V is not constant, it is controlled by a PID controller. After Smit (2000) it is:

$$V(x) = K_{PID}\,\omega_0^2(\dot{x}/\omega_d + x + \omega_i \int^t x\,\mathrm{d}t), \tag{8.8}$$

with

K_{PID}	overall gain,
ω_0^2	natural frequency of PID-controller,
ω_d	characteristic frequency for derivative part,
ω_i	characteristic frequency for integral part.

The capacitive system is used as an accelerometer. It is exposed to an external force F_{ext}, resulting from the non-conservative forces acting on the satellite. The control voltage V is adjusted, so that the proof mass stays in its nominal position. The equation of motion of the proof mass can now be stated as:

$$M\ddot{x} = F_{ext} + F_{cap}(V(x), x). \tag{8.9}$$

Insertion of the linearized expressions from eqs. (8.7) and (8.8) yields:

$$\begin{aligned} \ddot{x} &= -\frac{2\epsilon_0 A V_p K_{PID}}{Md^2}\,\omega_0^2\left(\dot{x}/\omega_d + x + \omega_i \int x\,\mathrm{d}t\right) \\ &\quad + \frac{2\epsilon_0 A \bar{V}_t^2}{Md^3} x + F_{ext}/M. \end{aligned} \tag{8.10}$$

This expression is in agreement with the one given by Stanton et al. (1998).

The proof mass is kept almost motionless in the center of the electrode cage. We get:

$$\ddot{x} = F_{cap}/M + F_{ext}/M, \tag{8.11}$$

$$\approx 0$$

$$\Rightarrow F_{cap}/M \approx -F_{ext}/M. \tag{8.12}$$

The actual measurement of the accelerometer is the control voltage that has to be applied on the proof mass to keep it at its nominal position. The displacement x from the nominal position is very small, so we can say that:

$$F_{cap}/M \approx -\frac{2\epsilon_0 A V_p K_{PID}}{Md^2}\,\omega_0^2\left(\dot{x}/\omega_d + x + \omega_i \int x\,\mathrm{d}t\right) \approx -F_{ext}/M, \tag{8.13}$$

meaning that the external force is related to the control voltage $V(x)$ by:

$$F_{ext}/M \approx \frac{2\epsilon_0 A V_p}{Md^2}\,V(x) \approx G_{el} \cdot V(x). \tag{8.14}$$

G_{el} is the so called electrostatic gain, i.e. the scale factor that has to be applied to the control voltage in order to transform it into an acceleration. For each electrode pair, one control voltage is measured. The measured voltages are transformed into accelerations by applying the appropriate electrostatic gains. In case there is more than one electrode pair per degree of freedom, the individual values are averaged. We get for the vector of measured linear accelerations $\overline{\gamma}_a$ in the accelerometer reference frame (ARF):

$$\overline{\gamma}_a = \begin{pmatrix} (G_{X1} \cdot V_{X1} + G_{X2} \cdot V_{X2} + G_{X3} \cdot V_{X3})/3 \\ (G_{Y1} \cdot V_{Y1} + G_{Y2} \cdot V_{Y2})/2 \\ G_Z \cdot V_Z \end{pmatrix} \approx \overline{\gamma}_{Drag}. \tag{8.15}$$

8.4. Measurement model

In the measurement model, we will first take a closer look at the effects contributing to the linear acceleration measurement. If there is a displacement of the accelerometer relative to the center of mass of the satellite, not only accelerations due to the nonconservative forces but also accelerations due to gravitational forces and angular motion act on the proof mass. The basic equation is, cf. Hudson (2003):

$$\overline{\gamma}_A = (\underline{G}_{ij} + \underline{\Omega}_{jk}\underline{\Omega}_{ik} + \underline{\dot{\Omega}}_{ik})\delta\overline{\mathrm{r}} + \overline{\gamma}_{Drag}, \tag{8.16}$$

with

$\overline{\gamma}_A$	vector of measured accelerations,
$\underline{G}_{ij}$	matrix of gravity gradients,
$\underline{\Omega}_{ik}$	matrix of angular velocities of satellite,
$\underline{\dot{\Omega}}_{ik}$	matrix angular accelerations of satellite,
$\delta\overline{\mathrm{r}}$	vector containing the displacements of accelerometer from center of mass,
$\overline{\gamma}_{Drag}$	vector of accelerations due to nonconservative forces (drag).

A time variability of the center of mass offset is neglected. The location of the center of mass varies in time due to fuel consumption, but the rate of this variation is very slow. It is assumed that the mass trim assembly is able to keep the center of mass within its specified range of 100 µm to the proof mass of the accelerometer, cf. Stanton et al. (1998) and Wang (2003). The effects of the individual contributors are displayed in figure 8.4. We realize that the acceleration caused by the gravity gradients and the angular velocity is smaller than the specified measurement error of the accelerometer. The acceleration caused by the angular acceleration is larger than the accelerometer measurement error but smaller than the K-band measurement error. Therefore it seems that the displacement of the accelerometer proof mass from the satellite center of mass can be neglected. Thus the acceleration on the proof mass caused by the external forces becomes:

$$\overline{\gamma}_a = \overline{\gamma}_{Drag}. \tag{8.17}$$

Next the connection between external accelerations and the measurement of the accelerometer is investigated. The assumption that the internal forces equal the external ones perfectly is not fully true. Oberndorfer (2000) states as measurement model:

$$\overline{\mathrm{F}}_{cap}/M = \underline{K}_{0,A} + \underline{K}_{1,A}\overline{\gamma}_A + \underline{K}_{lm,A}\overline{\gamma}_A + \underline{K}_{2,A}\overline{\gamma}_A\overline{\gamma}_A + noise, \tag{8.18}$$

with

$\underline{K}_{0,A}$	bias,
$\underline{K}_{1,A}$	scale factor (linear),
$\underline{K}_{2,A}$	quadratic factor,
$\underline{K}_{lm,A}$	coupling and misorientation matrix,
$noise$	measurement noise.

The bias term is mainly caused by that term in equation (8.10) that only depends on the displacement of the proof mass from its nominal position.

In this study, we neglected the quadratic factor and the coupling and misorientation of the accelerometer axes. The quadratic factor is specified to be about 10 s^2/m, cf. Stanton et al. (1998), assuming a variation of the linear acceleration at a level of about $5 \cdot 10^{-7}$ $\mathrm{m/s}^2$, the resulting error is below $2.5 \cdot 10^{-12}$ $\mathrm{m/s}^2$. The misalignment and coupling is specified to be below $1 \cdot 10^{-4}$ rad, cf. Stanton et al. (1998), the resulting error is below $1 \cdot 10^{-10}$ $\mathrm{m/s}^2$.

The noise consists of two terms: acceleration noise and position noise. Acceleration noise is white with an additional $1/f$ component below a corner frequency f_0:

$$noise_a(f) = A_a\sqrt{1 + f_0/f} \quad \left[\mathrm{m/s}^2/\sqrt{\mathrm{Hz}}\right]. \tag{8.19}$$

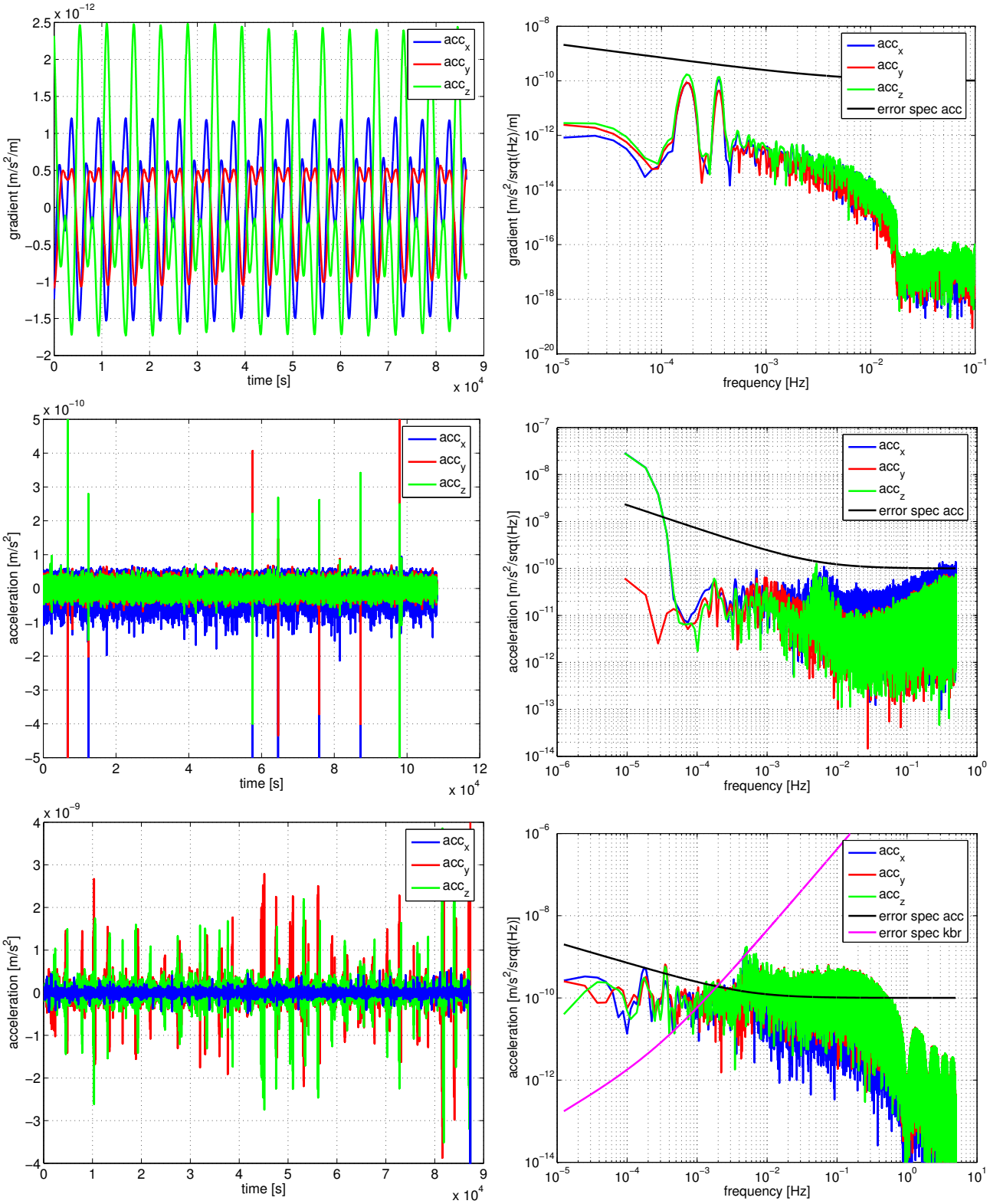

Figure 8.4: Influence of a 0.1 mm offset of the accelerometer proof mass from the satellite's center of mass. The top row shows the acceleration caused by the gravity gradient. The second row shows the acceleration caused by the angular velocity and the third row shows the acceleration caused by the angular acceleration. All effects are below the specified error for the accelerometers resp. for the K-band.

$f_0 = 0.1$ for the less-sensitive axis and $f = 0.005$ for the sensitive axes.

Position noise is white:

$$noise_p(f) = A_p \quad \left[\mathrm{m/s^2}/\sqrt{\mathrm{Hz}}\right]. \tag{8.20}$$

Thus, we arrive at the simplified model:

$$\overline{\Gamma}_a = \underline{K}_{0,A} + \underline{K}_{1,A}\overline{\gamma}_A + noise_a(f) + noise_p(f). \tag{8.21}$$

Table 8.2 shows the error specifications for the accelerometer. The noise term specified is the sum of position and acceleration noise.

Table 8.2: SuperSTAR error specifications for the linear acceleration measurement.

parameter	sensitive axes	less-sensitive axis
bias	$< 2 \cdot 10^{-6}$ m/s^2	$< 50 \cdot 10^{-6}$ m/s^2
scaling factor	1 ± 0.02	1 ± 0.02
noise	$\sqrt{(1 + 0.005/f)} \cdot 10^{-10}$ m/s^2	$\sqrt{(1 + 0.1/f)} \cdot 10^{-9}$ m/s^2

8.5. Dynamic measurement model

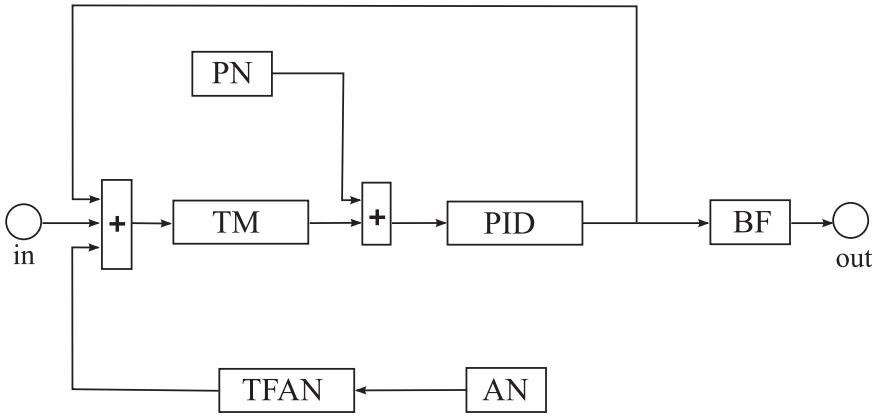

Figure 8.5: Dynamic measurement model for one axis.

The above mentioned measurement model does not reflect the dynamics of the measurement process. To model the dynamics, we have implemented eq. (8.10) in SIMULINK, a MATLAB toolbox used for the simulations. Figure 8.5 shows the dynamic model. External accelerations enter to the left and are then passed to the block denoted as 'TM', that represents the proof mass dynamics, i.e. the transfer from accelerations on the proof mass to a new position of the proof mass. The position detection mechanism is simulated by adding position noise ('PN') to the proof mass position. This position is then passed to the block denoted as 'PID', that implements the PID-controller. Via feedback the controller exerts a corrective acceleration on the proof mass to move it back to its nominal position. The acceleration noise enters the model as white noise in the block 'AN'. The block 'TFAN' than transforms this white noise into colored noise fulfilling the specifications in table 8.2. At the output of the accelerometer a third order butterworth filter ('BF') is applied for the purpose of anti-aliasing. Let us now have a look at the dynamic error due to noise, see Fig. 8.6. The rise at low frequencies is caused by acceleration noise. The acceleration noise of the sensitive axes is lower than that of the less-sensitive axis. Acceleration noise combines all effects that induce parasitic accelerations on the proof mass: stiffness of the gold

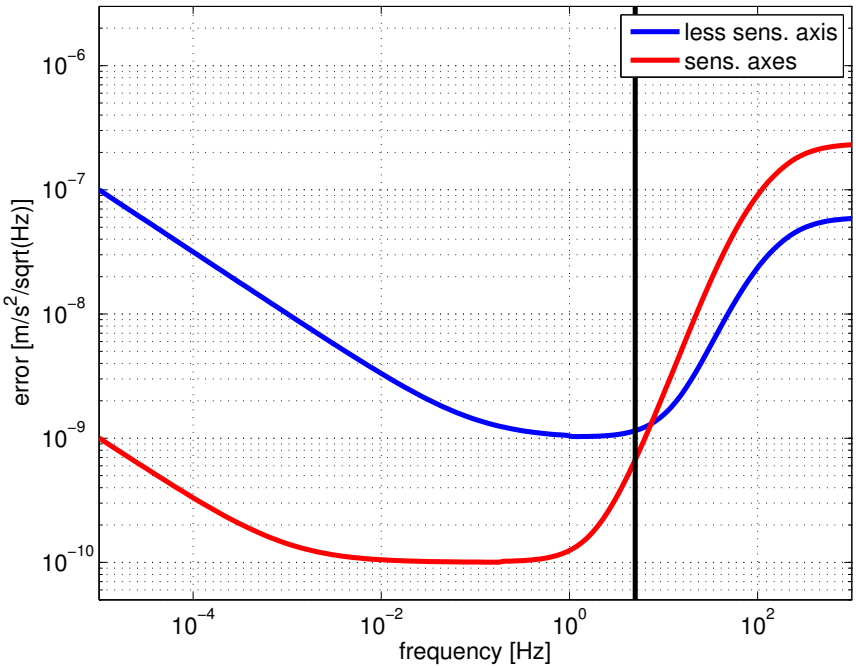

Figure 8.6: Root PSD of the dynamic acceleration measurement error due to noise. Upper line represents less-sensitive axis, lower line sensitive axes. The vertical black line is the Nyquist frequency (5 Hz) corresponding to the accelerometer output sampling rate (10 Hz). The error rises at high frequencies due to position noise and at low frequencies due to acceleration noise.

wire, Lorentz force[1], influence of the Earth's magnetic field and others. The rise at high frequencies is caused by position noise. We notice that the position noise of the sensitive axes is higher than that of the less-sensitive axis. The black line indicates the Nyquist frequency (5 Hz) of the designated output frequency of the accelerometer (10 Hz). We note that there is much energy in the error signal at frequencies of 5 Hz and above. If the signal had been sampled unchanged, aliasing would occur and spoil the measurement. That is the reason for the implementation of an anti-aliasing filter at the output of the accelerometer, a third order butterworth filter with a cut-off frequency of 3 Hz. The effect of this filter is depicted in figure 8.7. The anti-aliasing filter effectively reduces the signal energy at high frequencies, so that no degradation of the measurement will occur. The resulting instrument noise rises at low frequencies with a rate of $1/\sqrt{f}$ in the root PSD. At high frequencies, the noise is white at a level of $1 \cdot 10^{-9}$ m/s$^2/\sqrt{\text{Hz}}$ for the less-sensitive axis and $1 \cdot 10^{-10}$ m/s$^2/\sqrt{\text{Hz}}$ for the sensitive axes.

[1]The Lorentz force is the force exerted on a charged particle in an electromagnetic field. In this case the proof mass is the charged particle moving in the magnetic field of the Earth.

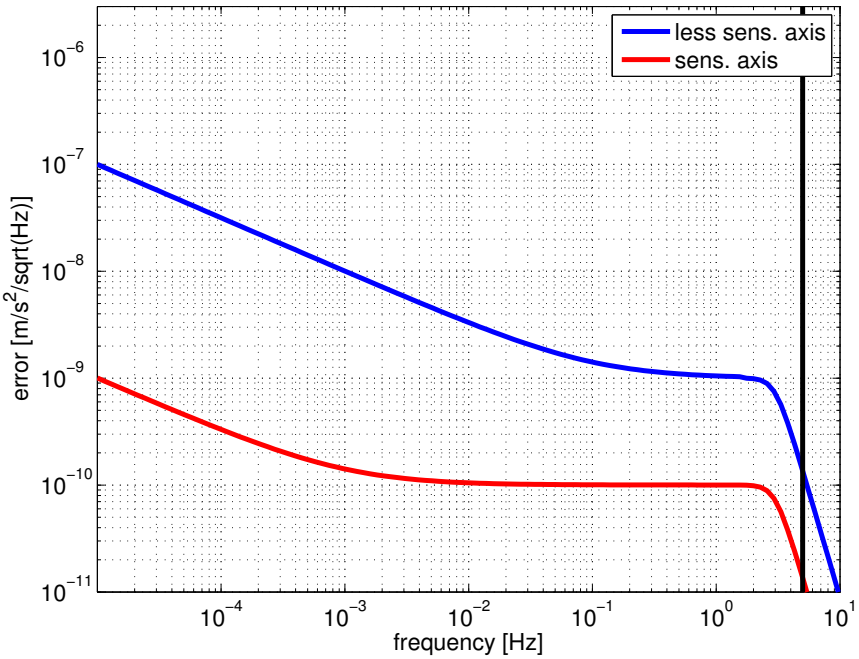

Figure 8.7: Root PSD of the dynamic measurement error at the output of the accelerometer. The blue line represents less-sensitive axis, the red line the sensitive axes. The vertical black line is the Nyquist frequency (5 Hz) of the accelerometer output sampling rate (10 Hz). In contrast to figure 8.6, the signal energy at frequencies of 3 Hz and above is diminished through the application of the butterworth filter.

9. Star sensor

9.1. Introduction

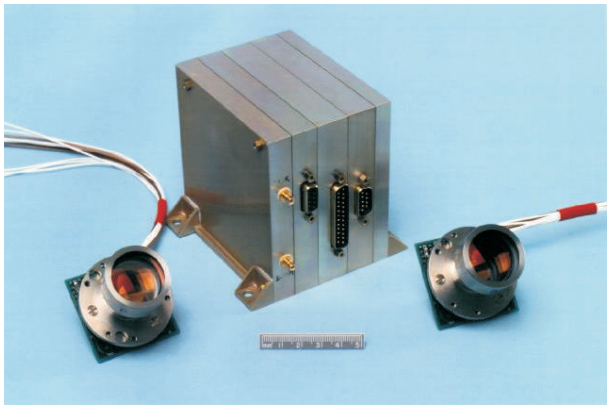

Figure 9.1: The star sensor, consisting of the two sensor heads and the processing unit.

The purpose of the star tracker is to determine the absolute orientation of the satellite with respect to an inertial system. In order to accomplish this task, digital star images taken by each of the two sensor heads are processed. The observed stellar constellations are compared to stellar maps and catalogues (e.g. the HIPPARCOS catalogue) inside the processing unit by means of image processing. The derived orientation is the orientation with respect to the reference frame of the used star catalogue. The star sensor or Advanced Stellar Compass (ASC) used on the GRACE satellites is identical to the star sensor used for the CHAMP mission. It is manufactured by the department of automation of the Technical University of Denmark (DTU). It was used and tested for the missions Teamsat, ASTRID 2 und Ørsted. The database contains 13 000 of the brightest stars from the HIPPARCOS catalogue. An orientation that deviates more than 10 arcseconds from the star catalogue data is rejected. The typical duration of an attitude acquisition is about 200 ms. The attitude is given as a set of quaternions.

9.2. Logical model

In this section we describe the logical measurement model of the star sensor. The described method corresponds to the 'geometric method' described in Wertz (1991). As described before, in principle the star sensor is a digital camera taking images of its field of view. How are these images converted into an orientation of the satellite? First of all, the star sensor does not deliver the orientation of the satellite fixed coordinate system with respect to the inertial coordinate system, but the orientation of its own instrument coordinate system, the star sensor reference system, with respect to the inertial coordinate system underlying the used star catalogue. Consequently, as an additional measurement the orientation of the star sensor reference frame with respect to the satellite fixed reference frame is required. This will introduce an additional error to be accounted for later in the description of the level 1a to level 1b processing of the star sensor data.

Let us now set up the logical steps that lead from the digital image of the sky to the derived orientation. The first step consists in comparing the taken image to known patterns of star constellations from the

star catalogue contained in the star sensor processing unit. We will not go into details about the image recognition strategy, cf. Wertz (1991), let us just assume that the stars on the taken image have been identified correctly. Assume now that a set of inertial coordinates of the stars and a corresponding set of coordinates in the star sensor reference frame in the form of pixel coordinates are available, see figure 9.2. The next step is to transform the coordinates of the stars to angle measurements corresponding to the angle between the position vector of the stars on a unit sphere and the z-axis of the SSRF. This transformation can only be achieved by an on ground calibration of the star sensor cameras: The camera is rotated by a known angle and the coordinate change of a target is recorded, see figure 9.3. With this set of angle measurements, the vector components of the z-axis of the star sensor reference frame (SSRF) can be determined:

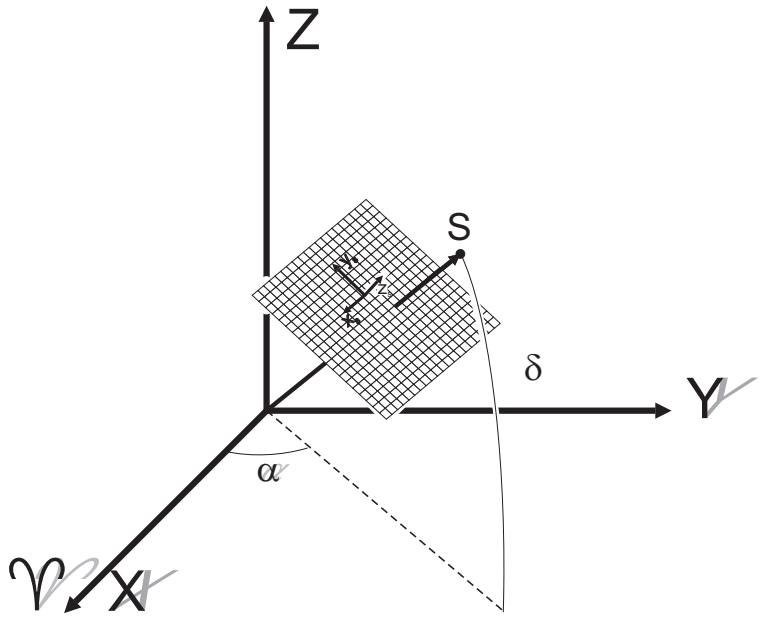

Figure 9.2: Overview of the star sensor reference frame and the inertial reference frame.

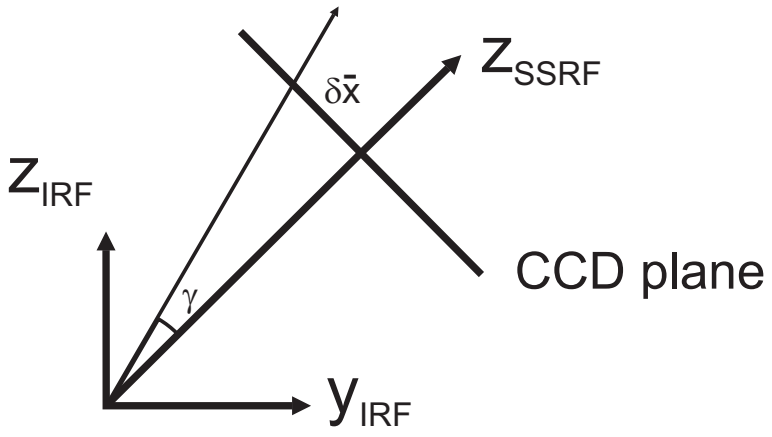

Figure 9.3: Mapping of the coordinates of an observed star to an angle measurement.

$$\begin{aligned}
\widehat{\mathrm{X}}_{S_1}^{IRF} \cdot \widehat{\mathrm{Z}}_{SSRF}^{IRF} &= \cos(\gamma_{S_1}), \\
\widehat{\mathrm{X}}_{S_2}^{IRF} \cdot \widehat{\mathrm{Z}}_{SSRF}^{IRF} &= \cos(\gamma_{S_2}), \\
\widehat{\mathrm{X}}_{S_3}^{IRF} \cdot \widehat{\mathrm{Z}}_{SSRF}^{IRF} &= \cos(\gamma_{S_3}), \\
&\vdots \quad \vdots \\
\widehat{\mathrm{X}}_{S_n}^{IRF} \cdot \widehat{\mathrm{Z}}_{SSRF}^{IRF} &= \cos(\gamma_{S_n})
\end{aligned} \tag{9.1}$$

or writing explicitly the dot products:

$$\begin{aligned}
X_{S_1} \cdot X_z + Y_{S_1} \cdot Y_z + Z_{S_1} \cdot Z_z &= \cos(\gamma_{S_1}), \\
X_{S_2} \cdot X_z + Y_{S_2} \cdot Y_z + Z_{S_2} \cdot Z_z &= \cos(\gamma_{S_2}), \\
X_{S_3} \cdot X_z + Y_{S_3} \cdot Y_z + Z_{S_3} \cdot Z_z &= \cos(\gamma_{S_3}), \\
&\vdots \quad \vdots \\
X_{S_n} \cdot X_z + Y_{S_n} \cdot Y_z + Z_{S_n} \cdot Z_z &= \cos(\gamma_{S_n}),
\end{aligned} \tag{9.2}$$

where we define:

$$\widehat{\mathrm{X}}_{S_n}^{IRF} = \begin{pmatrix} X_{S_n} \\ Y_{S_n} \\ Z_{S_n} \end{pmatrix} = \begin{pmatrix} \cos(\delta_{S_n})\cos(\alpha_{S_n}) \\ \cos(\delta_{S_n})\sin(\alpha_{S_n}) \\ \sin(\delta_{S_n}) \end{pmatrix}, \tag{9.3}$$

$$\widehat{\mathrm{Z}}_{SSRF}^{IRF} = \begin{pmatrix} X_z \\ Y_z \\ Z_z \end{pmatrix}, \tag{9.4}$$

where α_{S_n} and δ_{S_n} are the azimuth and declination of the observed stars given in the inertial reference frame. The equations can then be rewritten as a standard linear least squares estimation problem:

$$\underline{\mathrm{A}} \cdot \overline{\mathrm{x}} = \overline{\mathrm{y}}, \tag{9.5}$$

with the matrix of the partial derivatives

$$\underline{\mathrm{A}} = \begin{pmatrix} \cos(\delta_{S_1})\cos(\alpha_{S_1}) & \cos(\delta_{S_1})\sin(\alpha_{S_1}) & \sin(\delta_{S_1}) \\ \cos(\delta_{S_2})\cos(\alpha_{S_2}) & \cos(\delta_{S_2})\sin(\alpha_{S_2}) & \sin(\delta_{S_2}) \\ \cos(\delta_{S_3})\cos(\alpha_{S_3}) & \cos(\delta_{S_3})\sin(\alpha_{S_3}) & \sin(\delta_{S_3}) \\ \vdots & \vdots & \vdots \\ \cos(\delta_{S_n})\cos(\alpha_{S_n}) & \cos(\delta_{S_n})\sin(\alpha_{S_n}) & \sin(\delta_{S_n}) \end{pmatrix}, \tag{9.6}$$

the vector of unknowns

$$\overline{\mathrm{x}} = \begin{pmatrix} X_z \\ Y_z \\ Z_z \end{pmatrix} \tag{9.7}$$

and the vector of observations

$$\overline{\mathrm{y}} = \begin{pmatrix} \cos(\gamma_{S_1}) \\ \cos(\gamma_{S_2}) \\ \cos(\gamma_{S_3}) \\ \vdots \\ \cos(\gamma_{S_n}) \end{pmatrix}. \tag{9.8}$$

The unknown components of the Z-axis of the SSRF are then given by:

$$\overline{\mathrm{x}} = \left(\underline{\mathrm{A}}^{\mathrm{T}} \cdot \underline{\mathrm{A}}\right)^{-1} \cdot \underline{\mathrm{A}}^{\mathrm{T}} \cdot \overline{\mathrm{y}}. \tag{9.9}$$

Now the Z-axis of the SSRF is defined. In order to define the full orientation of the SSRF with respect to the IRF, we have to derive the components of either the X- or Y-axis of the SSRF in the IRF, as the third axis can be derived through completion of the orthonormal system. We follow the same approach as before: we derive angles between the position vectors to stars and the coordinate axis whose components we want to derive. As both the X- and Y-axis lie in the plane of the CCD-Sensor, it is not possible, as for the Z-axis, to measure the angles directly through the measured coordinates of the digital image, we have to derive virtual measurements by forming the cross product between the Z-axis and the position vectors of the detected stars, thus creating a set of vectors that all lie in the CCD plane, see figure 9.4. The cross products are formed in the SSRF using the measured CCD coordinates and in the IRF:

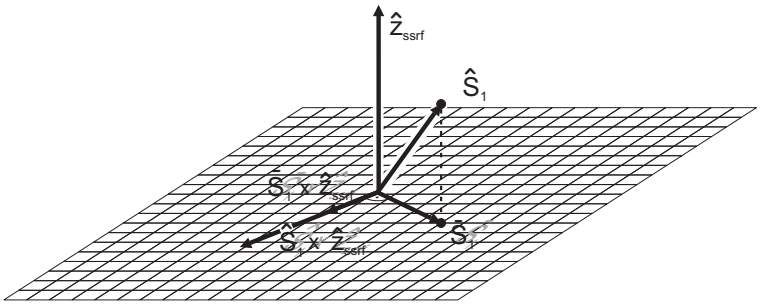

Figure 9.4: Derivation of the virtual vectors in the CCD plane for the derivation of the X- and Y-axis of the SSRF

$$\begin{aligned}
\overline{\mathrm{V}}_{S_1}^{SSRF} &= \overline{\mathrm{X}}_{S_1}^{SSRF} \times \widehat{\mathrm{Z}}_{SSRF}^{SSRF}, \\
\overline{\mathrm{V}}_{S_2}^{SSRF} &= \overline{\mathrm{X}}_{S_2}^{SSRF} \times \widehat{\mathrm{Z}}_{SSRF}^{SSRF}, \\
\overline{\mathrm{V}}_{S_3}^{SSRF} &= \overline{\mathrm{X}}_{S_3}^{SSRF} \times \widehat{\mathrm{Z}}_{SSRF}^{SSRF}, \\
&\vdots \quad \vdots \\
\overline{\mathrm{V}}_{S_n}^{SSRF} &= \overline{\mathrm{X}}_{S_n}^{SSRF} \times \widehat{\mathrm{Z}}_{SSRF}^{SSRF}
\end{aligned} \tag{9.10}$$

is the set of virtual vectors in the SSRF and

$$\begin{aligned}
\widehat{\mathrm{V}}_{S_1}^{IRF} &= \widehat{\mathrm{X}}_{S_1}^{IRF} \times \widehat{\mathrm{Z}}_{SSRF}^{IRF}, \\
\widehat{\mathrm{V}}_{S_2}^{IRF} &= \widehat{\mathrm{X}}_{S_2}^{IRF} \times \widehat{\mathrm{Z}}_{SSRF}^{IRF}, \\
\widehat{\mathrm{V}}_{S_3^{IRF}} &= \widehat{\mathrm{X}}_{S_3}^{IRF} \times \widehat{\mathrm{Z}}_{SSRF}^{IRF}, \\
&\vdots \quad \vdots \\
\widehat{\mathrm{V}}_{S_n}^{IRF} &= \widehat{\mathrm{X}}_{S_n}^{IRF} \times \widehat{\mathrm{Z}}_{SSRF}^{IRF}
\end{aligned} \tag{9.11}$$

is the set of virtual vectors in the IRF. Now the angles between the X- or Y-axis and the virtual vectors in the SSRF can be derived by forming the dot products between the virtual axes and the coordinate

axis whose components are to be derived:

$$\begin{aligned}
\frac{\overline{\mathrm{V}}_{S_1}^{SSRF}}{|\overline{\mathrm{V}}_{S_1}^{SSRF}|} \cdot \widehat{\mathrm{X}}_{SSRF}^{SSRF} &= \cos(\gamma_{S_1}), \\
\frac{\overline{\mathrm{V}}_{S_2}^{SSRF}}{|\overline{\mathrm{V}}_{S_2}^{SSRF}|} \cdot \widehat{\mathrm{X}}_{SSRF}^{SSRF} &= \cos(\gamma_{S_2}), \\
\frac{\overline{\mathrm{V}}_{S_3}^{SSRF}}{|\overline{\mathrm{V}}_{S_3}^{SSRF}|} \cdot \widehat{\mathrm{X}}_{SSRF}^{SSRF} &= \cos(\gamma_{S_3}), \\
&\vdots \quad \vdots \\
\frac{\overline{\mathrm{V}}_{S_n}^{SSRF}}{|\overline{\mathrm{V}}_{S_n}^{SSRF}|} \cdot \widehat{\mathrm{X}}_{SSRF}^{SSRF} &= \cos(\gamma_{S_n}).
\end{aligned} \tag{9.12}$$

The derived angles can then be used to set up a system of equations similar to the one used for the derivation of the components of the Z-axis in the IRF. From this system of equations, the components of the coordinate axis to be determined can be estimated as described above, here as an example for the X-axis. Finally the third missing coordinate axis is derived by forming the cross product between the two already derived ones:

$$\widehat{\mathrm{Y}}_{SSRF}^{IRF} = -(\widehat{\mathrm{X}}_{SSRF}^{IRF} \times \widehat{\mathrm{Z}}_{SSRF}^{IRF}), \tag{9.13}$$

here as an example for the Y-axis. The reason why the orientation of the Z-axis of the SSRF can be determined much more accurately than the orientation of the X- or Y-axes is that their orientation is determined using the described virtual vectors. The accuracy of these vectors is depending not only on the accuracy of the derived star coordinates but also on the accuracy of the derived Z-axis components. But there is an additional aspect to be considered: if you imagine that the star sensor is rotated about its line of sight, it is clear that the position change of the observed stars depends on their distance from the line of sight. This means that it makes a difference which stars are used for the derivation of the virtual vectors and thus the X- and Y-axes; preferably stars at the border of the image should be used. This is in contrast to the derivation of the Z-axis orientation; there the position of the observed stars has no influence, as the position change due to a rotation about either the X- or Y-axis of the SSRF is the same for all observed stars.

9.3. Measurement model

The actual measurement of the star sensor are the pixel coordinates of the observed stars, that are then transformed into the orientation of the SSRF with respect to the IRF as described above. The orientation can be parameterized as a Direction Cosine Matrix (DCM) , that has the following properties:

$$\overline{\mathrm{X}}_{SSRF} = \underline{\mathrm{R}}_{IRF\_SSRF} \cdot \overline{\mathrm{X}}_{IRF}, \tag{9.14}$$

i.e. it transforms a vector from the IRF to the SSRF. According to Wertz (1991) we get for $\underline{\mathrm{R}}_{IRF\_SSRF}$:

$$\underline{\mathrm{R}}_{IRF\_SSRF} = \begin{pmatrix} \widehat{\mathrm{X}}_{SSRF} \cdot \widehat{\mathrm{X}}_{IRF} & \widehat{\mathrm{X}}_{SSRF} \cdot \widehat{\mathrm{Y}}_{IRF} & \widehat{\mathrm{X}}_{SSRF} \cdot \widehat{\mathrm{Z}}_{IRF} \\ \widehat{\mathrm{Y}}_{SSRF} \cdot \widehat{\mathrm{X}}_{IRF} & \widehat{\mathrm{Y}}_{SSRF} \cdot \widehat{\mathrm{Y}}_{IRF} & \widehat{\mathrm{Y}}_{SSRF} \cdot \widehat{\mathrm{Z}}_{IRF} \\ \widehat{\mathrm{Z}}_{SSRF} \cdot \widehat{\mathrm{X}}_{IRF} & \widehat{\mathrm{Z}}_{SSRF} \cdot \widehat{\mathrm{Y}}_{IRF} & \widehat{\mathrm{Z}}_{SSRF} \cdot \widehat{\mathrm{Z}}_{IRF} \end{pmatrix}, \tag{9.15}$$

where

$\widehat{\mathrm{X}}_{IRF}, \widehat{\mathrm{Y}}_{IRF}, \widehat{\mathrm{Z}}_{IRF}$	are the base vectors of the source system, here the IRF,
$\widehat{\mathrm{X}}_{SSRF}, \widehat{\mathrm{Y}}_{SSRF}, \widehat{\mathrm{Z}}_{SSRF}$	are the base vectors of the target system, here the SSRF.

We will think of $\widehat{\mathrm{X}}_{SSRF}, \widehat{\mathrm{Y}}_{SSRF}, \widehat{\mathrm{Z}}_{SSRF}$, the base vectors of the target system in the source system, as the actual measurements. The base vectors of the source system given in the source system have the simple form:

$$\widehat{\mathrm{X}}_{IRF} = \begin{pmatrix} 1 \\ 0 \\ 0 \end{pmatrix}, \widehat{\mathrm{Y}}_{IRF} = \begin{pmatrix} 0 \\ 1 \\ 0 \end{pmatrix}, \widehat{\mathrm{Z}}_{IRF} = \begin{pmatrix} 0 \\ 0 \\ 1 \end{pmatrix}. \tag{9.16}$$

Thus equation (9.15) simplifies to:

$$\underline{\mathrm{R}}_{IRF\_SSRF} = \begin{pmatrix} x_1 & x_2 & x_3 \\ y_1 & y_2 & y_3 \\ z_1 & z_2 & z_3 \end{pmatrix}, \tag{9.17}$$

when

$$\widehat{\mathrm{X}}_{SSRF} = \begin{pmatrix} x_1 \\ x_2 \\ x_3 \end{pmatrix}, \widehat{\mathrm{Y}}_{SSRF} = \begin{pmatrix} y_1 \\ y_2 \\ y_3 \end{pmatrix}, \widehat{\mathrm{Z}}_{SSRF} = \begin{pmatrix} z_1 \\ z_2 \\ z_3 \end{pmatrix}. \tag{9.18}$$

The star sensor delivers the measured orientation not as a DCM but in terms of a quaternion (cf. Wertz (1991)):

$$q_4 = \pm\frac{1}{2}\sqrt{(1 + x_1 + y_2 + z_3)}, \tag{9.19}$$

$$q_1 = \frac{1}{4q_4}(y_3 - z_2), \tag{9.20}$$

$$q_2 = \frac{1}{4q_4}(z_1 - x_3), \tag{9.21}$$

$$q_3 = \frac{1}{4q_4}(x_2 - y_1). \tag{9.22}$$

9.4. Error model

As demonstrated before, the measured orientation can be represented as a measurement of the coordinate axes of the SSRF in the IRF. A measurement error can thus be represented as a deviation of the measured coordinate axes from the true axes:

$$\widehat{\mathrm{X}}_{meas} = \widehat{\mathrm{X}}_{true} + \delta\overline{\mathrm{x}}. \tag{9.23}$$

It is to be noted that the measured vector as well as the true vector are unit vectors, but the error vector is not a unit vector. Thus we get for the DCM:

$$\underline{\mathrm{R}}_{IRF\_SSRF} = \begin{pmatrix} \left(\widehat{\mathrm{X}}_{true} + \delta\overline{\mathrm{x}}\right) \cdot \widehat{\mathrm{X}}_{IRF} & \left(\widehat{\mathrm{X}}_{true} + \delta\overline{\mathrm{x}}\right) \cdot \widehat{\mathrm{Y}}_{IRF} & \left(\widehat{\mathrm{X}}_{true} + \delta\overline{\mathrm{x}}\right) \cdot \widehat{\mathrm{Z}}_{IRF} \\ \left(\widehat{\mathrm{Y}}_{true} + \delta\overline{\mathrm{y}}\right) \cdot \widehat{\mathrm{X}}_{IRF} & \left(\widehat{\mathrm{Y}}_{true} + \delta\overline{\mathrm{y}}\right) \cdot \widehat{\mathrm{Y}}_{IRF} & \left(\widehat{\mathrm{Y}}_{true} + \delta\overline{\mathrm{y}}\right) \cdot \widehat{\mathrm{Z}}_{IRF} \\ \left(\widehat{\mathrm{Z}}_{true} + \delta\overline{\mathrm{z}}\right) \cdot \widehat{\mathrm{X}}_{IRF} & \left(\widehat{\mathrm{Z}}_{true} + \delta\overline{\mathrm{z}}\right) \cdot \widehat{\mathrm{Y}}_{IRF} & \left(\widehat{\mathrm{Z}}_{true} + \delta\overline{\mathrm{z}}\right) \cdot \widehat{\mathrm{Z}}_{IRF} \end{pmatrix}. \tag{9.24}$$

Again we can simplify to:

$$\underline{\mathrm{R}}_{IRF\_SSRF} = \begin{pmatrix} (x_1 + \delta x_1) & (x_2 + \delta x_2) & (x_3 + \delta x_3) \\ (y_1 + \delta y_1) & (y_2 + \delta y_2) & (y_3 + \delta y_3) \\ (z_1 + \delta z_1) & (z_2 + \delta z_2) & (z_3 + \delta z_3) \end{pmatrix}, \tag{9.25}$$

where

$$\widehat{\mathrm{X}}_{true} = \begin{pmatrix} x_1 \\ x_2 \\ x_3 \end{pmatrix}, \widehat{\mathrm{Y}}_{true} = \begin{pmatrix} y_1 \\ y_2 \\ y_3 \end{pmatrix}, \widehat{\mathrm{Z}}_{true} = \begin{pmatrix} z_1 \\ z_2 \\ z_3 \end{pmatrix} \tag{9.26}$$

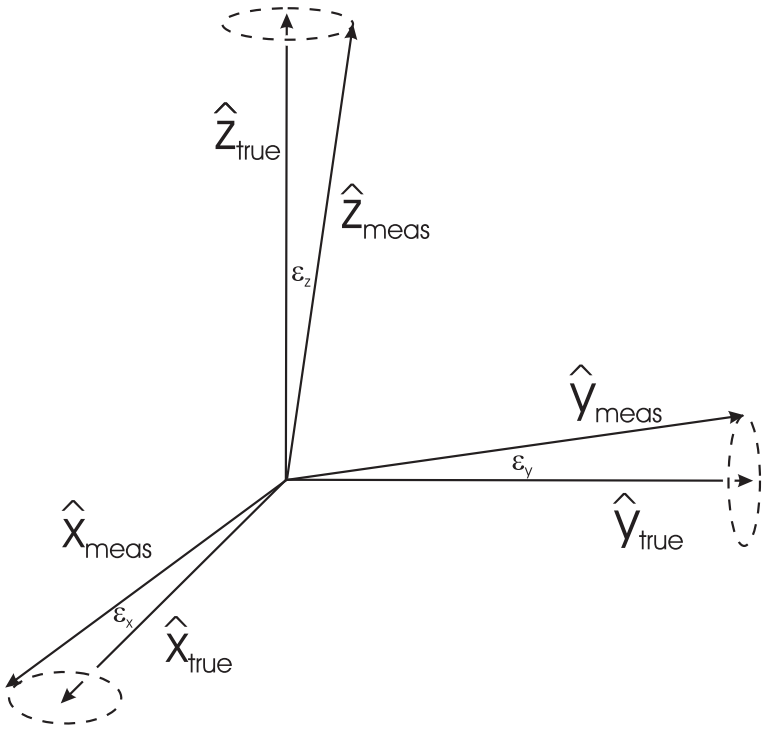

Figure 9.5: Star sensor error model, picture of the measured and true coordinate axes.

and

$$\delta\overline{\mathrm{x}} = \begin{pmatrix} \delta x_1 \\ \delta x_2 \\ \delta x_3 \end{pmatrix}, \delta\overline{\mathrm{y}} = \begin{pmatrix} \delta y_1 \\ \delta y_2 \\ \delta y_3 \end{pmatrix}, \delta\overline{\mathrm{z}} = \begin{pmatrix} \delta z_1 \\ \delta z_2 \\ \delta z_3 \end{pmatrix}. \tag{9.27}$$

$$q_4 = \pm\frac{1}{2}\sqrt{(1 + x_1 + \delta x_1 + y_2 + \delta y_2 + z_3 + \delta z_3)}, \tag{9.28}$$

$$q_1 = \frac{1}{4q_4}(y_3 + \delta y_3 - z_2 - \delta z_2), \tag{9.29}$$

$$q_2 = \frac{1}{4q_4}(z_1 + \delta z_1 - x_3 - \delta x_3), \tag{9.30}$$

$$q_3 = \frac{1}{4q_4}(x_2 + \delta x_2 - y_1 - \delta y_1). \tag{9.31}$$

The requirements for the star sensor derived orientation are given in Stanton et al. (1998) in terms of pointing accuracy of the measured coordinate axes. The requirement for the roll axis is tighter than for the pitch/yaw axis, as it is crucial for the K-band measurement quality that the two K-band horns point at each other as accurately as possible. The influence of a misalignment of the pitch/yaw axis on the K-band measurement quality is significantly smaller resulting in a less tight requirement. Let us now discuss the contributors to the star sensor measurement error. Considering figure 9.6, it is clear that first of all the measurement error depends on the accuracy of the star positions. By taking the image, an additional error arises, because each optical system is subject to image errors that result from imperfections of the used optical components. This abberation can be corrected for, as it is systematic, but there remains an error. The analog image delivered by the optical system is digitized by the CCD sensor, that has only a finite resolution. Therefore an additional error arises. The total measurement error can thus be described as:

$$\delta\overline{\mathrm{x}} = \delta\overline{\mathrm{x}}_{SC} + \delta\overline{\mathrm{x}}_{OS} + \delta\overline{\mathrm{x}}_{CCD}, \tag{9.32}$$

where

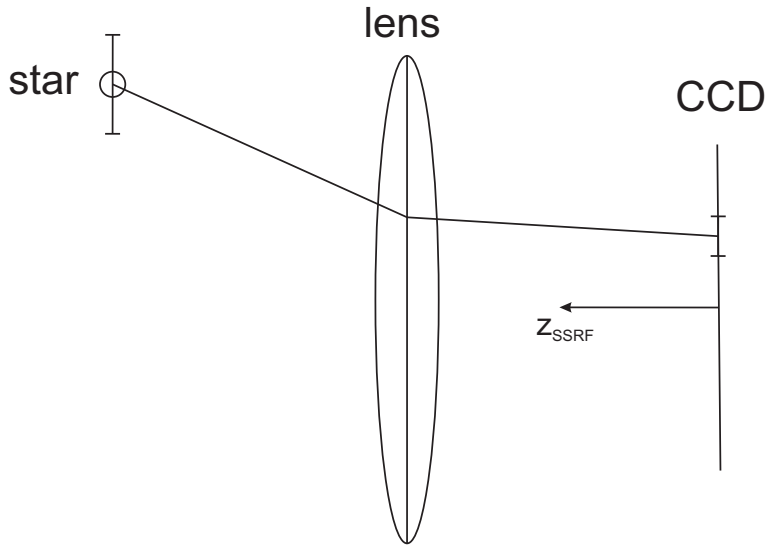

Figure 9.6: Overview of the star camera and image taking process.

$\delta\overline{\mathrm{x}}_{SC}$	is the error component due to the position errors in the star catalogue,
$\delta\overline{\mathrm{x}}_{OS}$	is the error component due to the optical system,
$\delta\overline{\mathrm{x}}_{CCD}$	is the error component due to the image digitization of the image by the CCD sensor.

This error is then propagated depending on the method used for the determination of the orientation, that has not necessarily to be the same as the one outlined in the logical model section. Therefore no full error propagation from the level of the pixel coordinates to the derived orientation will be conducted. We will assume that the star sensor just delivers an orientation with a certain error. According to Jørgenson (1999), the error term can also be characterized in the following way:

- Noise Equivalent Angle (NEA): this is the RMS noise of successive attitude updates when the star tracker is repeatedly taking the same image,
- relative accuracy: the accuracy of the star tracker taking an image series obtained from a known attitude motion pattern,
- absolute accuracy: long term accuracy

and in its combination is assumed to be white noise. There is certainly a correlation between the subsequently derived attitudes, but this correlation is neglected in this work.

For error simulation, the measurement error can be treated as the angle ε between the true and the measured axis, and thus the error vectors $\delta\overline{\mathrm{x}}$, $\delta\overline{\mathrm{y}}$, $\delta\overline{\mathrm{z}}$ can be determined as

$$\cos\varepsilon = \widehat{\mathrm{X}}_{true} \cdot (\widehat{\mathrm{X}}_{true} + \delta\overline{\mathrm{x}}) = \widehat{\mathrm{X}}_{true} \cdot \widehat{\mathrm{X}}_{meas}, \tag{9.33}$$

where the true axes are known. Figure 9.5 depicts the measured and the true axes.

From the instrument manufacturer only the maximum values for the angles between the true and measured axes, ε_x, ε_y and ε_z are known. The direction towards which the measured axis is tilted is arbitrary. We will now show the derivation of the error vectors $\delta\overline{\mathrm{x}}$, $\delta\overline{\mathrm{y}}$, $\delta\overline{\mathrm{z}}$. Considering figure 9.7, the

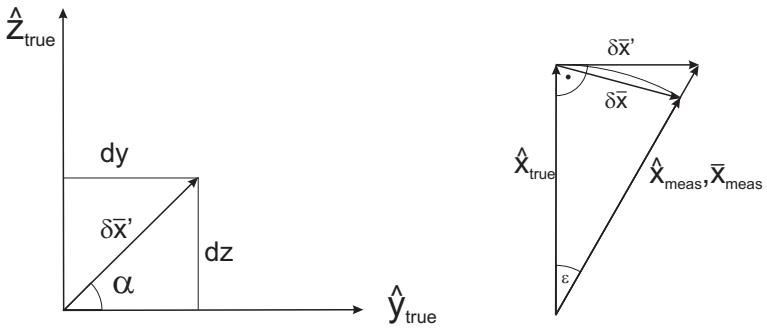

Figure 9.7: Geometric relations between measured and true axes, shown here for the x-axis.

following vectors can be derived:

$$\delta\bar{\mathrm{x}}' = \begin{pmatrix} 0 \\ \tan\varepsilon_x \cdot \cos\alpha_x \\ \tan\varepsilon_x \cdot \sin\alpha_x \end{pmatrix}, \tag{9.34}$$

$$\delta\bar{\mathrm{y}}' = \begin{pmatrix} \tan\varepsilon_y \cdot \cos\alpha_y \\ 0 \\ \tan\varepsilon_y \cdot \sin\alpha_y \end{pmatrix}, \tag{9.35}$$

$$\delta\bar{\mathrm{z}}' = \begin{pmatrix} \tan\varepsilon_z \cdot \cos\alpha_z \\ \tan\varepsilon_z \cdot \sin\alpha_z \\ 0 \end{pmatrix}. \tag{9.36}$$

Now the measured axes can be derived as:

$$\widehat{\mathrm{X}}_{meas} = \frac{\widehat{\mathrm{X}}_{true} + \delta\bar{\mathrm{x}}'}{|\widehat{\mathrm{X}}_{true} + \delta\bar{\mathrm{x}}'|}, \tag{9.37}$$

$$\widehat{\mathrm{Y}}_{meas} = \frac{\widehat{\mathrm{Y}}_{true} + \delta\bar{\mathrm{y}}'}{|\widehat{\mathrm{Y}}_{true} + \delta\bar{\mathrm{y}}'|}, \tag{9.38}$$

$$\widehat{\mathrm{Z}}_{meas} = \frac{\widehat{\mathrm{Z}}_{true} + \delta\bar{\mathrm{z}}'}{|\widehat{\mathrm{Z}}_{true} + \delta\bar{\mathrm{z}}'|} \tag{9.39}$$

and

$$\delta\bar{\mathrm{x}} = \frac{\widehat{\mathrm{X}}_{true} + \delta\bar{\mathrm{x}}'}{|\widehat{\mathrm{X}}_{true} + \delta\bar{\mathrm{x}}'|} - \widehat{\mathrm{X}}_{true}, \tag{9.40}$$

$$\delta\bar{\mathrm{y}} = \frac{\widehat{\mathrm{Y}}_{true} + \delta\bar{\mathrm{y}}'}{|\widehat{\mathrm{Y}}_{true} + \delta\bar{\mathrm{y}}'|} - \widehat{\mathrm{Y}}_{true}, \tag{9.41}$$

$$\delta\bar{\mathrm{z}} = \frac{\widehat{\mathrm{z}}_{true} + \delta\bar{\mathrm{z}}'}{|\widehat{\mathrm{Z}}_{true} + \delta\bar{\mathrm{z}}'|} - \widehat{\mathrm{Z}}_{true}. \tag{9.42}$$

For error simulation we can assume that the axes of the true system and the IRF are collinear, meaning

$$\widehat{\mathrm{X}}_{IRF} = \widehat{\mathrm{X}}_{true} = \begin{pmatrix} 1 \\ 0 \\ 0 \end{pmatrix}, \widehat{\mathrm{Y}}_{IRF} = \widehat{\mathrm{Y}}_{true} = \begin{pmatrix} 0 \\ 1 \\ 0 \end{pmatrix}, \widehat{\mathrm{Z}}_{IRF} = \widehat{\mathrm{Z}}_{true} = \begin{pmatrix} 0 \\ 0 \\ 1 \end{pmatrix}. \tag{9.43}$$

Thus we derive:

$$\delta\bar{\mathrm{x}} = \frac{1}{\sqrt{1+\tan^2\varepsilon_x}} \begin{pmatrix} 1-\sqrt{1+\tan^2\varepsilon_x} \\ \tan\varepsilon_x \cdot \cos\alpha_x \\ \tan\varepsilon_x \cdot \sin\alpha_x \end{pmatrix}, \tag{9.44}$$

$$\delta\bar{\mathrm{y}} = \frac{1}{\sqrt{1+\tan^2\varepsilon_y}} \begin{pmatrix} \tan\varepsilon_y \cdot \cos\alpha_y \\ 1-\sqrt{1+\tan^2\varepsilon_y} \\ \tan\varepsilon_y \cdot \sin\alpha_y \end{pmatrix}, \tag{9.45}$$

$$\delta\bar{\mathrm{z}} = \frac{1}{\sqrt{1+\tan^2\varepsilon_z}} \begin{pmatrix} \tan\varepsilon_z \cdot \cos\alpha_z \\ \tan\varepsilon_z \cdot \sin\alpha_z \\ 1-\sqrt{1+\tan^2\varepsilon_z} \end{pmatrix}. \tag{9.46}$$

The pointing accuracy requirements for GRACE are 30 µrad or 6 arcseconds for the x-axis and 240 µrad or 50 arcseconds for the orientation of the y- and z-axis, i.e. $\varepsilon_x = 30$ µrad and $\varepsilon_y = \varepsilon_z = 240$ µrad. The measured quaternions are then given as:

$$\begin{aligned} q_4 &= \pm\frac{1}{2}\sqrt{\left(4+\frac{1-\sqrt{1+\tan^2\varepsilon_x}}{\sqrt{1+\tan^2\varepsilon_x}}+\frac{1-\sqrt{1+\tan^2\varepsilon_y}}{\sqrt{1+\tan^2\varepsilon_y}}+\frac{1-\sqrt{1+\tan^2\varepsilon_z}}{\sqrt{1+\tan^2\varepsilon_z}}\right)} \\ &= \pm\frac{1}{2}\sqrt{\left(1+\frac{1}{\sqrt{1+\tan^2\varepsilon_x}}+\frac{1}{\sqrt{1+\tan^2\varepsilon_y}}+\frac{1}{\sqrt{1+\tan^2\varepsilon_z}}\right)}, \end{aligned} \tag{9.47}$$

$$q_1 = \frac{1}{4q_4}\left(\frac{(\tan\varepsilon_y \sin\alpha_y)}{\sqrt{1+\tan^2\varepsilon_y}} - \frac{(\tan\varepsilon_z \sin\alpha_z)}{\sqrt{1+\tan^2\varepsilon_z}}\right), \tag{9.48}$$

$$q_2 = \frac{1}{4q_4}\left(\frac{(\tan\varepsilon_z \cos\alpha_z)}{\sqrt{1+\tan^2\varepsilon_z}} - \frac{(\tan\varepsilon_x \sin\alpha_x)}{\sqrt{1+\tan^2\varepsilon_x}}\right), \tag{9.49}$$

$$q_3 = \frac{1}{4q_4}\left(\frac{(\tan\varepsilon_x \cos\alpha_x)}{\sqrt{1+\tan^2\varepsilon_x}} - \frac{(\tan\varepsilon_y \cos\alpha_y)}{\sqrt{1+\tan^2\varepsilon_y}}\right). \tag{9.50}$$

Since for small angles $\tan x \approx x$, we can simplify the above equations without loss of generality to:

$$q_4 = \pm\frac{1}{2}\sqrt{\left(1+\frac{1}{\sqrt{1+\varepsilon_x^2}}+\frac{1}{\sqrt{1+\varepsilon_y^2}}+\frac{1}{\sqrt{1+\varepsilon_z^2}}\right)}, \tag{9.51}$$

$$q_1 = \frac{1}{4q_4}\left(\frac{(\varepsilon_y \sin\alpha_y)}{\sqrt{1+\varepsilon_y^2}} - \frac{(\varepsilon_z \sin\alpha_z)}{\sqrt{1+\varepsilon_z^2}}\right), \tag{9.52}$$

$$q_2 = \frac{1}{4q_4}\left(\frac{(\varepsilon_z \cos\alpha_z)}{\sqrt{1+\varepsilon_z^2}} - \frac{(\varepsilon_x \sin\alpha_x)}{\sqrt{1+\varepsilon_x^2}}\right), \tag{9.53}$$

$$q_3 = \frac{1}{4q_4}\left(\frac{(\varepsilon_x \cos\alpha_x)}{\sqrt{1+\varepsilon_x^2}} - \frac{(\varepsilon_y \cos\alpha_y)}{\sqrt{1+\varepsilon_y^2}}\right). \tag{9.54}$$

Figure 9.8 gives an example of simulated star sensor noise. The component q_4 is $\cos(\Phi)$ and the other three components q_1 to q_3 are the rotation vector. For q_4 an error angle can be derived directly, for the vector components the angle between the true and measured vector is derived. The figure shows the component error angle in arc seconds. We notice that the error is about $1 \cdot 10^{-8}$ rad for $\cos(\Phi)$ or about 11 arcseconds for the rotation angle Φ and $1 \cdot 10^{-4}$ rad or about 9 arcseconds for the rotation vector elements.

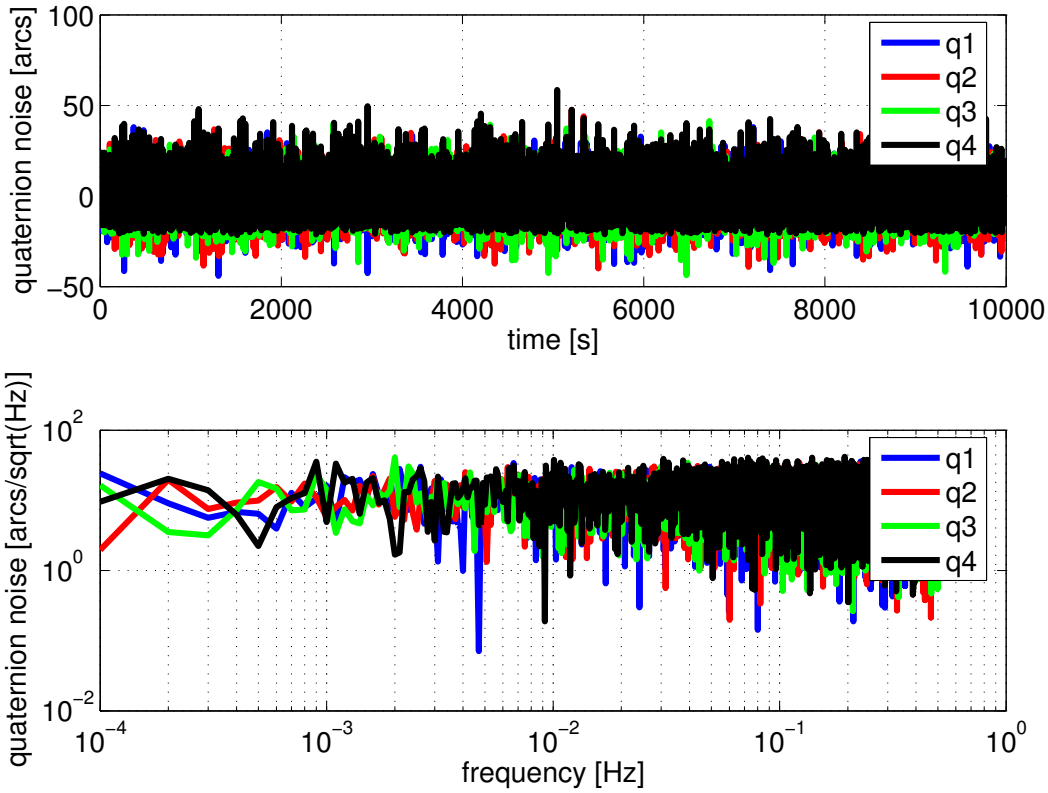

Figure 9.8: Simulated quaternion noise expressed in arcseconds resp. arcseconds/$\sqrt{\text{Hz}}$. For all components the noise is similar in the spectral and in the time domain.

Table 9.1: Standard deviation of the simulated quaternion components expressed in arc seconds.

component	σ [arcseconds]
$q4$	11
$q1$	9
$q2$	9
$q3$	9

10. K-band system

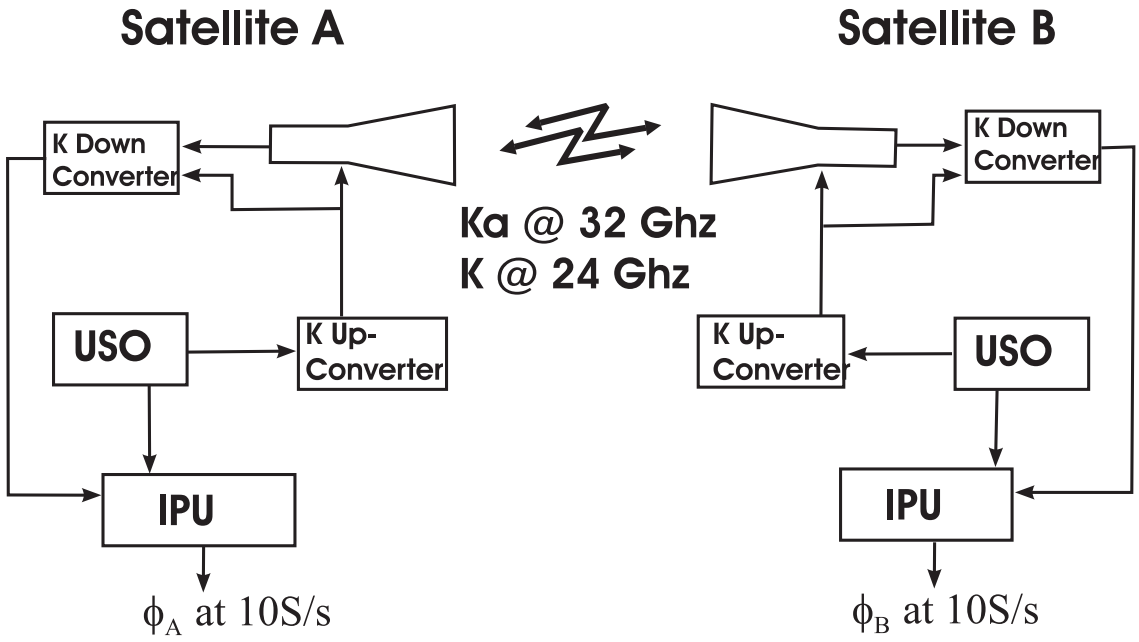

Figure 10.1: Schematic view of the K-band microwave-link system, Thomas (1999)

10.1. Introduction

The K-band ranging system (KBR) is the key instrument of the GRACE mission. A schematic overview is shown in figure 10.1. Each satellite is equipped with a horn used for transmission and reception of the intersatellite dual-band μ-wave signals at 24 GHz for K-band and 32 GHz for Ka-band. The horns are based on the type of feed horns used in JPL's Deep Space Network. The transmitted signals on the K- and Ka-band are sinusoidal. On each band there is a frequency offset between the two satellites signals of 0.5 MHz. The signals are generated by an ultra stable oscillator (USO). Upon reception the signals of each band are down-converted to 0.5 MHz using the transmitted signal of the same band as a reference. In the instrument processing unit (IPU) the phase is extracted and delivered to the on-board data handling (OBDH) computer at a nominal sample rate of 10 S/s.

10.2. Logical model

The purpose of the phase measurements is to measure the biased distance between the two GRACE satellites. The phase measurement itself is the measurement of the phase difference between the signal received from satellite B and a reference signal at satellite A or vice versa. But how can this phase difference be used to derive the range between two satellites? Let us assume that the two satellites are separated by a certain distance. On each satellite there is an oscillator. Let us further assume that the two oscillators are perfectly synchronized, i.e. their phases agree perfectly, and that they run at

identical frequencies. If now the signal from the oscillator on satellite A is sent over the distance A/B and received at satellite B, the phase difference between signal A and signal B will give information about the distance: If the phase difference was zero, we would know that the distance is an integer multiple of the wavelength of the sent signal, if the difference was different from zero, we would know that the separation distance is an integer multiple of the signal wavelength plus the measured phase difference converted into a residual distance using the velocity of light. This would require that somehow the integer number of wavelengths is known, in order to derive an absolute value for the inter-satellite distance. In reality this value is not known, i.e. using only the phase measurement, one can only determine a biased range. In addition, the assumptions made before do not hold in reality: The oscillators of the two satellites are not perfectly synchronized, there is an offset (clock error), which leads to a systematic phase difference between the two satellite signal phases. In addition, the frequencies of the oscillators are not constant, there are frequency errors that also lead to unwanted phase differences. Also the travel through the medium from one satellite to the other influences the phase of the emitted (received) signal: Depending on the amount of electrons along the signal path, the phase is changed more or less. The received signal consists not only of the directly received signal, but contains contributions from reflections at the satellites surfaces, which also leads to unwanted phase alterations. Additionally, there are errors resulting from the necessary analog to digital conversions, the phase extraction itself and the cable delay. These considerations are formulated mathematically in the next section in order to arrive at the measurement model.

10.3. Measurement model

The measurement model formulation is given in Kim (2000). We get for the extracted phase values at a nominal epoch t:

$$\phi_A^B = \phi_A(t+\Delta t_A) - \phi^B(t+\Delta t_A) + N_A^B + I_A^B + d_A^B + \epsilon_A^B, \tag{10.1}$$
$$\phi_B^A = \phi_B(t+\Delta t_B) - \phi^A(t+\Delta t_B) + N_B^A + I_B^A + d_B^A + \epsilon_B^A, \tag{10.2}$$

with

ϕ_A^B	differential phase measurement at GRACE A,
ϕ_B^A	differential phase measurement at GRACE B,
t	nominal reception time,
Δt_A, Δt_B	clock errors on GRACE A and GRACE B,
$\phi_A(t+\Delta t_A)$	GRACE A receiver reference phase,
$\phi^B(t+\Delta t_A)$	GRACE B transmitted phase received by GRACE A,
$\phi_B(t+\Delta t_A)$	GRACE B receiver reference phase,
$\phi^A(t+\Delta t_B)$	GRACE A transmitted phase received by GRACE B,
N_A^B, N_B^A	integer ambiguities,
d_A^B, d_B^A	phase shift due to neutral atmosphere, instrument offset, multipath a.s.o.,
$\epsilon_A^B, \epsilon_B^A$	random measurement noise.

GRACE A is the leading satellite and GRACE B is the trailing satellite. The unit of the phase measurement is cycles. Each reference phase consists of the true reference phase $\bar{\phi}$ and the phase error $\delta\phi$ due to oscillator drift:

$$\phi_A = \bar{\phi}_A + \delta\phi_A, \tag{10.3}$$
$$\phi_B = \bar{\phi}_B + \delta\phi_B. \tag{10.4}$$

The received phase can also be described in terms of the transmitted phase using the transmission time τ_B^A from satellite A to satellite B:

$$\phi^A(t) = \phi_A(t - \tau_B^A). \tag{10.5}$$

The transmission time is different for each satellite, as they are moving: the leading satellite flies 'away' from the signal, the trailing satellite flies 'into' the signal wave. Substitution of eq. (10.3) to (10.5) into eq. (10.1) and (10.2) yields:

$$\begin{aligned}\phi_A^B &= \bar{\phi}_A(t+\Delta t_A) + \delta\phi_A(t+\Delta t_A) - \bar{\phi}_B(t+\Delta t_A-\tau_A^B) - \delta\phi_B(t+\Delta t_A-\tau_A^B)\\ &+ N_A^B + I_A^B + d_A^B + \epsilon_A^B, \qquad (10.6)\\ \phi_B^A &= \bar{\phi}_B(t+\Delta t_B) + \delta\phi_B(t+\Delta t_B) - \bar{\phi}_A(t+\Delta t_B-\tau_B^A) - \delta\phi_A(t+\Delta t_B-\tau_B^A)\\ &+ N_B^A + I_B^A + d_B^A + \epsilon_B^A. \qquad (10.7)\end{aligned}$$

The phase at measured reception time $t+\Delta t_A$ can be linearized at the nominal time t as:

$$\bar{\phi}_A(t+\Delta t_A) \approx \bar{\phi}_A(t) + \dot{\bar{\phi}}_A(t)\cdot\Delta t_A. \qquad (10.8)$$

Also the phase at the transmit time $t+\Delta t_A-\tau_B^A$ can be linearized at the nominal time t as:

$$\bar{\phi}_A(t+\Delta t_B-\tau_A^B) \approx \bar{\phi}_A(t) + \dot{\bar{\phi}}_A(t)\cdot\Delta t_B - \dot{\bar{\phi}}_A(t)\cdot\tau_B^A. \qquad (10.9)$$

The phase error can be linearized in the same way:

$$\begin{aligned}\delta\phi_A(t+\Delta t_A) &\approx \delta\phi_A(t) + \delta\dot{\phi}_A(t)\cdot\Delta t_A,\\ \delta\phi_A(t+\Delta t_B-\tau_B^A) &\approx \delta\phi_A(t) + \delta\dot{\phi}_A(t)\cdot\Delta t_B - \delta\dot{\phi}_A(t)\cdot\tau_B^A. \qquad (10.10)\end{aligned}$$

The rate of phase change $\dot{\bar{\phi}}_A(t)$ is equivalent to the nominal frequency f_A, the rate of phase change error $\delta\dot{\phi}_A(t)$ is therefore equivalent to the frequency error δf_A. These results lead to:

$$\begin{aligned}\phi_A^B &= \bar{\phi}_A(t) + f_A\cdot\Delta t_A + \delta\phi_A(t) + \delta f_A\cdot\Delta t_A - \bar{\phi}_B(t) - f_B\cdot\Delta t_A + f_B\cdot\tau_A^B\\ &- \delta\phi_B(t) - \delta f_B\cdot\Delta t_A + \delta f_B\cdot\tau_A^B + N_A^B + I_A^B + d_A^B + \epsilon_A^B\\ &= \bar{\phi}_A(t) - \bar{\phi}_B(t) + \delta\phi_A(t) - \delta\phi_B(t) + (f_A-f_B)\cdot\Delta t_A + (\delta f_A-\delta f_B)\cdot\Delta t_A\\ &+ (f_B+\delta f_B)\cdot\tau_A^B + N_A^B + I_A^B + d_A^B + \epsilon_A^B, \qquad (10.11)\\ \phi_B^A &= \bar{\phi}_B(t) + f_B\cdot\Delta t_B + \delta\phi_B(t) + \delta f_B\cdot\Delta t_B - \bar{\phi}_A(t) - f_A\cdot\Delta t_B + f_A\cdot\tau_B^A\\ &- \delta\phi_A(t) - \delta f_A\cdot\Delta t_B + \delta f_A\cdot\tau_B^A + N_B^A + I_B^A + d_B^A + \epsilon_B^A\\ &= \bar{\phi}_B(t) - \bar{\phi}_A(t) + \delta\phi_B(t) - \delta\phi_A(t) + (f_B-f_A)\cdot\Delta t_B + (\delta f_B-\delta f_A)\cdot\Delta t_B\\ &+ (f_A+\delta f_A)\cdot\tau_B^A + N_B^A + I_B^A + d_B^A + \epsilon_B^A. \qquad (10.12)\end{aligned}$$

The time tag error Δt_A can be expressed in terms of the phase error $\delta\phi_A$ as, cf. Kim (2000):

$$\Delta t_A = -\frac{\delta\phi_A(t)}{f_A}, \qquad (10.13)$$

which yields:

$$\begin{aligned}\phi_A^B &= \bar{\phi}_A(t) - \bar{\phi}_B(t) + f_B\cdot\tau_A^B + \left(1 - \frac{f_A-f_B}{f_A} - \frac{\delta f_A-\delta f_B}{f_A}\right)\cdot\delta\phi_A(t) - \delta\phi_B(t),\\ &+ \delta f_B\cdot\tau_A^B + \epsilon_{system}^A + N_A^B + I_A^B + d_A^B \qquad (10.14)\\ &= \bar{\phi}_A(t) - \bar{\phi}_B(t) + f_B\cdot\tau_A^B + \epsilon_{uso}^{A,B} + \epsilon_{system}^A + N_A^B + I_A^B + d_A^B. \qquad (10.15)\end{aligned}$$

The measured phase value consists of the difference of the two reference phases, a term depending on the transmission time and error terms. The phase error consists of five terms:

1. Error due to USO instability,
2. error due to system noise,
3. error due to phase ambiguity,
4. error due to Ionosphere delay,
5. error due to phase shift due to atmosphere, multipath and others.

10.4. Error model

Error due to USO instability

$$\epsilon_{uso}^{A,B} = \left(1 - \frac{f_A - f_B}{f_A} - \frac{\delta f_A - \delta f_B}{f_A}\right) \cdot \delta\phi_A(t) - \delta\phi_B(t) + \delta f_B \cdot \tau_A^B. \tag{10.16}$$

The error due to USO instability consists of five terms. The first three terms are a scaling of the phase error $\delta\phi_A(t)$ of the receiving satellite, depending on the phase error itself, the frequency difference $f_A - f_B$ of the two satellites USOs and the frequency error difference $\delta f_A - \delta f_B$. The error due to frequency difference and frequency error difference is expected to be smaller than the phase error itself, as they are scaled by the nominal frequency. As fourth term, the phase error $\delta\phi_B(t)$ due to USO instability from the sending satellite enters the error equation linearly. The last term consists of the frequency error δf_B of the sending satellite's USO times the transmission time τ_A^B.

Usually the error behavior of an oscillator is specified in terms of an Allan variance, but it is more convenient to specify the error in terms of a power spectral density. From Thomas (1999) we get for the phase noise of the oscillators in terms of [rad^2/Hz]:

$$S_{\delta\phi} = 3.16 \cdot 10^{-16} + \frac{8.38 \cdot 10^{-13}}{f^2} + \frac{5.74 \cdot 10^{-14}}{f^3} + \frac{6.39 \cdot 10^{-17}}{f^4}. \tag{10.17}$$

The frequency error is the time derivative of the phase error, as

$$\delta f = \delta\dot{\phi}(t) = 2\pi f \delta\phi. \tag{10.18}$$

So we get for the frequency error PSD:

$$\begin{aligned} S_{\delta\omega} &= (2\pi f)^2 \cdot (S_{\delta\phi}) \\ &= (2\pi f)^2 \cdot \left(3.16 \cdot 10^{-16} + \frac{8.38 \cdot 10^{-13}}{f^2} + \frac{5.74 \cdot 10^{-14}}{f^3} + \frac{6.39 \cdot 10^{-17}}{f^4}\right). \end{aligned} \tag{10.19}$$

The phase and frequency error pertain to the USO normal frequency f_0. To scale them to K resp. Ka Band and to transform from [rad^2] to [cycle^2], we get:

$$S_{\delta\phi}^{f_{K/Ka}} = \left(\frac{f_{K/Ka}}{2\pi \cdot f_0}\right)^2 \cdot S_{\delta\phi}, \tag{10.20}$$

$$S_{\delta f}^{f_{K/Ka}} = \left(\frac{f_{K/Ka}}{2\pi \cdot f_0}\right)^2 \cdot (2\pi f)^2 \cdot (S_{\delta\phi}). \tag{10.21}$$

As the error is random, differentiation of the phase errors of the two satellites does not cancel but double them, thus we can rewrite eq. (10.16) and specify the PSD of the phase error:

$$S_{\epsilon_{uso}}^{K/Ka} = \left(2 + \left(\frac{\Delta f}{f_{K/Ka}}\right)^2 + \left(\frac{2S_{\delta f}^{f_{K/Ka}}}{f_{K/Ka}}\right)^2\right) \cdot S_{\delta\phi}^{f_{K/Ka}} + S_{\delta f}^{f_{K/Ka}} \cdot \tau_A^B. \tag{10.22}$$

Figure 10.2 shows the root PSD of the phase noise due to the USO error. As expected, it increases strongly at low frequencies and levels out to white noise at high frequencies. Figure 10.3 shows the root PSD of the frequency noise due to the USO error. As the frequency noise is the time derivative of the phase noise, it shows a $\frac{1}{f}$ behavior at low frequencies and also rises proportional to f at high frequencies. Figure 10.4 shows the root PSD of the contributions of all phase noise sources. It can be stated that the largest contributor by far is the phase noise itself, only at frequencies above 100 Hz the frequency error scaled by the transmission time is dominating. The error due to the frequency offset of the two satellites oscillators is five orders of magnitude smaller than the phase error, the error due to the frequency error is even ten orders of magnitude smaller. For error simulations, it is sufficient to consider the phase noise and the frequency error scaled by the transmission time.

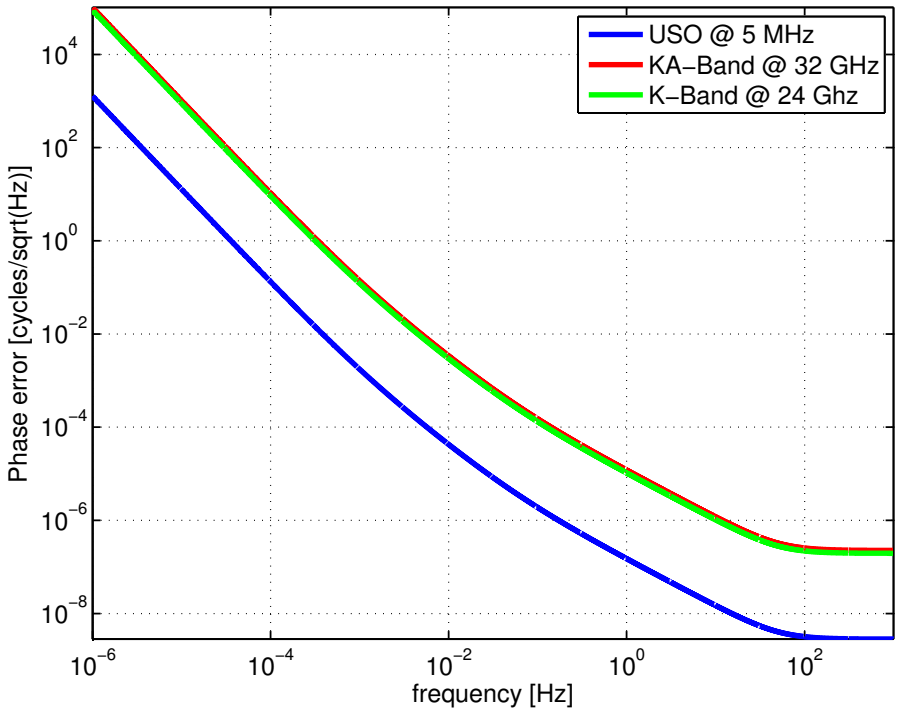

Figure 10.2: Root PSD of the phase noise due to USO instability. The phase noise shows a $\frac{1}{f^2}$ behavior at low frequencies and then converges into white noise at high frequencies.

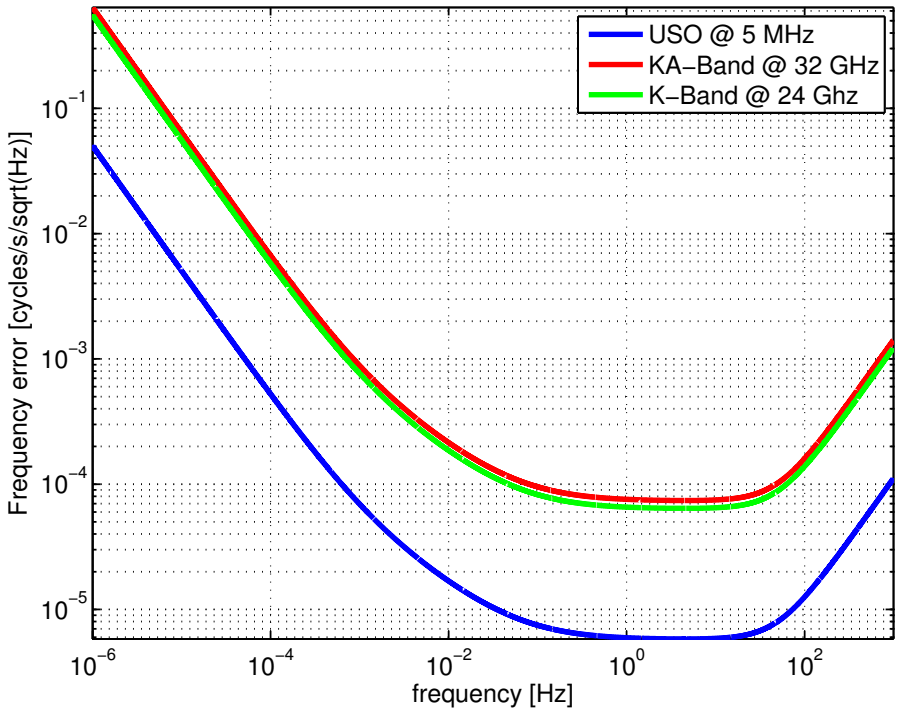

Figure 10.3: Root PSD of the frequency noise due to USO instability. The frequency noise is the time derivative of the phase noise. The frequency error increases at low as well as at high frequencies.

Error due to system noise

The system noise consists mainly of two effects: the background noise and the thermal noise, i.e. the measurement error caused by the K-band system itself due to ,e.g., the analog to digital conversion,

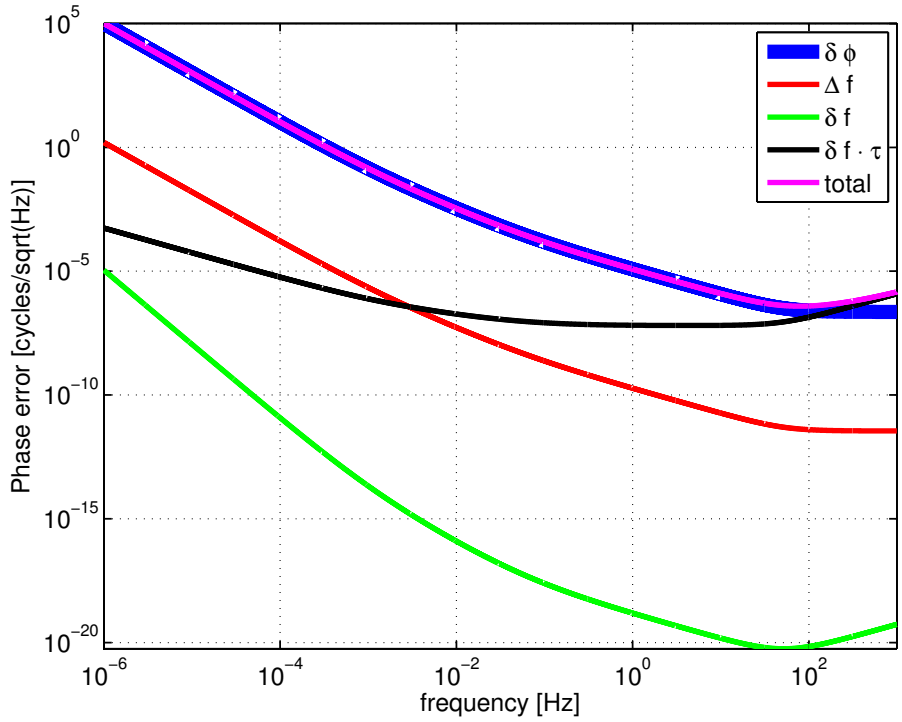

Figure 10.4: Root PSD of the phase measurement error contributors due to USO noise. The largest contributors are the phase errors and the frequency errors scaled by the transmission time between the two satellites, followed by the error contribution dependent on the frequency offset between the two satellites. The contribution of the frequency errors is smallest.

the phase measurement process and the error caused by temperature variations. According to Thomas (1999), the system noise is white and can be approximated by the following equation:

$$\epsilon_{system} = \frac{1}{2\pi SNR} \text{ [cycles]}, \tag{10.23}$$

in units of cycles, which corresponds to a system noise error of 53 µcycles 1-σ standard deviation for 1 s data with a typical value for the Signal to Noise Ratio (SNR) of $SNR = 2800$.

Error due to phase ambiguity

From the incoming signal not only the phase with respect to the internal signal is derived, but there is also a counter that counts the integer number of cycles received. The distance between the two satellites can be expressed as an integer number of cycles plus the length corresponding to the phase difference. The recorded number of cycles differs from the true number of cycles by an integer number, the so-called integer phase ambiguity N_A.

Error due to ionosphere delay

On its way between the two satellites, the K-band signal is delayed depending on the density of free electrons along the signal path. The Total Electron Content (TEC) is a measure for this quantity. The electrons lead to a phase shift, i.e. a phase error that is inversely proportional to the carrier frequency and directly proportional to the TEC along the signal path:

$$I_A = \frac{TEC_B^A}{f_B} \text{ [cycles]}. \tag{10.24}$$

The error varies from epoch to epoch and is dependent on the actual state of the ionosphere. As the actual frequencies of the satellite oscillators can be estimated, a ionosphere free linear combination can be formed and thus the error can be eliminated, see chapter 15, and is therefore not explicitly modeled here.

Error due to phase shift caused by the atmosphere and multipath

According to Kim (2000), the error due to multipath can be neglected, as it is well below the level of one micrometer. This is only true if the mutual orientation of the GRACE satellites stays within certain boundaries. For this work, it is assumed that the attitude control system fulfills the requirements and that the effect of multi-path can therefore be neglected.

Total phase error

Figure 10.5 shows the total phase error. The total phase error is the sum of the above discussed individual error sources; here the error is specified as a root PSD, thus the error due the phase ambiguity does not contribute as it is a constant that is visible on the zero frequency of the PSD. The error due to the ionosphere is not included. We note that at low frequencies the error due to USO instability dominates and leads to a $1/f^2$ rise. At high frequencies the system noise dominates as white noise with a level of about $53 \cdot 10^{-6}$ cycles/$\sqrt{\text{Hz}}$. Especially the strong rise at low frequencies in the total

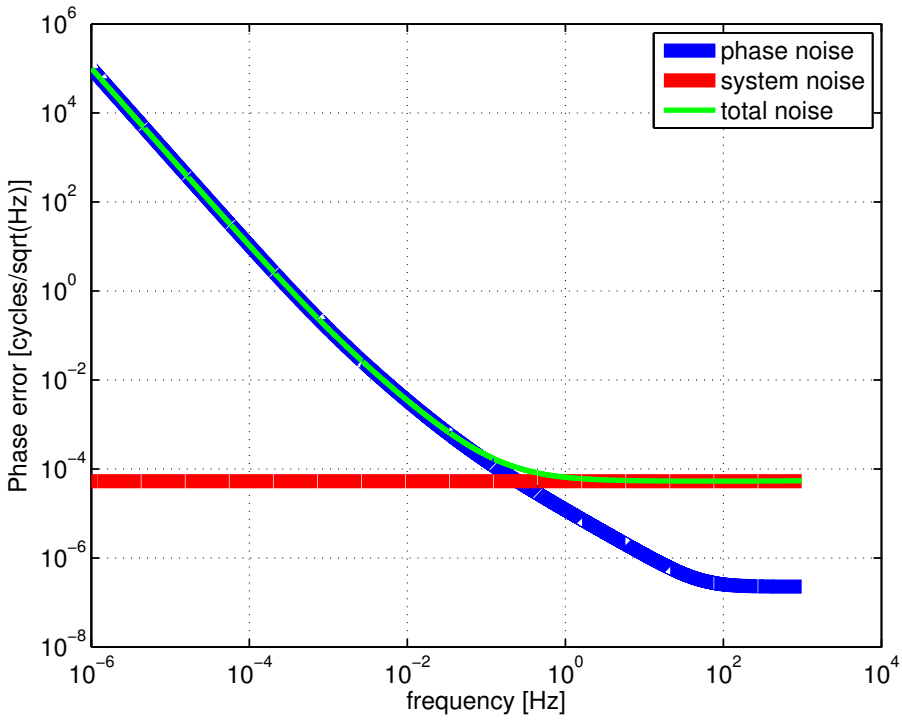

Figure 10.5: Total phase measurement error due to the phase noise and system noise. The USO noise dominates at low frequencies and rises with a $\frac{1}{f^2}$ slope, i.e. it causes a strong drift in the phase measurements. At high frequencies, the white system noise is the dominating phase error contributor.

error would deteriorate the use of the phase measurements for range determination; only through the combination of the phase measurements of the two satellites an inter-satellite range of a considerable quality can be derived, see chapter 15.

11. GPS Receiver

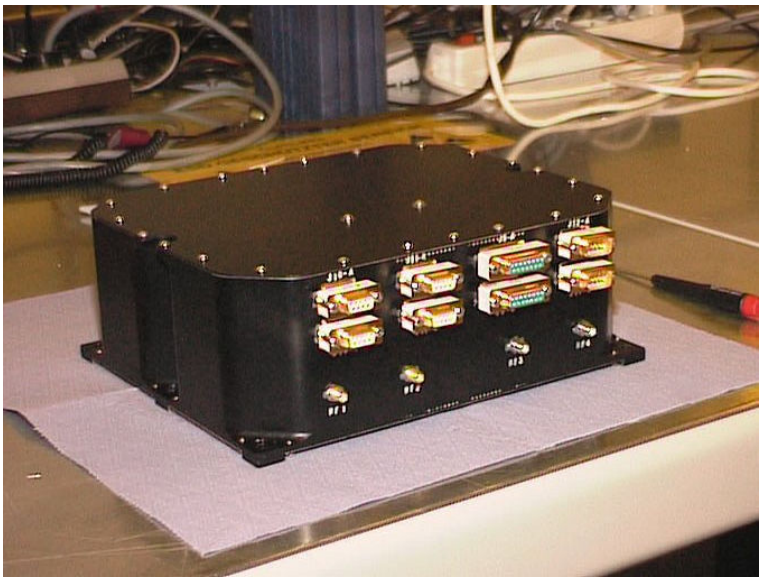

Figure 11.1: Black-Jack GPS receiver flight model, from www.gfz-potsdam.de.

11.1. Introduction

On both GRACE satellites a space approved Black-Jack Global Positioning System (GPS) receiver is installed, see figure 11.1. In contrast to the K-band ranging system, the GPS receiver is a passive ranging system, i.e. it does no emit electromagnetic signals, it only receives them via the GPS antenna. The signal source are the GPS satellites. We will not give a detailed description of the GPS, the interested reader may consult Rothacher (2001), also for additional literature. We will only give a brief overview of the different available signals and give simple measurement models for the code and phase measurements. Figure 11.2 shows an overview of the different signals emitted by the GPS satellites. All signals are driven by an oscillator running at a frequency of 10.23 MHz. The two carrier signals L1 at 1575.42 MHz and L2 at 1227.60 MHz are generated by a scaling of the oscillator frequency. The L1 and L2 signals are used for the phase measurements. Both carrier signals are modulated by the code signals: L1 is modulated by the Clear Access / Coarse Aquisition (C/A) code at 1.023 MHz and the Protected/Precise code P1 at 10.23 MHz. L2 is modulated by the P2 code at 10.23 MHz. There is no C/A code on L2. The satellite message contains additional information needed for the position determination process: the GPS satellite position, the satellite clock error, the health status of the satellite and others.

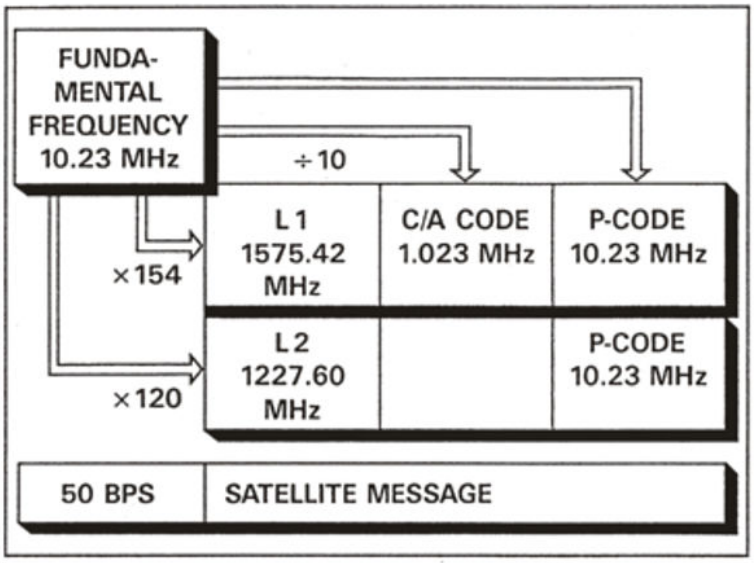

Figure 11.2: Overview of the Signal emitted by the GPS satellites, from Rothacher (2001).

11.2. Measurement models

We will now give the measurement models for the pseudorange and phase measurements from Rothacher (2001).

11.2.1. Pseudorange measurements

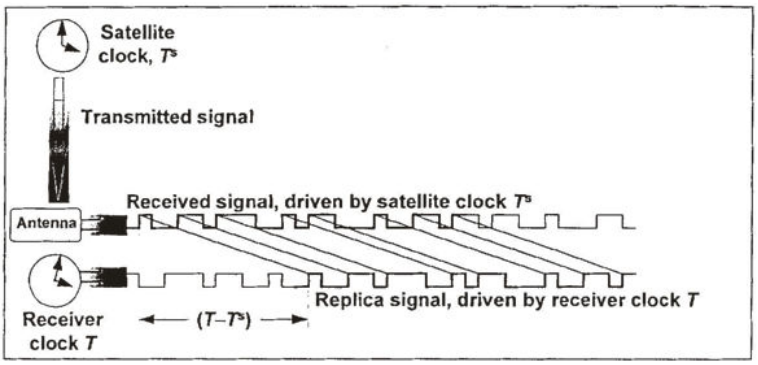

Figure 11.3: Pseudorange or Code measurement, from Blewitt (2006).

The measurement principle of the pseudorange measurements is shown in figure 11.3. The received signal from the GPS satellite is compared to a reference signal generated by the receiver. Assuming that both the receiver and the satellite clock are perfectly synchronized and that the signal travels through vacuum, the time shift between the two signals determined by the receiver correlator is the transmission time of the received signal from the GPS satellite to the receiver. The signal speed is the velocity of light, so the distance between satellite j and the receiver A is given by:

$$P_A^j = c \cdot (T_r - T^s), \tag{11.1}$$

with

P_A^j measured range between satellite j and the receiver A,
c velocity of light,
T_r epoch of signal reception,
T^s sending epoch.

In reality, the satellite and receiver clock are not synchronized, the signal travels not through vacuum and there are additional error sources including the measurement noise. The measured range is not the true one and is therefore called pseudorange. A more realistic measurement model is:

$$P_A^j = \rho_A^j - \delta\rho_{A,ion}^j + \delta\rho_{A,rel}^j + \delta\rho_{A,mul,C}^j + c\delta t_A + c\delta t^j + c\beta^j + c\beta_A + \epsilon_{A,C}^j, \tag{11.2}$$

with

P_A^j pseudorange measurement between satellite j and the receiver A,
ρ_A^j geometric distance between satellite j and the receiver A,
$\delta\rho_{A,ion}^j$ influence of the ionosphere,
$\delta\rho_{A,rel}^j$ relativistic correction due to the velocity and potential difference between receiver and satellite,
$\delta\rho_{A,mul,C}^j$ the influence of multipath on the code measurement,
$c\delta t_A$ range error due to the receiver clock error,
$c\delta t^j$ range error due to the satellite clock error,
$c\beta^j$ signal delay on satellite j (from signal generation until emission),
$c\beta_A$ signal delay in the receiver (from the antenna to the correlator),
$\epsilon_{A,C}^j$ code measurement error.

11.2.2. Carrier phase measurements

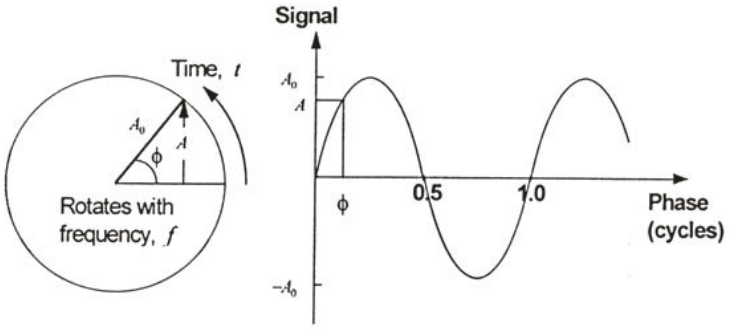

Figure 11.4: Carrier phase measurement, from Blewitt (2006).

During a uniform rotation with the frequency f, the phase angle or phase increases linearly with time (cf. figure 11.4):

$$\Phi = f \cdot t + \Phi_0, \tag{11.3}$$

where Φ_0 is the unknown initial phase. The carrier phase measurement of the receiver is the phase difference between the receiver reference phase and the received phase from satellite j:

$$\phi_A^j = \Phi_{0,r} - \Phi_{GPS,r}^j, \tag{11.4}$$

with

ϕ_A^j phase measurement of the receiver A to satellite j,
$\Phi_{0,r}$ reference phase at signal reception time T_r,
$\Phi_{GPS,r}^j$ received phase from GPS satellite j at signal reception time T_r.

The receiver can only measure the fractional phase of the received signal from the GPS satellite, therefore the emitted signal differs from the receipt signal by an integer number of cycles:

$$\Phi^j_{GPS,r} = \Phi^{GPS,s}_j - N^j_A, \tag{11.5}$$

with

$\Phi^{GPS,s}_j$	GPS phase (cycles) emitted by satellite j at T_s,
N^j_A	integer number of full cycles contained in $\Phi^{GPS,j}_j$, so called 'integer phase ambiguity'.

The phase ambiguity has to be solved, if the true distance between satellite and receiver is to be derived, otherwise the phase measurement delivers only a biased range.

Using equation (11.3), we rewrite the expressions for the reference phase of the receiver and the phase received from the GPS satellite:

$$\begin{aligned} \Phi_{0,r} &= fT_r + \alpha_A, \\ \Phi^j_{GPS,r} &= fT^s + \alpha^j - N^j_A, \end{aligned}$$

where α^j is the signal delay on satellite j from generation till emission and α_A is the signal delay in the receiver from the antenna to the correlator.

The measurement model then becomes:

$$\begin{aligned} \phi^j_A &= \Phi_{0,r} - \Phi^j_{GPS,r} \\ &= fT_r + \alpha_A - (fT^s + \alpha^j - N^j_A) \\ &= f(T_r - T^s) + \alpha_A - \alpha^j + N^j_A. \end{aligned} \tag{11.6}$$

We can transform the phase measurement in cycles into a distance measurement by multiplication by the nominal wavelength $\lambda = c/f$:

$$\begin{aligned} L^j_A &= \lambda\phi^j_A \\ &= c(T_r - T^s) + \lambda(\alpha_A - \alpha^j + N^j_A). \end{aligned} \tag{11.7}$$

This measurement model is again not realistic as it makes the same assumptions as the simple model for the pseudorange measurement. A realistic model is given by:

$$L^j_A = \rho^j_A + \delta\rho^j_{A,ion} + \delta\rho^j_{A,rel} + \delta\rho^j_{A,mul,\phi} + c\delta t_A + c\delta t^j + \lambda(N^j_A - \alpha^j + \alpha_A) + \epsilon^j_{A,\phi}, \tag{11.8}$$

with

L^j_A	measured range between satellite j and the receiver$A$,
ρ^j_A	geometric distance between satellite j and the receiver A,
$\delta\rho^j_{A,ion}$	influence of the ionosphere,
$\delta\rho^j_{A,rel}$	relativistic correction due to the velocity and potential difference between receiver and satellite,
$\delta\rho^j_{A,mul,\phi}$	the influence of multipath on the phase measurement,
$c\delta t_A$	range error due to the receiver clock error,
$c\delta t^j$	range error due to the satellite clock error,
$\epsilon^j_{A,\phi}$	phase measurement error.

11.3. Error model

The error model we will use for the data analysis is simple, we model the phase measurement error and the code measurement error as white noise of a certain power. The other error sources are neglected as they are not random but systematic, at least over short time intervals. During the real data analysis, only consecutive epochs, where the same satellite has been tracked, are used. The noise specifications are given in table (11.1).

Table 11.1: Noise level specifications for the Black-Jack GPS receiver from Stanton et al. (1998).

observation type	noise level 1σ [cm] 10 s sampling	error [$\sqrt{\text{PSD}}$ cm/s^2/$\sqrt{\text{Hz}}$]
code measurements	100	400
phase measurements	1	4

Part IV.

Real data processing and analysis

12. Data levels overview

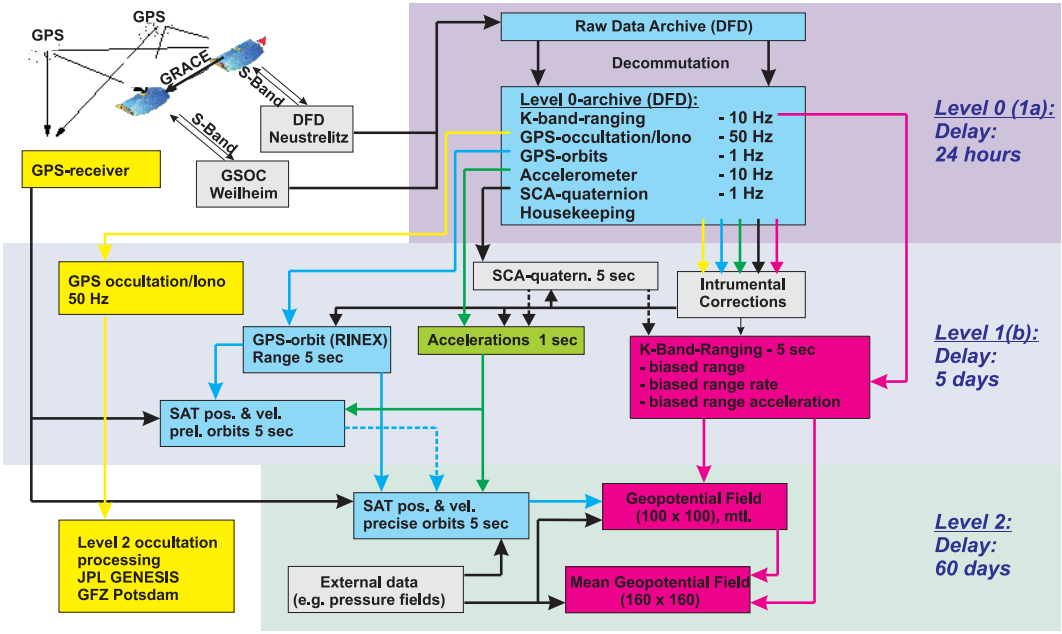

Figure 12.1: Overview of the different data levels

In figure 12.1 an overview over the different data levels is shown. In principle, there are three data levels: level 0, level 1 and level 2. Level 0 corresponds to the raw instrument data, level 2 corresponds to the level of products like gravity fields for a large user community. The intermediate level 1 can be split up into level 1a and level 1b. Level 1a represents the calibrated instrument data given in their native coordinate frames, see section D.5, and at their original sample rate. Here 'calibrated' means converted into engineering units and arranged to cover one day per file. The original level 0 data is dumped by the satellites at each fly-by at the ground stations in Weilheim and Neustrelitz and therefore available in chunks covering about one revolution of the satellites. Several processing steps are necessary to transform the calibrated instrument data (level 1a) to the gravity field determination input data (level 1b).

13. Data products overview

13.1. Science data products

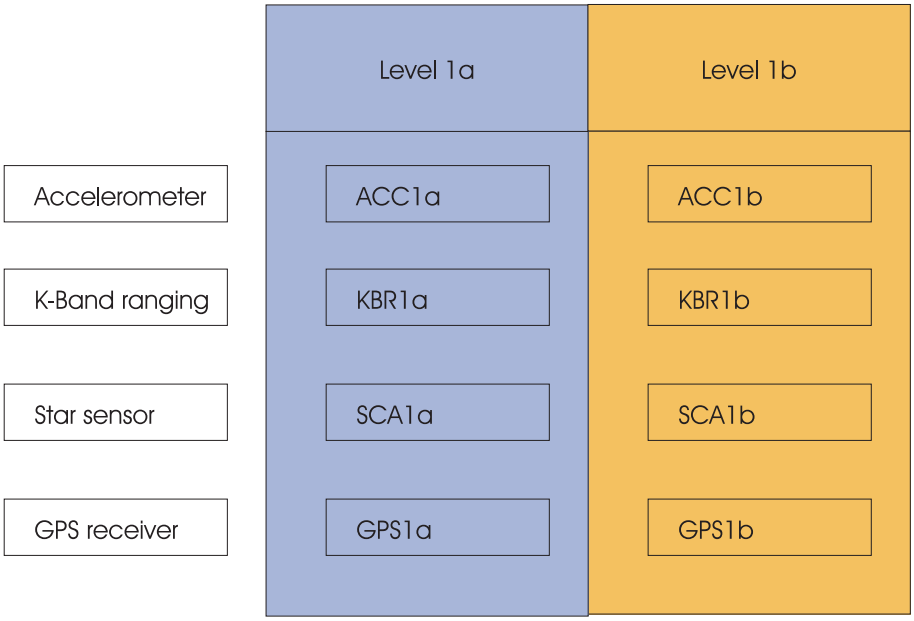

Figure 13.1: Overview of the GRACE data products of the main elements fo the sensor system.

The description of the GRACE data products can be found in Bettadpur (2007). In figure 13.1, the data products for the science data stream are depicted. The accelerometer data products for level 1a are labeled ACC1A, the products for level 1b are labeled ACC1B. As there is one accelerometer on each satellite, there is a separate product for each satellite. The star sensor data are labeled SCA1A for level 1a and SCA1B for level 1b. Each satellite possesses two star sensor heads. The data from the two heads are contained separately in the level 1a product. The level 1b product contains the orientation resulting from the combination of the two sensor heads. Again there is one product for each satellite. The K-band ranging data products are labeled KBR1A for the level 1a and KBR1B for the level 1b. The level 1a contains the phase measurements for the Ka and the K-band, there is one product for each satellite. The level 1b product contains the derived intersatellite range, range rate and range acceleration. Therefore there is only one product for the two satellites.

13.2. Housekeeping data products

The housekeeping data products contain ancillary data. For this work, the following housekeeping products were used, description from Bettadpur (2007):

Name	Description
TIM1B	On-board data handler to GPS time mapping
CLK1B	Precise clock solution
USO1B	Ultra stable oscillator frequency estimate
THR1B	Thruster activation data
MAG1B	Magnetometer and magnetotorquer data

13.3. Data set description

The data set investigated covers August in 2003. For the star tracker, the accelerometer and the K-band ranging system, L1a data as well as L1b data were available. For the GPS receiver data, only L1b data were available. Concerning auxiliary data like thruster activation data, magnetic torque rods activation data and others, only the L1b data are considered.

14. Level 1a data analysis

The measurements of each instrument are analyzed in order to identify the performance of the instrument. The analysis also aims at a thorough understanding of the instruments' data. Unexpected behavior shall be identified and, if possible, also the underlying reasons. For the GPS receiver no L1a data were available for analysis.

14.1. Analysis of the star tracker data

The L1a star tracker data product contains the data from both sensor heads of the star tracker of each satellite. The delivered quaternions represent the transformation from the inertial reference frame (IRF) to the star sensor reference frame (SSRF). In order to compare the measurements of both heads, it is necessary to transform them into quaternions representing the rotation from the IRF to the science reference frame (SRF):

$$\overline{\mathrm{Q}}_{irf}^{srf} = \overline{\mathrm{Q}}_{irf}^{ssrf} \star \overline{\mathrm{Q}}_{ssrf}^{srf}. \tag{14.1}$$

The information about the orientation of the SSRF w.r.t. the SRF is derived pre-launch, as well as post-launch, during calibration maneuvers. It is also interesting to analyze the angular rates derived from the quaternions and to assess their performance, as they may be combined with the accelerometer measurements in the L1a to L1b processing. For details about the derivation of the angular rates from an orientation representation, see appendix C for more details.

Figure (14.1) shows the time series of the star tracker measurements of GRACE A and B for a sample day. Let us first take a look at the data from GRACE A shown in the left panels. First we realize that the data delivered by head 2 show a sinusoidal behavior. The period of the oscillation is about once every two revolutions. At a first glance this may seem strange, as usually all the sensor measurements show a strong signal at the orbit frequency. The reason lies in the definition of the quaternions. They depend on the square root of the change of the coordinate axes. The axes change with the orbit frequency, the square root of this change is then an oscillation at half the orbit frequency. The data of head 1 are different. Once every revolution all quaternion elements change their sign simultaneously and have the opposite sign of the data delivered by head 2 until the next change happens. Then the signs of the data agree until the next change and so on. The reason is that for this sample day the orbit of GRACE A is oriented towards the Sun/Moon in such a way, that once every revolution the sunlight/moonlight blinds head 1 and interrupts the data delivery, marked as invalid data in the figure. When the data delivery recommences, the quaternions have either the same or the opposite sign as the quaternions from head 2. A change of sign of all quaternion components does not change the represented orientation, therefore head 1 and 2 give the same orientation during times of simultaneous data delivery.

The right panels of figure 14.1 show the same period for the data delivered by the star sensor heads of GRACE B. As GRACE B is rotated by 180° about the z-axis compared to GRACE A, head 1 delivers data continuously and head 2 is blinded by the Sun/Moon every revolution, interrupting the data delivery (marked again as invalid data).

The top panels of figure 14.2 show the root PSD of the star tracker quaternions of GRACE A. Let us first take a look at the root PSD of the data from head 1 (top left panel). The frequency range at low frequencies is limited because of the multiple Sun/Moon intrusions. At high frequencies, the root PSD becomes white noise at a frequency of about $2 - 3 \cdot 10^{-2}$ Hz. The noise level seems to be slightly better

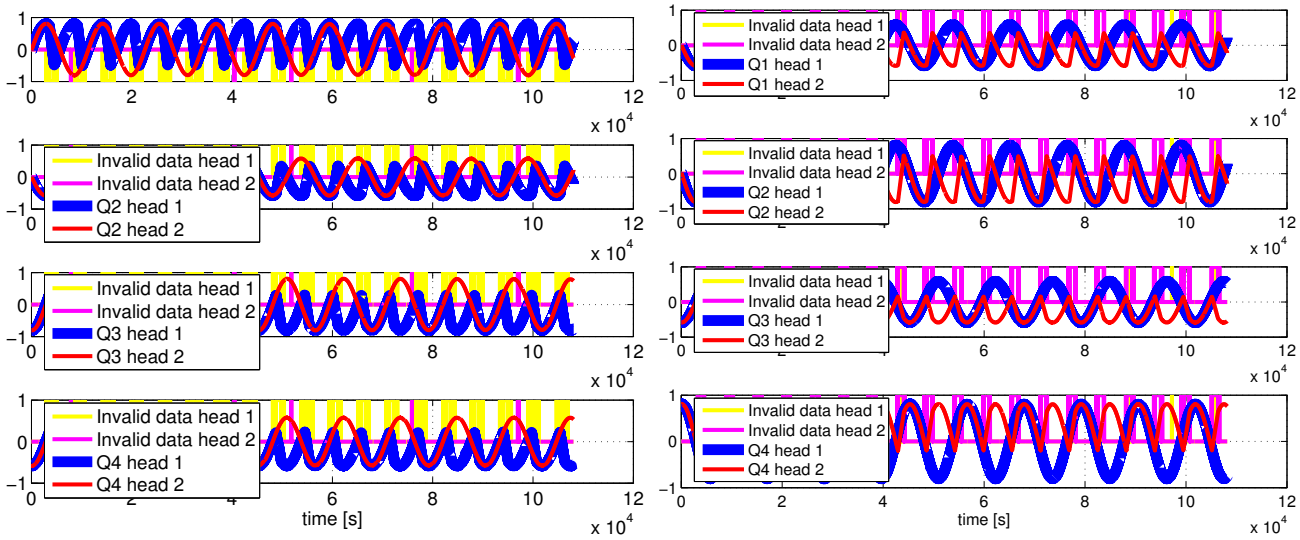

Figure 14.1: Left panels: Time series of the star tracker quaternions of GRACE A, head 1 and head 2, for a sample day. Right panels: Time series of the star tracker quaternions of GRACE B.

than specified. The frequency range at low frequencies of the root PSD of the data from head 2 (top right panel) is larger, as for this example head 2 is not blinded by the Sun/Moon and delivers data continuously. Therefore we note a strong signal on half the orbit frequency at about $9 - 10 \cdot 10^{-5}$ Hz. Concerning the behavior at high frequencies, the same conclusions hold as for the data from head 1: The noise level is slightly better than specified.

The two lower panels show the root PSD of the data delivered from the star sensor heads on GRACE B. As here head 1 (lower left panel) delivers data continuously and head 2 (lower right panel) is blinded regularly by the Sun/Moon, the frequency range of the root PSD of the data from head 2 is limited and therefore the signal at half the orbit frequency is not resolved. Concerning the noise level, it seems that the data delivered from head 1 do not meet the required noise level. The reason is that the data from head 1 are interrupted due to invalid measurements, although this occurs much less often than on head 2. In order to derive the root PSD for a full day, the gaps were filled by interpolation. The interpolated data differ significantly from the measured ones and cause a noise level that is higher than specified. We will determine the noise level later, when we analyze the difference of both heads.

Let us take a look at the angular rates derived from the quaternions in figure 14.3.

First, we analyze the angular rates on GRACE A in the time domain, shown in the top left three panels. As expected, the rates about the x- and the z-axis show no bias, but the y-axis does show a bias of about $1.1 \cdot 10^{-3}$ rad/s, that corresponds to a full rotation about the y-axis during one revolution. The satellites rotate about their y-axis once per full revolution, as the attitude control maintains the satellite earth pointing. Intervals of invalid data exhibit strong oscillations. The noise of the rate about the x-axis is significantly smaller than the noise of the angular rates about the y- and z-axis. It is smaller because this rotation is perfectly perpendicular to the line of sight of each star camera head. The rotations about the y- and z-axis are only partly perpendicular to the line of sight of the camera heads and therefore determined less well.

The root PSD of the angular rates on GRACE A are shown in the top right panel. For all axes, there is peak at the orbit frequency. The x- and z-axis show a second peak at about $1 \cdot 10^{-3}$ Hz. A third peak is visible at about $5 - 6 \cdot 10^{-3}$ Hz, that is most prominent for the y-axis and less pronounced for the x- and z-axis. The cause seems to lie in the attitude control system, that causes angular accelerations through the magnetic torque rods and the cold gas thrusters, we will investigate this later. The constant angular velocity about the y-axis does not show up in the root PSD. Starting from about $1 \cdot 10^{-2}$ Hz, noise starts to dominate the spectrum and rises to a level of about $5 \cdot 10^{-4}$ rad/s/$\sqrt{\text{Hz}}$. The noise level at the

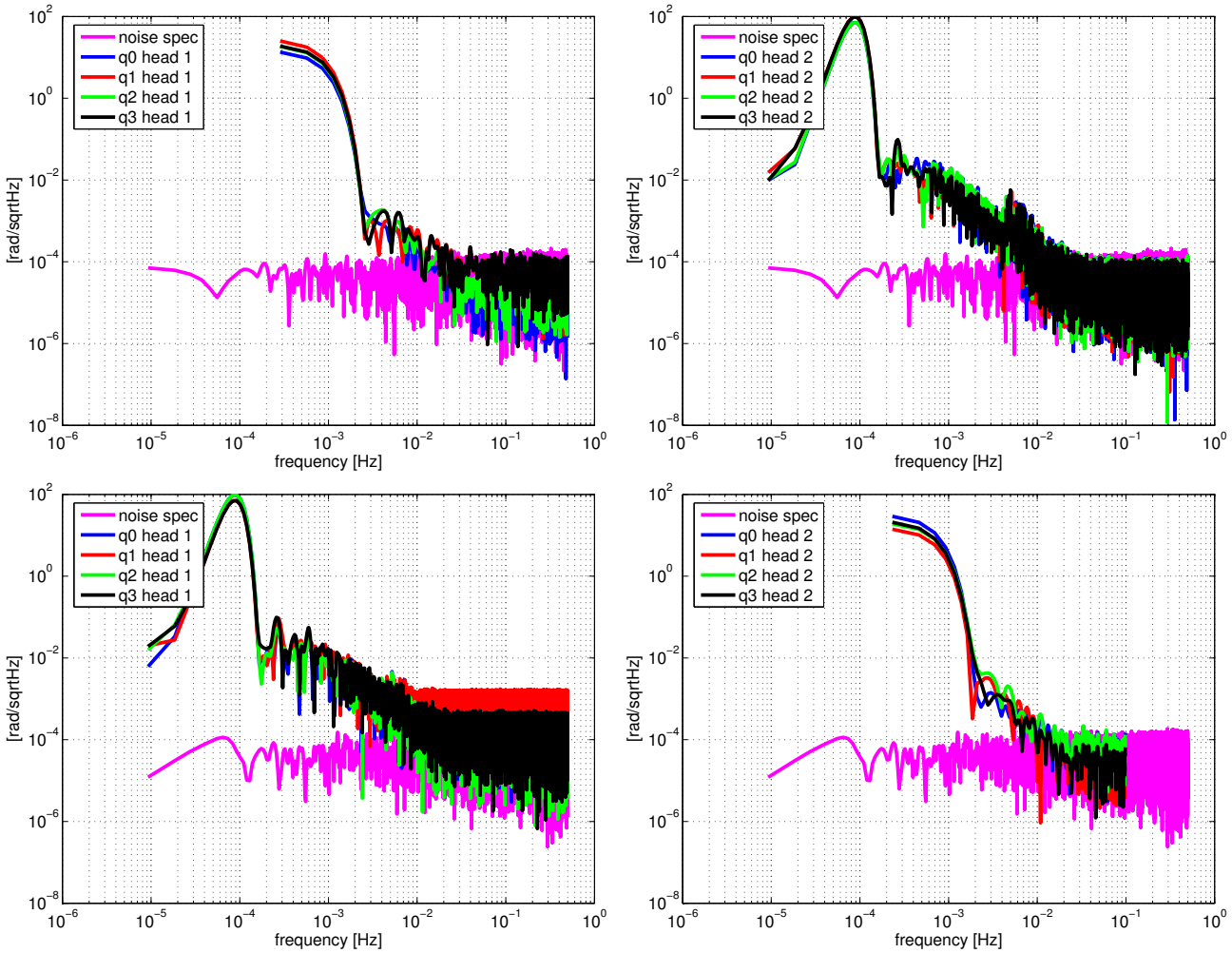

Figure 14.2: Top panels: root PSD of the star tracker quaternions of GRACE A, head 1 (left) and head 2 (right), for a sample day. Bottom panels: root PSD of the star tracker quaternions of GRACE B, head 1 (left) and 2 (right).

high frequencies is higher than the signals from the attitude control system, therefore one recognizes only noise in the time series of the angular rates.

The time series of the angular rates on GRACE B is shown in the lower left three panels. The observations made for GRACE A seem also to be true for GRACE B. The noise level of the angular rate about the x-axis is significantly smaller than that of the rates about the other axes. It is interesting that it seems as if the noise level of the rates derived from head 2, that is regularly blinded by the Sun/Moon, is significantly lower than that of the rates derived from head 1. That is not true, the reason lies in different sampling rates: the data from head 1 are sampled at 1 Hz, the data from head 2 at 0.2 Hz. Due to the reduced bandwidth of the data from head 2, its noise level is also reduced significantly.

The root PSD of the angular rates from GRACE B in the lower right panel shows the same behavior as the root PSD of the angular rates from GRACE A.

Another possibility to assess the performance of the star sensor heads is to compare their data directly. In principle they should provide the same orientation, if one neglects systematic errors resulting, e.g., from imperfect knowledge of the orientation of the respective sensor head with respect to the satellite body frame. The difference of the sensor head measurements should give an indication of an upper limit of the sensor error, as random noise adds up when being subtracted. Figure 14.4 shows the difference of the sensor head measurements.

The top left panel shows a period where data from both heads on GRACE A are available. It seems that the difference depends on the time difference to the epoch where the Sun/Moon blinds sensor head 1.

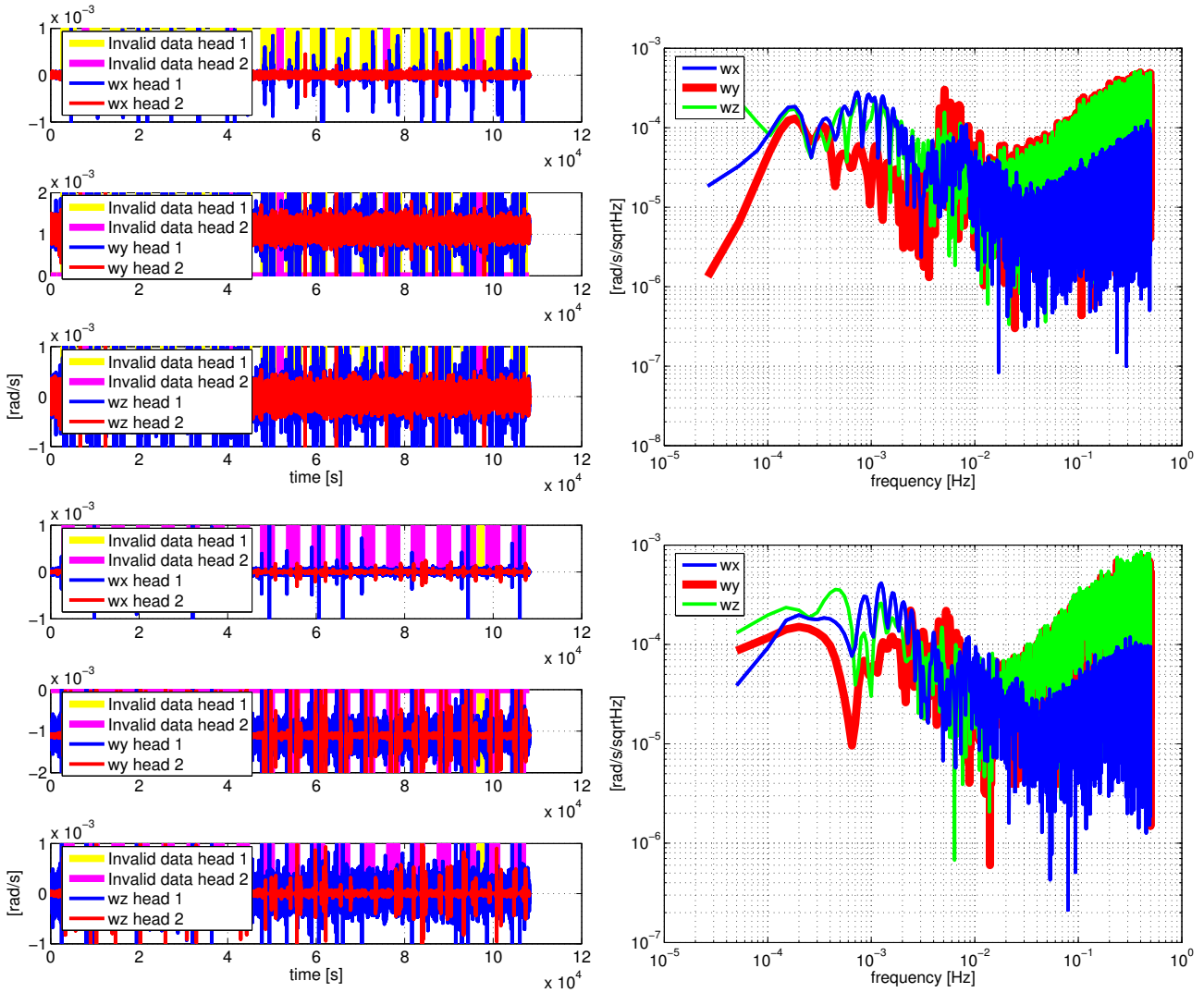

Figure 14.3: Top left three panels: time series of the star tracker derived angular rates of GRACE A, head 1 and head 2. Top right panel: root PSD of star tracker derived angular rates of GRACE A. Lower left three panels: time series of the star tracker derived angular rates of GRACE B, head 1 and head 2. Lower right panel: root PSD of star tracker derived angular rates of GRACE B.

The closer the Sun/Moon intrusion, the larger the oscillation of the difference. We assume that the data quality of the sensor head that is not blinded regularly by the Sun/Moon remains constant. It seems then sensible to assume that the data quality of the sensor had that is blinded regularly varies with time. For a possible sensor head's data combination, only epochs at a certain distance from Sun/Moon intrusions should be used or the data should be weighted accordingly.

The top right panel shows the root PSD of the difference. The observations made in the time domain are confirmed. One would expect only white noise for the difference, assuming a white noise behavior of the sensor error. But the PSD shows a slight rise towards low frequencies. This drift results from the deterioration of the data of the regularly blinded sensor head towards the full Sun/Moon intrusions. The noise level is estimated to be lower than $2 \cdot 10^{-4}$ rad/s/$\sqrt{\text{Hz}}$, which agrees with the specification.

The comparison of the data of both sensor heads on GRACE B (see lower left and lower right panel of figure 14.4) delivers the same results.

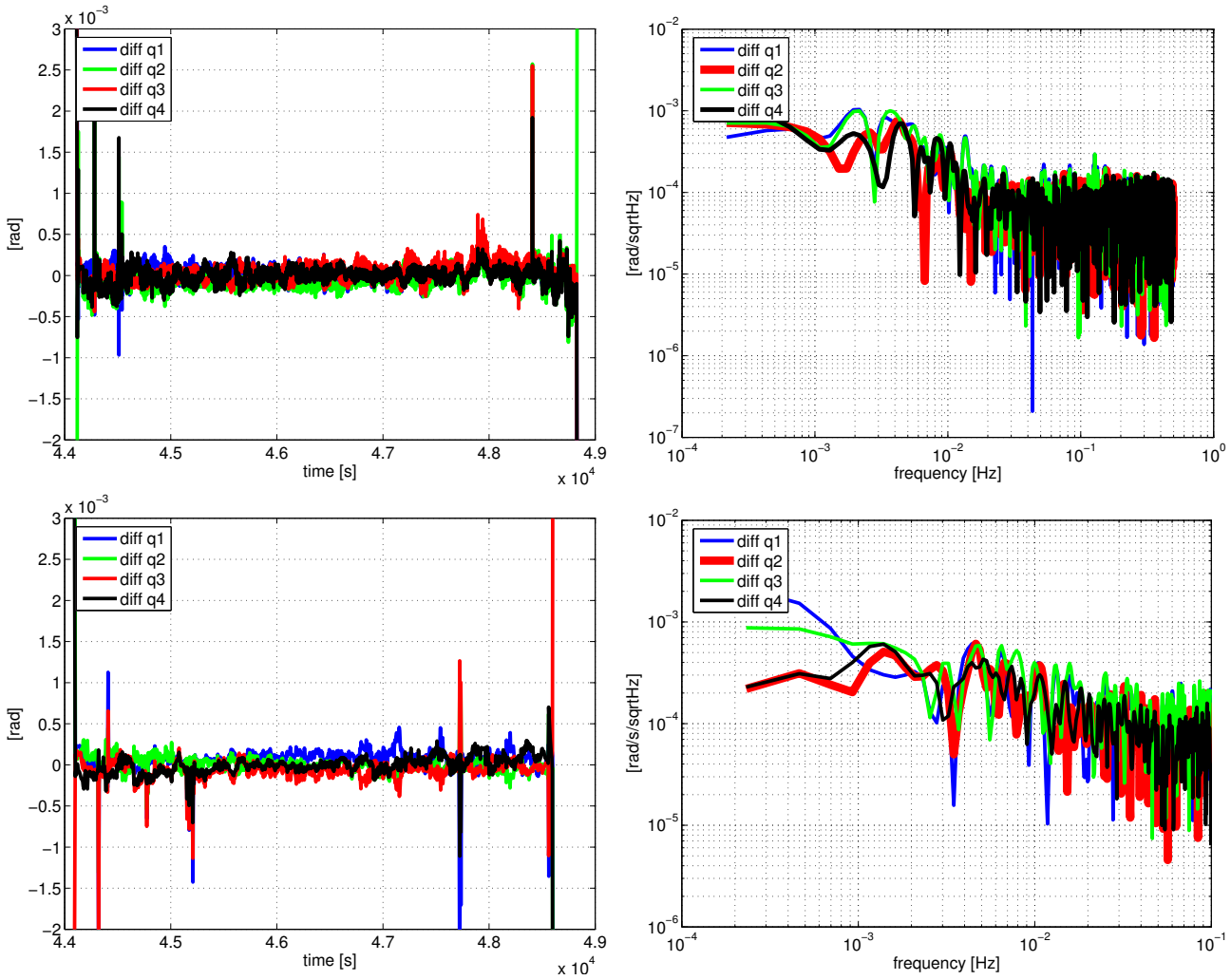

Figure 14.4: Top left panel: Difference of the measurements of sensor head 1 and 2 on GRACE A in the time domain. Top right panel: root PSD of the difference of the measurements of sensor head 1 and 2 on GRACE A. Lower left panel: Difference of the measurements of sensor head 1 and 2 on GRACE B in the time domain. Lower right panel: root PSD of the difference of the measurements of sensor head 1 and 2 on GRACE B.

14.2. Analysis of the accelerometer data

The purpose of the accelerometers is to measure the surface forces that act on the satellites. The K-band measurements, that contain both the effects of the gravitational forces and the surface forces, can then be corrected for the latter. From the surface force models for air drag, solar radiation pressure and albedo, we know that air drag is the dominating surface force with a magnitude of several $1 \cdot 10^{-7}$ m/s^2 for the along-track component, one order of magnitude less for the cross-track component and the radial component for an orbit height between 450 and 500 km. The analysis of the accelerometer data will be conducted in two steps:

- Comparison of the measurements with drag models.
- Analysis of different events like twangs, peaks and thruster firings.

The accelerometer measurements consist of the measured linear accelerations and the measured angular accelerations. Let us first take a look at the linear accelerations. One would expect the signal shown in the two top panels of figure 14.5 from simulations: In terms of magnitude, the along-track component should be strongest, followed by the radial component and the cross-track component. All components should show a strong once per revolution signal in the root PSD. In addition, the along-track component should be biased at a level of about $2 \cdot 10^{-7}$ m/s^2. The measurements seem to be different, cf. the two middle and bottom panels of figure 14.5.

Concerning the cross-track component, it can be stated that the increased magnitude is caused by the effect of the thruster events.

We also notice that the radial component's magnitude is larger by far than the magnitude of the along-track or cross-track components. Apart from linear accelerations acting on the satellite surface, any effect that causes a movement of the accelerometer cage against the proof mass is a possible candidate to explain the difference between model and actual measurement:

- Angular accelerations and velocities: they map into the linear accelerations as Coriolis and centrifugal accelerations, if the accelerometer is not perfectly placed at the center of mass. In this category the attitude control system is included as well. The thruster firings play a dominant role, as they cause the strongest and abrupt angular accelerations of all types of attitude control.
- Vibrations of the satellite body due to thermal effects. During the design of the satellite structure, great efforts were made to minimize the thermal expansivity of the satellite structure, but remaining effects could be detected by the accelerometers, assuming a sufficient magnitude of the vibrations.
- Electromagnetic effects resulting from the operation of heater switches of the satellite.

The effects dominating the radial component seem to be irregular and not correlated with thruster events. So we can exclude angular effects to be the cause. The large magnitude suggests that the reason lies in the second candidate and that the origin of the effects lies in vibrations of the satellite. Taking a closer look in figure 14.6, the dominating feature, so called twangs, are visible. They are strongest on the radial component of the linear accelerations.

The situation is similar for GRACE B, see lower panels in figure 14.5. We can draw the same conclusions as for GRACE A: The signal of the radial component is dominating and larger than the signal of the other components. Concerning the root PSD, the signal at 1 Hz, that is very pronounced for GRACE A, is less pronounced. When we take a closer look at the features of the radial component in figure 14.6, we realize that again the twangs are likely the dominant effect.

Therefore, we will now investigate the 'twangs' in more detail.

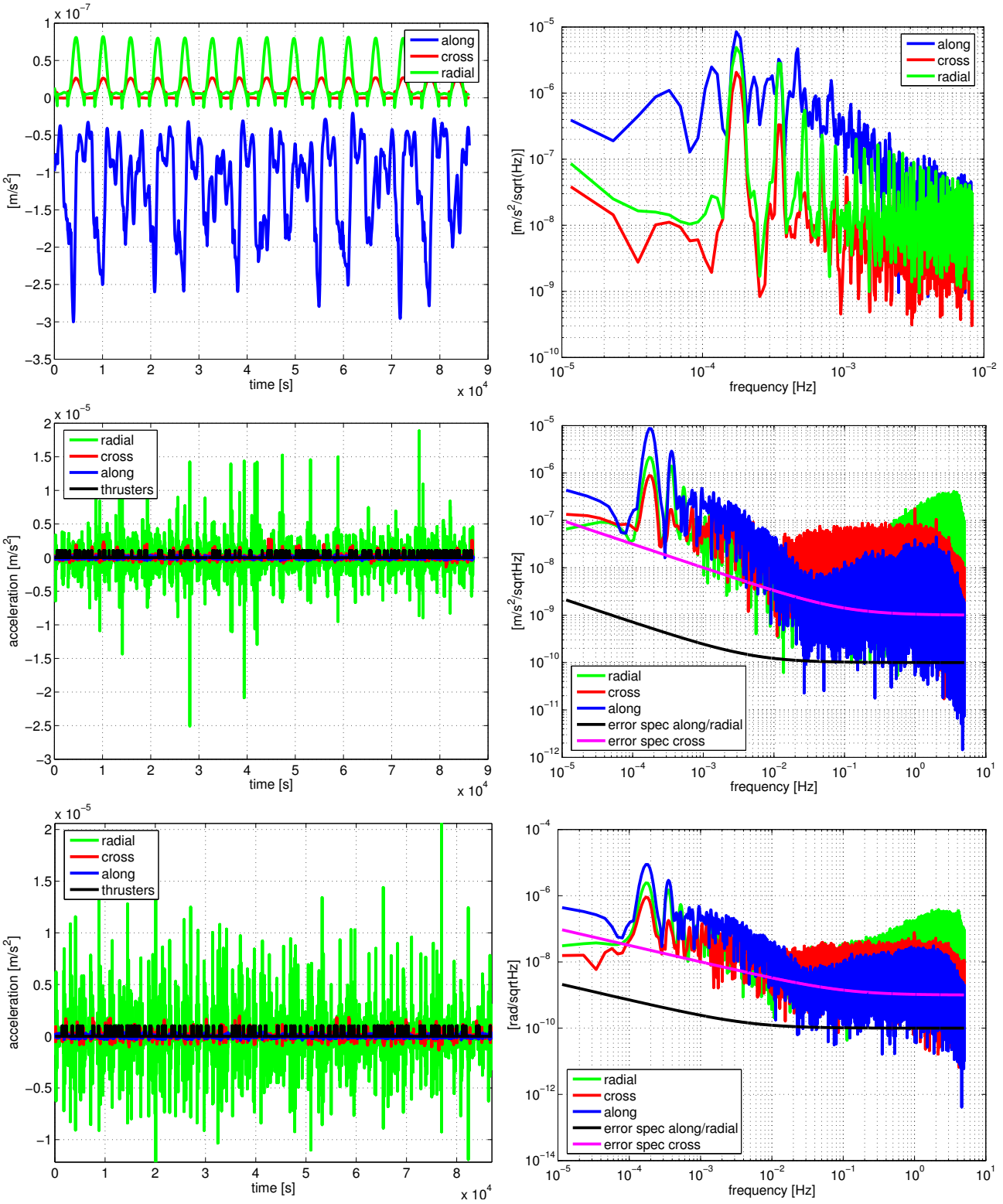

Figure 14.5: Upper left panel: Time series of simulated surface forces including air drag, solar radiation pressure and Earth albedo. Upper right panel: root PSD of the simulated surface forces. Middle left panel: Time series of the measured linear accelerations on GRACE A. Middle right panel: Root PSD of the linear accelerations on GRACE A. Lower left panel: Time series of the measured linear accelerations on GRACE B. Lower right panel: Root PSD of the linear accelerations on GRACE B.

14.2.1. Twangs

In Hudson (2003) and in Flury (2004), this phenomenon has been investigated in detail. Figure 14.7

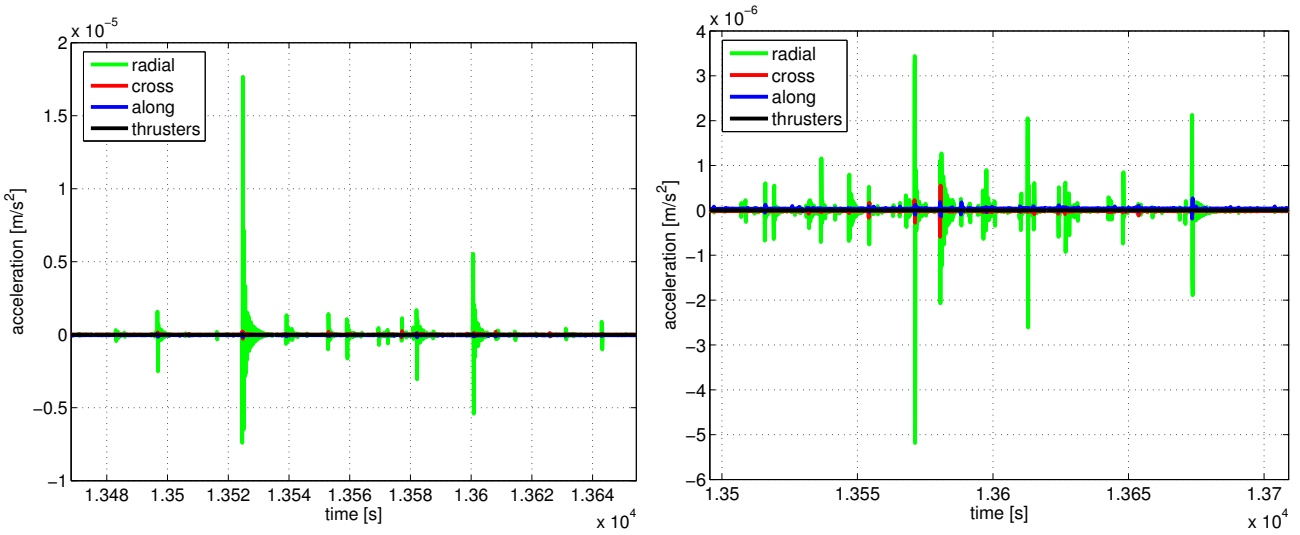

Figure 14.6: Close-up of the measured linear accelerations on GRACE A and B. The measurement is dominated by 'twangs', that are analyzed in a separate section. The twangs occur mainly on the radial component of the linear accelerations, but also on the along and cross-track components.

shows some examples of twangs. In general, they look like a damped oscillation, their duration is about 5 s, their magnitude varies from $1 \cdot 10^{-5} - 1 \cdot 10^{-7}$ m/s^2. According to Flury (2004), about 30 % of the observed radial accelerations, about 3 % of the cross-track accelerations and about 1% of the along-track observations are affected by twangs. Figure 14.8 shows the root PSD of the sample twangs. We notice that there is a maximum at about 4 Hz, that was also seen by Hudson (2003). It is assumed that the rise at low frequencies is due to the underlying acceleration signal. The relevant question is: are the twangs actual accelerations acting on the satellites or not. In Hudson (2003) it is assumed that the reason for the twangs are thermal effects of the foil that covers the bottom of the satellites. The thermal effects could consist in an expansion or contraction of the foil caused by solar illumination, that would cause vibrations of the satellite frame and thus show up in the accelerometer measurements. As the vibrations are not caused by surface forces acting on the satellite, these signals can be seen as a measurement error affecting the measurement performance. For the determination of the accelerometer performance, only periods can be used where no twangs occur.

As the foil covers the bottom of the satellites that always points towards the Earth, the Earth radiation variation could be correlated with the twang events. In order to test this hypothesis, the Earth albedo model described earlier was used to simulate long and short-wave albedo for a given GRACE orbit. The result is shown in figure 14.9. There seems to be a correlation between the maxima of the long-wave albedo, the Earth shadow exit and entry and the twang events. Considering table (5.1), one realizes that about 80 % of the IR radiation are absorbed by the bottom, i.e. are transformed into heat. At the maxima of the long-wave albedo, the foil temperature should also be increased. This seems to agree with the observation in Hudson (2003), where increased twang activity has been observed during periods of increased foil temperature. This assumption is very speculative however.

14.2.2. Peaks

Twangs are not the only disturbance visible in the acceleration measurements, that is supposedly not caused by real accelerations. Figure 14.10 shows examples of peak effects for GRACE A and B.

We notice that all axes are affected equally and that also the magnitudes are equal: about $4 - 6 \cdot 10^{-8}$ m/s^2. According to Flury et al. (2007), these effects are correlated with switches of the heating system of the satellites. They affect about 40% of the along-track measurements and about 30 % of the cross-track and radial measurements. The assumption is that the change in the current of the heater

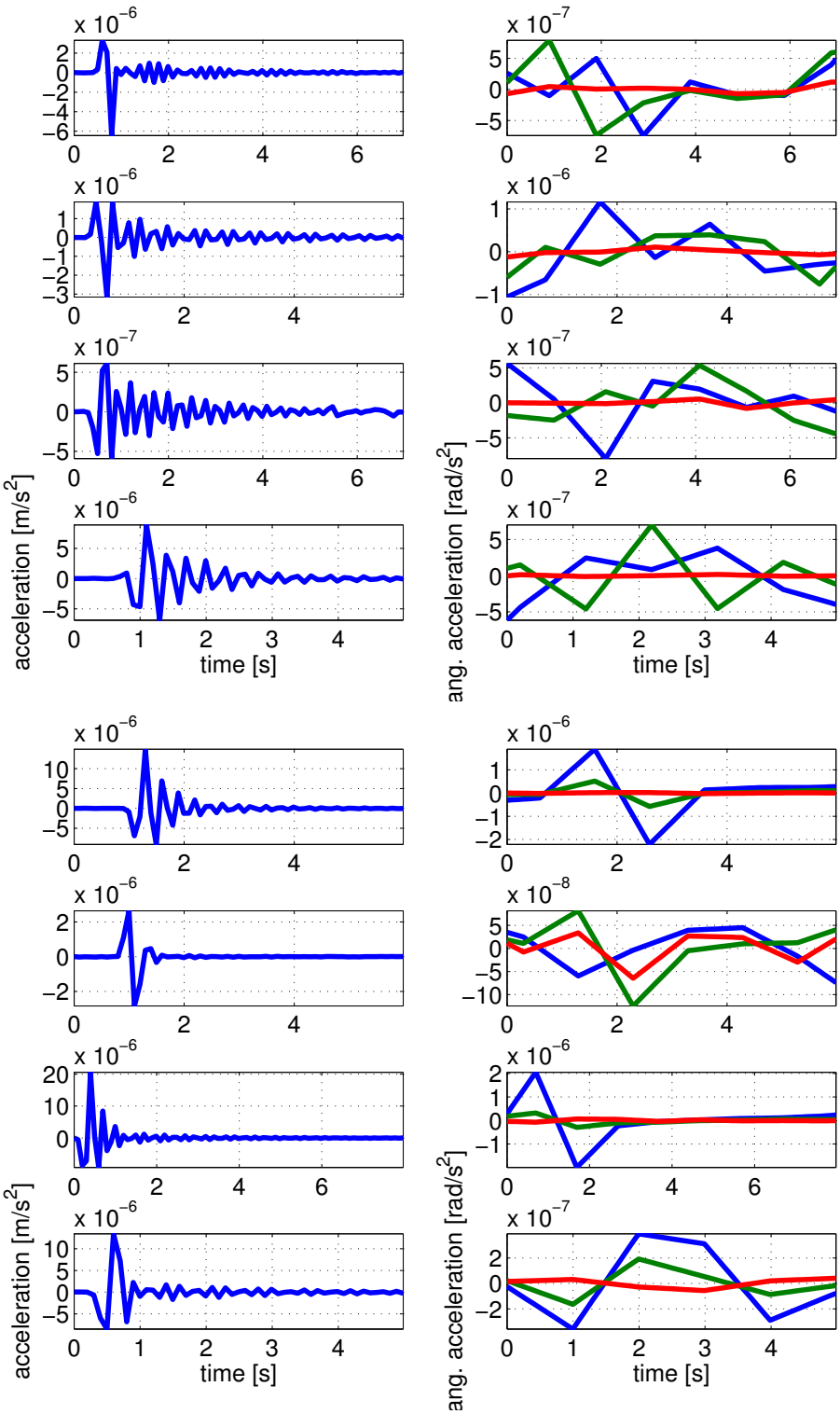

Figure 14.7: Examples for 'twangs' on GRACE A (upper three rows) and GRACE B (lower three rows). The left panels show the linear accelerations, the right panels show the angular accelerations.

circuits has an effect on the linear acceleration measurement. This would mean that the effects are again not caused by surface forces acting on the satellites and would then contribute to the measurement error budget. For the accelerometer performance determination, periods containing the peaks should not be used.

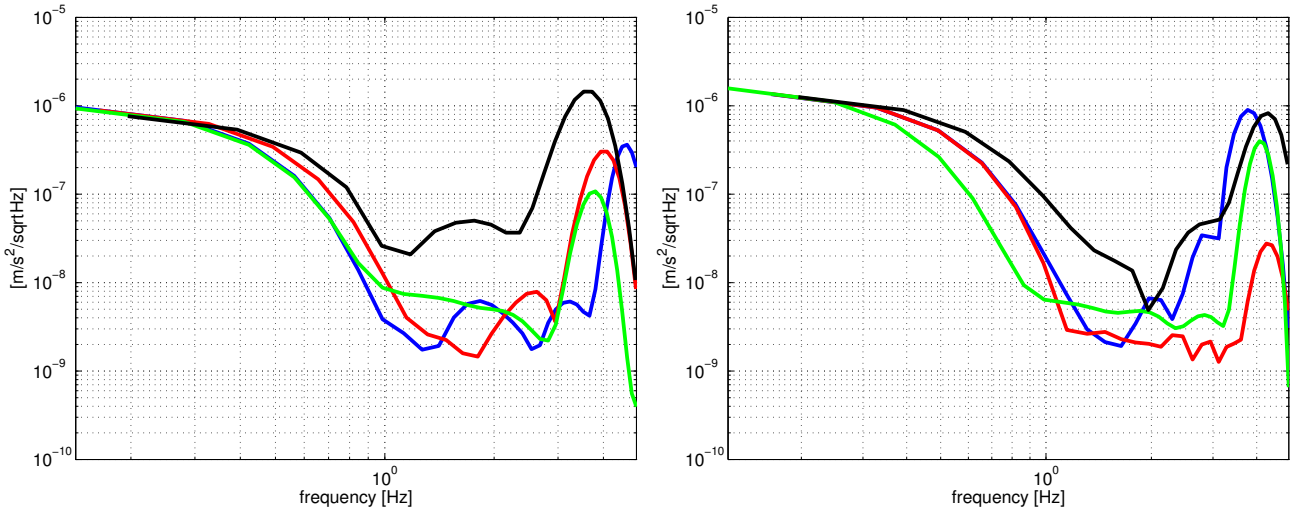

Figure 14.8: Root PSD of sample twangs. We notice a large maximum at 4 Hz, a smaller one between 1 and 2 Hz and a rise at low frequencies. The signal power is about $1 \cdot 10^{-6}\ m/s^2/\sqrt{Hz}$

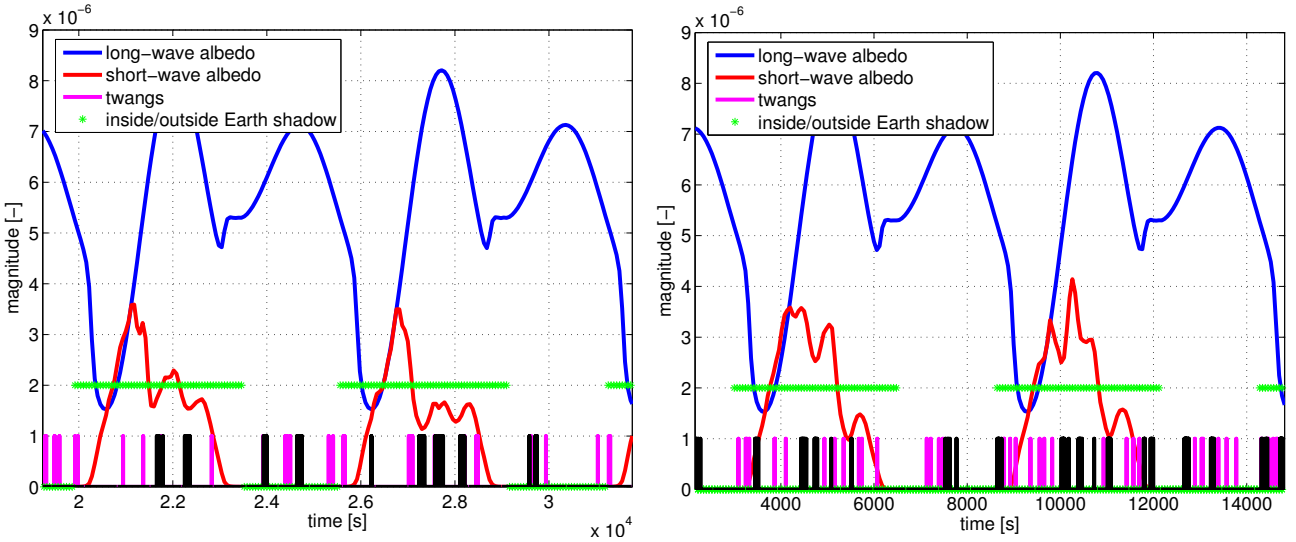

Figure 14.9: Correlation of twang events with Earth albedo for GRACE A and B. Direct albedo is the IR radiation emitted by the Earth, short-wave albedo is the radiation caused by diffuse reflection of solar radiation incident on the Earth. The satellite is outside the Earth shadow if the green stars are on the zero line.

14.2.3. Thruster events

Thruster events are part of the angular control system. Therefore thruster events map into the measured linear accelerations only if:

- the proof mass of the accelerometer is not perfectly placed in the center of mass,
- there is a misalignment between the thrusters of a thruster pair, different thrust forces or reaction times.

In the first case, the effect visible in the measurement is not caused by a real acceleration on the satellite, in the second case, there is an actual linear acceleration on the satellite. Figure 14.11 shows the time series and the root PSD of sample thruster events on GRACE A and B. The thruster events show up as a sudden spike in the accelerometer measurements. The magnitudes are about $1 - 2 \cdot 10^{-6}$ m/s^2 for

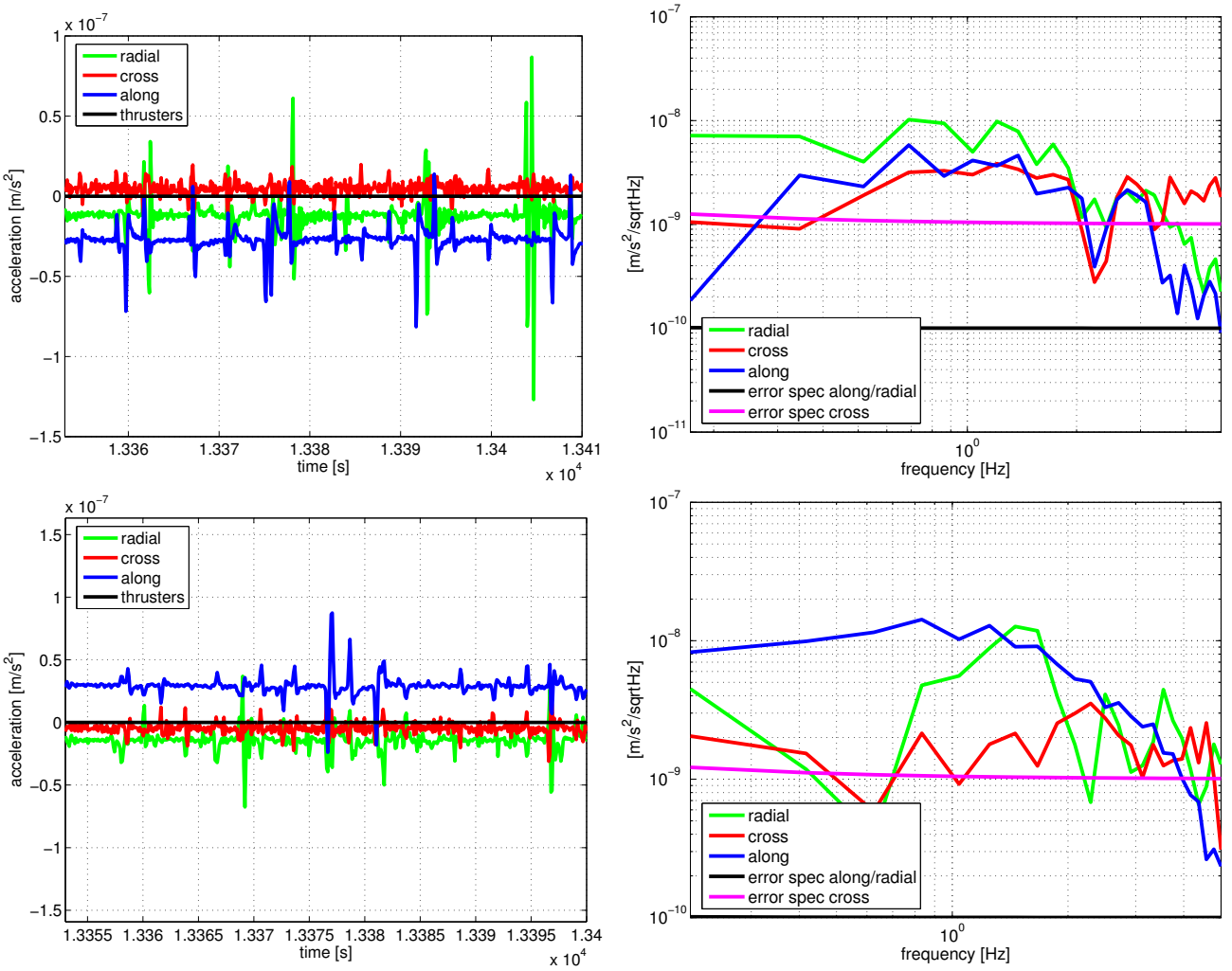

Figure 14.10: Close-up of linear acceleration measurements on GRACE A and B showing the peak effects. We notice that the effects are visible on all axes. The magnitudes seem to be equal on all axes. In the considered period no thruster events occur.

the cross-track component, followed by about $2 - 4 \cdot 10^{-7}$ m/s^2 for the radial component and about $2 - 4 \cdot 10^{-8}$ m/s^2 for the along-track component. The mass trim assembly and regular center of mass determination calibration maneuvers ensure that the offset of the center of mass of the GRACE satellites to the accelerometer proof mass stays within 100 micrometers, cf. Wang (2003). Therefore it can safely be assumed that the mapping of the thruster events into the linear accelerations is due to thruster misalignment. The measured signal then represents an actual acceleration and it is necessary that it is measured as it will be contained in the K-band measurements as well.

In order to understand not only the effect of the thruster events on high frequencies of the spectrum of the measurements, but also the long term effects, a time series of thruster events was generated from the thruster activation data of a sample day and then passed through a filter that is similar to the on-board filter that is applied in course of the analog to digital conversion process. Figure 14.12 shows the time domain representation and the root PSD of the filtered and unfiltered thruster events time series. We realize that the filter increases the interval of the thruster events and also alters the amplitudes. When we analyze the root PSD, a prominent peak at 1 Hz is visible, that is also visible in the accelerometer measurements. It seems that this peak is caused by the thruster events mapping into the linear accelerations. The thruster events occur always at the same fractional epoch, i.e. the time difference between two thruster events is an integer number of seconds. At low frequencies, the signal caused by the thruster events is white noise at a level of about $1 \cdot 10^{-8}$ m/s$^2\sqrt{\text{Hz}}$. At frequencies higher than 3 Hz, the signal amplitude is damped by the applied anti-aliasing filter.

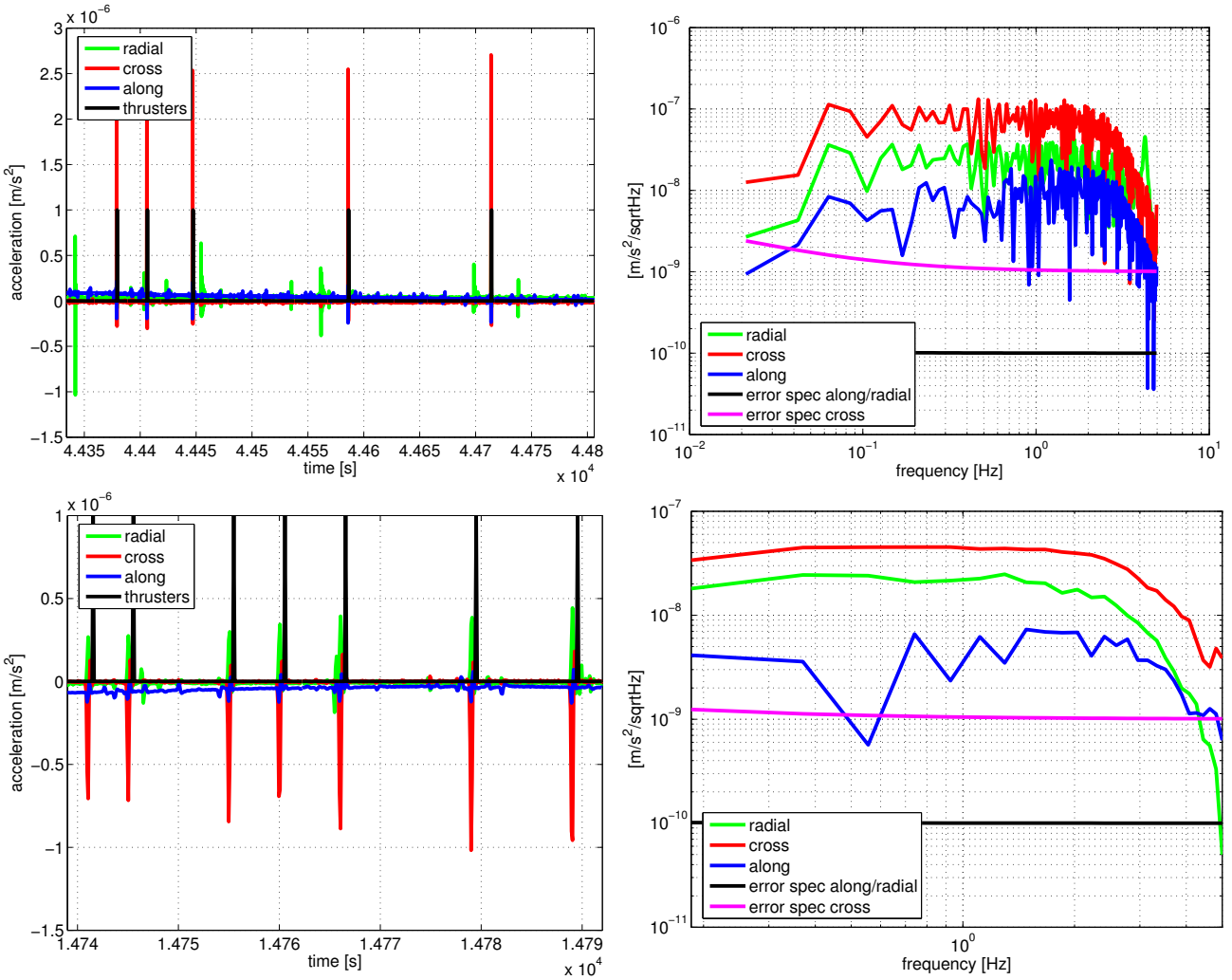

Figure 14.11: Thruster events in the time domain (left panels) and in the frequency domain (right panels) for GRACE A and B. We notice that the cross-track linear accelerations are affected most, followed by the radial linear accelerations and the along-track linear accelerations. Taking a look the root PSD, we realize that the magnitude of the effects of the thruster events range from $1 \cdot 10^{-8}\ m/s^2/\sqrt{Hz}$ to $1 \cdot 10^{-7}\ m/s^2/\sqrt{Hz}$, significantly above the error specifications of the accelerometer. The peaks in the time domain show up as horizontal lines in the frequency domain as expected. The decay starting at about 2-3 Hz is due to the on-board butterworth filter.

14.2.4. Accelerometer performance estimation

For the performance determination of the accelerometers itself, only periods where no twangs, peaks or thruster events occur can be used. The analysis of periods that supposedly are only affected by the accelerometer noise delivers the results presented in table (14.1). As for the gravity field determination the differential acceleration is needed, we present an estimate of its performance as well. It seems that the accelerometer performance on the sensitive axes (along-track and radial) is about 5 times worse than specified, the performance of the less-sensitive axes (cross-track) seems to agree with the specified performance. The performance of the differential acceleration measurement should be about $\sqrt{2}$ times the performance of the along-track components, which approximately seems to be the case, its overall performance is about two times the specified level. Of course the selected periods may be affected by other effects than only the measurement noise, so the numbers presented are only estimated and should be considered as an upper limit.

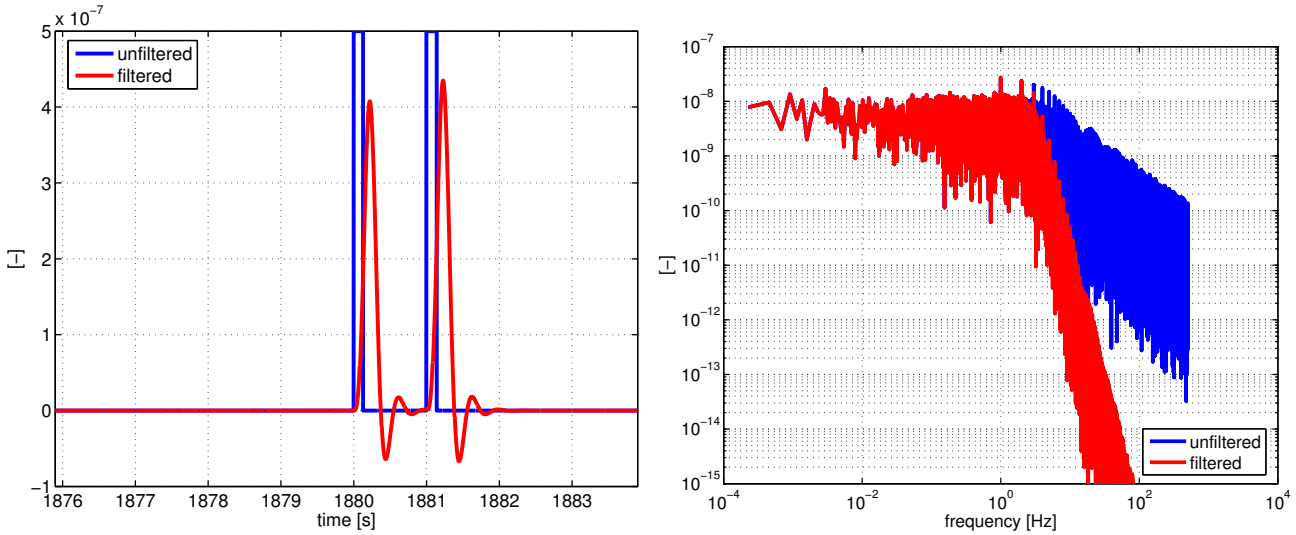

Figure 14.12: Left panel: thruster events in the time domain before and after the filtering of the on-board anti-aliasing filter. Right panel: root psd of thruster events before and after the application of the anti-aliasing filter.

Table 14.1: Estimated single accelerometer errors for GRACE A and B and estimated error of the differential acceleration measurements.

observation type	σ [m/s^2]	σ spec. [m/s^2]	PSD [m/s^2/sqrtHz]	PSD spec. [m/s^2/$\sqrt{\text{Hz}}$]
GRACE A				
along-track	$1 \cdot 10^{-09}$	$2 \cdot 10^{-10}$	$5 \cdot 10^{-10}$	$1 \cdot 10^{-10}$
cross-track	$2 \cdot 10^{-09}$	$2 \cdot 10^{-09}$	$9 \cdot 10^{-10}$	$1 \cdot 10^{-09}$
radial	$1 \cdot 10^{-09}$	$2 \cdot 10^{-10}$	$6 \cdot 10^{-10}$	$1 \cdot 10^{-10}$
GRACE B				
along-track	$9 \cdot 10^{-10}$	$2 \cdot 10^{-10}$	$4 \cdot 10^{-10}$	$1 \cdot 10^{-10}$
cross-track	$2 \cdot 10^{-09}$	$2 \cdot 10^{-09}$	$1 \cdot 10^{-09}$	$1 \cdot 10^{-09}$
radial	$1 \cdot 10^{-09}$	$2 \cdot 10^{-10}$	$6 \cdot 10^{-10}$	$1 \cdot 10^{-10}$
Differential acceleration	$1.4 \cdot 10^{-09}$	$6 \cdot 10^{-10}$	$6 \cdot 10^{-10}$	$3 \cdot 10^{-10}$

14.2.5. Linear acceleration measurement performance estimation

For the determination of the performance of the linear acceleration measurement, the differential linear acceleration is investigated, as it is used later for the gravity field determination, cf. figure 14.13. The signal looks very noisy and there seems to be no clear once per revolution signal. The order of magnitude is about $2 - 4 \cdot 10^{-7}$ m/s^2. The right panel shows the root PSD of the differential acceleration and the major constituents arising not from surface forces. We notice a peak at once per revolution that is less prominent as for the linear accelerations themselves. The signal then decreases to about $2 - 3 \cdot 10^{-2}$ Hz, where the signal seems to level out into white noise. Looking at the root PSD of the thruster events of the same day, one realizes that the thruster events seem to be responsible for the flat spectrum. The characteristic peak at 1 Hz and multiples is also caused by the thruster events. The peak effects mainly cause an effect at frequencies higher than $2 - 3 \cdot 10^{-2}$ Hz and rise to a level of about $1 \cdot 10^{-8}$ m/s^2/$\sqrt{\text{Hz}}$. At frequencies lower than $2 - 3 \cdot 10^{-2}$ Hz the peak effect is below the specified measurement accuracy. The twangs seem to affect high frequencies mainly as well. The magnitude of their effect rises to a level of about $1 \cdot 10^{-8}$ m/s^2/$\sqrt{\text{Hz}}$. At frequencies lower than $2 \cdot 10^{-1}$ Hz, the twang effect is below the specified measurement accuracy. One should also keep in mind that during the L1a to L1b processing

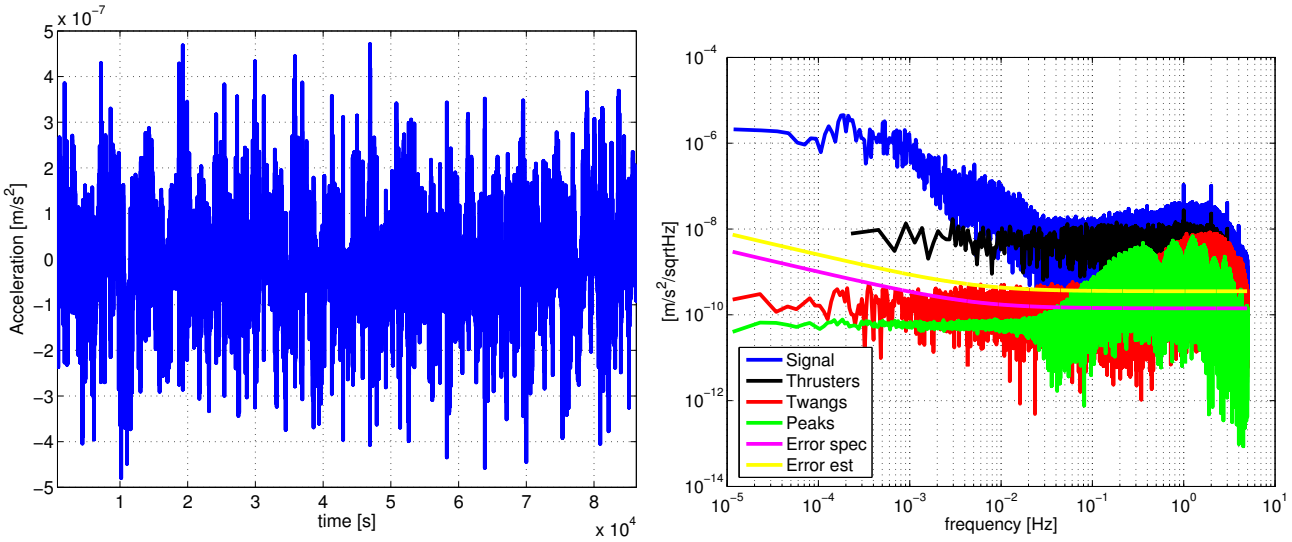

Figure 14.13: Left panel: Time series of the differential accelerations for a sample day. Right panel: Root PSD of the differential acceleration and the major constituents arising not from surface forces.

the bandwidth of the measurement is reduced to about 0.1 (5 s sampling) resp 0.5 Hz (1 s sampling). The effects visible in the differential acceleration measurement caused by the thruster events represent real accelerations, assuming the K-band measurements contain them as well, they do not contribute to the error budget of the measurement. The peak and twang effects contribute to the error budget of the measurement, as they are supposedly no real accelerations. As their influence for a 5 s sampling is below the measurement error specification, it seems that they can be neglected. For a 1 s sampling however, it seems that they would rise the measurement error to a level of about $1 \cdot 10^{-9}$ m/s$^2/\sqrt{\text{Hz}}$, so it may be worthwile to think about a way of correcting these effects. As conclusion, we can state that the performance of the linear acceleration measurement is about $6 \cdot 10^{-10}$ m/s$^2/\sqrt{\text{Hz}}$, i.e. about 2 times higher than the performance specification, if 5 s data is used. If 1 s data is used and the effects of the twangs and peaks are not corrected for, the performance is estimated to be about $1 \cdot 10^{-9}$ m/s$^2/\sqrt{\text{Hz}}$ or about 3 times the specified performance.

14.2.6. Angular accelerations

The angular accelerations are measured by forming differences between the control voltages of the individual electrode pairs and scaling the difference with the appropriate electrostatic gain that transforms from [V] to [rad/s^2].

The angular acceleration measurements will not be investigated as thoroughly as the linear acceleration measurements, as their role for the gravity field determination process is limited to the attitude determination. Figure 14.14 shows the time series of the angular acceleration measurements on GRACE A and B. We notice many spikes caused by thruster events, but also effects that are caused by the magnetic torquers. The root PSD is almost flat, apart from peaks at once and twice per revolution and at about $5 \cdot 10^{-3}$ Hz, the latter one is caused by the magnetic torquers, cf. figure 14.15. At high frequencies, the signal decreases and reaches minima at 1 Hz and multiples. This seems to be caused by the fact that the original sampling rate of the rotational accelerations is 1 Hz and not 10 Hz as for the linear acceleration measurements, cf. Bettadpur (2007). The two lower panels show the time series and root PSD of the angular accelerations measurements on GRACE B. They are similar to those on GRACE A, except for the peak at about 0.1 Hz in the root PSD of the cross-track component. Its origin is unknown. Figure 14.16) shows a close-up of the angular accelerations. The peaks are caused by thruster events.

The thruster events' effect on the angular accelerations is strongest for rotations about the along-track

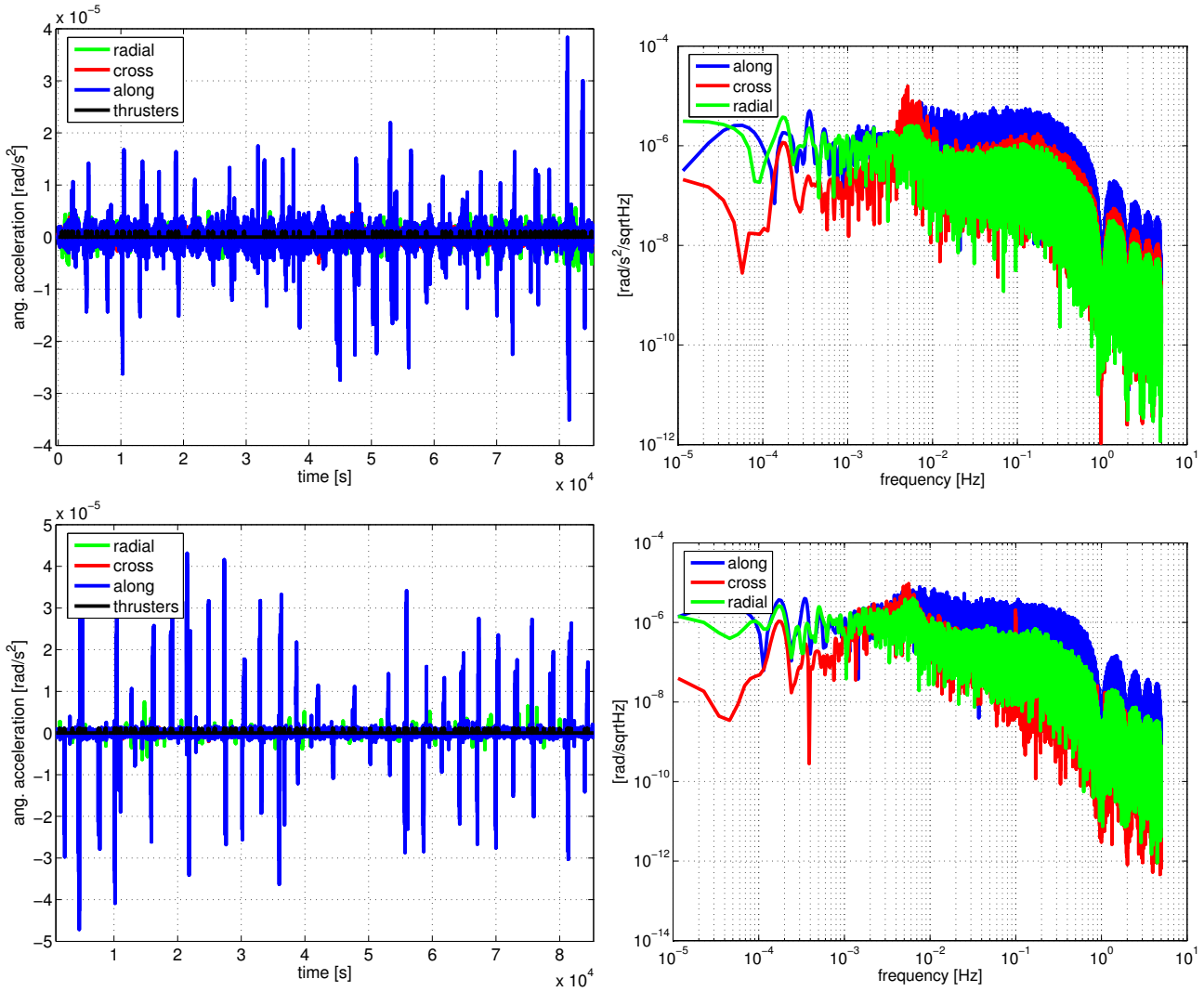

Figure 14.14: Top left panel: Time series of the rotational acceleration measurement on GRACE A. Top right panel: Root PSD of the rotational acceleration measurement on GRACE A. Bottom left panel: Time series of the rotational acceleration measurement on GRACE B. Bottom right panel: Root PSD of the rotational acceleration measurement on GRACE B.

axis, followed by the angular accelerations about the radial axis. The rotation about the cross-track axis is controlled almost entirely by the magnetic torquers, cf. table 14.2. The rotations about the cross-track and the radial axis can be controlled by the magnetic torquers due to the orientation of the magnetic field of the Earth. The magnetic torquers exert the following torque on the satellite:

$$\overline{\mathrm{T}}_m = \overline{\mathrm{D}} \times \overline{\mathrm{B}}, \tag{14.2}$$

with

$\overline{\mathrm{T}}_m$ the resulting torque,
$\overline{\mathrm{D}}$ the dipole moment of the torquer,
$\overline{\mathrm{B}}$ the field vector of the magnetic field.

The magnetic field vector is usually oriented parallel to the along-track direction, therefore most of the time only the rotations about the y- and the z-axis can be controlled by the magnetic torquers.

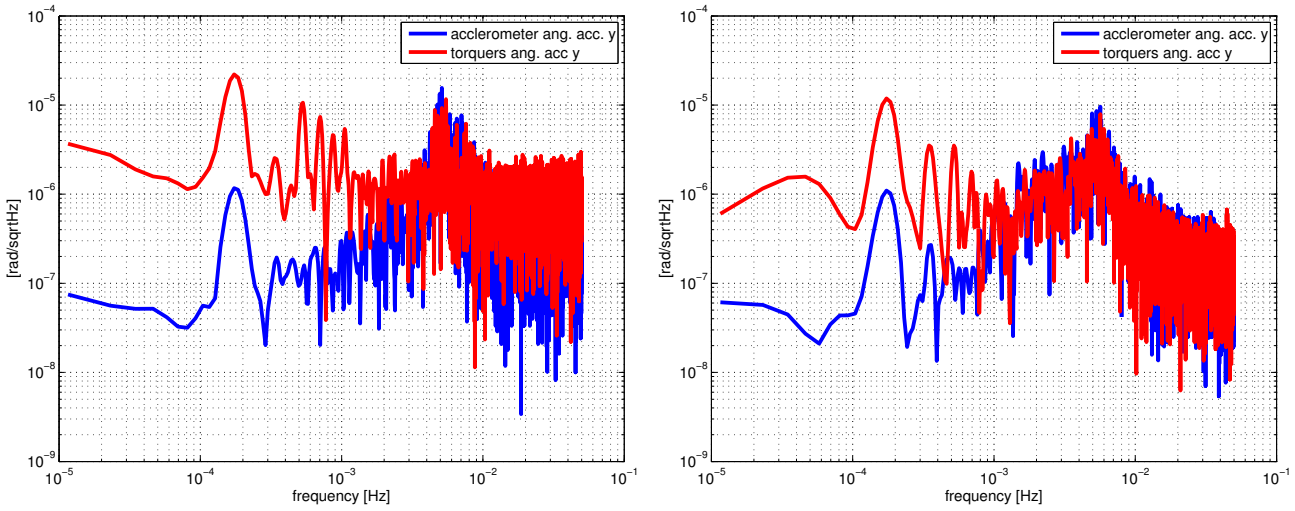

Figure 14.15: Root PSD of the angular accelerations induced by the magnetic torquers on the cross-track axis. It seems that the torquer activities are responsible for the characteristic peak at $5 \cdot 10^{-3}$ Hz. It is suspected that the discrepancy of the torquer induced angular accelerations and the measured ones results from the fact that also the surface forces and gravitational torques cause angular accelerations. The measurement is the sum of all effects.

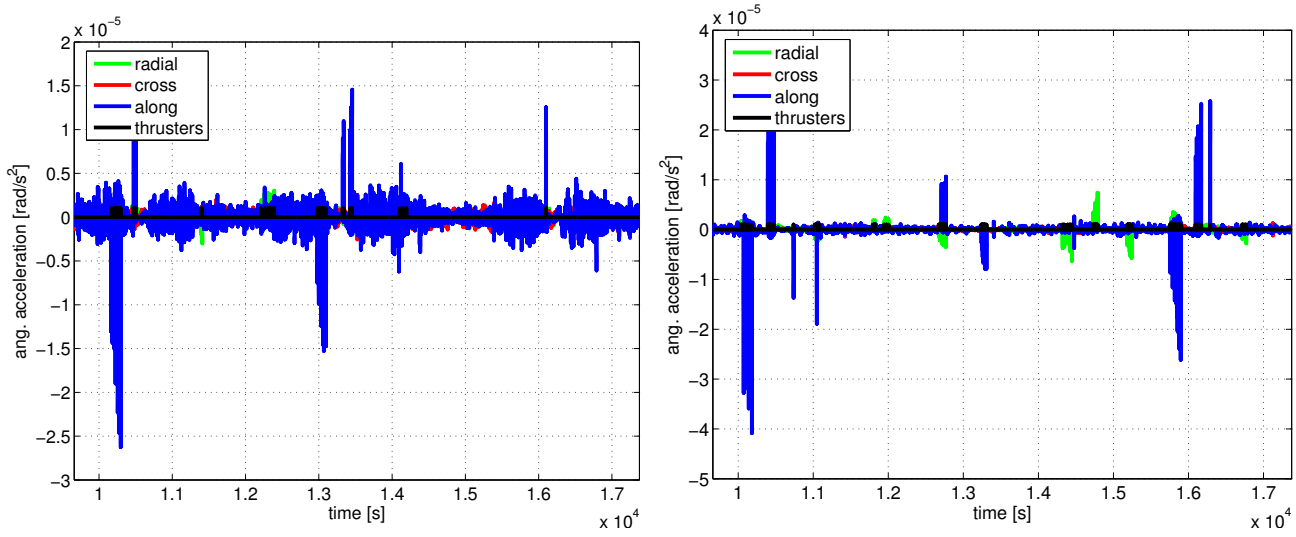

Figure 14.16: Close-up of the angular acceleration measurements. We notice that mainly the accelerations about the along-track axis are affected by thruster events, followed by the accelerations about the radial axis. The number of thruster events on the cross-track axis is significantly smaller as mainly the magnetic torquers are used to control the rotation about this axis.

Table 14.2: Thruster activation times on GRACE A and GRACE B for a sample day. Most thruster events occur on the along-track axis, followed by the radial axis and the cross-track axis. The cross-track axis is controlled by the magnetic torquers.

Thruster pair #	Rotation axis	On time [ms]
GRACE A		
1	- radial	8000
2	+ cross	50
3	+ radial	6500
4	- cross	180
5	- along	28000
6	+ along	23000
GRACE B		
1	- radial	6000
2	+ cross	30
3	+ radial	6500
4	- cross	30
5	- along	43500
6	+ along	43500

14.3. Analysis of the K-band and Ka-band ranging data

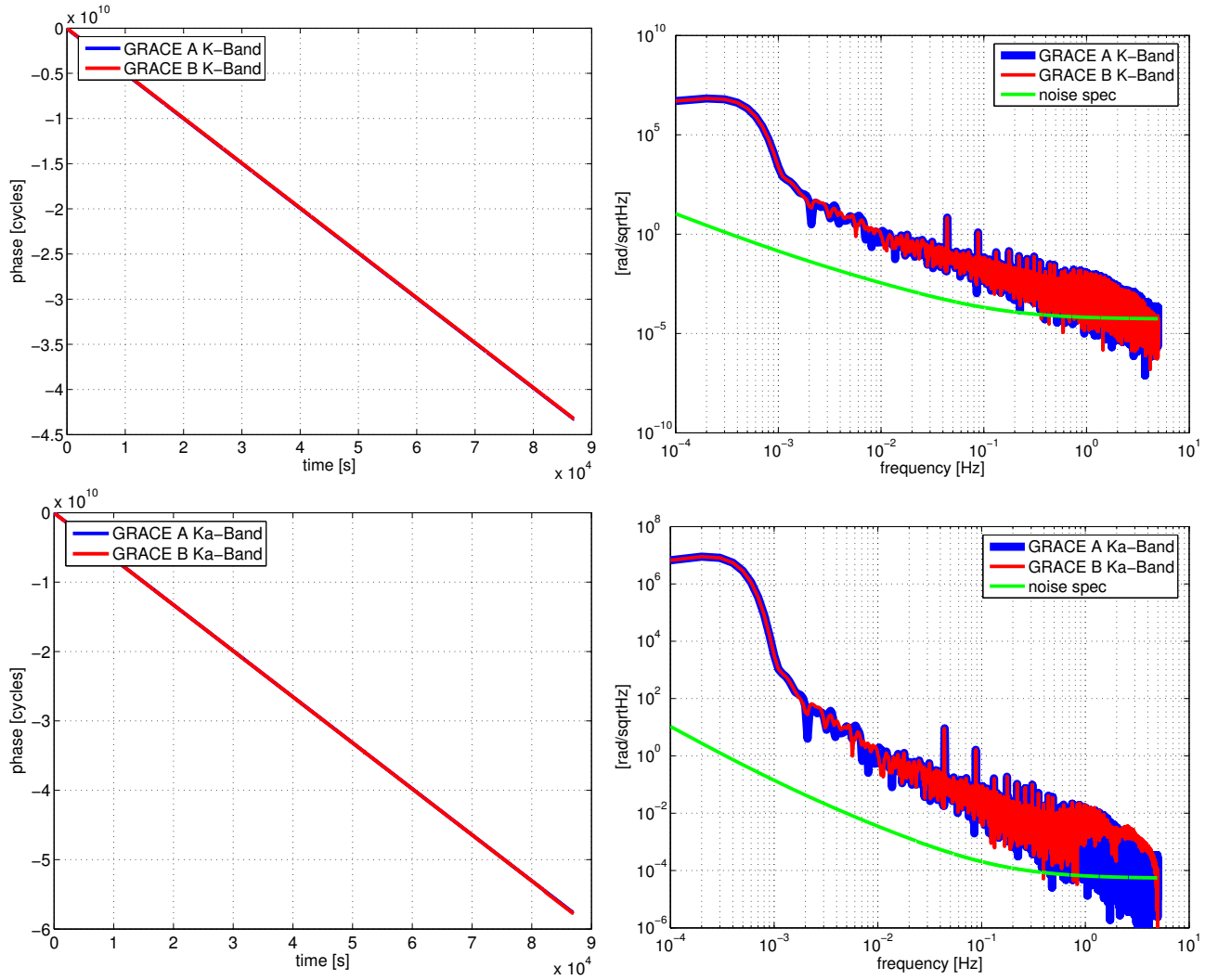

Figure 14.17: Left panels: Time series of K- and Ka-band measurements, where the receiver wrapping has been removed. As expected, the measurements look like a straight line. The contained variation due to the relative motion of the satellites is not visible. Right panels: Root PSD of the K-band and the Ka-band measurements. The green line represents the respective error specification. We notice a peak at once per revolution. As the time series, that can be analyzed, is rather short due to phase breaks, the frequency resolution is limited. At high frequencies, the root PSD should approach the error specification, but at about $4 \cdot 10^{-2}$ Hz and multiples, peaks are visible.

The K-band and Ka-band measurements are the principal measurements of the GRACE satellites. K-band and Ka-band phases are measured separately on each satellite and then combined in the ground processing to form the ionosphere-free dual one-way biased range. The phase measurement consists of the full number of incoming waves received plus the measurement of the actual phase angle, i.e. one expects that the phase measurement is a straight line, its magnitude increasing towards infinity. As the numerical resolution of the receiver is limited, a wrap around occurs when the phase measurements magnitude exceeds a certain value, meaning that the phase counter is reset to the smallest resp. largest number the receiver can represent. The wrap around value is usually an integer number of cycles, for the GRACE receivers it is 10^8 cycles. A wrap around occurs usually every 200 seconds. Figure 14.17 shows the time series and the root PSD of the phase measurements for both satellites. As expected the phase measurements are a straight line in the time domain, after the receiver wrapping is removed. But the root PSD reveals more. It shows a peak at once per revolution, but there are also peaks at $4 \cdot 10^{-2}$ Hz and multiples. In order to display this effect, the first and second time derivative of the phase measurements are investigated. Figure 14.18 shows the first derivative of the phase measurements.

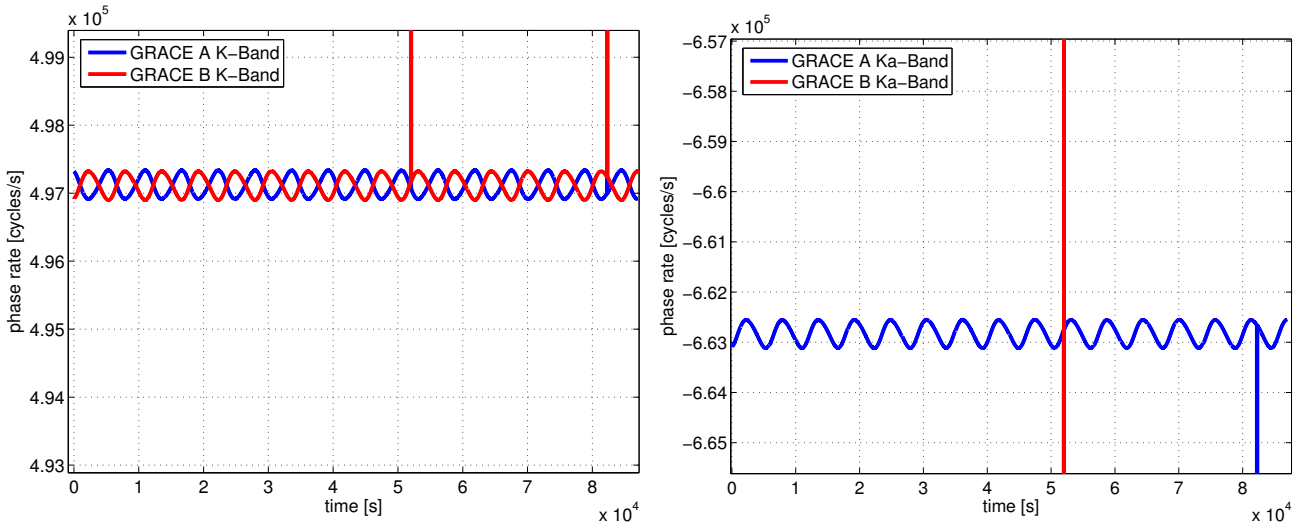

Figure 14.18: Time series of the K-band (left panel) and Ka-band (right panel) phase rate. No effect at $4 \cdot 10^{-2}$ Hz is visible.

There is no effect visible, that could cause a peak at $4 \cdot 10^{-2}$ Hz, so we take a look at the second derivative, the phase acceleration.

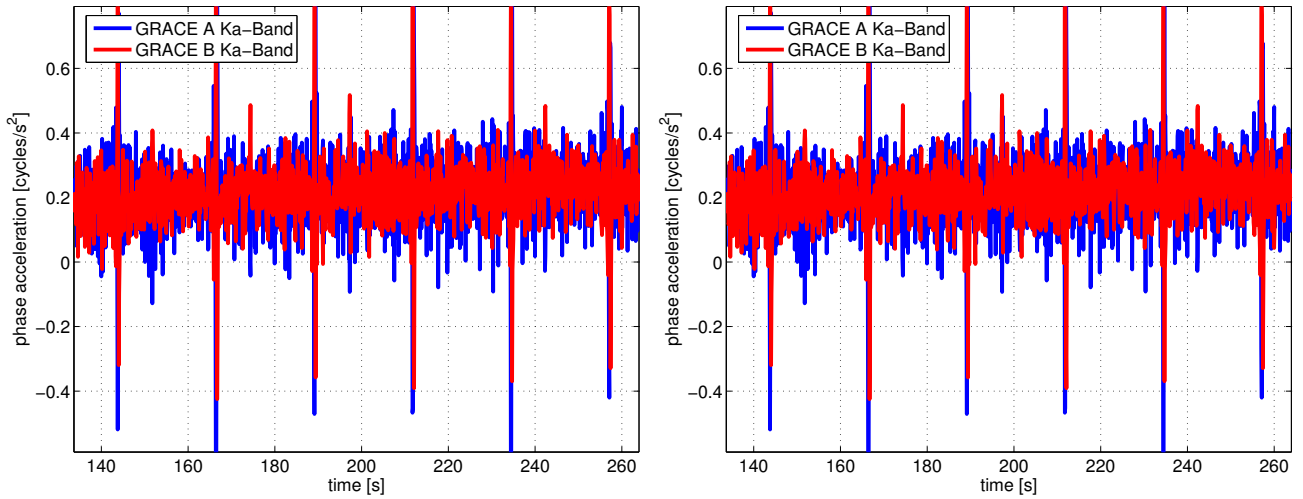

Figure 14.19: Close-up of the second derivative of the K-band and Ka-band phase measurements. The effect causing the signal at $4 \cdot 10^{-2}$ Hz is visible in the measurements of both satellites. The magnitude is identical, the sign opposite.

Figure 14.19 shows a close-up of the K-band and Ka-band phase acceleration. The effect causing the signal at $4 \cdot 10^{-2}$ Hz or every 25 seconds is visible there. It is contained in the data of both satellites on both the K-band and the Ka-band measurements. The magnitude of the effect on one band seems to be the same on both satellites, but the sign is opposite. The possible cause is a regular deviation of the USO of one satellite from its nominal frequency: A clock error will affect both, the K-band and Ka-band, as the USO drives both of them and would show up in the measurements of both satellites with opposite sign, as from the incoming phase the reference phase is subtracted.

Phase measurement performance assessment

In order to assess the performance of the phase measurements, only periods shorter than 25 seconds can be used, because of the regular clock jump contained in the measurements. The requirement of about $1 \cdot 10^{-4}$ cycles/$\sqrt{\text{Hz}}$ derived from Thomas (1999) is met for both K- and Ka-band measurements

on both satellites, actually they seem to perform slightly better. A thorough performance analysis will be conducted on the level 1b data, as there the range, range rate and range acceleration is available for analysis.

15. Level 1a to level 1b processing

In this part of the work, the processing steps from level 1a to level 1b are reviewed for each instrument and possible alternatives are evaluated. The propagation of the original instrument errors into the derived products is investigated as well, in order to yield a realistic error budget for each instrument. The processing steps and algorithms that are applied by JPL are described in Wu et al. (2006).

15.1. K-band

The principal processing steps are shown in figure 15.1. First, the time tags of the measurements have

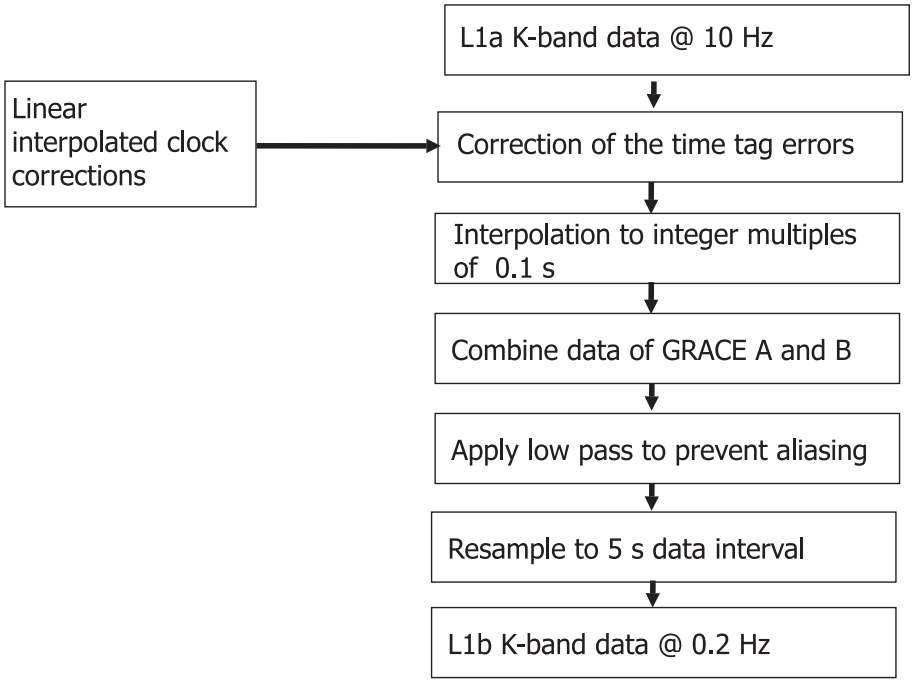

Figure 15.1: Processing steps for the derivation of L1b K-band data from L1a K-band data.

to be corrected for various effects:

- Missed interrupts,
- constant offsets,
- satellite clock errors.

Missed interrupts

Missed interrupts can occur for both K-band and Ka-band measurements on both satellites independently. If the IPU misses a hardware interrupt, it causes a constant time tag error. In the so called Sequence of Events File (SOE), the offset due to missed interrupts for both K- and Ka-band measurements is recorded.

Constant offsets

Due to a software problem in the onboard software until version 147 (cf. Wu et al. (2006)), there is an additional constant offset to be accounted for in the time tag correction.

Satellite clock errors

As the satellite clock is driven by the USO, the derived time tags are erroneous due to the frequency instability of the USO. The corresponding corrections are determined during the precise orbit determination process. The clock corrections are given typically at a sampling rate of 5 minutes and have thus to be interpolated to the corresponding measurement epochs. It is important to apply first the corrections for the missed interrupts and the constant offsets to the original time tags and then these 'corrected' time tags can be used for the interpolation.

The corrected time tags are thus derived as:

$$t_{corr} = t_{meas} + \Delta t_{mi} + \Delta t_{offset} + \Delta t_{clock}. \tag{15.1}$$

The next processing step is the interpolation to multiples of 0.1 s. The following steps are conducted:

- Unification of the receiver wrapping,
- Identification of outliers and phase breaks.

Unification of the receiver wrapping

The onboard receiver of the GRACE satellites can only store values within $\pm 10^8$ cycles. This leads to a wrap around of the phase measurements every 200 seconds. The wrap around is corrected by comparing the difference of two consecutive phase measurements against a threshold. If the threshold is reached, 10^8 cycles are either added or subtracted. The phase measurements then fulfill the condition:

$$-0.5 \cdot 10^8 \leq (\phi_n - \phi_{n-1}) \leq 0.5 \cdot 10^8. \tag{15.2}$$

Identification of outliers and phase breaks

An outlier occurs, if the measurement of a single epoch is an anomalous value. Outliers can be identified in the case of two frequency measurements by analyzing the so called 'range free' observation:

$$\phi_{test} = \phi_K - \frac{f_K}{f_{Ka}} \cdot \phi_{Ka}. \tag{15.3}$$

The phase measurements are the fractional number of received cycles. Depending on the frequency of the signal, the slope of the phase measurement varies. By scaling the Ka-band measurement to the K-band frequency, the slope of the scaled Ka-band measurements is adopted to that of the K-band measurements. The difference of the two should then be only a constant, as the individual initial phase counter values are different. Outliers are identified by comparing the first derivative to a threshold.

Phase breaks are a different matter. During a phase break, the signal is lost and the cycle counter is reset to an arbitrary value, resulting in a step in the measured data. In order to identify phase breaks, the data is separated into subsets of a certain length. The first value of the subset is selected as a reference. The difference to the other values in the chunk is formed. If the difference is larger than a threshold, starting from a certain epoch until the end of the chunk, a phase break has been identified. Again the 'range free' observation is used. As the range free observation is a combination of the K-band

and the Ka-band observation, it can not be identified if the outlier or phase break occurs in both bands. In order to correct for the effects of the ionosphere, a ionosphere free linear combination of the K-band and Ka-band observables has to be formed at a later stage. Therefore always both measurements have to be available.

As a next step, the data from GRACE A and B is combined through the following substeps:

- Derivation of the DOWR for K- and Ka-band,
- elimination of the influence of the ionosphere.

Derivation of the DOWR for K- and Ka-band

In order to derive the dual one way range, the phase measurements of the same band from both satellites are added. We continue from equation (10.12):

$$\begin{aligned}\Phi_{AB} = \phi_A^B + \phi_B^A &= \bar{\phi}_A(t) - \bar{\phi}_B(t) + f_B \cdot \tau_A^B + \epsilon_{uso}^A + \epsilon_{system}^A + N_A^B + I_A^B + d_A^B \\ &+ \bar{\phi}_B(t) - \bar{\phi}_A(t) + f_A \cdot \tau_B^A + \epsilon_{uso}^B + \epsilon_{system}^B + N_B^A + I_B^A + d_B^A \\ &= (f_B \cdot \tau_A^B + f_A \cdot \tau_B^A) + (\epsilon_{uso}^A + \epsilon_{uso}^B) + (\epsilon_{system}^A + \epsilon_{system}^B) \\ &+ (N_A^B + N_B^A) + (I_A^B + I_B^A) + (d_A^B + d_B^A). \end{aligned} \tag{15.4}$$

Note that f_A and f_B are either the K-band or the Ka-band frequency of satellite A or B, i.e. the formulation is applicable to both the K-band and the Ka-band measurements. We notice that the phases themselves cancel out and that, as the measurement, the frequencies times the transmission time remain plus the sums of the individual error terms. The sum of the phase measurements is still a phase measurement. To transform it into a range measurement, the following step is necessary, cf. Kim (2000):

$$R_{AB} = \frac{c}{f_A + f_B} \cdot \Phi_{AB}. \tag{15.5}$$

Let us take a closer look at the range term and neglect the error terms for the time being:

$$R_{AB} = \frac{c}{f_A + f_B} \cdot (f_B \cdot \tau_A^B + f_A \cdot \tau_B^A) = \frac{1}{f_A + f_B} \cdot (f_B \cdot \rho_A^B + f_A \cdot \rho_B^A). \tag{15.6}$$

The range ρ_A^B is the magnitude of the vector between the position of satellite B at the epoch $t - \tau_A^B$ and the position of the satellite A at epoch t, the range ρ_B^A is the magnitude of the vector between the position of satellite A at the epoch $t - \tau_B^A$ and the position of satellite B at epoch t. Both differ from the range ρ between the positions at epoch t, the so called 'instantaneous range', that is the observable desired for the gravity field determination. ρ_A^B is too short, as satellite B is moving towards the signal emitted by satellite A during the measurement, ρ_B^A is too long, as satellite A is moving away from the signal emitted by satellite B. Figure 15.2 shows the geometric situation between the instantaneous range and the measured ranges. In order to derive the instantaneous range, a straightforward idea would be

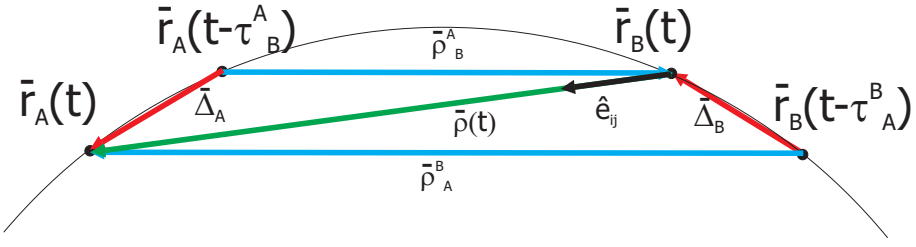

Figure 15.2: Geometric relations between the instantaneous Range and the measured ranges from Kim (2000).

to directly derive it using GPS derived positions. The position accuracy of the GPS based GRACE orbits are on the level of about 1 cm, cf. Kim (2000), and therefore not accurate enough to be used directly. Using the geometric situation, we can define the measured ranges as:

$$\rho_B^A = \sqrt{(\overline{\rho} - \overline{\Delta}_A)^T \cdot (\overline{\rho} - \overline{\Delta}_A)}, \tag{15.7}$$

$$\rho_A^B = \sqrt{(\overline{\rho} + \overline{\Delta}_B)^T \cdot (\overline{\rho} + \overline{\Delta}_B)}. \tag{15.8}$$

The vectors $\bar{\Delta}_A$ and $\bar{\Delta}_B$ are the position differences between the satellites positions at the sending epochs $t - \tau_B^A$ resp. $t - \tau_A^B$ and the nominal epoch t. In reality, their magnitude is about 15 m compared to a mean distance between the satellites of 200 km. The right hand side can be expanded into a Taylor series around $\bar{\Delta}_A = 0$, resp. $\bar{\Delta}_B = 0$:

$$\begin{aligned}
\rho_B^A &= \sqrt{\rho^2} + \frac{\partial}{\partial \overline{\Delta}_A} \left[\sqrt{(\overline{\rho} - \overline{\Delta}_A)^T \cdot (\overline{\rho} - \overline{\Delta}_A)} \right]_{\overline{\Delta}_A = 0} \cdot \overline{\Delta}_A \\
&= \rho + \left[\frac{\frac{1}{2} \cdot 2 \cdot (\overline{\rho} - \overline{\Delta}_A) \cdot -1}{\sqrt{(\overline{\rho} - \overline{\Delta}_A)^T \cdot (\overline{\rho} - \overline{\Delta}_A)}} \right]_{\overline{\Delta}_A = 0} \cdot \overline{\Delta}_A \\
&= \rho - \frac{\overline{\rho}}{\rho} \cdot \overline{\Delta}_A \\
&= \rho - \widehat{\mathrm{e}}_{AB} \cdot \overline{\Delta}_A, \qquad (15.9) \\
\rho_A^B &= \rho + \widehat{\mathrm{e}}_{AB} \cdot \overline{\Delta}_B. \qquad (15.10)
\end{aligned}$$

The displacement vectors $\bar{\Delta}_A$ and $\bar{\Delta}_B$ can be approximated using the satellite velocity vectors:

$$\bar{\Delta}_A = \dot{\bar{\mathrm{r}}}_A \cdot \tau_B^A, \tag{15.11}$$

$$\bar{\Delta}_B = \dot{\bar{\mathrm{r}}}_B \cdot \tau_A^B. \tag{15.12}$$

So we get for the measured range:

$$\begin{aligned}
R_{AB} &= \frac{1}{f_A + f_B} \cdot (f_B \cdot \rho_A^B + f_A \cdot \rho_B^A) \\
&= \frac{1}{f_A + f_B} \cdot \left(f_B \cdot (\rho + \widehat{\mathrm{e}}_{AB} \cdot \dot{\bar{\mathrm{r}}}_B \cdot \tau_A^B) + f_A \cdot (\rho - \widehat{\mathrm{e}}_{AB} \cdot \dot{\bar{\mathrm{r}}}_A \cdot \tau_B^A) \right) \\
&= \rho - \left(\frac{f_A}{f_A + f_B} \cdot \widehat{\mathrm{e}}_{AB} \cdot \dot{\bar{\mathrm{r}}}_A \cdot \tau_B^A - \frac{f_B}{f_A + f_B} \cdot \widehat{\mathrm{e}}_{AB} \cdot \dot{\bar{\mathrm{r}}}_B \cdot \tau_A^B \right) \\
&= \rho - \Delta R_{ttc}, \\
\Rightarrow \rho &= R_{AB} + \Delta R_{ttc}, \qquad (15.13) \\
\widehat{\mathrm{e}}_{AB} &= \frac{\bar{\mathrm{r}}_B - \bar{\mathrm{r}}_A}{|\bar{\mathrm{r}}_B - \bar{\mathrm{r}}_A|}. \qquad (15.14)
\end{aligned}$$

In order to derive the instantaneous range ρ, we have to add the transmission time correction ΔR_{ttc} to the measured range R_{AB}. The transmission time correction has to be derived from positions and velocities derived in the precise orbit determination. These quantities can be seen as observations with a corresponding observation error. We will now estimate the magnitude of the error using the assumptions about the quality of the derived positions and velocities displayed in table 15.1.

In order to estimate the magnitude of the error, it is assumed that $f_A = f_B$. So we get for the error of the transmission time correction:

$$\begin{aligned}
\delta \Delta R_{ttc} &\simeq 2 \cdot \frac{1}{2} \cdot \left(\delta \widehat{\mathrm{e}}_{AB} \cdot |\dot{\bar{\mathrm{r}}}_B| \cdot |\tau_A^B| + |\widehat{\mathrm{e}}_{AB}| \cdot \delta \dot{\bar{\mathrm{r}}}_B \cdot |\tau_A^B| + |\widehat{\mathrm{e}}_{AB}| \cdot |\dot{\bar{\mathrm{r}}}_B| \cdot \delta \tau_A^B \right) \qquad (15.15) \\
&\simeq 2 \cdot \frac{1}{2} \cdot \left(8.0 \cdot 10^{-7} + 2.0 \cdot 10^{-7} + 1.0 \cdot 10^{-14} \right) \mathrm{m} \\
&\leq 1.0\ \mu\mathrm{m}.
\end{aligned}$$

Table 15.1: Magnitudes and accuracies of the input quantities used for the derivation of the transmission time correction.

quantity	magnitude	accuracy (σ)
line of sight unit vector $\widehat{\mathrm{e}}_{AB}$	1.0	$< 5.0 \cdot 10^{-8}$
velocity of satellite A,B $\dot{\mathrm{r}}_{A,B}$	< 7700 m/s	$< 0.1 \cdot 10^{-3}$ m/s
transmission time $\tau_{A,B}^{A,B}$	$< 2 \cdot 10^{-3}$ s	$< 1 \cdot 10^{-11}$ s

As the error is below the micrometer level, it is assumed that the correction can be derived in post processing with sufficient accuracy. It can be neglected in the error model. The transmission time correction we derived differs from the one given in Kim (2000). There, the range rate derived from GPS observations is used. The formulation provided here has the advantage that it is based on quantities that are given in the L1b orbit files (GNV1B).

The transmission times are derived using the given positions and velocities: From the positions at the nominal epochs, a transmission time is derived. Using the given velocities and the transmission time, a new position is derived and so on. This iterative procedure converges very fast, as the velocity of the satellites is relatively small compared to the velocity of light.

Let us now take a closer look at the range noise resulting from the USO noise. The resulting range noise is the sum of the USO noise given in equation (10.16):

$$\begin{aligned}
\delta R_{uso} &= \frac{c}{f_A + f_B} \cdot (\varepsilon_{uso}^A + \varepsilon_{uso}^B) \\
&= \frac{c}{f_A + f_B} \cdot \left[\left(1 - \frac{f_A - f_B}{f_A} - \frac{\delta f_A - \delta f_B}{f_A} \right) \cdot \delta\phi_A(t) - \delta\phi_B(t) + \delta f_B \cdot \tau_A^B \right. \\
&+ \left. \left(1 - \frac{f_B - f_A}{f_B} - \frac{\delta f_B - \delta f_A}{f_B} \right) \cdot \delta\phi_B(t) - \delta\phi_A(t) + \delta f_A \cdot \tau_B^A \right] \\
&= \frac{c}{f_A + f_B} \cdot \left[\left(-\frac{f_A - f_B}{f_A} - \frac{\delta f_A - \delta f_B}{f_A} \right) \cdot \delta\phi_A(t) + \delta f_B \cdot \tau_A^B \right. \\
&+ \left. \left(-\frac{f_B - f_A}{f_B} - \frac{\delta f_B - \delta f_A}{f_B} \right) \cdot \delta\phi_B(t) + \delta f_A \cdot \tau_B^A \right] . \qquad (15.16)
\end{aligned}$$

It is noteworthy that the combination of the two phase measurements eliminates the direct influence of the phase error; only the phase error scaled by the carrier frequency difference, the phase error scaled by the frequency error and the frequency error scaled by the transmission time remains. As shown in figure 10.4, the contribution of the phase error scaled by the frequency error can be neglected without loss of generality. In addition, we neglect the difference in the times of flight. We examine now the range error due to one oscillator:

$$\delta R_{uso} = \frac{c}{f_A + f_B} \cdot \left(\delta f \cdot \tau - \frac{f_A - f_B}{f_A} \cdot \delta\phi \right) . \qquad (15.17)$$

In analogy to Kim (2000) and Thomas (1999), we can now derive the transfer function $G(f)$ from the oscillator phase noise to the range noise, i.e. we examine the influence of the derivation of the range on the resulting range error. A transfer function is defined as the ratio of the spectrum of the output and

the spectrum of the input, in our case the ratio of the spectra of the range noise and the phase noise:

$$\begin{aligned}
\sqrt{G(f)} &= \frac{\mathcal{F}(\delta R_{uso})}{\mathcal{F}(\delta\phi)} \\
&= \frac{\mathcal{F}\left[\frac{c}{f_A+f_B}\cdot\left(\delta f\cdot\tau-\frac{f_A-f_B}{f_A}\cdot\delta\phi\right)\right]}{\mathcal{F}(\delta\phi)} && (15.18)\\
&= \frac{c}{f_A+f_B}\cdot\left[\frac{\mathcal{F}(\delta\dot{\phi})\cdot\tau-\frac{f_A-f_B}{f_A}\cdot\mathcal{F}(\delta\phi)}{\mathcal{F}(\delta\phi)}\right] && (15.19)\\
&= \frac{c}{f_A+f_B}\cdot\left[\frac{i2\pi f\cdot\mathcal{F}(\delta\phi)\cdot\tau-\frac{f_A-f_B}{f_A}\cdot\mathcal{F}(\delta\phi)}{\mathcal{F}(\delta\phi)}\right] && (15.20)\\
&= \frac{c}{f_A+f_B}\left[\frac{f_B}{f_A}-(1-i2\pi f\cdot\tau)\right], && (15.21)
\end{aligned}$$

which is identical to the formulation given by Kim (2000) and Thomas (1999), they give for the transfer function:

$$\sqrt{G(f)}=\frac{c}{f_A+f_B}\left[\frac{f_B}{f_A}-(e^{-i2\pi f\cdot\tau})\right]. \tag{15.22}$$

As τ is very small ($< 1\cdot10^{-3}$) and the considered frequency range is below 5 Hz, the exponential function can be approximated as

$$e^{-ix}=\cos(x)-i\sin(x)=1-ix. \tag{15.23}$$

Insertion yields then

$$\sqrt{G(f)}=\frac{c}{f_A+f_B}\left[\frac{f_B}{f_A}-(1-i2\pi f\cdot\tau)\right], \tag{15.24}$$

which is identical to the result we derived. The transfer function for the oscillator error PSD is the square of the transfer function for the spectrum, so we get for the range error PSD due to the oscillator noise, assuming the same phase noise for both satellites:

$$\begin{aligned}
S_{\delta R_{uso}} &= 2\cdot G(f)\cdot S_{\delta\phi}^{f_{K/Ka}} \\
&= 2\cdot\left(\frac{c}{f_A+f_B}\right)^2\cdot\left[\frac{f_B}{f_A}-(1-i2\pi f\cdot\tau)\right]^2\cdot S_{\delta\phi}^{f_{K/Ka}}. && (15.25)
\end{aligned}$$

If the time tag errors of both satellite clocks are corrected and thus the time scales of the satellites are synchronized to a common time scale like the IGS time scale, the time tag error difference can assumed to be zero, meaning that in the above equation the frequencies f_B and f_A can be assumed to be identical:

$$\begin{aligned}
f_A &= f_B \quad \text{and} \\
S_{\delta R_{uso}} &= 2\cdot\left(\frac{c}{f_A+f_B}\right)^2\cdot[1-(1-i2\pi f\cdot\tau)]^2\cdot S_{\delta\phi}^{f_{K/Ka}} \\
&= 2\cdot\left(\frac{c}{f_A+f_B}\right)^2\cdot[+(i2\pi f\cdot\tau)]^2\cdot S_{\delta\phi}^{f_{K/Ka}}. && (15.26)
\end{aligned}$$

For error simulations, we may neglect the frequency offset $\Delta f=f_A-f_B$ and assume $f_A=f_B$, but only for the $\frac{c}{f_A+f_B}$ term. Then the expressions of the range error due to the oscillator noise simplify to:

$$\begin{aligned}
S_{\delta R_{uso}} &= \left(\frac{c}{\sqrt{2}\cdot f_{K/Ka}}\right)^2\cdot\left[\frac{f_B}{f_A}-(1-i2\pi f\cdot\tau)\right]^2\cdot\left(\frac{f_{K/Ka}}{2\pi\cdot f_o}\right)^2 S_{\delta\phi} \\
&= \left(\frac{c}{\sqrt{2}\cdot 2\pi\cdot f_o}\right)^2\cdot\left[\frac{f_B}{f_A}-(1-i2\pi f\cdot\tau)\right]^2\cdot S_{\delta\phi}, && (15.27)
\end{aligned}$$

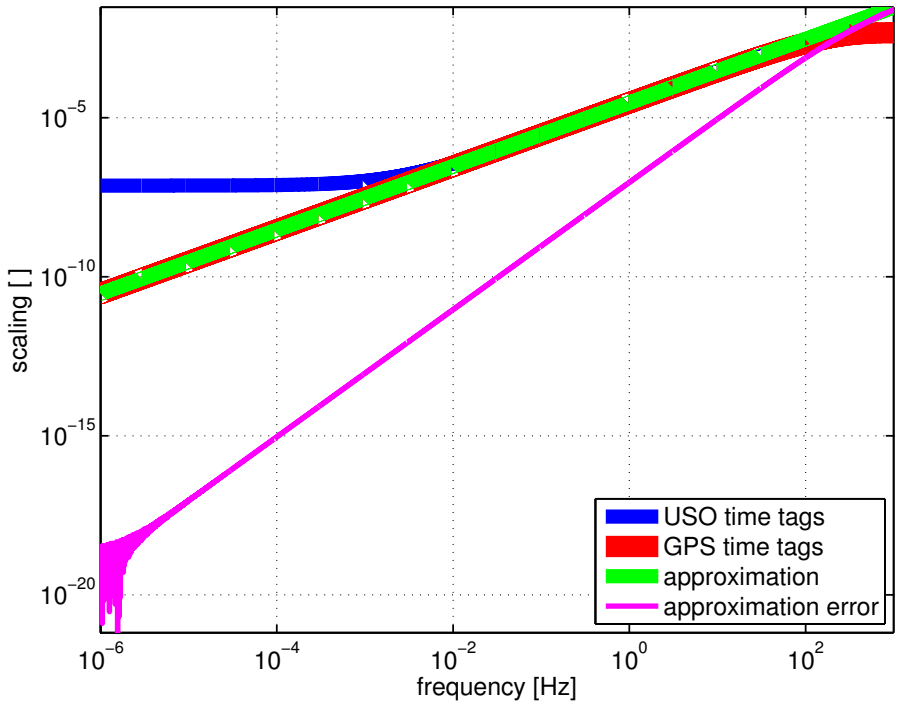

Figure 15.3: Transfer function that is applied to the oscillator phase noise by the combination of the phase measurements of the individual satellites. The pink curve shows the error of the approximate form of the transfer function.

for the use of USO time tags and

$$S_{\delta R_{uso}} = \left(\frac{c}{\sqrt{2} \cdot 2\pi \cdot f_o}\right)^2 \cdot [+(i2\pi f \cdot \tau)]^2 \cdot S_{\delta\phi}, \tag{15.28}$$

for the use of GPS time tags, i.e. in this approximated form the range error due to oscillator noise is the same for both K-band and Ka-band measurements, which is important in the next processing step.

Figure 15.3 shows the transfer function that is applied to the oscillator noise by the combination of the phase measurements for the use of USO time tags and for the use of GPS derived time tags. We notice that the combination reduces the phase noise substantially at low frequencies. The reduction is much stronger, if GPS derived time tags are used, i.e. the time tag errors of the satellites are derived in the course of the orbit determination. In this case only the frequency error remains. Therefore the transfer function is a straight line corresponding to $2\pi f$. If the USO time tags are used, the transfer function converges to f_B/f_A at low frequencies. We also notice that the quality of the approximated transfer function is sufficient for the purpose of error simulations. Regardless which time tags are used, the reduction of the phase error is significant and without this reduction the quality of the phase measurements would be degraded at low frequencies. For the real data processing the GPS time tags will be applied; therefore the corresponding error will be used subsequently.

Elimination of the influence of the ionosphere

After the previous processing step, we have now derived a range for each the K-band and the Ka-band. The advantage of a two frequency measurement is that the influence of the ionosphere can be eliminated.

The phase delay due to the influence of the ionosphere is given by

$$I_A = \frac{TEC_B^A}{f_B}, \tag{15.29}$$

for the received signal at satellite A. In principal the TEC is different for both satellite signals, as they move during the measurement, but we will neglect this small effect here, so we can say that:

$$TEC_B^A = TEC_A^B. \tag{15.30}$$

For the range error due to ionosphere we get:

$$\begin{aligned} \delta R_{iono} &= \frac{c}{f_A + f_B} \cdot \left(\frac{TEC}{f_A} + \frac{TEC}{f_B} \right) \\ &= \frac{c}{f_A + f_B} \cdot \left((f_A + f_B) \cdot \frac{TEC}{f_A \cdot f_B} \right) \\ &= c \cdot \frac{TEC}{\bar{f}^2}, \qquad \text{where} \qquad \bar{f}^2 = f_A \cdot f_B. \end{aligned} \tag{15.31}$$

f is either the K-band or the Ka-band effective frequency. Reconsidering eq. (15.29) we see that

$$I_K = \frac{TEC}{\bar{f}_K^2}, \tag{15.32}$$

$$I_{Ka} = \frac{TEC}{\bar{f}_{Ka}^2}. \tag{15.33}$$

So there is a relation between I_K and I_{Ka},

$$I_K = \frac{\bar{f}_{Ka}^2}{\bar{f}_K^2} \cdot I_{Ka}, \tag{15.34}$$

that enables us to form the so called 'ionosphere free' linear combination:

$$R = \frac{\bar{f}_K^2 \cdot R_K - \bar{f}_{Ka}^2 R_{Ka}}{\bar{f}_K^2 - \bar{f}_{Ka}^2}. \tag{15.35}$$

Insertion yields:

$$\begin{aligned} R &= \frac{1}{(\bar{f}_K^2 - \bar{f}_{Ka}^2)} \cdot \Big[(\bar{f}_K^2 - \bar{f}_{Ka}^2) \cdot \rho - (\bar{f}_K^2 \cdot \Delta R_{tof}^K - \bar{f}_{Ka}^2 \cdot \Delta R_{tof}^{Ka}) \\ &+ (\bar{f}_K^2 \cdot \frac{\bar{f}_{Ka}^2}{\bar{f}_K^2} \cdot I_{Ka} - \bar{f}_{Ka}^2 \cdot I_{Ka}) + (\bar{f}_K^2 - \bar{f}_{Ka}^2) \cdot \delta R_{uso} + (\bar{f}_K^2 \cdot \delta R_{system}^K - \bar{f}_{Ka}^2 \cdot \delta R_{system}^{Ka}) \Big] \\ &= \rho - \Delta R_{ttc}^{iono\_free} + \delta R_{uso} + \frac{(\bar{f}_K^2 \cdot \delta R_{system}^K - \bar{f}_{Ka}^2 \cdot \delta R_{system}^{Ka})}{(\bar{f}_K^2 - \bar{f}_{Ka}^2)}, \end{aligned} \tag{15.36}$$

with

$$\Delta R_{ttc}^{iono\_free} = (\bar{f}_K^2 \cdot \Delta R_{ttc}^K - \bar{f}_{Ka}^2 \cdot \Delta R_{ttc}^{Ka}), \tag{15.37}$$

the for the effect of the ionosphere corrected transmission time correction. The oscillator noise passes the ionosphere correction unaffected, as it is independent of the carrier frequency using the above described simplifications.

Let us now take a closer look at the range error due to the system noise:

$$\delta R_{system} = \frac{(\bar{f}_K^2 \cdot \delta R_{system}^K - \bar{f}_{Ka}^2 \cdot \delta R_{system}^{Ka})}{(\bar{f}_K^2 - \bar{f}_{Ka}^2)}. \tag{15.38}$$

For the error PSD for both satellites, assuming the same system noise, we get:

$$\begin{aligned} S_{\delta R_{system}} &= 2 \cdot \frac{\left[(f_K^2)^2 \cdot \left(\frac{c}{2 \cdot f_K} \right)^2 + (f_{Ka}^2)^2 \cdot \left(\frac{c}{2 \cdot f_{Ka}} \right)^2 \right] \cdot S_{system}}{\left(f_K^2 - f_{Ka}^2 \right)^2} \\ &= \frac{\left[f_K^2 + f_{Ka}^2 \right]}{\left(f_K^2 - f_{Ka}^2 \right)^2} \cdot \left(\frac{c}{\sqrt{2}} \right)^2 \cdot S_{system}, \end{aligned} \tag{15.39}$$

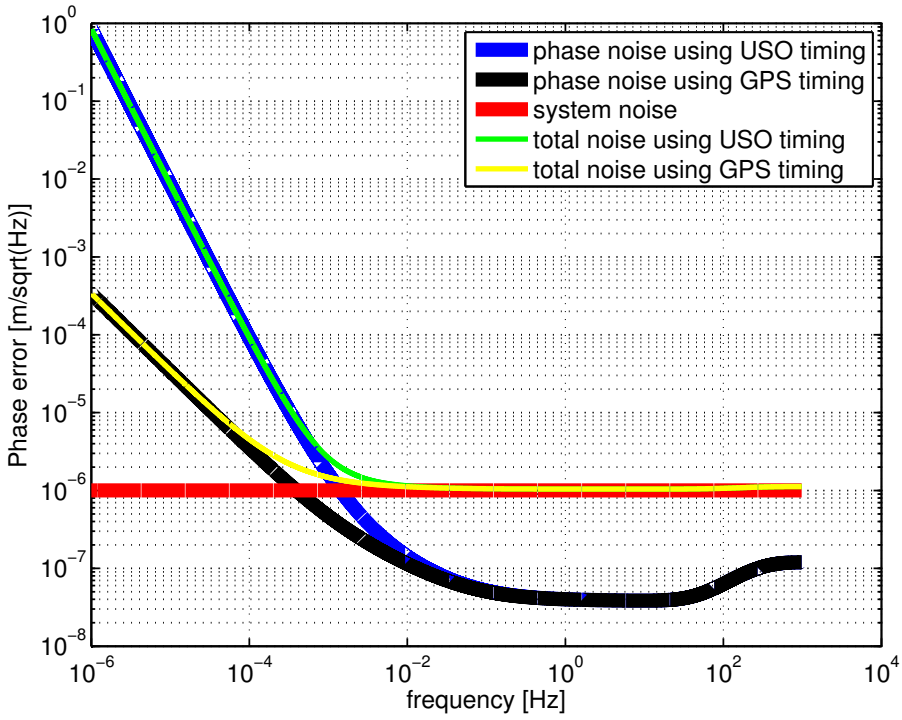

Figure 15.4: Total range error after the ionosphere free linear combination.

which gives a standard deviation of about 1 µm for a 1 s sampling.

Figure 15.4 shows the resulting overall range error after the ionosphere correction. We notice that the error resulting from the phase noise has been efficiently reduced by the combination of the satellite measurements forming the dual one way range. At high frequencies the error is dominated by the system noise.

Application of the low-pass filter

As the original data rate of 10 Hz for the K-band measurements is much higher than the desired output data rate of 0.2 Hz (5 s data), a low-pass filter has to be applied to the data in order to prevent aliasing effects on the resampled data. Moreover, not only the range derived from the K-band measurements, but also the range rate and range acceleration are to be derived. This is the reason why an analytic form of the applied filter is chosen, that can be differentiated in a closed form. We will briefly describe the derivation of the filter presented in Thomas (1999), but also discuss possible alternatives.

As the derived ranges are filtered during post-processing on ground, there are no restrictions on the used filter type, i.e. also filters that require 'future' measurements can be used. For the design of the required low-pass filter, the window method is used. We want a filter with a linear phase delay. A linear phase delay means that the filtered data is shifted by half the filter length in time compared to the unfiltered data. Therefore a FIR (Finite Impulse Response) filter is designed.

Filtering a signal in the time domain corresponds to a multiplication of the signal spectrum with the spectrum of the desired filter in the frequency domain. An optimal low-pass filter spectrum is a rectangle, meaning that up to a certain frequency, the so called 'cut-off frequency', the spectrum of the original signal is left unchanged. For frequencies larger than the cut-off frequency, the original spectral coefficients are set to zero. In the time domain, this operation corresponds to the convolution of the signal time series with the inverse Fourier transform of the rectangle, the *sinc*-function. Such a perfect low-pass filter cannot be realized, because the *sinc*-function is defined for the interval $[-\infty, +\infty]$, i.e. in

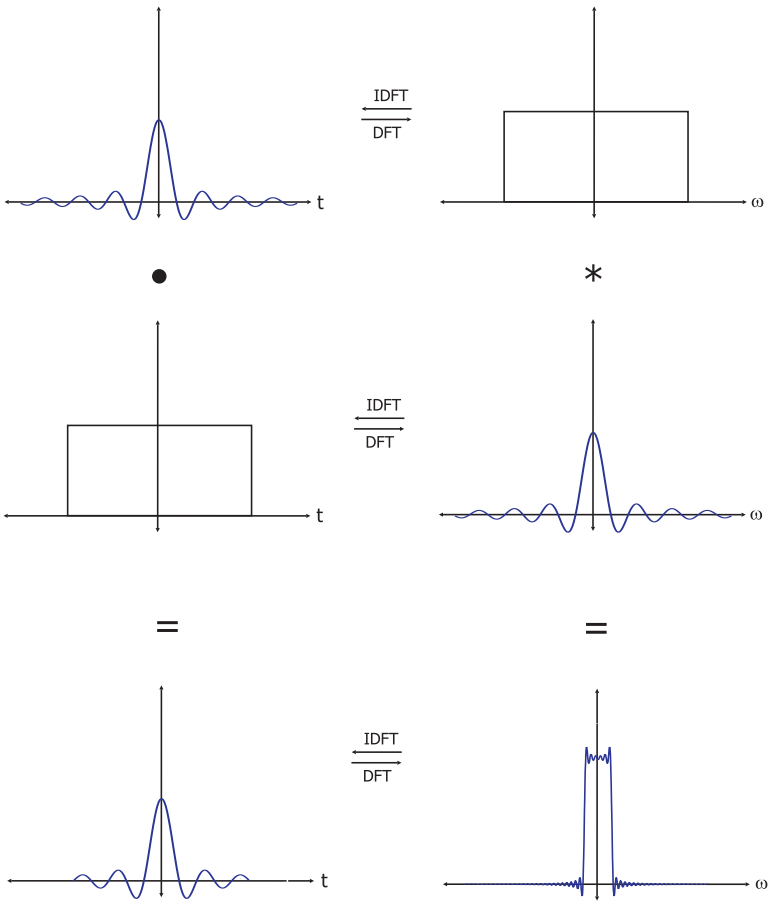

Figure 15.5: Impact of the chosen window function on the realization of a low-pass filter with the window method. Here, as an example, the window function chosen to limit the extend of the sinc-function is a rectangle. The left hand side shows the operation in the time domain, the right hand side the operation in the frequency domain.

order to conduct the filtering properly, it would be necessary to have a time series of infinite length. This is neither possible nor desirable for the practical data processing. In order to limit the *sinc*-function to an interval of finite extent, it is multiplied by a window function, that is zero outside the chosen interval and not zero inside the chosen interval. The length of this interval is the chosen filter length. A multiplication in the time domain corresponds to a convolution in the frequency domain, i.e. our optimal filter, the rectangle, is convolved with the Fourier transform of the window function, that was chosen to limit the width of the *sinc*-function in the time domain. Figure 15.5 shows the effect of the chosen window function on the optimal filter realization: As an example, a rectangle is chosen as the window function. The Fourier transform of the rectangle is again the *sinc*-function, so, if we consider the frequency domain, the optimal filter, the rectangle, is convolved with the *sinc*-function. Clearly the result is no longer a rectangle; there are unwanted oscillations in the pass-band as well as in he stop-band. This effect is well known as 'Gibbs effect'. Thus the deviation of the resulting filter from the optimal filter directly depends on the chosen window function. As we see with this example, the rectangle seems not to be suited as a window function, at least not for the K-band processing, as we want to preserve the high accuracy of the measurement, i.e. any oscillations due to filtering in the pass-band (also called 'ripple') should be as small as possible.

As the measurements are discrete and not continuous, a Discrete Fourier Transform (DFT) is applied and a rectangular window is not transformed into a *sinc* function but into a function of the kind of $\frac{\sin x}{\sin y}$ (cf. Best (1991), for details see appendix A. Let us now return to the problem of choosing a window function in order to limit the width of the time domain representation of the optimal low-pass filter.

In Thomas (1999), the chosen window function used to limit the time response of the ideal low-pass filter is a rectangle of width T_R that is convolved with itself N_c times. If T_R is chosen in a way that N_R, the

number of samples of the basic rectangle, is odd, then the filter length T_f becomes $N_R \cdot N_c/dt = N_f/dt$, where dt is the sampling interval. The 'N_c times self convolution' in the time domain can be expressed as a 'N_c times multiplication' in the frequency domain:

$$\begin{aligned} W[\omega] = W[k \cdot 2\pi/T_f] &= \left(\frac{\sin\left(k \cdot 2 \cdot \pi \cdot \frac{T_R}{2 \cdot T_f}\right)}{\sin\left(k \cdot 2 \cdot \pi \cdot \frac{dt}{2 \cdot dt \cdot N_f}\right)} \right)^{N_c} \\ &= \left(\frac{\sin\left(k \cdot 2 \cdot \pi \cdot \frac{T_f}{2 \cdot T_f \cdot N_c}\right)}{\sin\left(k \cdot \pi \cdot \frac{1}{N_f}\right)} \right)^{N_c} \\ &= \left(\frac{\sin\left(k \cdot \pi \cdot \frac{1}{N_c}\right)}{\sin\left(k \cdot \pi \cdot \frac{1}{N_f}\right)} \right)^{N_c}, \end{aligned} \tag{15.40}$$

with $T_R = T_f/Nc$. Thereby is ω the frequency in [rad/s] and $W[\omega]$ is the frequency response of the window function, that has to be multiplied with the time domain representation of the optimal low-pass filter. In Thomas (1999) and Wu et al. (2006) it is suggested to conduct this operation in the spectral domain as a convolution, we suggest to conduct it as multiplication in the time domain. We get for the filter representation $H_{LP}[n]$ in the time domain:

$$\begin{aligned} H_{LP}[n] &= W[n] \cdot LP[n] \\ H_{LP}[n] &= W[n] \cdot \frac{\sin\left(n \cdot dt \cdot \frac{B}{2}\right)}{\sin\left(n \cdot dt \cdot \frac{d\omega}{2}\right)} \cdot \frac{1}{N_f} \\ &= W[n] \cdot \frac{\sin\left(n \cdot dt \cdot \frac{B}{2}\right)}{\sin\left(n \cdot dt \cdot \frac{\pi}{T_f}\right)} \cdot \frac{1}{N_f}. \end{aligned} \tag{15.41}$$

The time domain representation of the window function $W[n]$ is derived as the inverse discrete Fourier transform of the frequency response of the window function:

$$W[n] = IDFT[W[\omega]]. \tag{15.42}$$

Let us now take a closer look at the window function, that has been chosen in Thomas (1999). As said before, in the time domain the window function is generated by a N_c times self convolution of a rectangle of width T_R. The final window function then has a width of $N_c \cdot T_R$ and is shown in blue in the upper panel of figure 15.6. This convolution is a multiplication in the spectral domain, multiplication in the spectral domain means filtering, i.e. this window function evolves from a rectangular window that is low-pass filtered by a cascade of filters with the DFT of a rectangle, namely the $\left(\frac{\sin x}{\sin y}\right)^{N_c}$-function. The window function we propose is the Kaiser window. It has the advantage that the drop-off level of the first side lobe can be selected as well as the transition width between pass-band and stop-band.

In order to assess the quality of the filter proposed by Thomas (1999) or our proposed filter, we first have to define the requirements for the filter. For the K-band measurements, the requirement is that the filter error should be smaller or equal to the measurement error we derived. Figure 15.6 shows a comparison of different window functions. In order to assess the performance of the window functions, we take a look at their frequency response. The perfect window would have a frequency response that consists of a Dirac function, the neutral element of convolution. This would require a rectangle of unlimited extend in the time domain, which is not realistic. So what we hope to achieve is a narrow and steep main lobe and well attenuated side lobes. When we take a look at the figure, we realize that in terms of a narrow and steep main lobe, the hamming and hanning window perform very well. They reach their first minimum at about $2 \cdot 10^{-3}$ Hz and therefore perform better in this respect than the Kaiser window or the convoluted rectangle window, but their side-lobe attenuation is much too high. So only the Kaiser window remains as candidate for an alternative filter. Figure 15.7 shows the

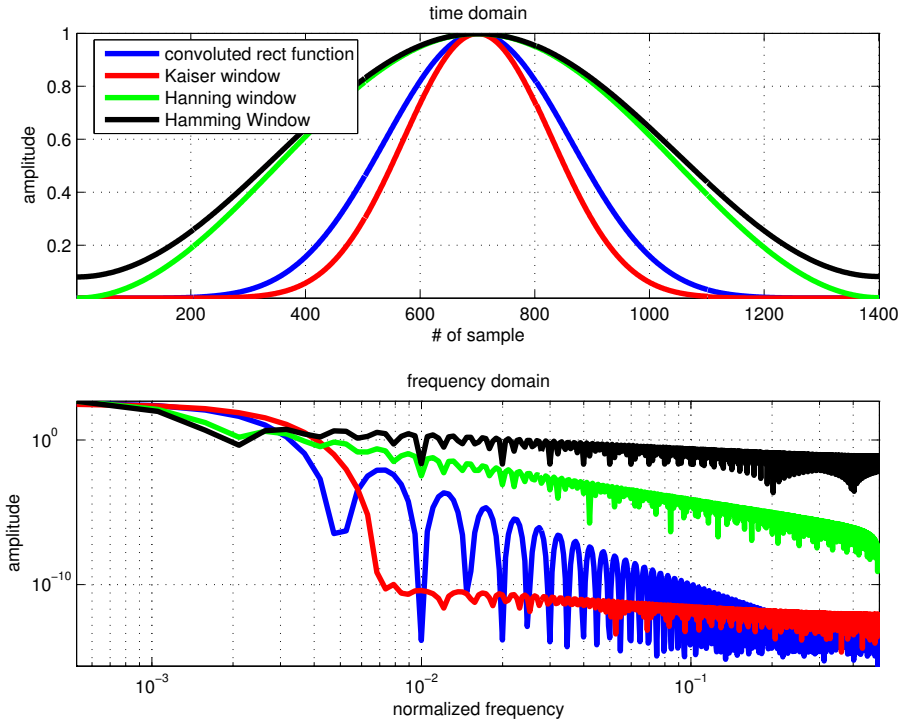

Figure 15.6: Comparison of the different window functions in order to limit the time response of the sinc function.

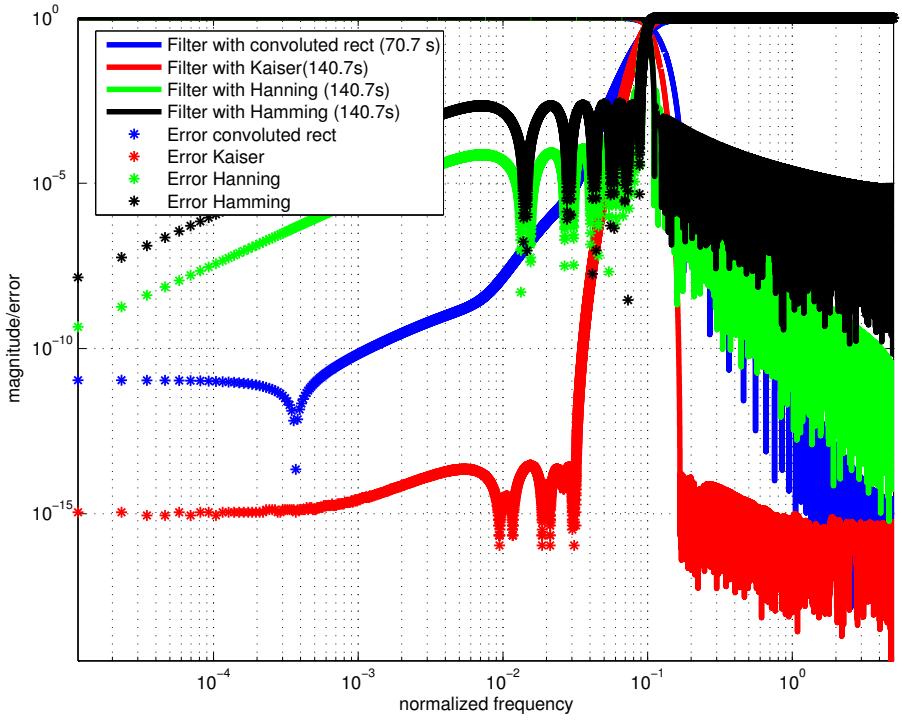

Figure 15.7: Relative filter error of the different filter candidates.

relative filter error of the filter candidates. We notice that the Kaiser filter performs significantly better than the convoluted rectangle filter. We also notice that our assumptions about the performance of the hamming and hanning filter are confirmed. Their performance is significantly worse than that of the Kaiser filter or the convoluted rectangle filter. The last step now consists in deriving the absolute error

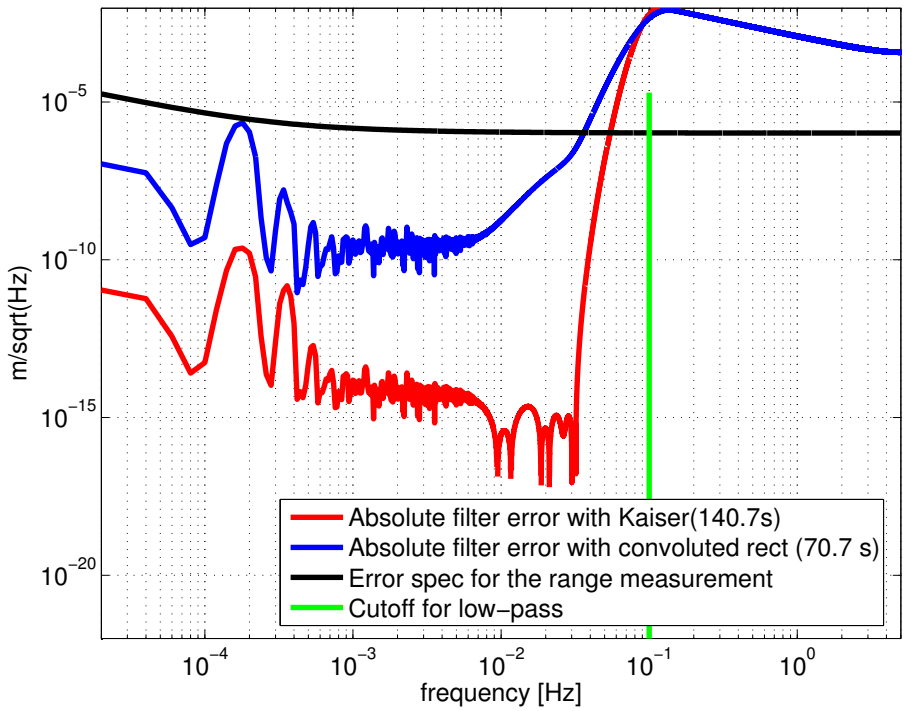

Figure 15.8: Absolute filter error of the Kaiser filter and the convoluted rectangle filter.

of the different filters. This is done by multiplying the relative filter error with the signal magnitude. Figure 15.8 shows the absolute filter error of the Kaiser filter and the convoluted rectangle filter. The black line represents the nominal K-band measurement performance for the range measurement. We notice that the original filter performs sufficiently, its absolute filter error is below the measurement error. Only at frequencies around once per revolution, where the signal is strongest, the filter error is close to the instrument error. The Kaiser filter performs significantly better, as its error is several orders of magnitude smaller than the nominal instrument error. The instrument error around frequencies of once per revolution is mainly determined by the phase noise of the oscillators, if they would perform better than specified, an improvement in data quality could be expected from the use of the Kaiser filter. The drawback of the Kaiser filter is the increased filter length, its length is twice that of the convoluted rectangle filter. A larger filter length means that more data is lost in case of gaps, as half the filter length has to be discarded if a gap is encountered. As conclusion, we state that the convoluted rectangle filter is adequate and efficient.

Derivation of the range rate and range acceleration

The range measurement is the basic quantity provided by the K-band system. As additional measurement types, the range rate and the range acceleration are provided by differentiation of the range measurement:

$$\dot{R}_{filt} = \frac{dR_{filt}}{dt} = IDFT\Big[H_D[\omega] \cdot DFT[R]\Big], \tag{15.43}$$

$$\ddot{R}_{filt} = \frac{d\dot{R}_{filt}}{dt} = \frac{d^2R_{filt}}{dt^2} = IDFT\Big[H_{DD}[\omega] \cdot DFT[R]\Big]. \tag{15.44}$$

The theoretical derivation of a first and second order differentiator is given in appendix A. We will now compare the convoluted rectangle single differentiator filter with the Kaiser single differentiator filter. The filter quality will not only be assessed in terms of the filter magnitude, but also in terms of the filters' phases. For a first order differentiator, the inflicted phase-angle change is expected to be $+\pi/2$.

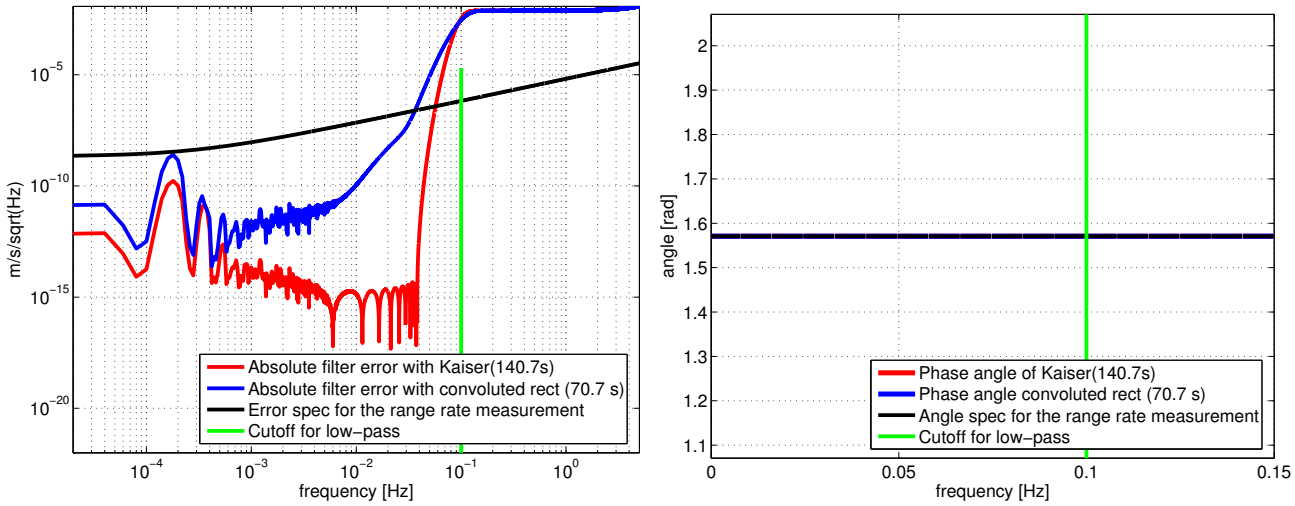

Figure 15.9: Comparison of the Kaiser and the convoluted rectangle filter in term of absolute filter error (left) and inflicted phase-angle change (right).

The comparison is shown in figure 15.9. We notice that for the absolute error magnitude the same observations hold as for the low-pass filter: the Kaiser filter performs better than the convoluted rectangle filter, but also the absolute error of the convoluted rectangle filter is still below the expected measurement error. Only for frequencies around once per revolution there might be some improvement from the use of the Kaiser filter, depending on the actual oscillator performance. Concerning the inflicted phase change, both filters perform equally well, in both cases it is exactly as expected. The results for the double differentiator are similar and are therefore not shown explicitly.

As a conclusion, we find that the Kaiser filter performs significantly better than the convoluted rectangle filter, but only at the cost of an increased filter length, which results in an increased data loss in case of gaps. The absolute filter error for both filters is below the specified instrument error and may therefore be neglected for the derivation of the error budget.

In order to filter the input signal, the derived ranges, with the filters $LP[n]$, $D[n]$ and $DD[n]$, there are again two possibilities: a convolution in the time domain or a multiplication in the frequency domain. We suggest to conduct the operation in the spectral domain. So we get for an input time series of range measurements $R[n]$ after the application of the respective filter:

$$R_{filt}[n] = IDFT\Big[H_{LP}[\omega] \cdot DFT[R[n]]\Big], \tag{15.45}$$

$$\dot{R}_{filt}[n] = IDFT\Big[H_{D}[\omega] \cdot DFT[R[n]]\Big], \tag{15.46}$$

$$\ddot{R}_{filt}[n] = IDFT\Big[H_{DD}[\omega] \cdot DFT[R[n]]\Big]. \tag{15.47}$$

Reduction of the measurements to the center of mass

The actual range measurement is the length (magnitude) of the vector between the KBR antenna phase centers of both satellites. For the gravity field determination, the magnitude (and its first and second derivative) of the vector between the centers of mass of both satellites is required. Therefore derived range, range rate and range acceleration have to be corrected. The situation is depicted in figure 15.10. The range between the centers of mass of the two satellites is given as:

$$R_{CoM} = dr_A + dr_B + r_{AB}, \tag{15.48}$$

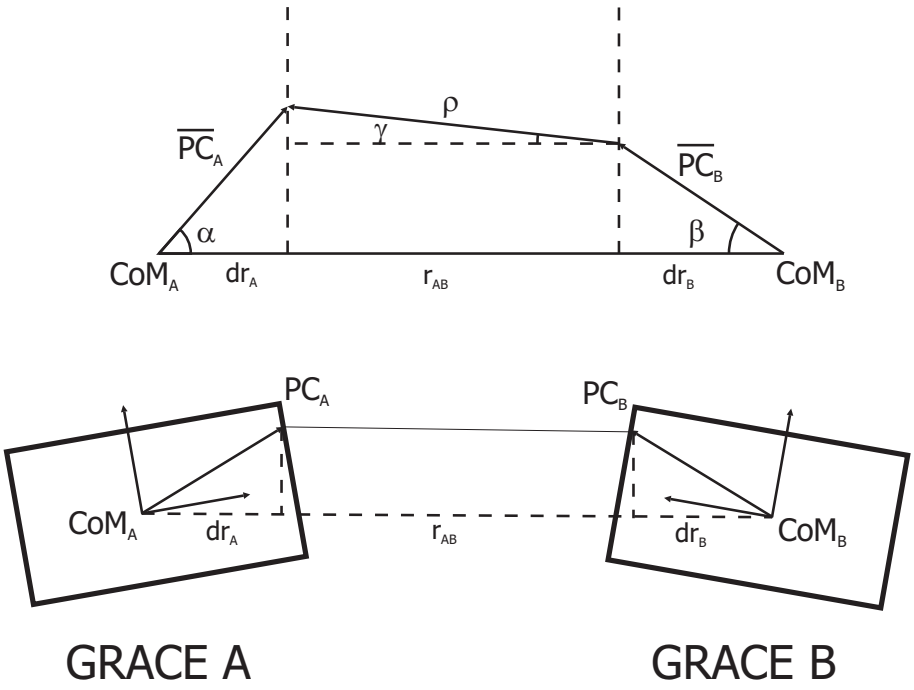

Figure 15.10: Reduction of the measured range to the distance between the centers of mass of the two GRACE satellites.

where

- dr_A is the projection of the vector between the center of mass of satellite A and the phase center of the K-band horn of satellite A on the line connecting the centers of mass of both satellites,
- dr_B is the projection of the vector between the center of mass of satellite B and the phase center of the K-band antenna of satellite B on the line connecting the centers of mass of both satellites,
- r_{AB} the projection of the measured range between the two satellites K-band antennas on the line connecting the centers of mass of both satellites.

The individual quantities are given as:

$$dr_A = |\overline{\mathrm{PC_A}}| \cdot \cos\alpha, \tag{15.49}$$
$$dr_B = |\overline{\mathrm{PC_B}}| \cdot \cos\beta, \tag{15.50}$$
$$r_{AB} = R_{filt} \cdot \cos\gamma. \tag{15.51}$$

For the derivation of the angles α, β, γ, the satellites' positions $\bar{\mathrm{r}}_A$ and $\bar{\mathrm{r}}_B$ are needed:

$$\cos\alpha = \widehat{\mathrm{e}}_{\mathrm{AB}} \cdot \widehat{\mathrm{PC}}_{\mathrm{A}}, \tag{15.52}$$
$$\cos\beta = \widehat{\mathrm{e}}_{\mathrm{AB}} \cdot \widehat{\mathrm{PC}}_{\mathrm{B}}, \tag{15.53}$$
$$\cos\gamma = \widehat{\mathrm{e}}_{\mathrm{AB}} \cdot \widehat{\mathrm{PC}}_{\mathrm{AB}} \tag{15.54}$$
$$\widehat{\mathrm{e}}_{\mathrm{AB}} = \frac{\overline{\mathrm{r_B}} - \overline{\mathrm{r_A}}}{|\overline{\mathrm{r_B}} - \overline{\mathrm{r_A}}|}, \tag{15.55}$$
$$\widehat{\mathrm{PC}}_{\mathrm{AB}} = \frac{\overline{\mathrm{r_B}} + \overline{\mathrm{PC_B}} - \overline{\mathrm{r_A}} - \overline{\mathrm{PC_A}}}{|\overline{\mathrm{r_B}} + \overline{\mathrm{PC_B}} - \overline{\mathrm{r_A}} - \overline{\mathrm{PC_A}}|}. \tag{15.56}$$

In order to perform these operations, the different vectors have to be available in the same coordinate system. It seems to be straightforward to use the IRF for the derivation of the correction. We will

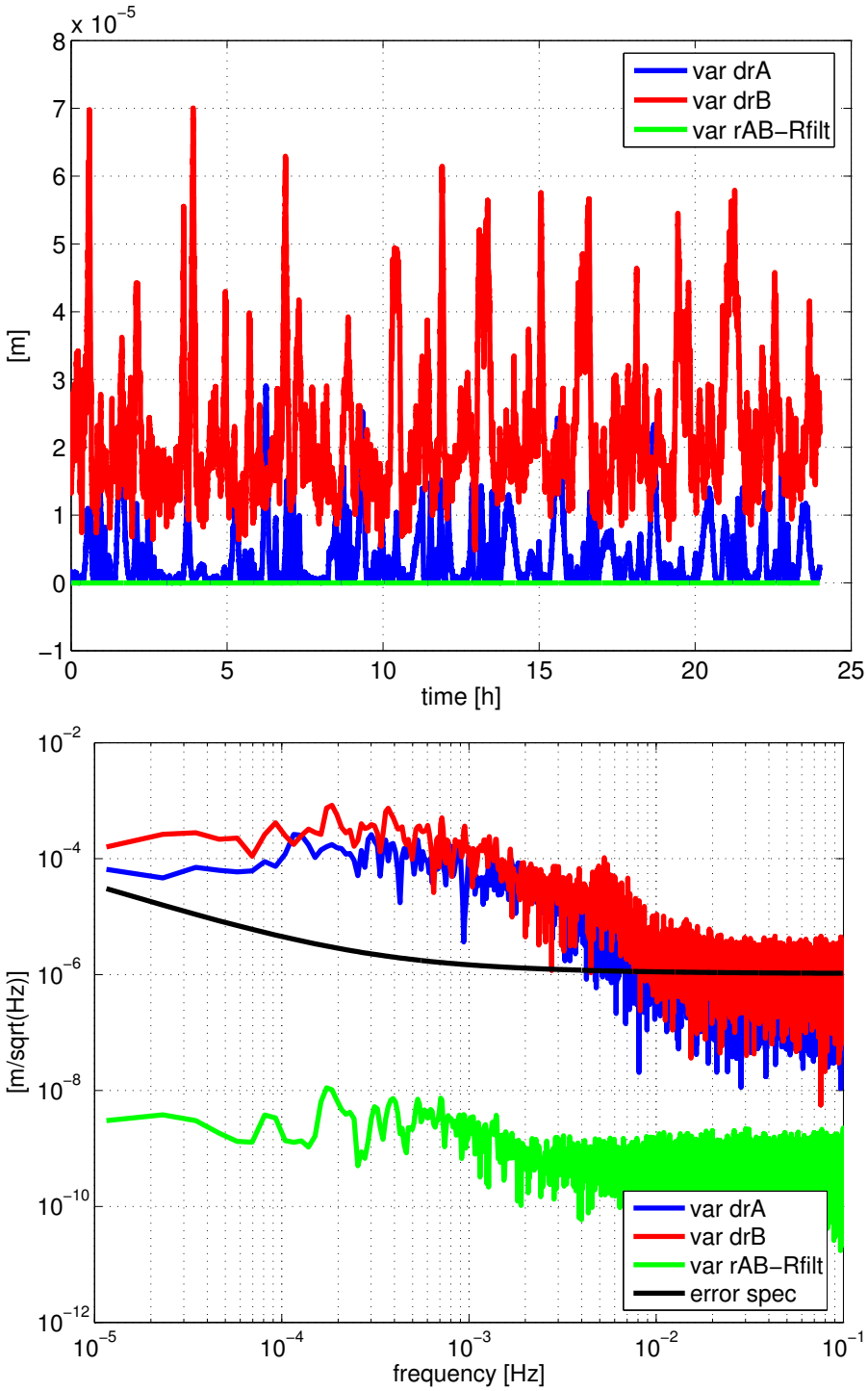

Figure 15.11: Variations of the different corrections to be applied on the measured range to derive the range between the CoM.

now assess the magnitude of the different corrections in order to determine their relevance. For the derivation of the correction, real GRACE L1b data, orbits and star sensor data was used. Figure 15.11 shows the variations of the different corrections. As the measured range is biased, not the mean value of the corrections, but only the variation is of importance. We realize that only the correction dr_A and dr_B have to be applied, the variation of the difference between r_{AB} and R_{filt} is well below the error of the measured range. Let us now determine the influence of these corrections on the error budget. Table 15.2 shows the assumed accuracies of the relevant input quantities. We get for the errors of the angles

Table 15.2: Accuracies and magnitudes of the input quantities used for the derivation of the center of mass reduction.

quantity	magnitude	accuracy (σ)
line of sight unit vector $\widehat{\mathrm{e}}_{\mathrm{AB}}$	1.0	$< 5.0 \cdot 10^{-8}$ m
unit vector between the phase centers $\widehat{\mathrm{PC}}_{\mathrm{AB}}$	1.0	$< 5.0 \cdot 10^{-8}$ m

α and β:

$$\delta(\cos\alpha) \approx \delta(\widehat{\mathrm{e}}_{\mathrm{AB}}) \cdot |\widehat{\mathrm{PC}}_{\mathrm{A}}| + |\widehat{\mathrm{e}}_{\mathrm{AB}}| \cdot \delta(\widehat{\mathrm{PC}}_{\mathrm{A}}) \approx 1.5 \cdot 10^{-7}, \tag{15.57}$$

$$\delta(\cos\beta) \approx \delta(\widehat{\mathrm{e}}_{\mathrm{AB}}) \cdot |\widehat{\mathrm{PC}}_{\mathrm{B}}| + |\widehat{\mathrm{e}}_{\mathrm{AB}}| \cdot \delta(\widehat{\mathrm{PC}}_{\mathrm{B}}) \approx 1.5 \cdot 10^{-7}. \tag{15.58}$$

We get for the errors of the range corrections:

$$\delta dr_A \approx \delta|\overline{\mathrm{PC}_{\mathrm{A}}}| \cdot \cos\alpha + |\overline{\mathrm{PC}_{\mathrm{A}}}| \cdot \delta\cos\alpha \approx 5 \cdot 10^{-7} \text{ m}, \tag{15.59}$$

$$\delta dr_B \approx \delta|\overline{\mathrm{PC}_{\mathrm{B}}}| \cdot \cos\beta + |\overline{\mathrm{PC}_{\mathrm{B}}}| \cdot \delta\cos\beta \approx 5 \cdot 10^{-7} \text{ m}. \tag{15.60}$$

Again, it seems that the corrections can be derived accurately enough and therefore they will not be included in the error budget. The corrections can only be derived with sufficient accuracy, if the variations of the K-band antennas phase center position is below one micrometer.

15.2. Accelerometer

The processing steps for the accelerometer data are shown in figure 15.12. First, the time tags have to be corrected for different errors.

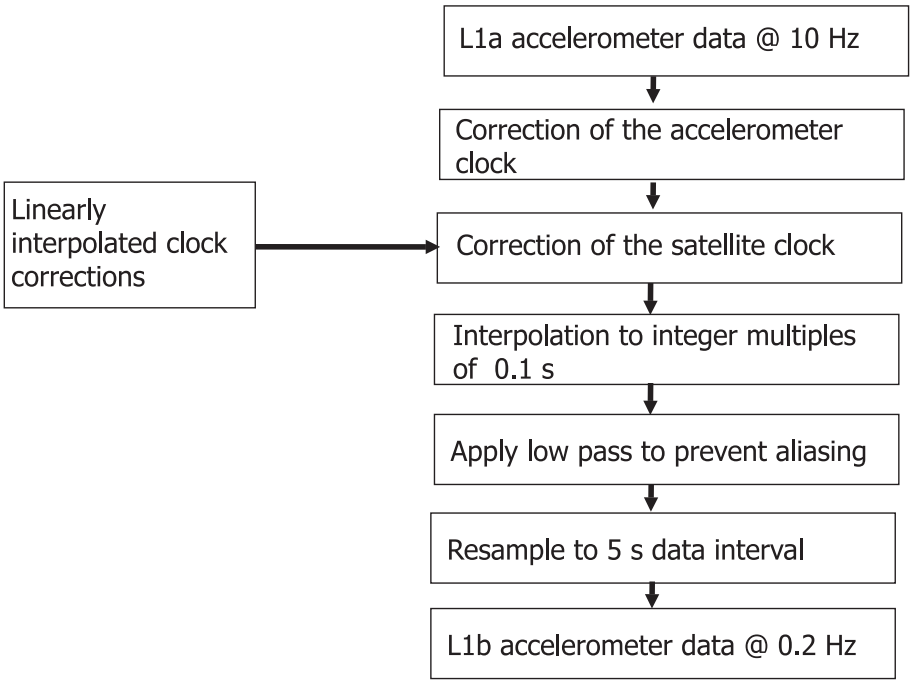

Figure 15.12: Processing steps for the derivation of L1b accelerometer data from L1a accelerometer data.

Correction of the accelerometer clock

The accelerometer data is time tagged using the time derived from the On Board Data Handler (OBDH) One Pulse Per Second (1PPS) generator, cf. Wu et al. (2006). This time scale is also used to derive the time tags of the housekeeping data. In order to convert the OBDH time tags to receiver time, it is necessary to apply a correction to the original accelerometer time tags. In general the OBDH time is synchronized to the receiver time, meaning that the correction then is zero. Only during reboots of the IPU, the synchronization between the OBDH time and the receiver time is lost, then correction has a non-zero value:

$$tt_{acc}^{rec} = tt_{acc}^{OBDH} + corr_{OBDH}^{rec}. \tag{15.61}$$

The correction is derived from the product TIM1B.

Correction of the satellite clock

The accelerometer time tags are now converted to receiver time. In order to convert them to GPS time, the receiver clock error has to be corrected. In addition, the delay of the butterworth low-pass filter used in the on-board processing has to be considered:

$$tt_{acc}^{gps} = tt_{acc}^{rec} + corr_{rec}^{gps} + corr_{butter}. \tag{15.62}$$

The corrections are derived via linear interpolation of the clock corrections given in CLK1B. The correction of the butterworth delay is a constant: 0.14 s.

The data is then interpolated to time tags that are integer multiples of 0.1 s. In the course of this interpolation, also data gaps are filled, using a cubic interpolation.

Application of the low-pass filter

For the accelerometer data processing, the same low-pass filter can be used as for the K-band processing. The requirements on the accuracy inside the pass-band are lower than for the K-band measurements, as the amplitudes of the accelerometer signal are significantly smaller. Assuming a maximum amplitude of $1 \cdot 10^{-6}$ m/s^2 and a measurement error of $1 \cdot 10^{-10}$ m/s^2 for the sensitive axes, a relative error of about $1 \cdot 10^{-4}$ is the requirement for the accuracy in the pass-band for the low-pass filter. This requirement can easily be met by the filter we proposed for the K-band data processing. In Wu et al. (2006) the bandwidth of the low-pass filters (35 mHz) differs from the one used for the K-band data (0.1 Hz). This seems to be inconsistent. For the gravity field determination, the K-band data has to be corrected for the effect of the non-gravitational forces using the accelerometer data. In our opinion, the accelerometer data should be provided with the same bandwidth as the K-band data. Again it is suggested to conduct the filtering in the frequency domain:

$$\overline{\mathrm{a}}_{filt} = IDFT\Big[H_{LP}[\omega] \cdot DFT[\overline{\mathrm{a}}_{raw}]\Big]. \tag{15.63}$$

The filtered data are compared to the unfiltered data and epochs, where the residuals are larger than a threshold, are marked.

The data is then resampled at intervals of 5 s. The last processing step consists of a transformation from the accelerometer frame to the satellite body fixed frame by switching the coordinate axes:

$$\widehat{\mathrm{X}}_{srf} = \widehat{\mathrm{Z}}_{arf}, \tag{15.64}$$

$$\widehat{\mathrm{Y}}_{srf} = \widehat{\mathrm{X}}_{arf}, \tag{15.65}$$

$$\widehat{\mathrm{Z}}_{srf} = \widehat{\mathrm{Y}}_{arf}. \tag{15.66}$$

15.3. Star Sensor

Figure 15.13 shows the processing steps for the star sensor data.

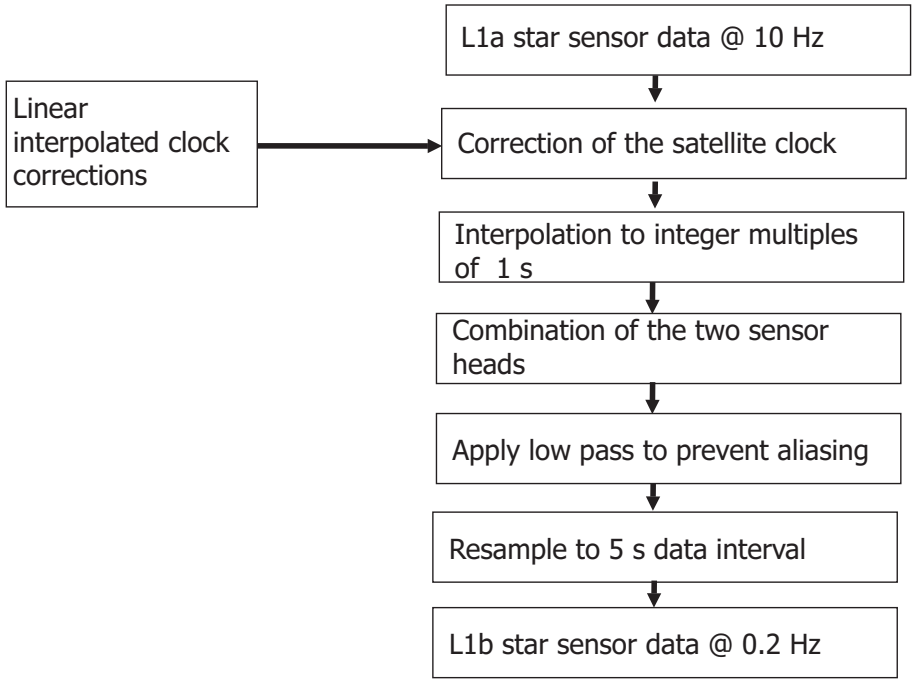

Figure 15.13: Processing steps for the derivation of L1b SCA data from L1a SCA data.

Conversion to the Satellite Reference Frame

The measured quaternions represent the orientation of the respective Star Sensor Reference Frame (SSRF) of each sensor head with respect to the Inertial Reference Frame (IRF), i.e. they represent a rotation that transforms from the IRF to a SSRF. For the data processing, the orientation of the Satellite Reference Frame (SRF) is desired. Therefore the measured quaternions have to be transformed, cf. equation (14.1):

$$\overline{\mathrm{Q}}_{irf}^{srf} = \overline{\mathrm{Q}}_{irf}^{ssrf} \star \overline{\mathrm{Q}}_{ssrf}^{srf}. \tag{15.67}$$

The quaternions $\overline{\mathrm{Q}}_{ssrf}^{srf}$, describing the orientation of the SSRF w.r.t. SRF, are derived during calibration maneuvers resp. have been determined pre flight on ground and are given in the Sequence of Events file (SOE). It is assumed that the accuracy of these quaternions is sufficient in order to neglect them in the error budget.

Outlier detection

In order to detect outliers in a measurement, a reference to which the measurements can be compared to has to be available. For the star sensor measurements, a reference can be generated using the orbit information, cf. appendix (D.2). The general idea is that there are no abrupt changes in the attitude data, so that any sudden change of the attitude exceeding a threshold is considered as an outlier.

Retain continuity

A simultaneous change in the sign of all quaternions does not change the orientation they represent. Discontinuities of this kind have to be removed. They are identified by formation of the first time derivative. An identified discontinuity is removed by multiplying the identified quaternion and all following ones by -1.

Apply time tag correction

The star sensor time tags are given in receiver time. In order to convert them to GPS time, the receiver clock error has to be corrected:

$$tt_{str}^{gps} = tt_{str}^{rec} + corr_{rec}^{gps}. \tag{15.68}$$

The corrections are derived via linear interpolation of the clock corrections given in CLK1B.

Combination of the data of the two sensor heads

Each of the two star tracker camera heads data is used to derive an orientation of the satellite, i.e. there are two time series of the satellite's orientation available. In order to exploit this redundancy, the data of both sensor heads are combined. The algorithm of the combination is described in Wu et al. (2006), the theory is discussed in Romans (2003). It is based on the fact that both star sensor heads should deliver the same orientation. The difference between both orientations is used to derive a correction for each orientation delivered by head 1 or head 2 in a least squares sense. The correction takes into account, that rotations about the line of sight of the star sensor are determined less accurate than rotations perpendicular to the line of sight. The 'difference' quaternion is:

$$\Delta\overline{\mathrm{Q}}_{12} = \left(\overline{\mathrm{Q}}_{\mathrm{irf,srf}}^{(1)}\right)^{-1} \star \overline{\mathrm{Q}}_{\mathrm{irf,srf}}^{(2)} = \left(1, \frac{1}{2}\overline{\Delta}_{12}\right). \tag{15.69}$$

The corrected quaternion is, cf. Wu et al. (2006):

$$\overline{\mathrm{Q}}_{\mathrm{irf,srf}}^{\mathrm{corr}} = \overline{\mathrm{Q}}_{\mathrm{irf,srf}}^{(1)} \star \left(1, \underline{\mathrm{M}} \cdot \frac{1}{2}\overline{\Delta}_{12}\right), \tag{15.70}$$

$$\underline{\mathrm{M}} = \frac{1}{2}\begin{pmatrix} 1 & 0 & 0 \\ 0 & 1 & -\lambda \\ 0 & -\lambda & 1 \end{pmatrix}, \tag{15.71}$$

$$\lambda = \frac{\kappa^2 - 1}{\kappa^2 + 1}, \quad \kappa = 8. \tag{15.72}$$

The formal error for rotations about the boresight of the sensor heads is about a factor κ greater than for rotations perpendicular to the boresight. The matrix $\underline{\mathrm{M}}$ is a scaling of the difference vector $\frac{1}{2}\overline{\Delta}_{12}$, whose components can be interpreted as difference angles $\frac{\delta\phi_x}{2}, \frac{\delta\phi_y}{2}, \frac{\delta\phi_z}{2}$ between the orientation delivered by head 1 and head 2, as the difference is assumed to be small. The scaling matrix $\underline{\mathrm{M}}$ takes also into account that the z-axes of the star sensor reference frames are orthogonal. For $\kappa = 1$, the correction is just the mean of the difference of the quaternions. This combination strategy does not take into account a possible degradation of data quality of a sensor head in the vicinity of Sun/Moon intrusions.

Combination with accelerometer data

The official data processing described in Wu et al. (2006) does not foresee the combination of the star sensor data and the accelerometer data. The general idea is to take advantage of the fact that the accelerometers not only measure linear accelerations, but also angular accelerations. To use this

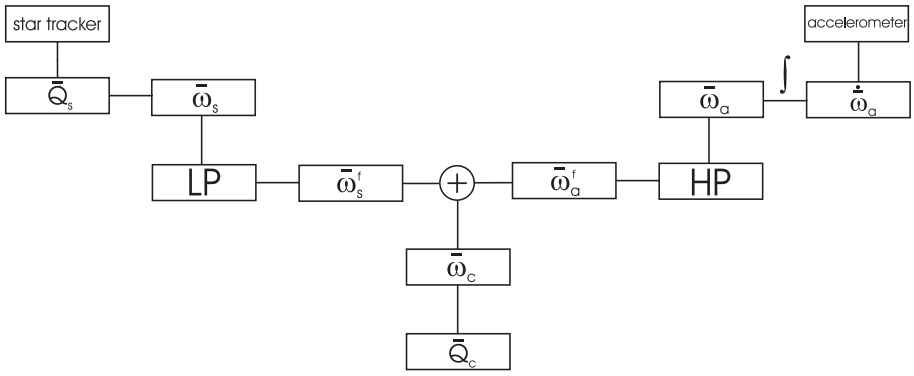

Figure 15.14: Overview of the combination of star sensor data with accelerometer data.

information for the orientation determination, a relation between angular acceleration and quaternions has to be established. The first step is to integrate the angular acceleration to get the angular velocity:

$$\overline{\omega}_{acc} = \int \dot{\overline{\omega}}_{acc} dt. \tag{15.73}$$

From the level of angular velocities, the quaternions can be derived using the formulas given in appendix (C). The combination with the information from the star tracker takes place on the level of the angular rate. We start with a comparison of the angular rates from star tracker and accelerometer. Figure 15.15 (left panel) shows the time series of the angular rate about the x-axis of the SRF derived from the star tracker (red) and the accelerometer. The angular rate of the star tracker is noisy, but shows the expected behavior: a zero mean value. The angular rate derived from the accelerometer (green) behaves differently, it shows a long periodic signal but is less noisy. These observations are confirmed when we consider the right panel of the figure, that shows the root PSD of the angular rate. The PSD of the angular rate from the accelerometer (green) behave more or less like a straight line rising at low frequencies and dropping at high frequencies. The one from the star tracker is different: it is horizontal until it starts to rise at about $1 \cdot 10^{-2}$ Hz. The PSDs agree in a region from $5 \cdot 10^{-4}$ Hz to about $3 \cdot 10^{-2}$ Hz. It is known that the accelerometer drifts, i.e. that the quality of accelerometer data decreases at low frequencies. The star sensor data are reliable at low frequencies but show low quality at high frequencies in terms of an increased noise level. The idea of the combination is to take the information at low frequencies from the star tracker and to take the information at high frequencies from the accelerometer by application of a high-pass respectively low-pass filter. The spectra of the filtered data are then added to yield the spectrum of the improved angular rate. The vertical black line in the right panel of the figure shows the proposed cut-off frequency: $3 \cdot 10^{-2}$ Hz. The principle is shown in figure 15.14.

The results of this procedure are shown in figure 15.16. The left panel shows the original measurements and the combined angular rate in blue. The filtered data from the star tracker (black) and from the accelerometer (magenta) are displayed as well. The combined angular rate is very similar to the filtered rate from the star tracker and is less noisy. The right panel shows the root PSDs. The filtered data show the effect of the applied low-pass respectively high-pass filter: for the star tracker data, only the low-frequency part of the spectrum remains, for the accelerometer, only the high-frequency part of the spectrum. The spectrum of the combined angular rate is the sum of both spectra.

For the resulting quaternion, we could expect that its spectrum shows the same behavior as the altered angular rate: a reduced noise level and therefore a damping of the high frequencies of its spectrum. This is not the case, as quaternions are not simply the integral of the angular rate, the relation between them is more complicated, compare appendix (C) for details.

The left panel of figure 15.17 shows the time series of one component of the resulting quaternion. The results for the other components are similar, they are therefore not shown. The difference (green)

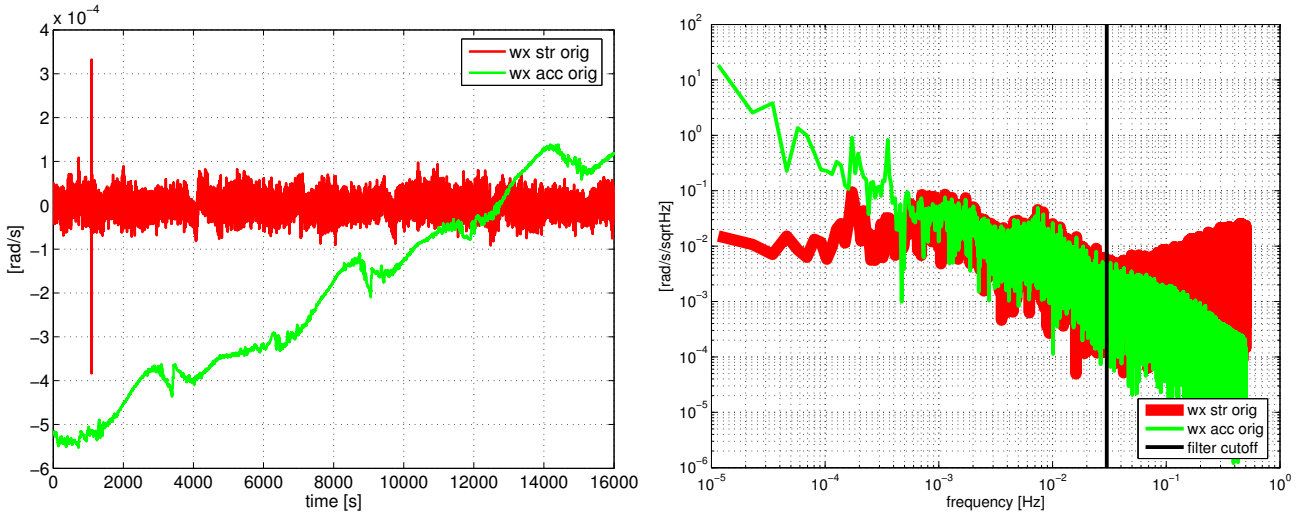

Figure 15.15: Left panel: Time series of the angular rate about the x-axis of the SRF derived from the star tracker measurements (red) and from the accelerometer measurements (green).

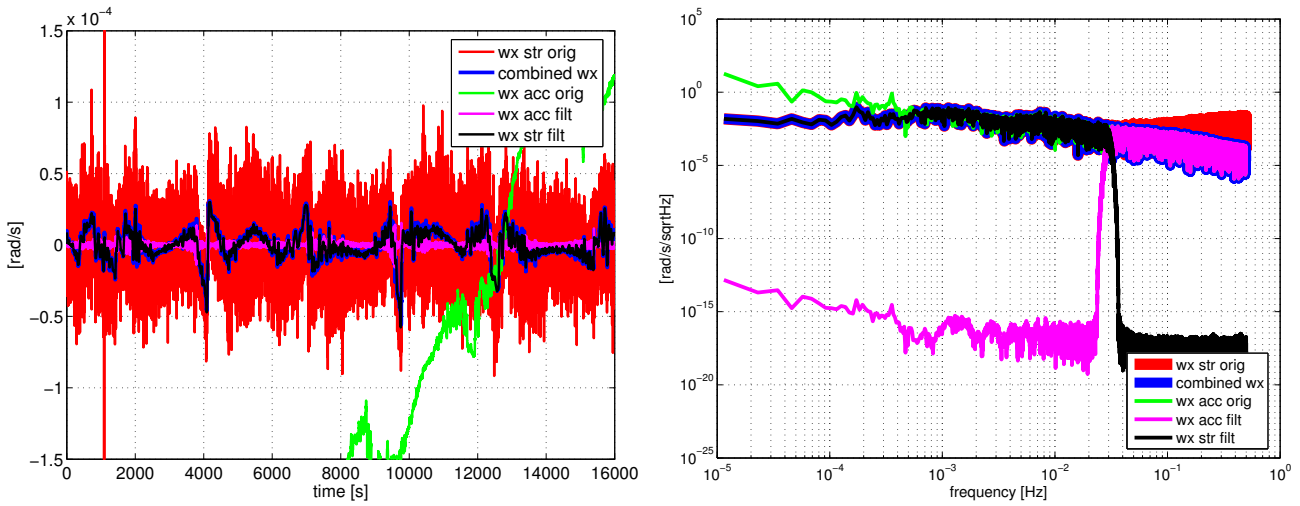

Figure 15.16: Left panel: Time series of the combined angular rate about the along-track axis in comparison to the original and filtered one. Right panel: Root PSD of the combined angular rate and the angular rates from the star tracker and the accelerometer before and after application of the high-pass and low-pass filter.

between the original (blue) and the combined (red) quaternion is small, it is at a level of $1 \cdot 10^{-4}$ rad. The right panel shows the root PSD of the resulting quaternion, the original one and the difference. The difference is larger than the quaternion noise level of about $1 \cdot 10^{-4}$ rad/$\sqrt{\text{Hz}}$ only between $5 \cdot 10^{-5}$ and $1 - 2 \cdot 10^{-4}$ Hz. At frequencies higher than $3 \cdot 10^{-2}$ Hz, the noise level is reduced.

As conclusion, we find that the combination of star tracker and accelerometer data improves the derived orientation at low as well as at high frequencies of the spectrum. The resulting orientation is smoother than the one derived from the star tracker measurement.

Application of the low-pass filter

For the star sensor data processing the same low-pass filter as the one that is used for the K-band processing can be used. The requirements on the accuracy inside the pass-band are lower than for the K-band measurements, as the amplitudes of the quaternions are significantly smaller than those of the K-Band measurements. Assuming a maximum amplitude of 1 and a measurement error of $1 \cdot 10^{-4}$ rad,

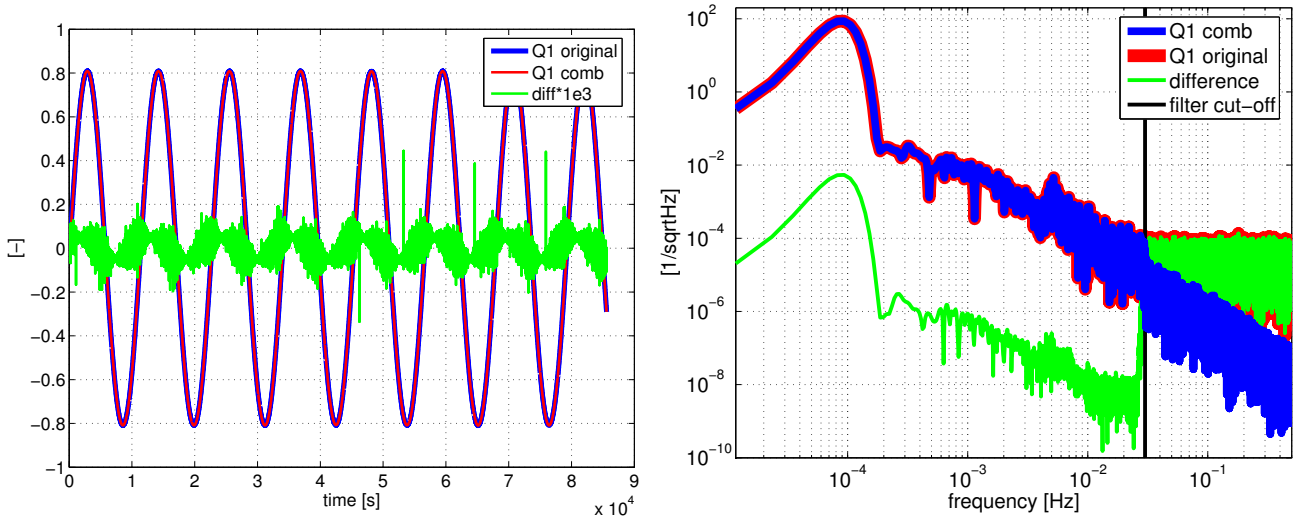

Figure 15.17: Left panel: Time series of the star tracker delivered quaternion (blue), the quaternion derived from the combined angular rate (red) and their difference scaled by a factor of 1000 (green). Right panel: Root PSD of the quaternions from the star tracker (blue) and the one derived from the combined angular rate (red) and their difference (green). Only at low frequencies the difference is larger than the quaternion noise level.

a relative error of about $1 \cdot 10^{-4}$ is the requirement for the accuracy in the pass-band for the low-pass filter. This requirement can easily be met by the filter we proposed or by the convoluted rectangle filter. Again it is suggested to conduct the filtering in the frequency domain:

$$\overline{\mathrm{Q}}_{filt} = IDFT\Big[H_{LP}[\omega] \cdot DFT[\overline{\mathrm{Q}}_{raw}]\Big]. \tag{15.74}$$

16. Level 1b analysis

In this chapter the L1b data are analyzed. For the accelerometer data, the difference between L1a data and L1b data consists mainly in a reduced bandwidth. For the K-band data, the bandwidth has been reduced, but also range rate and range acceleration have been derived from the range measurements. The L1b star sensor data also has a reduced bandwidth compared to the L1a star sensor data. In addition, the data from the sensor heads has been combined.

For the K-band, it will be tested if the difference in the pass-band of the applied low-pass filter is smaller than the specified measurement error. Especially for the accelerometer data, we will investigate if the peak and twang effects are still present in the L1b data. For the star sensor data, we will investigate the effect of the combination of the data from the two sensor heads. In addition, the performance of the K-band measurements and of the star sensor data will be assessed.

16.1. GPS receiver

We will give only a very brief analysis of the GPS data. For a thorough quality assessment, it would be necessary to conduct a precise orbit determination in order to correct the measurements for the error terms in equations (11.2) and (11.8) in chapter (11). There are six available observables: the C/A, P1 and P2 code measurements and the C/A, L1 and L2 phase measurements. By forming the difference between the C/A and P1 range measurements, respectively the C/A and L1 phase measurements, the noise level for the code and phase measurements can be assessed, cf. Jäggi and Svehla (2007). In order to assess the quality of the GPS measurements, we will estimate a noise level from their root PSD and compare it to the specification from Stanton et al. (1998), see table 16.1. The noise time series are

Table 16.1: Noise level specifications for the Black-Jack GPS receiver from Stanton et al. (1998).

observation type	noise level 1σ [cm] 10 s sampling	error $\sqrt{\text{PSD}}$ cm/s^2/$\sqrt{\text{Hz}}$
code measurements	100	400
phase measurements	1	4

derived from the following differences:

$$noise^{L1}_{code} = P^{L1}_{C/A} - P^{L1}_{P1}, \tag{16.1}$$

$$noise^{L1}_{phase} = L^{L1}_{C/A} - L^{L1}_{P1}. \tag{16.2}$$

It is to be noted, that by the subtraction of the observations the derived noise level is increased by a factor of two on the level of the PSD, respectively by a factor of $\sqrt{2}$ on the level of the root PSD.

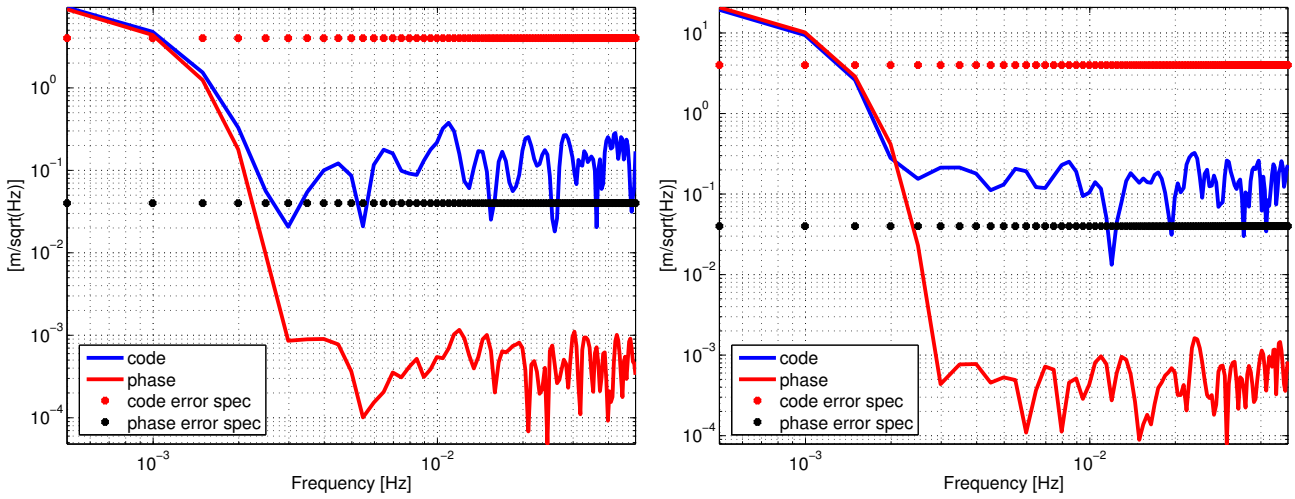

Figure 16.1: Left panel: Root PSD of the GPS measurements on GRACE A. Right panel: Root PSD of the GPS measurements on GRACE B.

The right panel of figure 16.1 shows the root PSD for GPS measurements on GRACE A to GPS satellite 11 as an example. The results for other satellites are similar. The root PSDs level out into what seems to be white noise at about $3 \cdot 10^{-3}$ Hz. The assumed noise levels are about 10 cm/$\sqrt{\text{Hz}}$ for the range measurements and about 1 mm/$\sqrt{\text{Hz}}$ for the phase measurements and therefore significantly below the requirements. The situation is the same for the measurements on GRACE B, displayed in the right panel of figure 16.1.

From Jäggi and Svehla (2007), it is known that the measurement performance derived from precise orbit determination is similar, it seems therefore that the derived noise level is realistic.

Conclusion

We can state that the performance of the GPS measurements fulfils the requirements, as the assumed noise level is considered as an upper limit for the real measurement noise. A noise level could be derived only for the measurements on the L1 carrier. It is not possible to derive a realistic noise level for the measurements on the L2 carrier, as on this frequency only one phase respectively code measurement is available. The measurement performance on L2 can only be determined in the course of a precise orbit determination.

16.2. K-band

The L1b K-band range measurements evolve from the combination of the L1a phase measurements of both satellites on both the K-band and the Ka-band. Therefore, there is only one product for both satellites. The range rate and the range acceleration are derived from the measured range in the course of the L1a to L1b processing, therefore they can not be compared with corresponding L1a data. Figure 16.2 shows the comparison of the L1a and L1b data. The upper left panel shows the time series of the range measurement. We recognize that the range measurement is very smooth. It varies with a magnitude of about 2.5 km. At a first glance, no difference between the L1a range and the L1b range is visible. The upper right panel shows the corresponding root PSD. As expected, the root PSD of the L1a and L1b range are almost identical up to the cut-off frequency of the applied low-pass filter. The filter proposed by Thomas (1999) has been applied. The difference inside the pass-band is slightly below the error specification for the range measurement. The peaks at $4 \cdot 10^{-2}$ Hz and $8 \cdot 10^{-2}$ Hz identified also in the L1a phase data is still visible, but with a reduced magnitude of about $4 \cdot 10^{-5}$ m/$\sqrt{\text{Hz}}$. That means that the combination of the measurements during the L1b processing diminishes this effect but does not fully remove it. At frequencies of about $2 \cdot 10^{-2}$ Hz, noise seems to dominate the measurement. The noise agrees well with the error specification, except for the peaks mentioned before. The peaks increase the standard deviation from the specified $3 \cdot 10^{-7}$ m to $4 \cdot 10^{-7}$ m or by 33% for 5 s data. As the effect is limited to two frequencies, the impact on the gravity field model determination is to be investigated.

The middle left panel shows the range rate, that varies with a magnitude of about 2.5 m/s. The middle right panel shows the corresponding root PSD, that is just the root PSD of the range multiplied by ω.

The lower left panel shows the range acceleration, the second derivative of the range. It varies with a magnitude of about $3 \cdot 10^{-3}$ m/s^2. The lower right panel shows the corresponding root PSD.

Performance assessment

Concerning the measurement performance, it can be stated that the K-band data fulfils the requirements, except for the effect at $4 \cdot 10^{-2}$ Hz and $8 \cdot 10^{-2}$ Hz. This effect deteriorates the performance, as if the noise would be higher by 33 % than specified or about $1.3 \cdot 10^{-6}$ m/$\sqrt{\text{Hz}}$ for 5 s data. We conclude that it may be sensible to reduce the bandwidth of the applied low-pass filter to about $2 - 3 \cdot 10^{-2}$ Hz and thus remove this effect from the data. The findings for the measurement performance of the range measurement are applicable to the range rate and the range acceleration measurement as well, as they are just derivatives of the range measurement.

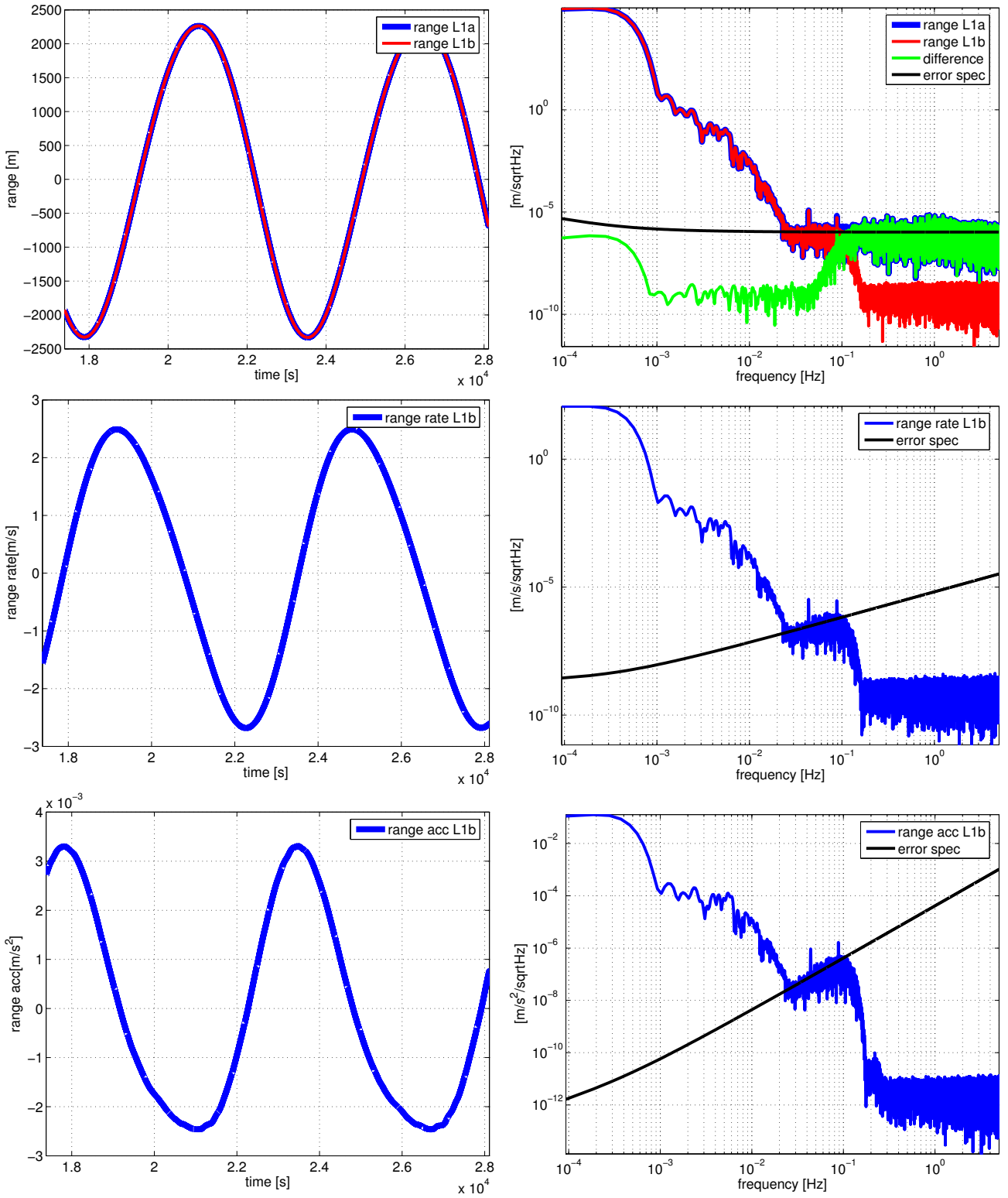

Figure 16.2: Comparison of the L1a and L1b K-band data. The left panels show the time series of the range, range rate and range.

16.3. Accelerometer

As the results for the analysis of the L1b data are similar for GRACE A and GRACE B, this analysis is restricted to the data from GRACE A. The L1b accelerometer data mainly evolves from the L1a accelerometer data through the application of an anti-aliasing low-pass filter. Therefore, one expects the L1b data to be a smoothed version of the L1a data. Figure 16.3 shows the comparison of the L1a and L1b data. The top row shows the measured along-track linear accelerations. The L1a data are dominated by the peak effects and thruster events. In this time series, no periodic behavior is visible. The magnitude is about $3 \cdot 10^{-7}$ m/s^2. The L1b data however show a periodic signal with a period of one revolution with a magnitude smaller than $2 \cdot 10^{-7}$ m/s^2. The periodicity is caused by the fact that all surface forces are caused by effects that are stationary compared to the motion of the satellite relative to the Earth. From one revolution to the other, the satellite encounters almost the same environment and therefore the measured acceleration is periodic with the orbit frequency. The top right panel shows the root PSD of the L1a and L1b data. There is no difference between the two up to the cut-off frequency of the low-pass filter. The signals are strongest at once and twice per revolution, then decaying until at about $2 \cdot 10^{-2}$ Hz the signal of the thruster events dominates the measurement. The signal at 1 Hz and multiples caused by the thruster events is slightly visible. The middle left panel shows the time series of the measured cross-track linear accelerations. The L1a signal is dominated by the twang effects and thruster events, its magnitude reaching up to $3 \cdot 10^{-6}$ m/s^2. That is one order of magnitude larger than the supposedly stronger signal of the along-track component. The L1b data is smaller by two orders of magnitude, reaching up to $0.2 \cdot 10^{-7}$ m/s^2, cf. figure 16.4. The middle panel at the right shows the root PSD of the cross-track linear accelerations. Again there is no difference between L1a and L1b data until the cut-off frequency of the applied low-pass filter. In both data, a strong once per revolution signal is visible. At about $2 \cdot 10^{-2}$ Hz, the signal seems to evolve into white noise at a level of about $1 \cdot 10^{-7}$ m/s^2/$\sqrt{\text{Hz}}$. In the L1a data, the signal at 1 Hz and multiples caused by the thruster events is visible.

The lower left panel shows the time series of the L1a and L1b radial linear acceleration measurements. Here, the L1a data's magnitude is largest, reaching up to $2 \cdot 10^{-5}$ m/s^2. The L1b signal magnitude is significantly smaller, reaching up to $0.5 \cdot 10^{-7}$ m/s^2, cf. figure 16.4. The L1a data is completely dominated by the twang effect and therefore shows no periodicity. In the L1b data, the orbital period is clearly visible, as expected. The lower left panel shows the root PSD of the measured radial accelerations. In both data, the signal at once per revolution is visible. At high frequencies, the L1a data is dominated by the twangs, reaching magnitudes of up to $1 \cdot 10^{-6}$ m/s^2/$\sqrt{\text{Hz}}$. The signal caused by the thrusters is not visible.

In section 14.2, we showed that the peaks and the twangs may have no effect on the lower frequencies, but the thrusters have. We will now compare sample periods of L1a data containing these effects with corresponding epochs of L1b data.

16.3.1. Disturbance effects: peaks, twangs and thruster events

We start with the peak effects. Figure 16.5 shows an example. It looks as if the peaks disappear after the low-pass filtering. The underlying long periodic signal is present, both in the L1a and L1b measurements. The results from section 14.2 confirm this assumption. The possible cause of the peak effects is the operation of switches used for the heating of the accelerometer, cf. Flury et al. (2007).

For the twangs, the findings of the section 14.2 concerning the influence on the lower frequencies of the accelerometer measurements are confirmed. The low-pass filtered L1b data seems not to show the twang effects, cf. figure 16.6.

As discussed in section 14.2, the thruster events influence the total spectrum, i.e. there should be an effect visible after the low-pass filtering. Figure 16.7 seems to confirm this assumption. The sharp peaks of the thruster events visible in the L1a data are still visible, but smoothed and smeared out in the L1b

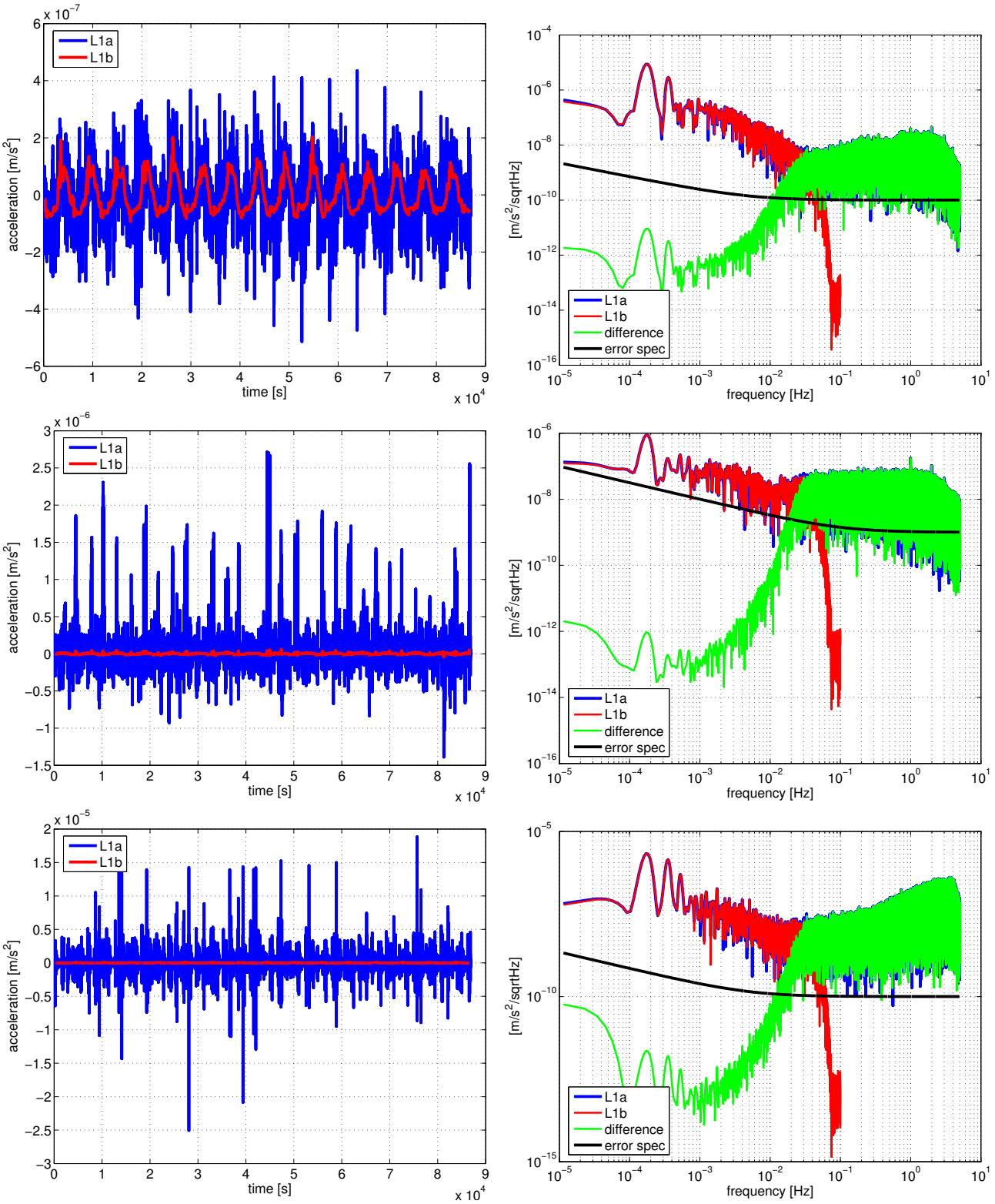

Figure 16.3: Comparison of L1a and L1b accelerometer data for GRACE A. The top row shows the measured along-track accelerations in the time and frequency domain, the middle row the measured cross-track accelerations and the bottom row the measured radial accelerations.

data. There is a part of the thruster events signal affecting only low frequencies that is preserved in the L1b data.

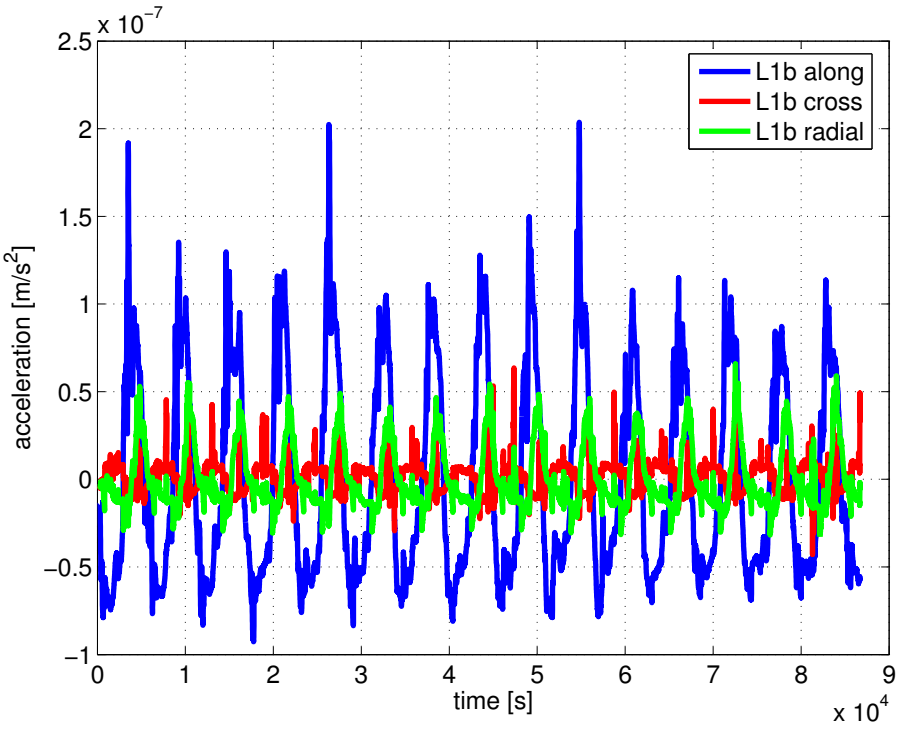

Figure 16.4: L1b accelerometer data for GRACE A.

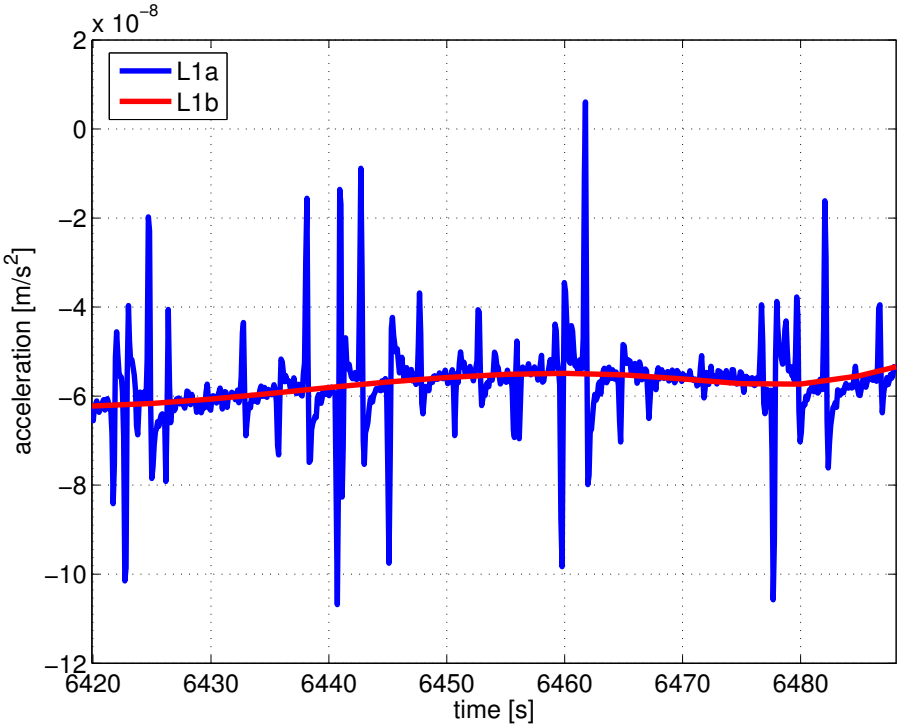

Figure 16.5: Comparison of a period of L1a along-track data containing the peak effect with the corresponding period of the L1b along-track data.

16.3.2. Performance assessment

Since the two effects that represent no actual acceleration on the satellites, the peaks and the twangs, are removed almost completely through the application of the low-pass filter, they do not contribute to

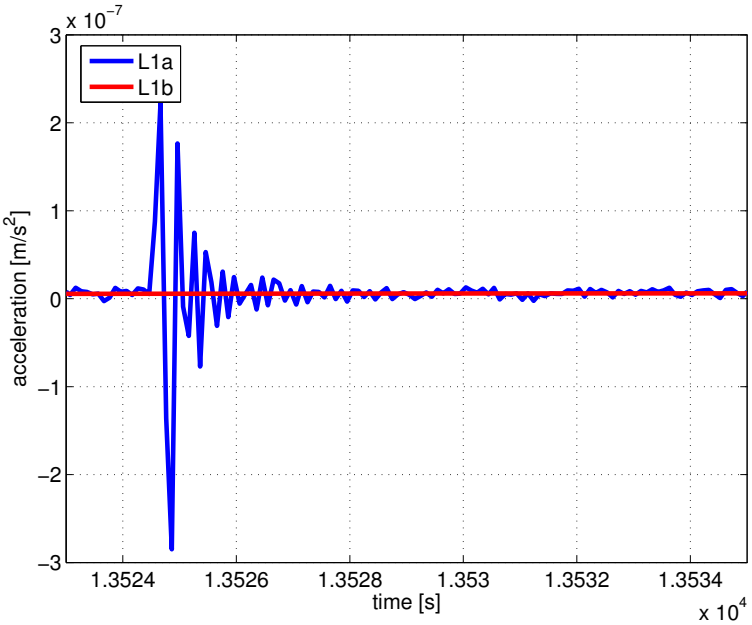

Figure 16.6: Comparison of a period of L1a radial data containing a twang with the corresponding period of the L1b radial data.

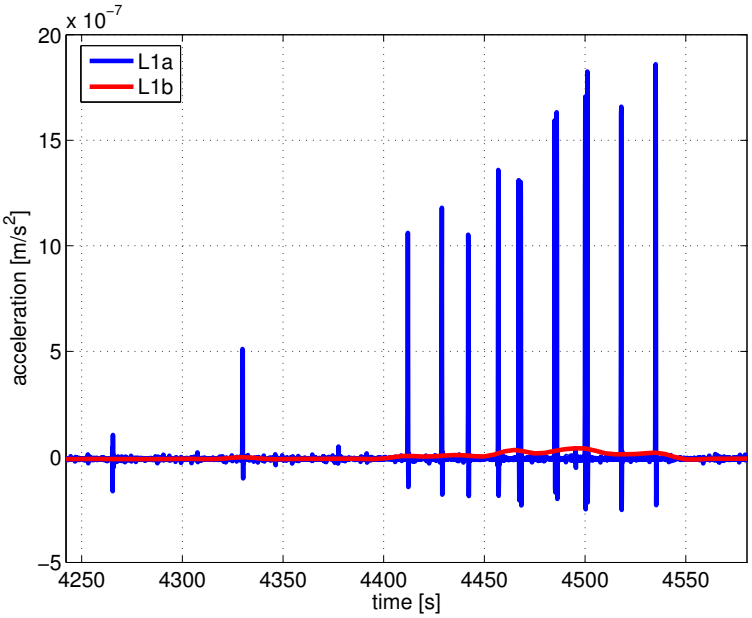

Figure 16.7: Comparison of a period of L1a radial data containing thruster events with the corresponding period of the L1b radial data

the measurement error significantly. The signal introduced into the linear acceleration measurement by the thruster activations represents an actual acceleration on the satellites, therefore it is desired that the accelerometers measure it. It does not contribute to the measurement error budget. In conclusion, the L1b measurement performance is close to the accelerometer performance derived during the L1a data analysis in table 14.1.

16.4. Star Sensor

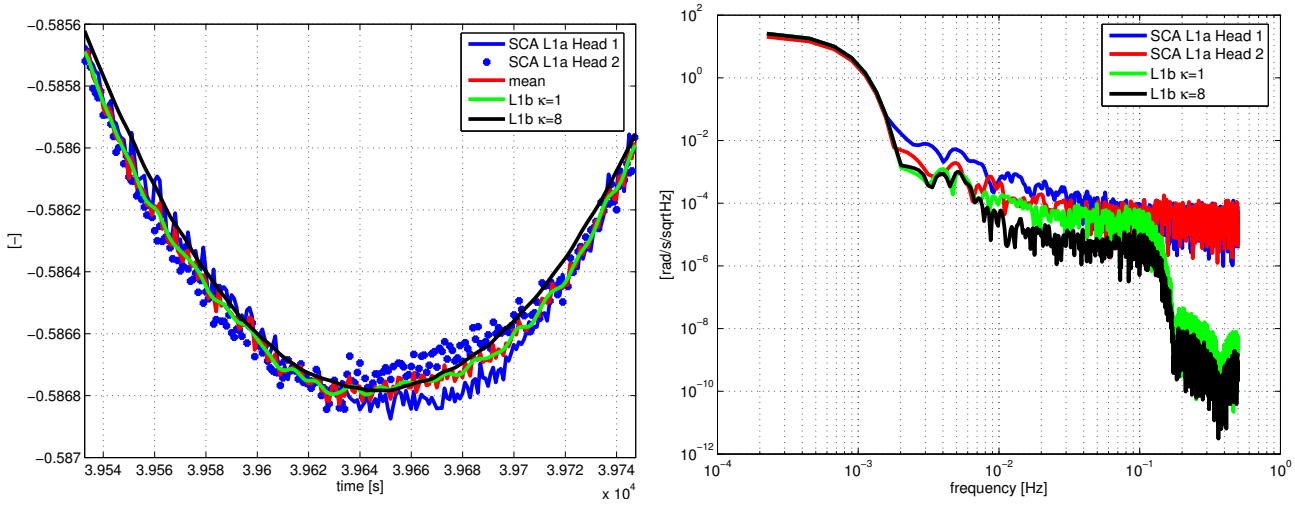

Figure 16.8: Comparison of the L1a and L1b star tracker data. The left panel shows the comparison in the time domain, the right panel shows the comparison in the frequency domain. The original data from both star sensor heads is compared to a simple mean and the result for different values of κ.

The star sensor L1b data is derived from the star sensor L1a through the combination of the data of both sensor heads if possible. The combination takes into account, that the orientation measurement is more accurate for rotations perpendicular to the line of sight of the star tracker. Figure 16.8 shows the comparison of the L1a and L1b data. On the left hand, the time series is shown. The blue lines represent original data from the two sensor heads. The red line represents the mean of both observations. We notice that if the scaling factor $\kappa = 1$, the mean values and the combined values agree, as described in section (15.3). The difference visible in the figure results from the different sampling rates of the L1a data (1 Hz) and the L1b data (0.2 Hz).

The black line represents the combined data for a realistic value of $\kappa = 8$. We realize that the combined data is different from the simple mean. We observe that for some time the combined data is more close the data of head 1, for other times, it is closer to the data of head 2.

The right panel shows the root PSD. As the extent of the analyzed time series is limited, the resolution at low frequencies is limited. When we compare the root PSD of the simple mean with the original spectra, we realize that the measurement noise could be reduced by a factor of about $\sqrt{2}$ as expected. When we compare the root PSD of the combined data with the spectra of the original data, we realize that the noise reduction reduction factor is about 5 times that of the simple mean.

Performance assessment

The specified performance for the star sensor data before the combination is about $1 \cdot 10^{-4}$ rad/$\sqrt{\text{Hz}}$ for quaternion components. The use of the most simple combination method, the derivation of the mean, would improve it to $\frac{1}{\sqrt{2}} \cdot 10^{-4}$ rad/$\sqrt{\text{Hz}}$. The optimal combination seems to reduce the measurement noise to a level of about $1 \cdot 10^{-5}$ rad/$\sqrt{\text{Hz}}$ at frequencies above 10^{-2} Hz. This noise level can be reduced further by the combination of the star tracker measurements with the accelerometer measurements, that is not applied during the standard data processing.

16.5. Combined analysis

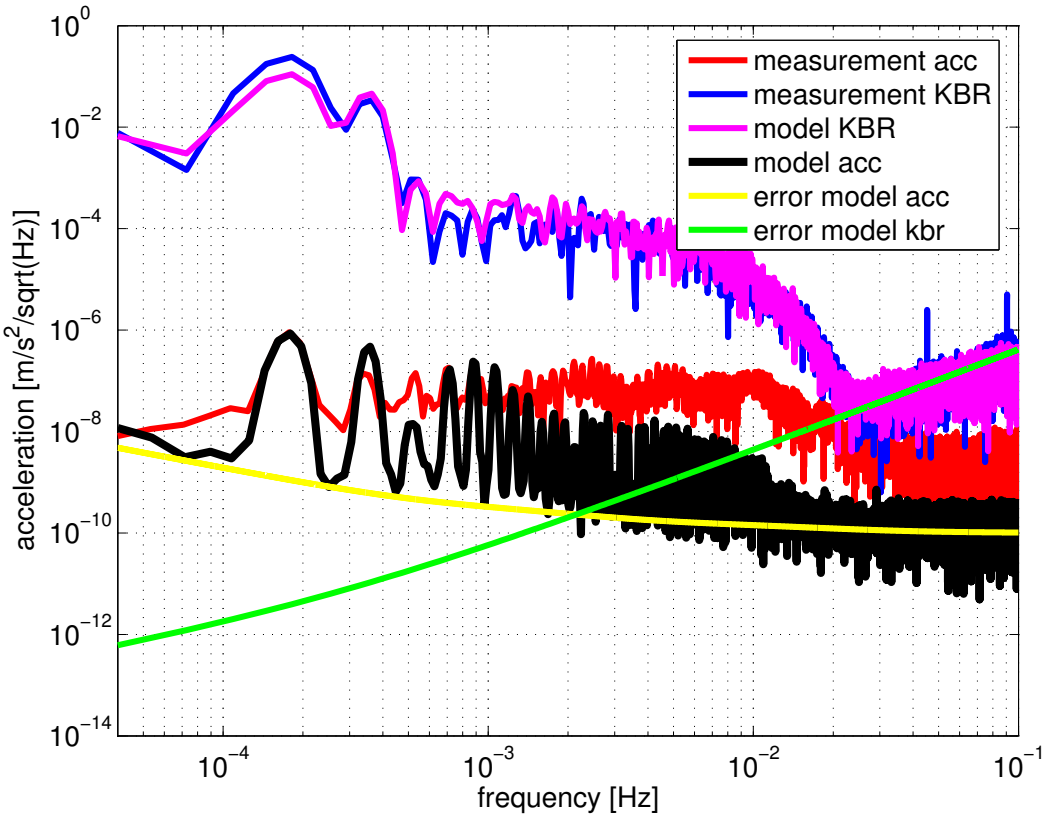

Figure 16.9: Combined analysis showing the differential linear acceleration and the K-band range acceleration measurement and models.

For gravity field analysis, the primary observable, the range / range rate / range acceleration, has to be corrected for the non-gravitational effects from the differential accelerometer measurements. The differential accelerometer measurement vector is derived as the difference of the measurements of GRACE B and A:

$$\bar{\mathrm{a}}_d = \bar{\mathrm{a}}_B - \bar{\mathrm{a}}_A. \tag{16.3}$$

Range, range rate and range acceleration are scalar measurements defined along the line between the mass centers of the two satellites. Therefore the differential acceleration vector measurement has to be projected on the line between the mass centers as well:

$$a_c \quad = \quad |\bar{\mathrm{a}}_d| \cdot (\hat{\mathrm{e}}_{AB} \cdot \hat{\mathrm{a}}_d)\,. \tag{16.4}$$

$\hat{\mathrm{e}}_{AB}$ is the unit vector between the mass centers.

Figure 16.9 shows the comparison of the measured K-band observation, the measured differential acceleration, the corresponding models and error specifications on the level of the differential acceleration, i.e. the K-band observable used is the range acceleration.

Concerning the K-band, we realize that the model and the measurement agree very well, except for the peaks at $4-5\cdot10^{-2}$ Hz and $9\cdot10^{-2}$ Hz. The order of magnitude of the differential acceleration measured by the K-band instrument is about $1\cdot10^{-1}$ m/s$^2/\sqrt{\mathrm{Hz}}$. The signal to noise ratio of 1 is reached at about $2\cdot10^{-2}$ Hz, from there on the noise dominates the measurement. The noise of the real measurement seems to agree well with the specification.

Concerning the differential acceleration, we realize that the model and the measurement do not agree well. The magnitude of the differential acceleration is about five orders of magnitude smaller than that

of the K-band measurements. It is about $1 \cdot 10^{-6}$ m/s$^2/\sqrt{\text{Hz}}$. The signal to noise ratio of 1 is reached at about $2 \cdot 10^{-2}$ Hz. The disagreement of the measured differential acceleration noise level and the specified noise is related to the thruster events mainly. It is assumed that the measurement performance agrees with the specification. The reason for the difference between the modeled acceleration measurement and the real one is twofold: on the one hand, the thruster events are not included in the model, on the other hand it seems that the used air density model is not accurate enough.

The curve of the specified error for the K-band intersects the differential acceleration measurement signal also at about $2 \cdot 10^{-2}$ Hz, i.e. the accelerometer measurements can contribute up to this frequency to the reduction of the K-band measurement for the surface forces. This frequency corresponds to resolution in terms of spherical harmonics of up to degree and order 100. In order to eliminate the influence of the supposedly erroneous effect on the K-band measurements at $4 - 5 \cdot 10^{-2}$ Hz and $9 \cdot 10^{-2}$ Hz, it is suggested to apply a low-pass filter with a cut-off frequency of $2 \cdot 10^{-2}$ Hz to both the accelerometer and the K-band data. Currently, filters with a different cut-off frequency are applied (cf. Wu et al. (2006)).

The conclusion of the combined analysis is that the K-band measurements as well as the accelerometer measurements provide meaningful information up to a frequency of about $2 \cdot 10^{-2}$ Hz over one day. During static gravity field analysis, when time series spanning months or years are used, the resolution may be improved, but it seems that it makes no sense to provide data with a higher sampling rate than the standard sampling rate of 0.2 Hz of the L1b products. We recommend to use the same cut-off frequency for the low-pass filter applied to the K-band data as for the filter applied to the accelerometer measurements: $2 \cdot 10^{-2}$ Hz.

Concerning the peak and twang effects, it can be concluded that they are not significant if the accelerometer data is used in combination with the K-band data as the K-band measurement noise level is higher than the magnitude of these effects.

17. Conclusions and discussion

In the following conclusions are drawn for each part of the work.

17.1. Gravitational forces on the satellites

Concerning the acceleration of the satellites caused by gravitational forces, the acceleration caused by the Earth is strongest, followed by the acceleration caused by the Moon, the Sun, the indirect tides by the Sun and the Moon, the ocean and pole tides and the frequency-dependent corrections to the solid Earth tides in terms of the mean value of the acceleration. An analysis in the frequency domain shows that the main power is at twice per revolution, as the satellites pass through the tidal ellipse. Only for the gravitational acceleration caused by the Earth, the main power is on once per revolution. Table 17.1 shows a comparison of the magnitude of the different effects in terms of an acceleration.

Table 17.1: Comparison of the gravitational accelerations caused by different sources.

Source	mean $[m/s^2]$	power on twice per rev $[m/s^2/\sqrt{Hz}]$	σ $[m/s^2]$
Earth	8.4	$3 \cdot 10^{-2}$ (on 1cpr)	$2 \cdot 10^{-2}$
Direct Sun	$4.5 \cdot 10^{-7}$	$1 \cdot 10^{-5}$	$1 \cdot 10^{-8}$
Direct Moon	$5.5 \cdot 10^{-7}$	$4 \cdot 10^{-6}$	$2 \cdot 10^{-7}$
Indirect Sun	$1.3 \cdot 10^{-7}$	$5 \cdot 10^{-6}$	$2 \cdot 10^{-9}$
Indirect Moon	$1.6 \cdot 10^{-7}$	$8 \cdot 10^{-5}$	$6 \cdot 10^{-8}$
Ocean	$5 \cdot 10^{-8}$	$2 \cdot 10^{-6}$	$2 \cdot 10^{-8}$
Pole	$1 \cdot 10^{-8}$	$6 \cdot 10^{-7}$	$5 \cdot 10^{-9}$
Freq. dep. corr.	$1 \cdot 10^{-8}$	$5 \cdot 10^{-9}$	$2 \cdot 10^{-9}$

17.2. Non-gravitational forces on the satellites

The non-gravitational forces, that act on the satellites, directly affect the K-band measurement as differential accelerations. As for gravity field determination only the gravitational forces by the Earth are the desired quantity, the non-gravitational forces are measured by the accelerometers in order to correct the K-band observations. In this work the forces caused by air drag, solar radiation pressure and Earth albedo have been investigated. The analysis in the spectral domain shows that, apart from a mean value, the main power is at once per revolution. Table 17.2 shows a comparison of the different effects in the satellite fixed reference frame. Air drag is the most dominant source of non-gravitational accelerations, followed by solar radiation pressure and by Earth albedo. Air drag causes a constant acceleration in the along-track direction plus a variation that is dependent on the air density and the satellite's velocity. Solar radiation pressure acts strongest in direction of the radial axis, as the orbit plane was aligned with the direction to the Sun for the analyzed time span. There is no bias due to the Earth shadow entry and exit of the satellite. Earth albedo also acts strongest in direction of the radial

Table 17.2: Comparison of the non-gravitational accelerations caused by different sources.

Source	along $[m/s^2]$	cross-track $[m/s^2]$	radial $[m/s^2]$
Air drag	$(-1.5 \pm 1) \cdot 10^{-7}$	$(0 \pm 1) \cdot 10^{-8}$	$(0.25 \pm 1) \cdot 10^{-8}$
Solar drag	$(0 \pm 2) \cdot 10^{-8}$	$(0 \pm 3) \cdot 10^{-8}$	$(0 + 7) \cdot 10^{-8}$
Albedo	$(0 \pm 1) \cdot 10^{-9}$	$(0 \pm 1) \cdot 10^{-9}$	$-(1.5 + 1) \cdot 10^{-8}$

axis, there is a constant acceleration due to the long-wave albedo caused by the IR radiation emitted by the Earth.

The comparison with the accelerometer measurements shows significant differences between the models and the measurement, regardless of the used air drag models. It is assumed that the challenge lies not in the force models themselves, i.e. the physical model describing the interaction of the atmospheric species and the satellite, but in the used air density model. Of course, there could also be a problem in the solar radiation pressure or the albedo model, but the magnitude of these effects is one order of magnitude smaller than that of the effects caused by the air drag and therefore of less concern.

Concerning the differential acceleration, it seems necessary to include the effect of the thruster events into the drag models, as this effect is a major constituent of the differential acceleration measurement. At low frequencies, the error of the air drag models and the air density model is responsible for the occurring differences.

The magnitude of the difference between the models and the measurement varies geographically. It seems that the largest differences occur close to the polar regions at latitudes higher respectively lower than $\pm 60°$.

A way to improve the air density model would be to estimate the air density from the accelerometer measurements. They have to be corrected for bias, scale factor and the influence from the thruster events. It may also be worthwhile to estimate the accommodation coefficients of the force models. The bias and scale factor of the accelerometers has to be determined during the orbit determination process: first the true orbit is determined, then a second orbit is determined by numerical integration of gravitational accelerations provided by models and of the accelerometer acceleration measurements. The accelerometer scale factor and bias can be determined from the difference of these two orbits.

17.3. Gravity field sensor system

The elements of the mathematical model of the gravity field sensor system are the GPS receiver, the K-band measurement system, the star sensor and the accelerometer.

For data analysis, there are two types of data available: the L1a data and the L1b data.

The L1a data is the unprocessed instrument data at the original sample rates of the corresponding instruments. The high data rate is used to identify the dominant effects in the measurements as well as the measurement and instrument performance.

The L1b data is the processed instrument data given at a reduced sample rate of 0.2 Hz. The sample rate is reduced to smooth the data and thereby remove effects that would deteriorate the quality of the derived gravity fields. A practical aspect is that the required storage space is reduced drastically by about 80 %.

Star sensor

For the star sensor, the measurement noise is assumed to be white. The noise magnitude depends on the direction of the observed rotation: rotations perpendicular to the line of sight of a star camera are determined more accurately than rotations about the line of sight. The measurement itself is delivered as quaternions. Their noise level is about 10 as/$\sqrt{\text{Hz}}$.

The star sensor measurement performance was found to be nominal. Depending on the orbit geometry, Sun/Moon intrusions occur once per revolution on one of the two sensor heads. It seems that the quality of the data from the blinded sensor head deteriorates in the vicinity of the Sun/Moon intrusions.

The processing of the star sensor data offers an interesting opportunity: Both sensor heads of one star sensor deliver the same orientation. Therefore it is possible to combine these measurements. The data from both sensor heads is combined in an optimal way, taking into account the difference in data quality for the derived orientation about the line of sight and perpendicular to the line of sight of the sensor head. The proposed combination method assumes constant data quality.

The L1b star sensor data evolves from this combination of data. It seems that the combination can reduce the noise level by a factor of 5-10 to a level of 10^{-5} rad/$\sqrt{\text{Hz}}$ compared to the noise level of the original measurement of 10^{-4} rad/$\sqrt{\text{Hz}}$.

We could also show that by combination of the accelerometer and the star sensor data, the noise level could be reduced and that also at lower frequencies an improvement at the order of some $1{\cdot}10^{-4}$ rad/$\sqrt{\text{Hz}}$ could be achieved.

Accelerometer

For the accelerometers, there are two dominant noise sources: the acceleration noise, i.e. parasitic accelerations on the proof mass of the accelerometers and the position noise due to deficiencies in the position detection of the proof mass. The accelerometer has two sensitive axes with a noise level of 10^{-10} m/s^2/$\sqrt{\text{Hz}}$ and a less-sensitive axis with a noise level of about 10^{-9} m/s^2/$\sqrt{\text{Hz}}$.

The analysis shows that the linear accelerometer measurements are dominated by three effects, apart from the 'normal' linear accelerations:

- thruster events,
- peaks,
- twangs.

The thruster events have the strongest impact on the measurement, followed by the peaks and the twangs. Only the thruster events seem to have an influence also on the lower frequencies of the measurement spectrum, while the effect of the peaks and twangs seems to be limited to frequencies above 10^{-2} Hz. As conclusion, we can state that the performance of the linear acceleration measurement is about $6 \cdot 10^{-10}$ m/s^2/$\sqrt{\text{Hz}}$, i.e. about 2 times higher than the performance specification, if 5 s data is used. If 1 s data is used and the effects of the twangs and peaks are not corrected, the performance is estimated to be about $1 \cdot 10^{-9}$ m/s^2/$\sqrt{\text{Hz}}$ or about 3-4 times above the specified performance. The effect on monthly gravity field models is estimated to be larger than that for static gravity field models, as there a longer time span is analyzed.

Concerning the rotational acceleration measurement, it was discovered that the thruster events and the magnetic torquers are the main contributors to the measured signal. The rotation about the along-track axis of the SRF is mainly controlled by the thrusters, followed by the rotation about the radial axis. The rotation about the cross-track axis - the highest rotational component - is mainly controlled by the magnetic torquers using the Earth's magnetic field.

The requirements for the accelerometer data for the data processing are not very high, the signal magnitude is several 10^{-7} m/s^2, the instrument accuracy about 10^{-10} m/s^2, i.e. a relative accuracy of about 10^{-4} is sufficient. If the peaks and twangs had an effect on the lower frequencies of the measurement, sophisticated processing algorithms would be needed in order to remove them in a sensible way, but it seems that their effect is limited to the frequencies higher than $1 - 2 \cdot 10^{-2}$ Hz, at least at a level significant above the instruments accuracy.

The L1b accelerometer data differs from the L1a data mainly in terms of its reduced bandwidth. Concerning the three dominant effects, the thruster events, the peaks and the twangs, it seems that only the thruster events have an effect on the L1b linear acceleration measurement. The effects of the twangs and the peaks seem to be smaller or at maximum at the level of the accuracy specified for the sensitive axes. For the official data processing, the bandwidth of the accelerometer data is different from the bandwidth of the K-band data: $3.5 \cdot 10^{-2}$ Hz vs. 0.1 Hz. The measurement performance is estimated to be about 3-4 times the error specification of 10^{-10} m/s$^2/\sqrt{\text{Hz}}$ for the sensitive axes and in agreement with the error specification of 10^{-9} m/s$^2/\sqrt{\text{Hz}}$ for the less-sensitive axis. This measurement performance assessment assumes that both the twangs and peaks are no real accelerations acting on the satellites and therefore have to be considered as an error. The performance of the accelerometers themselves seems to be significantly better but still slightly above the specifications.

K-band measurement system

For the K-band measurement system the phase noise and the system noise are the dominant noise sources.

Concerning the K-band measurement system, the performance was found to be nominal except for an periodic effect occurring about every 25 s. This effect is visible in the data of both satellites. The origin is unknown, it is assumed that a frequency change in the USO of one satellite is responsible for this effect. Concerning the measurement performance, the standard deviation is increased by 33%.

The K-band data is subject to the most demanding requirements for the data processing in terms of accuracy due to the large dynamic range (several km) and the high accuracy (1 µm). The K-band and Ka-band measurements of both satellites are combined in order to form a ionosphere-free biased range. Range rate and range acceleration are derived through application of a differentiator respectively double differentiator filter on the original range measurement. In order to reduce the bandwidth, the design of low-pass filters and single and double differentiators was investigated. As a filter type, the FIR filter was chosen and the window method for the design. It seems that the Kaiser window performs best as a window function. The relative accuracy of the derived filter is about 10^{-15}, but at the cost of an increased filter length, which means an increased amount of data loss in case of gaps. The filter, that is used for the official processing, performs worse but still sufficient, as the absolute filter error is just below the measurement accuracy. An important point for the reduction of the measurement to the line between the mass centers of the satellites is the knowledge of the phase center variations of the K-band antennae. It is assumed that the variation is below 1 µm.

The L1b K-band data still show the effect with a period of 25 s, although it is smaller than in the L1a data. Apart from it, the performance is slightly better than the expected $1 \cdot 10^{-6}$ µm$/\sqrt{\text{Hz}}$. Including this effect, the performance would correspond to a noise level of about $1.3 \cdot 10^{-6}$ µm$/\sqrt{\text{Hz}}$. The performance for the range rate and the range acceleration is similar, as they are just the derivatives of the measured range, their error level is also increased by 33%.

The combined analysis of the accelerometer and the K-band data showed that the accelerometer measurements can be used to reduce the K-band measurements for the effects of non-gravitational accelerations up to a frequency of about $2 \cdot 10^{-2}$ Hz.

The peak and twang effect seem to be not significant for the combination of the accelerometer data with the K-band data as the measurement noise of the K-band is higher than the magnitude of these effects.

GPS receiver

The noise level we derived is significantly below the requirements: about 1 mm/$\sqrt{\text{Hz}}$ for the phase measurement on L1 and about 10 cm/$\sqrt{\text{Hz}}$ for the code measurement on L1. A realistic measurement performance for the L2 measurements can only be derived in the course of a precise orbit determination.

18. Outlook

We close with some suggestions for future research.

18.1. Non-gravitational forces on the satellites

It seems that concerning the non-gravitational forces, the quality of the available air density models might not be sufficient. A possible solution could be to use the accelerometer measurements to estimate the air density together with the accommodation coefficients for each surface element. First, the accelerometer bias and scale factor have to be determined in the course of the orbit determination. An improved model for the air drag could be used to fill data gaps in the accelerometer measurements in a sensible way.

18.2. Level 1a to level 1b data processing

Applied low-pass filter

In order to eliminate the effect in the K-band measurements at $4 \cdot 10^{-2}$ Hz we suggest to use a low-pass filter with a cut-off frequency of $2 \cdot 10^{-2}$ Hz. We also suggest to use the same filter for all observation types, especially for the accelerometer measurements and the K-band measurements, as they are combined directly for the gravity field determination. The filter we derived is very accurate at the cost of an increased filter length. It might be worthwile to investigate a different filter type, e.g. IIR filters. They would have the advantage that they usually require a smaller filter length for achieving the same results as a FIR filter.

Attitude determination

The algorithm used in the official processing of the star sensor data does not take into account that the data from the head which is occasionally blinded by the Sun/Moon is degraded in the vicinity of the Sun/Moon intrusions. It does not use the possibility to combine the star tracker measurements with the accelerometer angular acceleration measurements. The method we used for the combination is simple, it might be worthwhile to investigate more elaborate methods, e.g. using a kalman filter. It would then be sensible to conduct both, the combination of the data from the two sensor heads and of the data from the accelerometer, inside one process. The advantage of the kalman filter would be that the current quality of the input data is estimated as well and the weighting is adjusted accordingly, so that the effect of the Sun/Moon intrusions or any other perhaps unknown effects deteriorating the data quality could be considered.

Acknowledgement

I am very grateful to Prof. R. Rummel for giving me the opportunity to conduct this research. I appreciate the interesting discussions, helpful comments and the precise questions.

I am also indebted to Prof. J. Müller for accepting the position of second advisor, his encouraging comments and helpful discussions.

I also want to thank the German Ministry for Education and Research (BMBF) for the funding of my work in the context of the German GEOTECHNOLOGIEN program.

Further thanks go to my colleagues, that always supported me and created a very amiable working atmosphere.

Last but not least I am grateful to my wife Anja for her support and patience, especially during the final phase of this work.

A. Discrete Fourier transform and discrete filters

A.1. Discrete Fourier Transform (DFT)

The discrete spectrum $X[k]$ of a time series $x[n]$ of N elements given at sampling intervals dt and spanning the interval $T = N \cdot dt$ is given by the Discrete Fourier Transform (DFT):

$$X[k] = \sum_{n=-N_h}^{N_h} x[n] \cdot \mathrm{e}^{-i2\pi \cdot \frac{k}{T} \cdot n \cdot dt}. \tag{A.1}$$

$N_h = (N-1)/2$ for odd N and $N_h = N/2$ for even N is half the number of samples. The time series $x[n]$ corresponding to a spectrum $X[k]$ is given by the Inverse Discrete Fourier Transform (IDFT):

$$x[n] = \frac{1}{N} \sum_{k=-N_h}^{N_h} X[k] \cdot \mathrm{e}^{i2\pi \cdot \frac{k}{T} \cdot n \cdot dt}. \tag{A.2}$$

A.2. Discrete filters

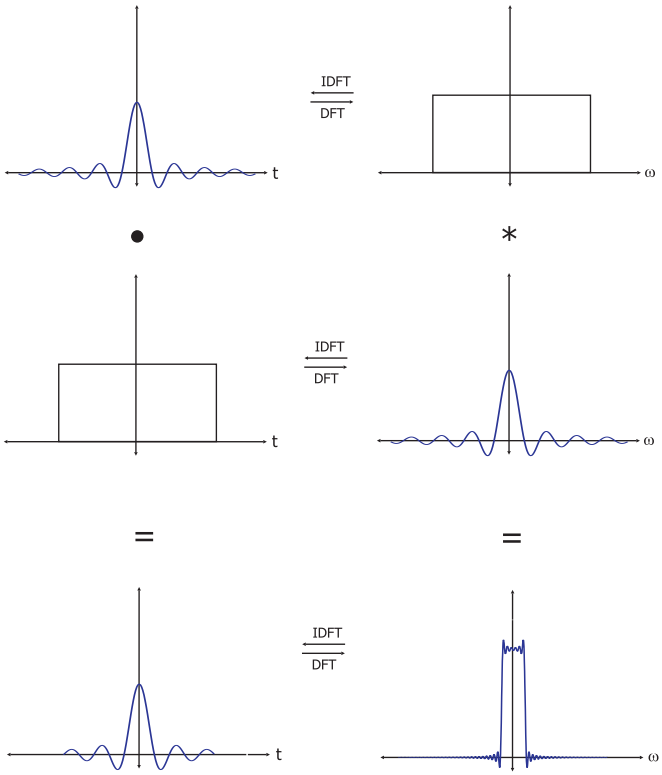

Figure A.1: Impact of the chosen window function on the realization of a low-pass filter with the window method. Here, as an example, the window function chosen to limit the extent of the sinc-function is a rectangle. The left hand side shows the operation in the time domain, the right hand side the operation in the frequency domain.

There are several filter types and design methods, cf. e.g. Best (1991). We use only FIR filters designed with the Window method, as there is no need for real-time processing and a linear phase delay, i.e. a constant time delay corresponding to half the filter length for the filtered data is required. The principle is shown in figure A.1. The desired frequency response of the filter is designed in the frequency domain. The corresponding function in the time domain usually has an unlimited extent. In order to limit the time response of the ideal filter, it is multiplied by a window function. In the figure, an ideal low-pass filter is designed in the frequency domain as a rectangle. The corresponding time domain representation is a function similar to $\frac{\sin x}{\sin y}$ with unlimited extent. The window function chosen to limit the time response is a rectangle. A multiplication in the time domain is a convolution in the frequency domain, i.e. the DFT of the rectangle is convolved with the ideal low-pass filter. The resulting filter deviates from the ideal one depending on the chosen window function.

In the following sections ideal low-pass, differentiator and double differentiator filters are derived.

A.3. Low-pass filter

Let us assume that the desired bandwidth of the low-pass filter is B and that the frequency sampling is $d\omega = \frac{2\pi}{T_f}$ where $T_f = N_f \cdot dt$ is the length of the filters' time response. The rectangle representing the filter shall be centered around the zero frequency. The time response of the filter $LP[n]$ at sample n can then be described as:

$$LP[n] = \frac{1}{N_f} \sum_{k=-N_h}^{N_h} 1 \cdot \mathrm{e}^{i2\pi \cdot \frac{k}{T_f} \cdot n \cdot dt}, \tag{A.3}$$

where $B = (2 \cdot N_h + 1) \cdot d\omega$. This equation can be rewritten as:

$$LP[n] = \frac{1}{N_f} \left[\sum_{k=0}^{N_h} 1 \cdot \mathrm{e}^{-ik \cdot d\omega \cdot n \cdot dt} + \sum_{k=0}^{N_h} 1 \cdot \mathrm{e}^{ik \cdot d\omega \cdot n \cdot dt} - 1 \right]. \tag{A.4}$$

Both series in the above equation are limited geometric series:

$$\sum_{n=0}^{N} x^n = \frac{x^{N+1} - 1}{x - 1}. \tag{A.5}$$

Therefore we get:

$$\begin{aligned}
LP[n] &= \frac{1}{N_f} \left[\frac{\mathrm{e}^{in \cdot dt \cdot d\omega \cdot (N_h+1)} - 1}{\mathrm{e}^{in \cdot dt \cdot d\omega} - 1} + \frac{\mathrm{e}^{-in \cdot dt \cdot d\omega \cdot (N_h+1)} - 1}{\mathrm{e}^{-in \cdot dt \cdot d\omega} - 1} - 1 \right] \\
&= \frac{1}{N_f} \left[\frac{\left[\mathrm{e}^{in \cdot dt \cdot d\omega \cdot (N_h)} - \mathrm{e}^{in \cdot dt \cdot d\omega \cdot (N_h+1)} - \mathrm{e}^{-in \cdot dt \cdot d\omega} + 1\right]}{1 - \mathrm{e}^{in \cdot dt \cdot d\omega} - \mathrm{e}^{-in \cdot dt \cdot d\omega} + 1} \right. \\
&+ \frac{\left[\mathrm{e}^{-in \cdot dt \cdot d\omega \cdot (N_h)} - \mathrm{e}^{-in \cdot dt \cdot d\omega \cdot (N_h+1)} - \mathrm{e}^{in \cdot dt \cdot d\omega} + 1\right]}{1 - \mathrm{e}^{in \cdot dt \cdot d\omega} - \mathrm{e}^{-in \cdot dt \cdot d\omega} + 1} \\
&+ \left. \frac{\left[-1 - 1 + \mathrm{e}^{in \cdot dt \cdot d\omega} + \mathrm{e}^{-in \cdot dt \cdot d\omega}\right]}{1 - \mathrm{e}^{in \cdot dt \cdot d\omega} - \mathrm{e}^{-in \cdot dt \cdot d\omega} + 1} \right] \\
&= \frac{1}{N_f} \left[\frac{\left[\mathrm{e}^{in \cdot dt \cdot d\omega \cdot (N_h)} + \mathrm{e}^{-in \cdot dt \cdot d\omega \cdot (N_h)} - \left(\mathrm{e}^{in \cdot dt \cdot d\omega \cdot (N_h+1)} + \mathrm{e}^{-in \cdot dt \cdot d\omega \cdot (N_h+1)}\right)\right]}{2 - \left(\mathrm{e}^{in \cdot dt \cdot d\omega} + \mathrm{e}^{-in \cdot dt \cdot d\omega}\right)} \right].
\end{aligned} \tag{A.6}$$

Using Euler's identity $\mathrm{e}^{i\phi} = cos(\phi) + i\sin(\phi)$, we see that the imaginary parts cancel out and that two times the real parts remain. The time response of the optimal low-pass filter becomes purely real, as

expected:

$$\begin{aligned} LP[n] &= \frac{1}{N_f}\left[\frac{2\cdot\cos(d\omega\cdot(N_h)\cdot n\cdot dt) - 2\cdot\cos(d\omega\cdot(N_h+1)\cdot n\cdot dt)}{2-2\cos(n\cdot dt\cdot d\omega)}\right] \\ &= \frac{1}{N_f}\left[\frac{\cos(d\omega\cdot(N_h)\cdot n\cdot dt) - \cos(d\omega\cdot(N_h+1)\cdot n\cdot dt)}{1-\cos(n\cdot dt\cdot d\omega)}\right]. \end{aligned} \tag{A.7}$$

Knowing that $\cos(x)-\cos(y) = -2\sin(\frac{x+y}{2})\cdot\sin(\frac{(x-y)}{2})$ and $1-\cos(2x) = 2\sin^2(x)$, we get:

$$\begin{aligned} LP[n] &= \frac{1}{N_f}\left[\frac{-2\sin(\frac{2N_h+1}{2}\cdot d\omega\cdot n\cdot dt)\cdot\sin(-1\cdot\frac{d\omega}{2}\cdot n\cdot dt)}{2\sin^2(n\cdot dt\cdot\frac{d\omega}{2})}\right] \\ &= \frac{1}{N_f}\left[\frac{\sin(n\cdot dt\cdot\frac{(2N_h+1)\cdot d\omega}{2})}{\sin(n\cdot dt\cdot\frac{d\omega}{2})}\right] \\ &= \frac{1}{N_f}\left[\frac{\sin(n\cdot dt\cdot\frac{B}{2})}{\sin(n\cdot dt\cdot\frac{d\omega}{2})}\right]. \end{aligned} \tag{A.8}$$

This result differs significantly from the results given e.g. in Meyer (1998), where as the inverse discrete Fourier transformation of the optimal low-pass filter the *sinc*-function is given. There it is assumed that the time series' extent is unlimited, which is never the case for practical applications.

The derived expression has a singularity for $n = 0$. As $\sin(x) = x$ for small x we get:

$$\lim_{n\to 0}\left(\frac{1}{N_f}\left[\frac{\sin(n\cdot dt\cdot\frac{B}{2})}{\sin(n\cdot dt\cdot\frac{d\omega}{2})}\right]\right) = \frac{1}{N_f}\left[\frac{n\cdot dt\cdot\frac{B}{2}}{n\cdot dt\cdot\frac{d\omega}{2}}\right] = \frac{1}{N_f}\left[\frac{B}{d\omega}\right]. \tag{A.9}$$

The derived expression for the inverse discrete Fourier transform of a rectangle in the spectral domain allows us to derive the expression for the discrete Fourier transform of a rectangle in the time domain because of the duality of the frequency and the time domain by exchanging dt with $d\omega$ and B with T_R, the time span of the rectangle:

$$RECT[k] = \sum_{n=-N_h}^{N_h} 1\cdot\mathrm{e}^{-i\cdot kd\omega\cdot ndt} = \frac{\sin(k\cdot d\omega\cdot\frac{T_R}{2})}{\sin(k\cdot d\omega\cdot\frac{dt}{2})}, \tag{A.10}$$

$$RECT[0] = \frac{T_R}{dt}. \tag{A.11}$$

The time domain representation of the filter is derived by multiplication with the chosen window function:

$$H_{LP}[n] = W[n]\cdot LP[n]. \tag{A.12}$$

A.4. High-pass filter

The high-pass filter can be specified easily in the frequency domain:

$$H_{HP}[k] = 1 - H_{LP}[k]. \tag{A.13}$$

The high-pass filter is kind of an inverse of the low-pass filter. The pass-band of the low-pass filter is the stop-band of the high-pass filter and vice versa.

The time domain representation can be derived in the following way, using equation (A.4):

$$\begin{aligned} HP[n] &= \frac{1}{N_f}\left[\sum_{k=-N_{hf}}^{-N_h-1} 1\cdot \mathrm{e}^{i2\pi\cdot\frac{k}{T_f}\cdot n\cdot dt} + \sum_{k=N_h+1}^{N_{hf}} 1\cdot \mathrm{e}^{i2\pi\cdot\frac{k}{T_f}\cdot n\cdot dt}\right] \\ &= \frac{1}{N_f}\left[\sum_{k=-N_{hf}}^{N_{hf}} 1\cdot \mathrm{e}^{i2\pi\cdot\frac{k}{T_f}\cdot n\cdot dt} - \sum_{k=-N_h}^{N_h} 1\cdot \mathrm{e}^{i2\pi\cdot\frac{k}{T_f}\cdot n\cdot dt}\right] \\ &= \frac{1}{N_f}\left[\frac{\sin(n\cdot dt\cdot\frac{(2N_{hf}+1)\cdot d\omega}{2}) - \sin(n\cdot dt\cdot\frac{B}{2})}{\sin(n\cdot dt\cdot\frac{d\omega}{2})}\right], \qquad \text{(A.14)} \\ HP[0] &= \frac{1}{N_f}\left[2N_{hf}+1-\frac{B}{d\omega}\right] = 1-\frac{1}{N_f}\left[\frac{B}{\cdot d\omega}\right]. \qquad \text{(A.15)} \end{aligned}$$

and the other results derived for the low-pass filter. $2N_h+1$ is the number of samples contained in the stop band of the filter, $2N_{hf}+1=N_f$ is the number of samples of the spectrum/time response of the filter. The time domain representation of the filter is derived by multiplication with the chosen window function:

$$H_{HP}[n] = W[n]\cdot HP[n]. \qquad \text{(A.16)}$$

A.5. Differentiator

Differentiation in the time domain corresponds to a multiplication in the frequency domain with $i\omega$. We will now use the same approach as for the design of the low-pass filter: First, the time domain representation of the 'optimal' differentiator will be derived.

$$\begin{aligned} D[n] &= IDFT[D[\omega]] = \frac{1}{N_f}\cdot\sum_{k=-N_h}^{N_h} 1\cdot ik\cdot d\omega\cdot \mathrm{e}^{ik\cdot d\omega\cdot n\cdot dt} \\ &= \frac{d}{d(n\cdot dt)}[LP[n]] = \frac{d}{dt}[LP[n]], \qquad \text{(A.17)} \end{aligned}$$

which is the time derivative of the optimal low-pass filter. The time domain representation of the optimal differentiator is then given by:

$$\begin{aligned} D[n] &= \frac{d}{d(n\cdot dt)}\left(\frac{\sin\left(n\cdot dt\cdot\frac{B}{2}\right)}{\sin\left(n\cdot dt\cdot\frac{d\omega}{2}\right)}\right)\cdot\frac{1}{N_f} \\ &= \frac{\frac{B}{2}\cos(n\cdot dt\cdot\frac{B}{2})\cdot\sin(n\cdot dt\cdot\frac{d\omega}{2}) - \frac{d\omega}{2}\cdot\cos(n\cdot dt\cdot\frac{d\omega}{2})\cdot\sin(n\cdot dt\cdot\frac{B}{2})}{\sin^2(n\cdot dt\cdot\frac{d\omega}{2})}\cdot\frac{1}{N_f}, \qquad \text{(A.18)} \\ D[0] &= \frac{\frac{B}{2}\cdot 1\cdot n\cdot dt\cdot\frac{d\omega}{2} - \frac{d\omega}{2}\cdot 1\cdot n\cdot dt\cdot\frac{B}{2}}{(n\cdot dt\cdot\frac{d\omega}{2})^2}\cdot\frac{1}{N_f} = 0. \qquad \text{(A.19)} \end{aligned}$$

As a second step, this time domain representation will again be limited by a multiplication with a window function:

$$H_D[n] = W[n]\cdot D[n]. \qquad \text{(A.20)}$$

A.6. Double differentiator

A double differentiator is derived in the same way: First, we get the time domain representation of the optimal double differentiator as the derivative of the optimal differentiator:

$$\begin{aligned}
DD[n] &= \frac{1}{N_f} \cdot \frac{d}{d(n \cdot dt)} \left(\frac{\frac{B}{2}\cos(ndt \cdot \frac{B}{2}) \cdot \sin(ndt \cdot \frac{d\omega}{2}) - \frac{d\omega}{2} \cdot \cos(ndt \cdot \frac{d\omega}{2}) \cdot \sin(ndt \cdot \frac{B}{2})}{\sin^2(ndt \cdot \frac{d\omega}{2})} \right) \\
&= \frac{1}{N_f} \cdot \frac{\left(\frac{d\omega^2}{4} - \frac{B^2}{4}\right) \cdot \sin(ndt \cdot \frac{B}{2}) \cdot \sin(ndt \cdot \frac{d\omega}{2}) \cdot \sin^2(ndt \cdot \frac{d\omega}{2})}{\sin^4(ndt \cdot \frac{d\omega}{2})} \\
&- 2\sin(ndt \cdot \frac{d\omega}{2}) \cdot \cos(ndt \cdot \frac{d\omega}{2}) \cdot \frac{d\omega}{2} \\
&\cdot \frac{\left(\cos(ndt \cdot \frac{B}{2}) \cdot \sin(ndt \cdot \frac{d\omega}{2}) \cdot \frac{B}{2} - \frac{d\omega}{2} \cdot \cos(ndt \cdot \frac{d\omega}{2}) \cdot \sin(ndt \cdot \frac{B}{2})\right)}{\sin^4(ndt \cdot \frac{d\omega}{2})} \\
&= \frac{1}{N_f} \cdot \frac{\left(\frac{d\omega^2}{4} - \frac{B^2}{4}\right) \cdot \sin(ndt \cdot \frac{B}{2})}{\sin(ndt \cdot \frac{d\omega}{2})} \\
&- \frac{2 \cdot \cos(ndt \cdot \frac{d\omega}{2}) \cdot \frac{d\omega}{2} \cdot \left(\cos(ndt \cdot \frac{B}{2}) \cdot \sin(ndt \cdot \frac{d\omega}{2}) \cdot \frac{B}{2} - \frac{d\omega}{2} \cdot \cos(ndt \cdot \frac{d\omega}{2}) \cdot \sin(ndt \cdot \frac{B}{2})\right)}{\sin^3(ndt \cdot \frac{d\omega}{2})}.
\end{aligned} \tag{A.21}$$

The value for $n = 0$ is then given by:

$$\begin{aligned}
DD[0] &= \frac{1}{N_f} \cdot \frac{\left(\frac{d\omega^2}{4} - \frac{B^2}{4}\right) ndt \cdot \frac{B}{2}}{ndt \cdot \frac{d\omega}{2}} \\
&- \frac{\left(2 \cdot \left(\cos(ndt \cdot \frac{B}{2}) \cdot \sin(ndt \cdot \frac{d\omega}{2}) \cdot \frac{B}{2} \cdot \frac{d\omega}{2} - \left(\frac{d\omega}{2}\right)^2 \cdot \cos(ndt \cdot \frac{d\omega}{2}) \cdot \sin(ndt \cdot \frac{B}{2})\right)\right)'}{\left(\sin^3(ndt \cdot \frac{d\omega}{2})\right)'} \\
&= \frac{1}{N_f} \cdot \left(\left[\frac{d\omega}{2}\right]^2 - \left[\frac{B}{2}\right]^2\right) \cdot \frac{B}{d\omega} \\
&- \frac{2 \cdot \left(-\sin(ndt \cdot \frac{B}{2}) \cdot \sin(ndt \cdot \frac{d\omega}{2}) \cdot \left(\frac{B}{2}\right)^2 \cdot \frac{d\omega}{2} + \left(\frac{d\omega}{2}\right)^3 \cdot \sin(ndt \cdot \frac{d\omega}{2}) \cdot \sin(ndt \cdot \frac{B}{2})\right)}{3\sin^2(ndt \cdot \frac{d\omega}{2}) \cdot \cos(ndt \cdot \frac{d\omega}{2}) \cdot \frac{d\omega}{2}} \\
&= \frac{1}{N_f} \cdot \left(\left[\frac{d\omega}{2}\right]^2 - \left[\frac{B}{2}\right]^2\right) \cdot \frac{B}{d\omega} \\
&- \frac{2}{3} \cdot \frac{(ndt)^2 \cdot \left(\frac{d\omega}{2}\right)^4 \cdot \left(\frac{B}{2}\right) - (ndt)^2 \cdot \left(\frac{B}{2}\right)^3 \cdot \left(\frac{d\omega}{2}\right)^2}{(ndt)^2 \cdot \left(\frac{d\omega}{2}\right)^3} \\
&= \frac{1}{N_f} \cdot \left(\left[\frac{d\omega}{2}\right]^2 - \left[\frac{B}{2}\right]^2\right) \cdot \frac{B}{d\omega} \\
&- \frac{2}{3}\left[\left(\frac{d\omega}{2}\right) \cdot \left(\frac{B}{2}\right) - \left(\frac{B}{2}\right)^3 \cdot \left(\frac{2}{d\omega}\right)\right] \\
&= \frac{1}{N_f} \cdot \frac{1}{3} \cdot \left(\left[\frac{d\omega}{2}\right]^2 - \left[\frac{B}{2}\right]^2\right) \cdot \frac{B}{d\omega}.
\end{aligned} \tag{A.22}$$

The time domain representation of the filter is derived by multiplication with the chosen window function:

$$H_{DD}[n] = W[n] \cdot DD[n]. \tag{A.23}$$

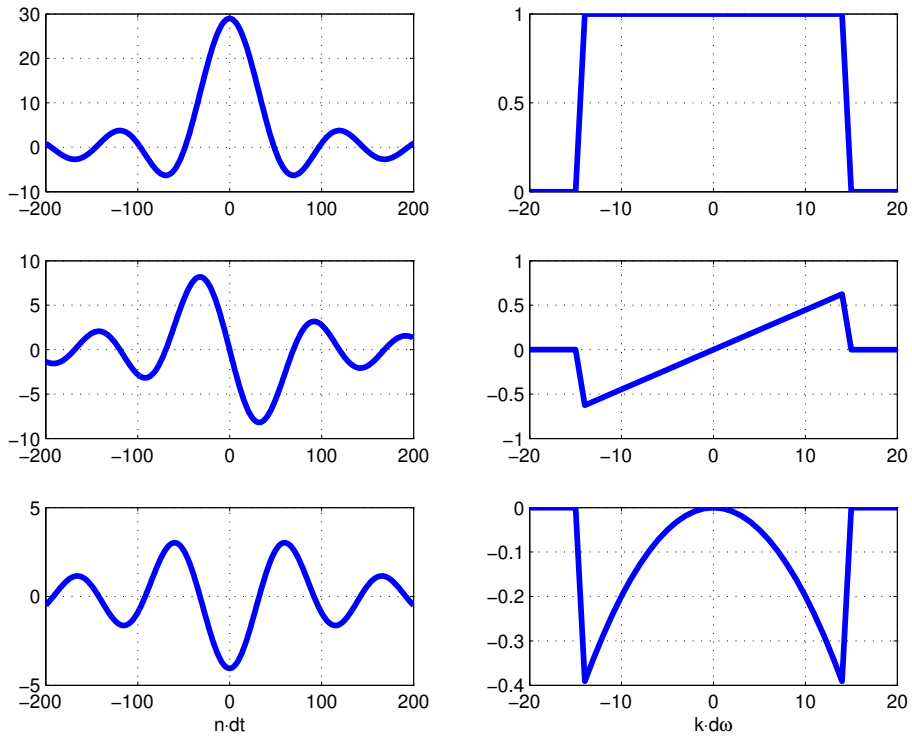

Figure A.2: Optimal low-pass filter, differentiator and double differentiator in the time and the frequency domain. The left hand panels show the time domain representation of the optimal low-pass filter, differentiator and double differentiator. The right hand panels show the corresponding representation in the frequency domain. Differentiation in the frequency domain corresponds to a multiplication with a straight line, double differentiation corresponds to a multiplication with a parabola.

A.7. Filter scaling

So far an important problem has not been addressed: the derived filters have to be scaled in order to approximate the optimal filters as good as possible. The scaling has to be a constant and independent of the frequency, as otherwise the multiplication by a frequency dependent scaling function would result in an undesired convolution of the time domain representation of the filter.

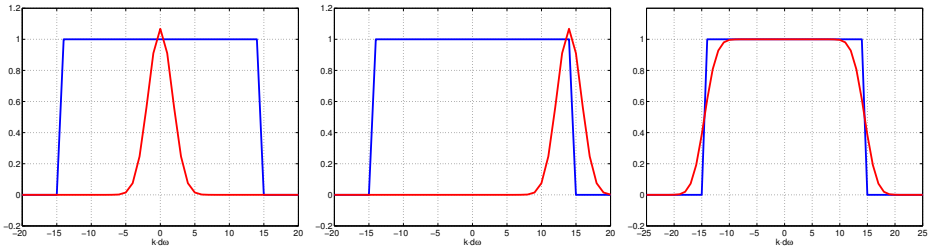

Figure A.3: Convolution of the optimal low-pass filter with the spectrum of the chosen window function. The rightmost figure shows the resulting spectrum (red) after the convolution.

Let us first return to the optimal low-pass filter. In the frequency domain, it is a rectangle of a certain extent with height one, cf. figure A.2. When the extent in the time domain is limited to the desired filter length, this rectangle is convolved with the frequency representation of the chosen window function. It is now assumed that the window function is symmetric and that the number of epochs covered is odd.

Then the spectrum of the unscaled filter is given as:

$$H_{LP}[\omega] = \sum_{j=-N_h}^{N_h} LP[\omega + j \cdot d\omega] \cdot W[j \cdot d\omega]. \tag{A.24}$$

During this convolution, the spectrum of the window function is moved against the spectrum of the low-pass filter. There are two principal situations, cf. figure A.3:

- The spectrum of the window function is completely inside the pass-band.
- The spectrum of the window function is partly outside the pass-band.

The speciality of the low-pass filter is that its value inside the pass-band is independent of the frequency, as it is one. So we get for frequencies where the first case is true:

$$\begin{aligned} H_{LP}[\omega] &= 1 \cdot \sum_{j=-N_h}^{N_h} W[j \cdot d\omega] \\ &= LP[\omega] \cdot \sum_{j=-N_h}^{N_h} W[j \cdot d\omega]. \end{aligned} \tag{A.25}$$

That means that the correct value, one, is replaced by the sum of the spectrum of the window function. The correct scaling factor is then just this number.

$$SF_{LP} = \sum_{j=-N_h}^{N_h} W[j \cdot d\omega], \tag{A.26}$$

$$H^s_{LP}[\omega] = \frac{H_{LP}[\omega]}{SF_{LP}}. \tag{A.27}$$

For the second case, where the spectrum of the window function is partly outside of the pass-band, the correct scaling becomes frequency dependent and is therefore not applied.

The spectrum therefore deviates from one in the frequency range close to the cut-off frequency, compare figure A.3.

For the high-pass filter, the same scaling factor as for the low-pass filter is applicable.

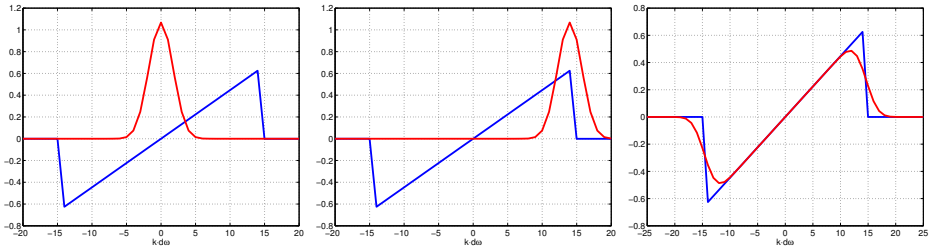

Figure A.4: Convolution of the optimal differentiator filter with the spectrum of the chosen window function. The rightmost figure shows the resulting spectrum (red) after the convolution.

Let us now derive the optimal scaling factor for the differentiator. As for the low-pass filter, only the case where the window function spectrum fully covers the pass-band has to be considered. If we now consider the spectrum of the optimal differentiator inside the pass-band across the window width, we

realize that it is symmetric, as it is a linear function of the frequency, cf. figure A.4:

$$\begin{aligned} H_D[\omega] &= \sum_{j=-N_h}^{N_h} D[\omega + j \cdot d\omega] \cdot W[j \cdot d\omega] \\ &= \sum_{j=-N_h}^{N_h} \omega \cdot W[j \cdot d\omega] + j \cdot d\omega \cdot W[j \cdot d\omega] \\ &= \sum_{j=-N_h}^{N_h} \omega \cdot W[j \cdot d\omega] \\ &= D[\omega] \cdot \sum_{j=-N_h}^{N_h} W[j \cdot d\omega]. \end{aligned} \tag{A.28}$$

The scaling factor is the same as for the low-pass filter:

$$SF_D = SF_{LP} = \sum_{j=-N_h}^{N_h} W[j \cdot d\omega], \tag{A.29}$$

$$H_D^s[\omega] = \frac{H_D[\omega]}{SF_D}. \tag{A.30}$$

Things are different for the double differentiator filter:

$$\begin{aligned} H_{DD}[\omega] &= \sum_{j=-N_h}^{N_h} DD[\omega + j \cdot d\omega] \cdot W[j \cdot d\omega] \\ &= \sum_{j=-N_h}^{N_h} -(\omega + j \cdot d\omega)^2 \cdot W[j \cdot d\omega] \\ &= -\sum_{j=-N_h}^{N_h} \omega^2 \cdot W[j \cdot d\omega] - \sum_{j=-N_h}^{N_h} 2 \cdot \omega \cdot j \cdot d\omega - \sum_{j=-N_h}^{N_h} (j \cdot d\omega)^2 \\ &= DD[\omega] \sum_{j=-N_h}^{N_h} W[j \cdot d\omega] - \sum_{j=-N_h}^{N_h} (j \cdot d\omega)^2 \\ &= DD[\omega] \sum_{j=-N_h}^{N_h} W[j \cdot d\omega] - \frac{1}{3}(\mathrm{d}\,\omega)^2 \cdot (N_h(N_h+1)(2N_h+1)). \end{aligned} \tag{A.31}$$

It is not possible to correct the effect of the application of the window function by a simple scaling:

$$H_{DD}^s[\omega] = \frac{H_{DD}[\omega] + \frac{1}{3}(\mathrm{d}\,\omega)^2 \cdot (N_h(N_h+1)(2N_h+1))}{\sum_{j=-N_h}^{N_h} W[j \cdot d\omega]}. \tag{A.32}$$

Although the applied corrections are constants, the values of the corrected filter in the stop band are no longer zero. A possible solution is to low-pass filter the corrected filter, but this seems not to be straightforward. The window method itself might not be suited ideally to design a double differentiator. In Wu et al. (2006) and Thomas (1999), the design of the differentiator and the double differentiator is proposed differently. There, the idea is to apply the derived low-pass filter on the ideal differentiator and the ideal double differentiator:

$$H_D[n] = IDFT[H_{LP}[\omega] \cdot i\omega], \tag{A.33}$$

$$H_{DD}[n] = IDFT[H_{LP}[\omega] \cdot -\omega^2]. \tag{A.34}$$

These operations are the same as taking the first respectively second order time derivative of the windowed low-pass filter.

B. Power spectral density (PSD) and standard deviation

The Power Spectral Density (PSD) of a discrete signal can be derived from its spectrum by, cf. Müller (2001), Oppenheim and Schafer (1989), Oppenheim and Schafer (1975) and Stoica and Moses (1997):

$$P[k \cdot \Delta f] = X[k \cdot \Delta f]^2 \cdot \frac{\Delta t}{SF}, \quad k = [-N/2; N/2], \tag{B.1}$$

for a two-sided PSD and

$$P[k \cdot \Delta f] = X[k \cdot \Delta f]^2 \cdot \frac{2\Delta t}{SF}, \quad k = [0; N/2], \tag{B.2}$$

for a one-sided PSD. The unit of the PSD is $\frac{\text{unit}^2}{\text{Hz}}$, where *unit* is the physical unit of the input signal. Two-sided means that also negative frequencies are considered, one-sided means that only the positive frequencies are considered. In this latter case, the spectrum has to be multiplied by two in order to obtain the full power. SF is a scaling factor depending on the chosen window function that is used to scale the time series. Usually a rectangle with height one and length $N \cdot \Delta t$ is used, then

$$SF = \sum_{n=0}^{N-1} |window[n \cdot \Delta t]|^2 = \sum_{n=0}^{N-1} |RECT[n \cdot \Delta t]|^2 = N. \tag{B.3}$$

The square of the standard deviation or variance of a certain bandwidth is approximated by the discrete integral over this band:

$$\sigma_{bw}^2 = \sum_{k=a}^{k=b} P[k \cdot \Delta f] \cdot \Delta f. \tag{B.4}$$

Two practical issues occur in the error modeling of sensors:

1. The standard deviation shall be approximated from a given (white) noise PSD.
2. The (white) noise PSD shall be approximated from a given standard deviation.

Now the considered band is the Nyquist interval, i.e. $k = [0; N]$ for the two-sided PSD respectively $k = [0; N/2]$ for the one-sided PSD, disregarding the difference between odd or even N, as a large N is assumed. We will only consider the commonly used one-sided PSD. From a given (white) noise PSD with a noise level of $A[\frac{\text{unit}^2}{\text{Hz}}]$, we estimate the variance and standard deviation as:

$$\sigma_A^2 = \sum_{k=0}^{N/2} A[k \cdot \Delta f] \cdot \Delta f = \frac{N}{2} \cdot A \cdot \frac{1}{N \cdot \Delta t} = \frac{A}{2\Delta t}, \tag{B.5}$$

$$\sigma_A = \sqrt{\frac{A}{2\Delta t}}. \tag{B.6}$$

The PSD corresponding to a given standard deviation of σ_B can be approximated by the inverse relation as:

$$P_B[k \cdot \Delta f] = 2\Delta t \cdot \sigma_B^2. \tag{B.7}$$

In MATLAB, the function *randn* can be used to simulate white noise with a certain standard deviation. As an example, let us assume that we want to simulate white noise with a power of $1 \cdot 10^{-}18 \frac{\mathrm{m}^2}{\mathrm{s}^4 \mathrm{Hz}}$ with a 1 s sampling. The corresponding standard deviation would then be $\sigma \approx 7 \cdot 10^{-10} \mathrm{m/s}^2$. The corresponding noise time series of length N can then be generated by

```
noise=7e-10*randn(N,1).
```

If one forms the difference between two uncorrelated noise signals, the noise does not cancel out but adds up in terms of noise power. If one considers the root PSD, the noise is increased by a factor of $\sqrt{2}$.

C. Orientation representations and coordinate transforms

Direction cosine matrix

An orientation representation is the description of the orientation of a coordinate system (target system) with respect to another coordinate system (source system). A very common way of representation is the direction cosine matrix (DCM). It is defined as (cf. Wertz (1991)):

$$\underline{\mathrm{R}}_s^t = \begin{bmatrix} \widehat{\mathrm{X}}_t^{s'} \\ \widehat{\mathrm{Y}}_t^{s'} \\ \widehat{\mathrm{Z}}_t^{s'} \end{bmatrix} = \begin{bmatrix} X_{t,1}^s & X_{t,2}^s & X_{t,3}^s \\ Y_{t,1}^s & Y_{t,2}^s & Y_{t,3}^s \\ Z_{t,1}^s & Z_{t,2}^s & Z_{t,3}^s \end{bmatrix}, \tag{C.1}$$

where

$$\widehat{\mathrm{X}}_t^s = \begin{pmatrix} X_{t,1} \\ X_{t,2} \\ X_{t,3} \end{pmatrix}, \tag{C.2}$$

$$\widehat{\mathrm{Y}}_t^s = \begin{pmatrix} Y_{t,1} \\ Y_{t,2} \\ Y_{t,3} \end{pmatrix}, \tag{C.3}$$

$$\widehat{\mathrm{Z}}_t^s = \begin{pmatrix} Z_{t,1} \\ Z_{t,2} \\ Z_{t,3} \end{pmatrix} \tag{C.4}$$

are the unit base vectors of the target coordinate system expressed in the source coordinate system. If the vectors are arranged row wise as described above, the resulting matrix $\underline{\mathrm{R}}_s^t$ transforms a vector from the source system to the target system by a multiplication from the left:

$$\overline{\mathrm{V}}_t = \underline{\mathrm{R}}_s^t \cdot \overline{\mathrm{V}}_s. \tag{C.5}$$

The inverse transformation is given by:

$$\overline{\mathrm{V}}_s = (\underline{\mathrm{R}}_s^t)^{-1} \cdot \overline{\mathrm{V}}_t, \tag{C.6}$$

where

$$(\underline{\mathrm{R}}_s^t)^{-1} = (\underline{\mathrm{R}}_s^t)' = \begin{bmatrix} X_{t,1}^s & Y_{t,1}^s & Z_{t,1}^s \\ X_{t,2}^s & Y_{t,2}^s & Z_{t,2}^s \\ X_{t,3}^s & Y_{t,3}^s & Z_{t,3}^s \end{bmatrix}. \tag{C.7}$$

The inverse of the rotation matrix is just its transpose as it is orthonormal. Consecutive rotations can be represented as a single rotation matrix:

$$\underline{\mathrm{R}}_a^c = \underline{\mathrm{R}}_b^c \cdot \underline{\mathrm{R}}_a^b. \tag{C.8}$$

Quaternions

The quaternion representation of a rotation involves the Euler symmetric parameters. Originally they were introduced by Hamilton and Whittaker; the following description is from Wertz (1991). A quaternion is a hypercomplex number, having one real part and three complex parts:

$$\begin{aligned} \overline{\mathrm{Q}}_s^t &= (q_0 + iq_1 + jq_2 + kq_3) \\ &= (\cos(\frac{\Phi}{2}) + \sin(\frac{\Phi}{2}) \cdot e_x + \sin(\frac{\Phi}{2}) \cdot e_y + \sin(\frac{\Phi}{2}) \cdot e_z), \qquad \text{(C.9)} \\ (\overline{\mathrm{Q}}_s^t)^{-1} &= (-q_0 + iq_1 + jq_2 + kq_3) = (q_0 - iq_1 - jq_2 - kq_3). \qquad \text{(C.10)} \end{aligned}$$

$q0 = \cos(\Phi/2)$ depends on the rotation angle Φ and $q1$ to $q3$ on the axis of the rotation. e_x, e_y, e_z are the components of the rotation axis. Consecutive rotations are represented by the multiplication of the quaternions representing the rotations from the right, not from the left as for the representation by the DCM:

$$\overline{\mathrm{Q}}'' = \overline{\mathrm{Q}} \star \overline{\mathrm{Q}}', \qquad \text{(C.11)}$$

$$\begin{bmatrix} q_1'' \\ q_2'' \\ q_3'' \\ q_0'' \end{bmatrix} = \begin{bmatrix} q_0' & q_3' & -q_2' & q_1' \\ -q_3' & q_0' & q_1' & q_2' \\ q_2' & -q_1' & q_0' & q_3' \\ -q_1' & -q_2' & -q_3' & q_0' \end{bmatrix} \cdot \begin{bmatrix} q_1 \\ q_2 \\ q_3 \\ q_0 \end{bmatrix}. \qquad \text{(C.12)}$$

The transformation of a vector can be accomplished by the following operation:

$$\overline{\mathrm{V}}_t = (\overline{\mathrm{Q}}_s^t)^{-1} \star \overline{\mathrm{V}}_s \star \overline{\mathrm{Q}}_s^t, \qquad \text{(C.13)}$$

where

$$\overline{\mathrm{V}}_s = \begin{pmatrix} x_s \\ y_s \\ z_s \\ 0 \end{pmatrix}, \quad \overline{\mathrm{V}}_t = \begin{pmatrix} x_t \\ y_t \\ z_t \\ 0 \end{pmatrix}. \qquad \text{(C.14)}$$

Direction cosine matrix to quaternion

From a direction cosine matrix $\underline{\mathrm{R}}_s^t$, the corresponding quaternion $\overline{\mathrm{Q}}_s^t$ can be derived in the following way, cf. Wu et al. (2006) and Wertz (1991):

$$\begin{aligned} q_0 &= \sqrt{1 + R_{1,1} + R_{2,2} + R_{3,3}}/2, \qquad \text{(C.15)} \\ q_1 &= -(R_{2,3} - R_{3,2})/4q_0, \qquad \text{(C.16)} \\ q_2 &= -(R_{3,1} - R_{1,3})/4q_0, \qquad \text{(C.17)} \\ q_3 &= -(R_{1,2} - R_{2,1})/4q_0, \qquad \text{(C.18)} \\ \overline{\mathrm{Q}}_s^t &= \begin{bmatrix} q_1 \\ q_2 \\ q_3 \\ q_0 \end{bmatrix}. \qquad \text{(C.19)} \end{aligned}$$

Quaternion to direction cosine matrix

From a given quaternion $\overline{\mathrm{Q}}_s^t$, the corresponding direction cosine matrix $\underline{\mathrm{R}}_s^t$ can be derived in the following way, cf. Wu et al. (2006) and Wertz (1991):

$$\underline{\mathrm{R}}_s^t = \begin{pmatrix} q_0^2 + q_1^2 - q_2^2 - q_3^2 & 2(q_1q_2 + q_0q_3) & 2(q_1q3 - q_0q_2) \\ 2(q_1q_2 - q_0q_3) & q_0^2 - q_1^2 + q_2^2 - q_3^2 & 2(q_2q3 + q_0q_1) \\ 2(q_1q3 + q_0q_2) & 2(q_2q3 - q_0q_1) & q_0^2 - q_1^2 - q_2^2 + q_3^2 \end{pmatrix}. \qquad \text{(C.20)}$$

Attitude dynamics

The dynamics of a body's attitude are reflected in the time dependency of its orientation. There are two possibilities for representing a change in the orientation:

- the source system changes,
- the target system changes.

The logic of dealing with changes of orientation depends on the application: If the source system changes, one transforms first back from the changed, 'new' source system to the original,'old' source system and then, using the original orientation, to the target system. If the target system changes one transforms to the 'old' target system by using the original orientation and then to the changed, 'new' target system.

Here, we will consider only the option of changing the target system. There are in principal two practical applications:

- The angular rates of the target system (satellite fixed body system) are known and the change in the orientation is to be derived,
- The time series of the orientation of the target system is given and the corresponding angular rates are to be derived.

Both aspects are treated by the 'kinematic equations' describing the connection between the orientation of a body and its angular velocity.

First, we will give formulations for the change in orientation resulting from known angular rates. If the orientation is represented by quaternions, we get the following formulation, cf. Wertz (1991):

$$\begin{aligned}
\overline{\mathrm{Q}}(t+\Delta t) &= \left\{ \cos\frac{\Delta\Phi}{2}\cdot\underline{1} + \sin\frac{\Delta\Phi}{2}\cdot\begin{bmatrix} 0 & e_z & -e_y & e_x \\ -e_z & 0 & e_x & e_y \\ e_y & -e_x & 0 & e_z \\ -e_x & -e_y & -e_z & 0 \end{bmatrix} \right\} \cdot \overline{\mathrm{Q}}(t) \\
&= \left\{ \cos\frac{\Delta\Phi}{2}\cdot\underline{1} + \frac{\sin\frac{\Delta\Phi}{2}}{\omega}\cdot\begin{bmatrix} 0 & \omega_z & -\omega_y & \omega_x \\ -\omega_z & 0 & \omega_x & \omega_y \\ \omega_y & -\omega_x & 0 & \omega_z \\ -\omega_x & -\omega_y & -\omega_z & 0 \end{bmatrix} \right\} \cdot \overline{\mathrm{Q}}(t). \qquad \text{(C.21)}
\end{aligned}$$

$\Delta\Phi = \sqrt{\omega_x^2+\omega_y^2+\omega_z^2}\cdot\Delta t = \omega\cdot\Delta t$ is the rotation angle during Δt and $\underline{1}$ is a 4×4 identity matrix. The angular velocities ω_x, ω_y, ω_z refer to the respective body axes. We simplify to get:

$$\begin{aligned}
\overline{\mathrm{Q}}(t+\Delta t) &= \overline{\mathrm{Q}}(t) \star \begin{pmatrix} \sin(\frac{\Delta\Phi}{2})\cdot\frac{\omega_x}{\omega} \\ \sin(\frac{\Delta\Phi}{2})\cdot\frac{\omega_y}{\omega} \\ \sin(\frac{\Delta\Phi}{2})\cdot\frac{\omega_z}{\omega} \\ \cos(\frac{\Delta\Phi}{2}) \end{pmatrix} \\
&= \overline{\mathrm{Q}}(t) \star \overline{\Upsilon}(t). \qquad \text{(C.22)}
\end{aligned}$$

From a given time series of quaternions, the angular rates can be derived in the following way:

$$\overline{\Upsilon}(t) = \overline{\mathrm{Q}}(t)^{-1} \star \overline{\mathrm{Q}}(t+\Delta t) = \begin{pmatrix} \upsilon_1 \\ \upsilon_2 \\ \upsilon_3 \\ \upsilon_4 \end{pmatrix}, \tag{C.23}$$

$$\Delta\Phi = 2 \cdot \arccos(\upsilon_4), \tag{C.24}$$

$$\omega = \Delta\Phi/\Delta t, \tag{C.25}$$

$$\omega_x = \upsilon_1 \cdot \frac{\omega}{\sin(\frac{\Delta\Phi}{2})}, \tag{C.26}$$

$$\omega_y = \upsilon_2 \cdot \frac{\omega}{\sin(\frac{\Delta\Phi}{2})}, \tag{C.27}$$

$$\omega_z = \upsilon_3 \cdot \frac{\omega}{\sin(\frac{\Delta\Phi}{2})}. \tag{C.28}$$

If we assume Δt and/or ω is small, we can use the small angles approximations

$$\begin{aligned} \cos(\frac{\Delta\Phi}{2}) &\approx 1, \\ \sin(\frac{\Delta\Phi}{2}) &\approx \frac{1}{2}\,\omega \cdot \Delta t \end{aligned}$$

to obtain

$$\begin{aligned} \overline{\mathrm{Q}}(t+\Delta t) &= \left\{ \underline{1} + \frac{1}{2} \cdot \Delta t \cdot \begin{bmatrix} 0 & \omega_z & -\omega_y & \omega_x \\ -\omega_z & 0 & \omega_x & \omega_y \\ \omega_y & -\omega_x & 0 & \omega_z \\ -\omega_x & -\omega_y & -\omega_z & 0 \end{bmatrix} \right\} \cdot \overline{\mathrm{Q}}(t) \\ &= \overline{\mathrm{Q}}(t) + \frac{1}{2} \cdot \Delta t \cdot \overline{\mathrm{Q}}(t) \star \begin{pmatrix} \omega_x \\ \omega_y \\ \omega_z \\ 0 \end{pmatrix} \\ &= \frac{1}{2} \cdot \Delta t \cdot \overline{\mathrm{Q}}(t) \star \begin{pmatrix} \omega_x \\ \omega_y \\ \omega_z \\ \frac{2}{\Delta t} \end{pmatrix} \\ &= \frac{1}{2} \cdot \Delta t \cdot \overline{\mathrm{Q}}(t) \star \overline{\Omega}(t). \end{aligned} \tag{C.29}$$

For the inverse task, the derivation of angular rates from a time series of quaternions, we obtain:

$$\overline{\Omega}(t) = 2 \cdot \overline{\mathrm{Q}}^{-1}(t) \star \frac{\overline{\mathrm{Q}}(t+\Delta t)}{\Delta t}. \tag{C.30}$$

For the orientation representation by DCM, we get:

$$\begin{aligned} \underline{\mathrm{R}}(t+\Delta t) &= \underline{\mathrm{R}}_{\omega} \cdot \underline{\mathrm{R}}(t) \\ &= \left[\begin{pmatrix} \frac{1}{\Delta t} & \omega_z & -\omega_y \\ -\omega_z & \frac{1}{\Delta t} & \omega_x \\ \omega_y & -\omega_x & \frac{1}{\Delta t} \end{pmatrix} \cdot \Delta t \right] \cdot \underline{\mathrm{R}}(t) \\ &= \left[\underline{\Omega}'(t) \cdot \Delta t \right] \cdot \underline{\mathrm{R}}(t). \end{aligned} \tag{C.31}$$

The angular rates can then be obtained from:

$$\underline{\Omega}'(t) = \frac{\underline{\mathrm{R}}(t+\Delta t)}{\Delta t} \cdot \underline{\mathrm{R}}^{-1}(t) = \frac{\underline{\mathrm{R}}(t+\Delta t)}{\Delta t} \cdot \underline{\mathrm{R}}'(t). \tag{C.32}$$

D. Coordinate frames

D.1. Inertial reference frame (IRF)

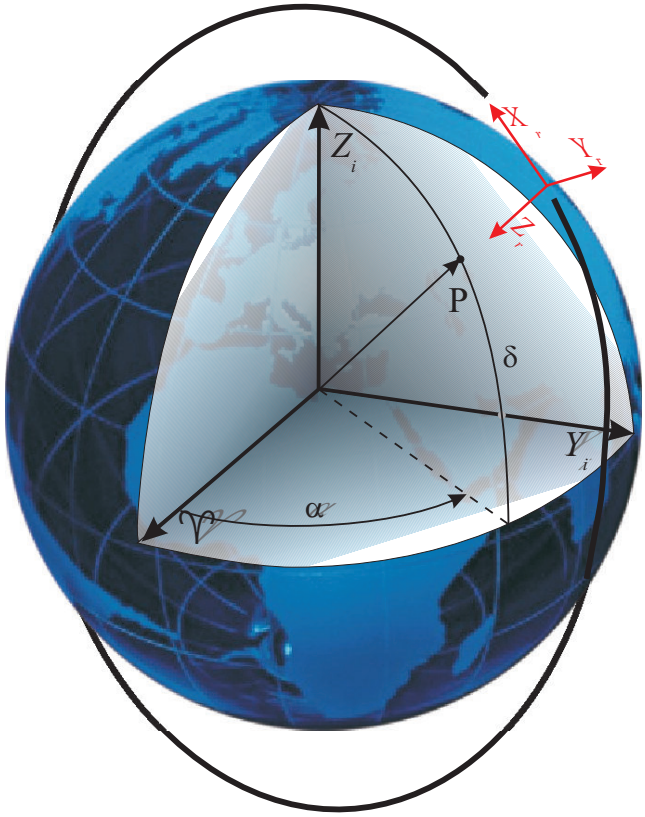

Figure D.1: Earth centered inertial reference frame

The origin of the inertial reference frame is the mass center of the Earth. The x-axis is defined by the Vernal Equinox, the z-axis is the rotation axis of the Earth at a reference epoch. The y-axis completes the right hand triad.

D.2. Orbit fixed reference frame (ORF)

Figure D.1 also shows the orbit fixed reference frame (in red). There are two types of ORFs:

1. Nadir/radial pointing ORF
2. Velocity pointing ORF

Both types can be derived from a orbit given in the IRF in the following way:

Nadir/radial pointing ORF

$$\widehat{\mathrm{Z}}_{ORF} = -\widehat{\mathrm{X}}^{sat}_{IRF}, \tag{D.1}$$
$$\widehat{\mathrm{Y}}_{ORF} = \widehat{\mathrm{Z}}_{ORF} \times \dot{\widehat{\mathrm{X}}}^{sat}_{IRF}, \tag{D.2}$$
$$\widehat{\mathrm{X}}_{ORF} = \widehat{\mathrm{Z}}_{ORF} \times -\widehat{\mathrm{Y}}_{ORF}. \tag{D.3}$$

Velocity pointing ORF

$$\widehat{\mathrm{X}}_{ORF} = \dot{\widehat{\mathrm{X}}}^{sat}_{IRF}, \tag{D.4}$$
$$\widehat{\mathrm{Y}}_{ORF} = \widehat{\mathrm{Z}}^{sat}_{IRF} \times \widehat{\mathrm{X}}_{ORF}, \tag{D.5}$$
$$\widehat{\mathrm{Z}}_{ORF} = \widehat{\mathrm{X}}_{ORF} \times \widehat{\mathrm{Y}}_{ORF}. \tag{D.6}$$

D.3. Earth-fixed reference frame (EFRF)

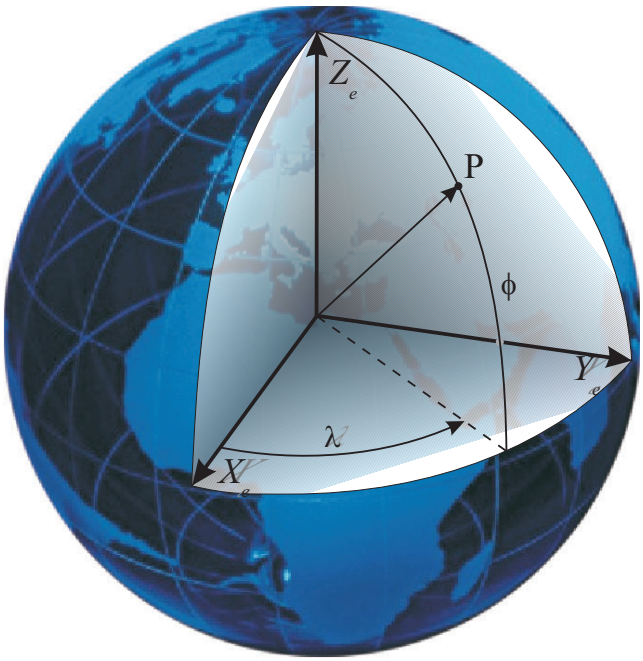

Figure D.2: Earth-Fixed Reference Frame (EFRF).

The origin of the earth-fixed reference frame is the mass center of the Earth. The direction of the x-axis is defined by the Greenwich meridian. The z-axis is the current rotation axis of the Earth. The y-axis completes the right hand triad. The transformation between EFRF and IRF is described e.g. in McCarthy (2006) and is not described here.

D.4. Satellite fixed reference frame (SRF)

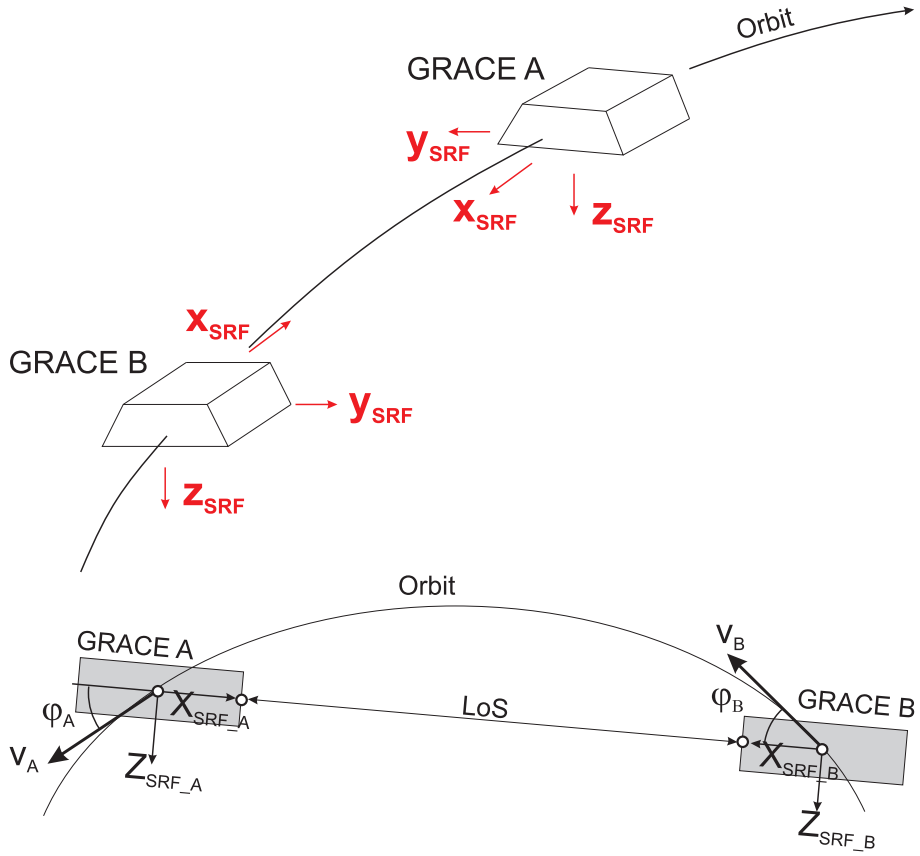

Figure D.3: Satellite fixed reference frame (SRF). The frame of GRACE A and B are oriented towards each other.

The Satellite fixed reference frame has its origin in the center of mass of the satellite. The x-axis is defined by the direction to the K-band horn, the z-axis is positive towards the radiator/nadir, the y-axis completes the right hand triad, cf. Bettadpur (2007). The relative orientation of the SRF of GRACE A and B is shown in the upper panel of figure D.3. For the leading satellite, the x-axis of the SRF is oriented opposite to the flight direction, for the trailing satellite, the x-axis points into flight direction. The lower panel of figure D.3 shows that the x-axes of the SRF of each satellite are not perfectly parallel to their velocity vectors. As the distance between the satellites is smaller than 200 km, this deviation is small.

D.5. Instrument frames

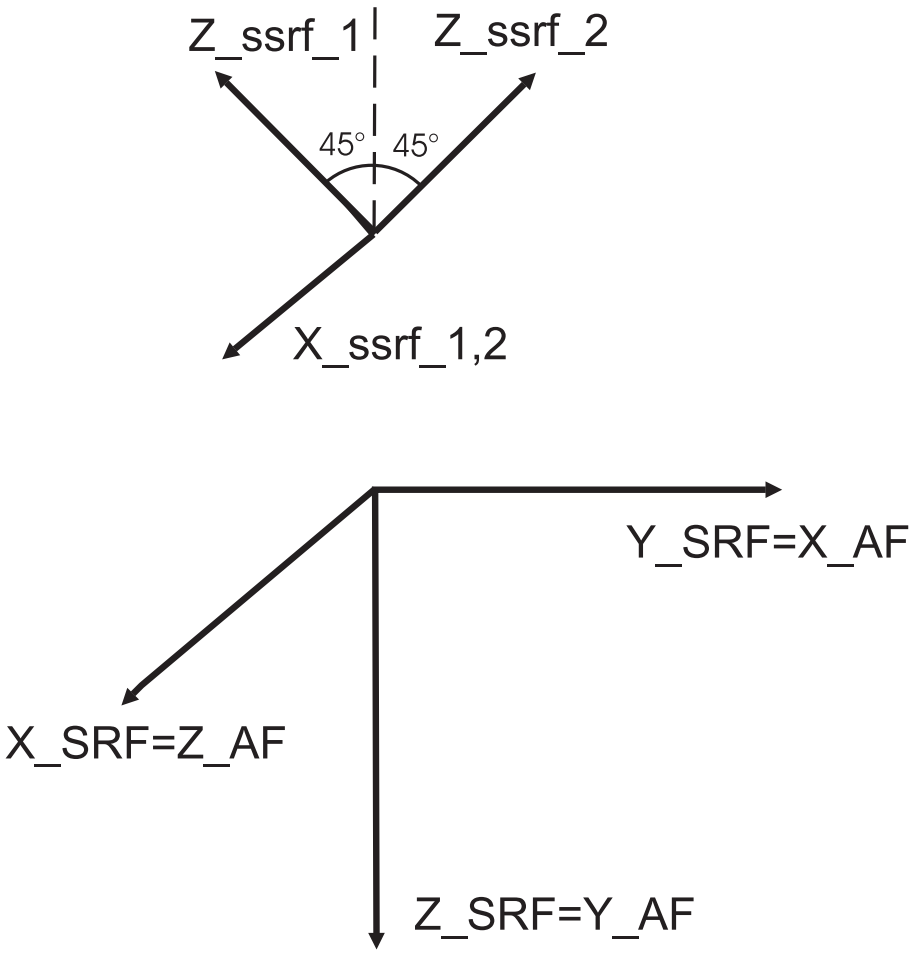

Figure D.4: Star sensor reference frame (SSRF) and accelerometer reference frame (AF).

The accelerometer frame (AF) is derived from the SRF only by a switching of axes, see figure D.4:

$$\begin{aligned}\widehat{\mathrm{X}}_{srf} &= \widehat{\mathrm{Z}}_{arf},\\ \widehat{\mathrm{Y}}_{srf} &= \widehat{\mathrm{X}}_{arf},\\ \widehat{\mathrm{Z}}_{srf} &= \widehat{\mathrm{Y}}_{arf}.\end{aligned}$$

The star sensor reference frames (SSRF) are identical to the SRF, except for a rotation by $\pm 45°$ about the x-axis. The z-axis of the SSRF defines the line of sight of the individual star sensor head.

Bibliography

Best, R. (1991). *Digitale Meßwertverarbeitung*. R. Ouldenbourg, München,Wien.

Bettadpur, S. (2007). Product Specification Document. Technical Report CSR-GR-03-02, Center for Space Research, The University of Texas at Austin.

Bhanderi, D. D. and Bak, T. (2005). Modelling Earth Albedo for Satellites in Earth Orbit. Technical report, American Institute of Aeronautics and Astronautics.

Blewitt, G. (2006). Lecture Notes.

ESA (2000). Space Engineering - Space Envrionment. Technical report, European Coorporation for Space Standardization.

Flury, J. (2004). Beiträge zur Signalanalyse der GRACE L1a Akzelerometerdaten.

Flury, J., Bettadpur, S., and Tapley, B. (2007). Precise Accelerometry Onboard the GRACE Gravity Field Satellite Mission. *Advances in Space Research*.

Gerstl, M. (1998). DOGS Version 4.04. Technical report, DGFI, München.

Hedin, A. E. (1987). MSIS-86 Thermospheric Model. *Journal of Geophysical Research*, 92(A5):4649–4662.

Hedin, A. E., Biondi, M. A., Burnside, R. G., Hernandez, G., Johnson, R. M., Killeen, T. L., Mazaudier, C., Meriwether, J. W., Salah, J. E., Sica, R. J., Smith, R. W., Spencer, N. W., Wickwar, V. B., and Virdi, T. S. (1991). Revised Global Model of Thermosphere Winds using Satellite and Ground-based Observations. *Journal of Geophysical Research*, 96(A5):7657–7688.

Hedin, A. E., Fleming, E. L., Manson, A. H., Schmidlin, F. J., Avery, S. K., Clark, R. R., Franke, S. J., Fraser, G. J., Tsuda, T., Vial, F., and Vincent, R. A. (1996). Empirical Wind Model for the upper, middle and lower Atmosphere. *Journal of Atmospheric and Terrestrial Physics*, 58:1421–1447.

Hedin, A. E., Spencer, N. W., and Killeen, T. L. (1988). Empirical Global Model of Upper Thermosphere Winds based on Atmosphere and Dynamics Explorer Satellite Data. *Journal of Geophysical Research*, 93(A9):9959–9978.

Hudson, D. (2003). In-Flight Characterization and Calibration of the SuperSTAR Accelerometer.

Jäggi, A. and Svehla, D. (2007). Personal Communication.

Jørgenson, J. L. (1999). In-Orbit Performance Of A Fully Autonomous Star Tracker. Technical report, Technical University of Denmark.

Josselin, V., Touboul, P., and Kielbasa, R. (1999). Capacitive Detection Scheme for Space Accelerometers Applications. *Sensors and Actuators, Elsevier Science Ltd.*, 78:92–98.

Kandel, R. (1980). *Earth and Cosmos*. Oxford, Pergamon Press, Ltd.

Kim, J. (2000). Simulation Study of a Low-Low Satellite-to-Satellite Tracking Mission. Technical report, University of Texas at Austin.

Klinkrad, H. and Fritsche, B. (1998). Orbit and Attitude Perturbations due to Aerodynamics and Radiation Pressure. Technical report, ESA.

Knechtel, E. and Pitts, W. (1973). Normal and Tangential Momentum Accommodation for Earth Satellite Conditions. *Astronautica Acta*, 18:171–184.

Koppenwallner, G. (1988). Aerodynamik von Satelliten. In Hallman and Ley, editors, *Handbuch der Raumfahrtechnik*, pages 438–482. Carl-Hauser Verlag, München.

Mazanek, D. D., Kumar, R. R., and Qu, M. (2000). Aerothermal Analysis and Design of the Gravity Recovery and Climate Experiment. Technical report, National Aeronautics and Space Administration.

McCarthy, D. D. (2006). IERS Conventions 2006. Technical report, IERS Technical Note 32.

Meyer, M. (1998). *Signalverarbeitung*. Friedrich Vieweg & Sohn, Braunschweig/Wiesbaden.

Montenbruck, O. and Gill, E. (2000). *Satellite Orbits*. Springer Verlag, Berlin, Heidelberg.

Müller, J. (2001). Die Satellitengradiometriemission GOCE. Technical report, Technical University of Munich.

Oberndorfer, H. (2000). Integrierte Sensoranalyse am Beisiel des Satelliten CHAMP. Technical Report Mu 1141/2-1, Institut für Physikalische und Astronomische Geodäsie, TU München.

Oppenheim, A. and Schafer, R. (1975). *Discrete-Time Signal Processing*. Prentice hall.

Oppenheim, A. and Schafer, R. (1989). *Discrete-Time Signal Processing*. Prentice hall.

Romans, L. (2003). Optimal Combination of Quaternions from Multiple Star Cameras. Technical report, Jet Propulsion Laboratory.

Rothacher, M. (2001). Vorlesungsskript Messmethoden der Physikalischen Geodäsie.

Sagirov, P. (1970). *Satellitendynamik*. Bibliographisches Institut, Mannheim, Germany.

Schaaf, S. A. and Chambre, P. L. (1961). *Flow of Rarefied Gases*. Princeton University Press, Princeton, New Jersey.

Smit, J. M. (2000). GOCE End to End Closed Loop Simulation, workpackage 210. *GOCE End to End Performance Analysis, ESTEC Contract No.12735/98/NL/GD*, 1:9–30.

Stanton, R., Bettadpur, S., Dunn, C., Renner, K.-P., and Watkins, M. (1998). GRACE Science & Mission Requirements Document. Technical Report 327 - 200, Jet Propulsion Laboratory.

Stoica, P. and Moses, R. (1997). *Introduction to Spectral Analysis*. Prentice hall.

Thalhammer, M. (1989). Nichtgravitative Kräfte und Drehmomente im Flugbereich Künstlicher Erdsatelliten.

Thomas, J. (1999). An Analysis of the Gravity Field Estimation Based on Dual-1-Way Intersatellite Biased Ranging. Technical report, Jet Propulsion Laboratory, Pasadena.

Touboul, P., Foulon, B., and Willemont, E. (1999). Electrostatic Space Accelerometers for Present and Future Missions. *Acta Astronautica, Elsevier Science Ltd.*, 45:605–617.

Wang, F. (2003). Study on Center of Mass Calibration and K-band Ranging System Calibration of the GRACE Mission.

Wermuth, M. (2000). Berechnung der Abschattung eines Satelliten. Technical report, Institut für Astronomische und Physikalische Geodäsie, TU München.

Wertz, J. R. (1991). *Spacecraft Attitude Determination and Control*. Kluwer Academic Publishers, Dordrecht/Boston/London.

Wu, S.-C., Kruizinga, G., and Bertinger, W. (2006). Algorithm Theoretical Basis Document for GRACE Level-1B Data Processing V1.2. Technical Report JPL D-27672, Jet Propulsion Laboratory.